

# Effects of QCD Radiation on Higgs Production at the Large Hadron Collider

A dissertation submitted to the  
SWISS FEDERAL INSTITUTE OF TECHNOLOGY ZÜRICH

for the degree of  
**Dr. Sc. ETH Zürich**

presented by  
**Fabian Stöckli**

Dipl.-Phys. ETH Zürich  
born September 11<sup>th</sup>, 1979  
citizen of Hermetschwil-Staffeln, AG  
Switzerland

<b>Prof. G. Dissertori</b>	examiner
<b>Prof. Z. Kunszt</b>	co-examiner
<b>Prof. B. R. Webber</b>	co-examiner



# Abstract

In this thesis a detailed discussion of higher-order QCD corrections up to next-to-next-to leading order (NNLO) for the Higgs production in the *Gluon-Fusion* channel at the LHC is presented. First the corrections are studied in dependence of the Higgs boson kinematics. It is found that they vary significantly within different Higgs boson phase-space regions, and only taking into account this dependency results in a reliable prediction for specific kinematic observables. The technique of differential re-weighting is discussed in order to incorporate the higher-order corrections into parton-shower MC event generators.

The QCD corrections are then discussed for the two specific Higgs decay modes,  $H \rightarrow \gamma\gamma$  and  $H \rightarrow WW \rightarrow l\nu l\nu$ , after the application of typical experimental selection cuts, using fully differential, fixed-order calculation methods. In latter case this is the first time a fully differential calculation has been performed at this order of perturbative QCD. It is found that in the case of  $H \rightarrow \gamma\gamma$  the corrections after applying the cuts behave very 'inclusive-like'. In the case of the decay  $H \rightarrow WW \rightarrow l\nu l\nu$  the corrections after the application of the selection cuts differ significantly from the inclusive case. The predictions at fixed NNLO for the cross-section after these cuts are tested against calculations including resummation of large logarithmic terms arising from multiple soft and collinear radiation. The results are found to agree within a remarkable precision, and thus it is concluded, that the predicted cross-section is very reliable.

Finally, the NNLO predictions for the cross-section are incorporated into a detector simulation for the CMS experiment. From this the expected experimental event rate is computed and the needed luminosities for an exclusion or a discovery of the Higgs boson with mass  $m_H=165$  GeV are estimated, including theoretical as well as experimental systematic uncertainties. It is found that the CMS experiment can discover/exclude with high probability a Higgs boson of this mass after collecting data corresponding to an integrated luminosity of less than  $\mathcal{L} = 1 \text{ fb}^{-1}$ , which is in agreement with earlier studies.



# Zusammenfassung

In der vorliegenden Dissertation werden die QCD Korrekturen bis zur zweiten Ordnung (englisch: next-to-next-to-leading order, NNLO) für die Higgs Produktion im *Gluon-Fusions* Prozess am LHC diskutiert. Zuerst werden diese Korrekturen in Abhängigkeit der Higgs Boson Kinematik studiert, und es stellt sich heraus, dass sie für verschiedenen Regionen des Higgs-Phasenraums variieren. Nur wenn diese Phasenraumabhängigkeit mitberücksichtigt wird, können zuverlässige Vorhersagen für bestimmte kinematische Observablen getroffen werden. Weiters wird die Technik des differentiellen Umgewichtens erläutert, die es erlaubt, solche Korrekturen höherer Ordnung in sog. *Partonschauer Monte Carlo Generatoren* zu integrieren.

Die Korrekturen werden dann in den zwei spezifischen Zerfallskanälen  $H \rightarrow \gamma\gamma$  und  $H \rightarrow WW \rightarrow \ell\nu\ell\nu$  studiert, nachdem typische experimentelle Schnitte angebracht wurden; dies mit Hilfe von komplett differentiellen Berechnungsmethoden. In Fall von  $H \rightarrow WW \rightarrow \ell\nu\ell\nu$  ist dies die erste Berechnung dieser Art bis zur NNLO. Es zeigt sich, dass sich die Korrekturen im Fall von  $H \rightarrow \gamma\gamma$  ähnlich verhalten wie für die inklusiven Wirkungsquerschnitte. Für den Zerfall in Leptonen über ein Paar von W Bosonen ist dies nicht der Fall. Die Voraussagen der Störungsrechnung bis zur NNLO für den Wirkungsquerschnitt nach dem Anbringen der experimentellen Schnitte werden daher mit Rechnungen verglichen, die dominante logarithmische Terme aufgrund mehrfacher weicher und ko-linearer Strahlung mitberücksichtigen. Es wird gezeigt, dass diese Resultate mit der Störungsrechnung bis zur NNLO übereinstimmen. Daher kann gefolgert werden, dass die Vorhersage der NNLO Störungsrechnung für den Wirkungsquerschnitt sehr zuverlässig ist.

Schliesslich werden die NNLO Vorhersagen für den Wirkungsquerschnitt mit einer Detektorsimulation für das CMS Experiment am LHC verbunden. Aus der daraus folgenden Vorhersage für die Anzahl erwarteter Higgs Ereignisse wird die Luminosität berechnet, welche benötigt wird, damit das CMS Experiment die Existenz eines Higgs Bosons mit Masse  $m_H = 165 \text{ GeV}$  entweder beweisen oder ausschliessen kann. Es stellt sich heraus, dass dies mit hoher Wahrscheinlichkeit nach einer integrierten Luminosität von weniger als  $1 \text{ fb}^{-1}$  möglich ist, in guter Übereinstimmung mit vorangegangenen Studien.



# Contents

<b>Introduction</b>	<b>1</b>
<b>I Phenomenology of the Higgs Boson at the LHC</b>	<b>5</b>
<b>1 The Standard Model of Particle Physics</b>	<b>7</b>
1.1 Symmetry and Interaction: Gauge Field Theory . . . . .	8
1.1.1 Abelian Example: QED . . . . .	9
1.1.2 Non-Abelian Local Symmetries . . . . .	11
1.2 The Glashow-Salam-Weinberg Model . . . . .	12
1.2.1 Higgs Mechanism and Gauge-Boson Masses . . . . .	12
1.2.2 Couplings To Fermions . . . . .	15
1.2.3 Fermion Mass Terms and the Higgs Boson . . . . .	17
1.3 Quantum Chromo Dynamics (QCD) . . . . .	19
1.3.1 Group Structure of $SU(3)$ . . . . .	19
1.3.2 QCD Lagrangian and Feynman Rules . . . . .	20
1.3.3 The Running of the Coupling and Asymptotic Freedom . . . . .	21
1.3.4 Hadronic Processes and Parton Density Functions . . . . .	23
1.3.5 Soft and Collinear Effects: Parton Evolution and Parton Shower . . . . .	25
1.3.6 Long Distance Effects: Hadronization . . . . .	27
1.3.7 Underlying Event and Multi-Parton Interactions . . . . .	29
1.4 Cross-Section and Decay-Width . . . . .	29
1.5 Tests and Limitations of the Standard Model . . . . .	30
<b>2 SM Higgs Phenomenology at the Large Hadron Collider</b>	<b>33</b>
2.1 Higgs Production and Decay Modes . . . . .	33
2.1.1 Production Processes and Cross-Sections . . . . .	33
2.1.2 Decay Modes and Branching Ratios . . . . .	36
2.1.3 Towards Discovering the Higgs . . . . .	38
2.2 Improving the Predictions: Higher Order QCD Effects . . . . .	39
2.2.1 Fixed-Order Calculation . . . . .	40
2.2.2 Re-Summation . . . . .	45

2.3	Higher Order QCD Effects and Event Generators: The Re-Weighting Technique . . . . .	50
2.3.1	The Re-Weighting Procedure . . . . .	51
2.3.2	Re-Weighting the <i>Gluon-Fusion</i> Process . . . . .	53
2.3.3	Limitations of the Re-Weighting Technique . . . . .	56
2.4	Conclusions of this Chapter . . . . .	56
<b>3</b>	<b>Higgs in the 'light' Mass Range: The Di-Photon Channel</b>	<b>59</b>
3.1	Fixed-Order Cross-Sections . . . . .	60
3.2	Re-Weighted Cross-Sections . . . . .	63
3.3	Kinematic Distributions . . . . .	65
3.4	Prompt Di-Photon Background and Signal Significance . . . . .	67
3.5	Conclusions of this Chapter . . . . .	68
<b>4</b>	<b>Higgs in the 'intermediate' Mass Range: The W-Pair Channel</b>	<b>69</b>
4.1	Final State Signature and Background Processes . . . . .	70
4.2	Fixed Order Results . . . . .	72
4.2.1	Differential Distributions . . . . .	73
4.2.2	Signal Cross-Section at the LHC . . . . .	77
4.3	Re-Summation Effects . . . . .	79
4.3.1	Differential Distributions . . . . .	79
4.3.2	Signal Cross-Section . . . . .	81
4.4	Jet Algorithm, Hadronization & the Underlying Event . . . . .	83
4.5	Conclusions of this Chapter . . . . .	86
<b>II</b>	<b>The Compact Muon Solenoid (CMS) Experiment at the LHC</b>	<b>87</b>
<b>5</b>	<b>Experimental Apparatus</b>	<b>89</b>
5.1	The Large Hadron Collider . . . . .	91
5.2	The Compact Muon Solenoid Experiment . . . . .	93
5.2.1	Central Tracking . . . . .	94
5.2.2	The Electromagnetic Calorimeter (ECAL) . . . . .	95
5.2.3	The Hadronic Calorimeter (HCAL) . . . . .	97
5.2.4	The Muon System . . . . .	98
5.2.5	The Trigger System . . . . .	99
<b>6</b>	<b>Physics Object Reconstruction</b>	<b>101</b>
6.1	Track Finding . . . . .	101
6.1.1	Local Reconstruction . . . . .	102
6.1.2	Seed Finding . . . . .	102



6.1.3	Pattern Recognition . . . . .	103
6.1.4	Final Fit . . . . .	103
6.2	Electron Reconstruction . . . . .	104
6.2.1	ECAL Stand-Alone Reconstruction . . . . .	104
6.2.2	Pixel Matching and Track Fitting . . . . .	105
6.3	Muon Reconstruction . . . . .	107
6.3.1	Stand-Alone Muon Reconstruction . . . . .	107
6.3.2	Global Muon Reconstruction . . . . .	108
6.4	Jet Reconstruction . . . . .	109
<b>7</b>	<b>Higgs Search in the WW Channel with the CMS Experiment</b>	<b>111</b>
7.1	Analysis Strategy . . . . .	112
7.2	Event Sample Production and Cross-Sections . . . . .	112
7.3	Object Identification and Selection Cuts . . . . .	113
7.3.1	Electron Identification . . . . .	114
7.3.2	Muon Identification . . . . .	117
7.3.3	Leptonic Selection Variables . . . . .	119
7.3.4	Jet Identification and Jet Veto . . . . .	122
7.3.5	Missing Transverse Energy . . . . .	123
7.4	Accepted Cross-Section and Uncertainties . . . . .	124
7.4.1	Systematic Uncertainty . . . . .	126
7.4.2	Theoretical Uncertainty . . . . .	126
7.4.3	Comparison of the Uncertainties . . . . .	128
7.5	Background Event-Rates . . . . .	129
7.6	Expected Signal Significance and Exclusion Limit . . . . .	131
7.7	Conclusions of this Chapter . . . . .	133
	<b>Conclusions</b>	<b>135</b>
<b>III</b>	<b>Appendix</b>	<b>137</b>
<b>A</b>	<b>Dirac Algebra</b>	<b>139</b>
<b>B</b>	<b>Higgs Production Cross-Sections</b>	<b>141</b>
B.1	N-Body Phase-Space . . . . .	142
B.1.1	1-Body Phase-Space . . . . .	142
B.1.2	2-Body Phase-Space . . . . .	142
B.2	<i>Higgs-Strahlung</i> Channel . . . . .	143
B.3	<i>Gluon-Fusion</i> Channel . . . . .	147

B.3.1	Matrix Element . . . . .	147
B.3.2	Evaluation of the Feynman Integral . . . . .	150
B.3.3	Cross-Section at the LHC . . . . .	152
<b>C</b>	<b>Sector Decomposition</b>	<b>155</b>
<b>D</b>	<b>The <math>H \rightarrow WW</math> Decay in FEHiP</b>	<b>159</b>
D.1	Concept . . . . .	159
D.2	Matrix Element . . . . .	161
D.3	$H \rightarrow WW$ Phase-Space . . . . .	162
D.4	$W \rightarrow \ell\nu\ell\nu$ Phase-Space . . . . .	165
D.5	Total Phase-Space . . . . .	166
D.6	Numerical Integration . . . . .	169
D.6.1	VEGAS algorithm . . . . .	169
D.6.2	Integrating the Higgs Process . . . . .	170
	<b>Bibliography</b>	<b>173</b>
	<b>List of Abbreviations</b>	<b>179</b>
	<b>Acknowledgment</b>	<b>181</b>

# Introduction

“[...] I've figured out numbers and what they're for [...]”  
(*Pearl Jam, Light Years*)

Breaking down the sheer infinite complexity of the universe into a handful of fundamental relations and characteristics is absolutely essential if one wishes to understand the phenomena within the matter and the space that enclose us. While the trial of formulating these relations must be as old as the spoken word, it needed the formalism of natural science in general and mathematics in particular to reward these trials with success, success in a twofold manner. First, only the mathematical formulation of phenomena allows a quantification and thus a verification against measured observations, second, it can in general be understood and tested by anyone.

Together with the deployment of the scientific tools, the idea that matter is built up from a limited set of fundamental components was raised. The idea that the profound constituents are the elements water, fire, earth and air was stated by the Greek philosopher Empedocles five centuries B.C.. Shortly thereafter Leucippus and Democritus established the principle that all matter is formed by extremely small, fundamental and indestructible particles, that they called *atoms*. The idea of the atoms was picked up by scientists in the 19<sup>th</sup> century, but only in the year 1909, with the experiment of Ernest Rutherford, it became clear that the atoms are not fundamental, but built up from a nucleus and surrounding electrons. With the discovery of the neutron in 1932 it was established that the nucleus itself is composed of smaller particles.

In the 50's and 60's of the 20<sup>th</sup> century a variety of collider experiments showed that there are many more particles with similar character as the protons and neutrons. It was suspected that they themselves are not fundamental, but formed by even smaller particles, the *quarks*. The *quark model*, which found a convincing confirmation in the discovery point-like constituents of the protons in 1969, allowed to classify all the known *hadrons* as compound objects of two or three quarks.

In parallel to the search for the basic components of matter, the question of how these components interact was posed. The work of James Clerk Maxwell was pioneering in this

---

respect. He discovered that electricity and magnetism are two phenomena of the same fundamental mechanism, the so called *electro-magnetism*. He formulated this observation in a set of equations, known as the *Maxwell equations*. These equations, together with the discovery of the quantum nature of physics and special relativity, formed later the very successful theory of *Quantum Electrodynamics* (QED).

Inspired by the success of the field theoretical formulation of the electro-magnetic force, the attempt was undertaken to describe the other forces, the *weak force* responsible for the decay of nuclei and the *strong force*, responsible for the formation of hadrons, which were discovered in the nuclear physics experiments of the 20<sup>th</sup> century, in a similar way. It was found that the strong interaction can be formulated as a relativistic field-theory of *color* charged quarks and gluons, known as *Quantum Chromodynamics* (QCD). The weak force could be combined with QED into the so called *Electro-Weak Interaction*, also known as *Glashow-Weinberg-Salam* (GWS) model. The GWS theory together with QCD form the nowadays most successful theory for the interaction of fundamental particles, referred to as the *Standard Model of Particle Physics*.

In general in such theories, also known as *Gauge Theories*, the particles responsible for the action of the force (the *Gauge- or Vector- Bosons*) have to be massless. Experiments showed however that the particles responsible for the weak interaction are massive. Fortunately a mechanism, the so called *Higgs mechanism*, is at hand to remedy this shortcoming. This mechanism, established and published in 1964 by Peter Higgs, as well as by Robert Brout and Francois Englert, allows the Gauge-Bosons to acquire a mass by the so-called *Electro-Weak Symmetry-breaking*. The price for this is the introduction of an additional particle, the *Higgs Boson*.

A variety of tests and precision measurements over the last decades gave very strong confidence in the Standard Model. The only missing piece is the Higgs particle, responsible for the masses of the fermions and the weak gauge bosons. The phenomenological understanding of the perturbative predictions for the Higgs particle beyond the lowest order and their consequences for an experimental observation are the core content of this thesis.

The thesis is divided into three parts. Part one is dedicated to the theoretical aspects of the Higgs phenomenology at hadron colliders. After a brief introduction of the Standard Model of Particle Physics in chapter 1 we turn in chapter 2 to the specific Higgs production processes and decay modes, where emphasis is put on the effects of higher order QCD radiation on the important Higgs observables. In chapters 3 and 4 we then discuss these effects for the two specific modes when the Higgs decays into two photons and into two W bosons.

---

The main focus of part two is the experimental aspect of the Higgs search with the *Compact Muon Solenoid* experiment (CMS) at the *Large Hadron Collider* (LHC). We explain the experimental apparatus in chapter 5 and the procedure of reconstructing the important quantities from the detector response in chapter 6. We conclude part two with a detailed study of the possible discovery/exclusion limit for a Higgs with mass  $m_H=165$  GeV with the CMS experiment, including detector effects and systematic uncertainties in chapter 7.

Finally in part three (appendix) we describe in more detail some of the calculations and methods used in the first two parts. After the bibliography a list of commonly used abbreviations can be found. In the presented thesis we use natural units throughout, i.e.  $c = \hbar = 1$ .



## Part I

# Phenomenology of the Higgs Boson at the LHC





# Chapter 1

## The Standard Model of Particle Physics

A large number of experiments give strong confidence in the picture that the particle content making up the matter in the universe consists of a set of fermions interacting via the exchange of vector bosons. Within this framework of the so called *Standard Model of Particle Physics* (SM) the fermions are divided into the group of leptons (the massive, electrically charged electron  $e$ , muon  $\mu$  and tau  $\tau$ , the almost massless, electrically neutral neutrinos  $\nu_e$ ,  $\nu_\mu$  and  $\nu_\tau$ , as well as their anti-particles) and the group of quarks (up  $u$ , down  $d$ , strange  $s$ , charm  $c$ , bottom  $b$  and top  $t$ ), which form bound states called hadrons (e.g. protons  $p$  and neutrons  $n$ ). We summarize the fermionic content of the Standard Model in Table 1.1. The fermions interact via three <sup>1</sup> forces: The *electromagnetic* interaction (*Quantum Electrodynamics*, QED), corresponding to the classical *Electrodynamics* first described in detail by Maxwell, the *Weak* interaction, responsible for the nucleon decays, and the *Strong* interaction, responsible for the formation of hadrons and atomic nuclei.

All these interactions have been successfully described within the framework of *relativistic Quantum Field Theories*. In what follows these theories will be briefly described focusing on the calculation-tools and consequences introduced by them needed in later stages of this thesis. More detailed discussions on Quantum Field Theories in general and the Standard Model in particular can e.g. be found in [1, 2].

We will start with the description of local symmetries, which imposed on the general Lagrangian for a free fermion field introduce additional mass-less vector fields, the *Gauge-Bosons*. From this the most general Lagrangian in the abelian case of the electro-magnetic

---

<sup>1</sup> It is not clear that these three forces are the only interaction mechanisms. One especially, but not exclusively, might be interested in the action of the gravitation. Nevertheless it has been shown that these three forces are sufficient to describe the elementary processes in particle physics to a very high precision.

	$1^{st}$ family	$2^{nd}$ family	$3^{rd}$ family
<i>leptons</i>	$\begin{pmatrix} \nu_e \\ e \end{pmatrix}$ $\begin{matrix} < 3 \text{ eV} \\ 0.511 \text{ MeV} \end{matrix}$	$\begin{pmatrix} \nu_\mu \\ \mu \end{pmatrix}$ $\begin{matrix} < 0.19 \text{ MeV} \\ 106 \text{ MeV} \end{matrix}$	$\begin{pmatrix} \nu_\tau \\ \tau \end{pmatrix}$ $\begin{matrix} < 18.2 \text{ MeV} \\ 1.777 \text{ GeV} \end{matrix}$
<i>quarks</i>	$\begin{pmatrix} u \\ d \end{pmatrix}$ $\begin{matrix} \sim 7 \text{ MeV} \\ \sim 3 \text{ MeV} \end{matrix}$	$\begin{pmatrix} c \\ s \end{pmatrix}$ $\begin{matrix} \sim 1.2 \text{ GeV} \\ \sim 115 \text{ MeV} \end{matrix}$	$\begin{pmatrix} t \\ b \end{pmatrix}$ $\begin{matrix} \sim 175 \text{ GeV} \\ \sim 4.25 \text{ GeV} \end{matrix}$

Table 1.1: Fermionic content of the *Standard Model of Particle Physics* with mass values divided into the three families, taken from [3].

interaction (QED) of fermions will be derived. The insights gained will then be deployed to construct the theory that describes the combined *Electroweak Interaction* as arising from a spontaneously broken  $SU(2) \times U(1)$  symmetry. The Feynman rules for the involved particles (fermions and gauge-boson), as well as for the additionally introduced Higgs boson will be discussed briefly.

In the next stage the field theory that describes the strong interaction (*Quantum Chromodynamics*, QCD) will be introduced using again the language of local symmetries. It will be shown that QCD is a so called asymptotically free theory, allowing to compute observable quantities for scattering processes using perturbative approaches if the momentum transfer  $Q$  in the process is large. Finally the important aspects of the non-perturbative regime of QCD relevant for collider experiments will be discussed, as implemented in full phenomenological simulations of processes appearing in hadron-hadron collisions.

The ingredients building up the solid framework of the *SM of Particle Physics* have been developed independently and over several years by many different people. We will not discuss nor follow any historical time-line; a very detailed and informative overview on the historical development of the *SM of Particle Physics* can e.g. be found in [4].

## 1.1 Symmetry and Interaction: Gauge Field Theory

In this section the most general Lagrangian  $\mathcal{L}$  for interacting fields is derived by starting with the postulate, that this Lagrangian  $\mathcal{L}$  is invariant (*symmetric*) under a certain set of transformations, i.e.

$$\mathcal{L} \rightarrow \mathcal{L}' = \mathcal{L}. \quad (1.1)$$

This will first be done for the symmetry-group  $U(1)$ , where the generators of the symmetry-group commute (the symmetry-group is *abelian*), then for a more general, non-abelian symmetry-group.

### 1.1.1 Abelian Example: QED

First, assume that the Lagrangian for the free, complex-valued Dirac-field  $\psi(x)$  (fermion-field) should be invariant under the transformations

$$\psi(x) \rightarrow e^{i\alpha(x)} \psi(x), \quad (1.2)$$

which corresponds to a  $U(1)$  transformation. The phase-rotation  $\alpha$  here is an arbitrary function of  $x$ , the symmetry is therefore called *local*. If  $\alpha$  is constant, the symmetry is called *global*. The construction of terms without derivatives is easy, i.e. the fermion mass term

$$\mathcal{L}_{\text{mass}} = m\bar{\psi}\psi \quad (1.3)$$

is obviously invariant under the transformation in eq. 1.2.

The construction of terms including derivatives (e.g. kinetic terms) is more complicated. The derivative of  $\psi$  in direction  $\eta$  is defined as <sup>2</sup>

$$\eta^\mu \partial_\mu \psi = \lim_{\varepsilon \rightarrow 0} \frac{\psi(x + \varepsilon\eta) - \psi(x)}{\varepsilon}, \quad (1.4)$$

describing a comparison of the field  $\psi$  at two infinitely separated points. But as seen in eq. 1.2 the field does not necessarily transform in the same way at these two points. In order to be able to define a meaningful derivative, the *comparator*  $U(y, x)$  has to be introduced, transforming as

$$U(y, x) \rightarrow U'(y, x) = e^{i\alpha(y)} U(y, x) e^{-i\alpha(x)} \quad (1.5)$$

The comparator can then be used to define the *covariant derivative* in direction  $\eta$  as

$$\eta^\mu D_\mu \psi(x) = \lim_{\varepsilon \rightarrow 0} \frac{\psi(x + \varepsilon\eta) - U(x + \varepsilon\eta, x)\psi(x)}{\varepsilon}. \quad (1.6)$$

In this way the comparator makes sure that the fields  $\psi$  and  $U\psi$  transform in the same way, and thus the field  $\psi$  and its covariant derivative  $D_\mu \psi$  transform also in the same way, namely as defined in eq. 1.2.

In order to be useful an expression for the comparator  $U$  has to be found. This can be achieved by Taylor-expanding  $U$  in the separation of the two points  $x$  and  $y$  as

$$U(x + \varepsilon\eta, x) = 1 - ig\varepsilon\eta^\mu A_\mu(x) + \mathcal{O}(\varepsilon^2), \quad (1.7)$$

where the constant  $g$  has been arbitrarily extracted from the term of order  $\varepsilon$ . The field  $A_\mu$  appearing in the coefficient of the expansion is called the *connection*. All terms of order  $\mathcal{O}(\varepsilon^2)$  vanish in the limit  $\varepsilon \rightarrow 0$  in the covariant derivative, which is then

$$D_\mu \psi(x) = \partial_\mu \psi(x) + igA_\mu(x)\psi(x). \quad (1.8)$$

---

<sup>2</sup> Summation over repeated indices is implied everywhere.

The transformation law for the connection field is

$$A_\mu \rightarrow A'_\mu = A_\mu - \frac{1}{g} \partial_\mu \alpha(x), \quad (1.9)$$

and the kinetic term for the Dirac-field can be written as

$$\mathcal{L}_{\text{kin}} = \bar{\psi} \gamma^\mu D_\mu \psi, \quad (1.10)$$

which is, by construction, invariant under the transformations defined in eq. 1.2. The simple demand that the Lagrangian should be invariant under local phase-rotations implies that a new field,  $A_\mu$ , has to be introduced.

To finalize the construction of the Lagrangian a kinetic term for the field  $A_\mu$  has to be constructed, i.e. a term that only depends on  $A_\mu$  and derivatives of it, but not on  $\psi$ . To do this we remark that, since the covariant derivative of the field  $\psi$  transforms like  $\psi$  itself, the covariant derivative of the covariant derivative, and thus the commutator of the covariant derivatives, will also transform in this way. The commutator of the covariant derivatives is

$$\begin{aligned} [D_\mu, D_\nu] \psi &= D_\mu D_\nu \psi(x) - D_\nu D_\mu \psi \\ &= [\partial_\mu, \partial_\nu] \psi + ig([\partial_\mu, A_\nu] - [\partial_\nu, A_\mu]) \psi - g^2 [A_\mu, A_\nu] \\ &= ig(\partial_\mu A_\nu - \partial_\nu A_\mu) \psi \equiv ig F_{\mu\nu} \psi, \end{aligned} \quad (1.11)$$

where it has been used explicitly that the derivatives  $\partial_\mu$ , as well as the components of the field  $A_\mu$  commute. The Field-Tensor  $F_{\mu\nu}$  is defined as

$$F_{\mu\nu} = \partial_\mu A_\nu - \partial_\nu A_\mu. \quad (1.12)$$

It can be concluded that all terms dependent on  $F_{\mu\nu}$  and its derivatives are locally symmetric. All other terms, namely a mass term for the connection-field  $A_\mu A^\mu$ , would break the symmetry under the local transformation from eq. 1.2.

If in addition invariance under the discrete transformations  $P$  (parity) and  $T$  (time inversion) is imposed, the most general Lagrangian is

$$\mathcal{L} = \bar{\psi} (i \not{D}) \psi - \frac{1}{4} (F_{\mu\nu})^2 - m \bar{\psi} \psi, \quad (1.13)$$

where the notation  $\not{D} = D_\mu \gamma^\mu$  has been used, with  $\gamma^\mu$  the Dirac-matrices<sup>3</sup>. Of course eq. 1.13 is the famous QED Lagrangian, describing the interaction of electrically charged fermions via the gauge-field (photon-field) and  $g = e$  is just the electric charge of the electron. It is worth stressing that the local gauge-symmetry forbids mass terms for the gauge-field, i.e. in order to preserve the symmetry the photons have to be massless.

---

<sup>3</sup> We use the so-called *chiral* representation for the Dirac-matrices. The exact definition as well as useful identities for the Dirac-algebra can be found in Appendix A.

### 1.1.2 Non-Abelian Local Symmetries

It has been demonstrated above how imposing a local  $U(1)$  symmetry constraint on the Lagrangian of the free fermion fields naturally demands the inclusion of a gauge-field. We now want to expand the discussion to any continuous group of transformations, represented by a set of  $n \times n$  unitary matrices  $V$ . The fields  $\psi$  then transform under this group as

$$\psi(x) = V(x)\psi(x). \quad (1.14)$$

The transformation can be expanded in the generators  $t^a$  of the group <sup>4</sup> as

$$V(x) = 1 + i\alpha^a(x)t^a + \mathcal{O}(\alpha^2), \quad (1.15)$$

where the  $x$ -dependence of the phases  $\alpha$  render the symmetry local again. The generators  $t^a$  are represented by  $n \times n$  hermitian matrices with  $n$  the dimension of the symmetry group.

The so called structure-constants of the symmetry group,  $f^{abc}$ , are defined by the commutation relation of the generators,

$$[t^a, t^b] = if^{abc}t^c. \quad (1.16)$$

It can be shown that there exists always a representation of the generators that renders the structure-constants totally anti-symmetric.

In analogy to the derivation for the QED Lagrangian, the derivative in the Lagrangian has to be replaced by the covariant derivative

$$D_\mu = \partial_\mu - igA_\mu^a t^a, \quad (1.17)$$

with a new field  $A_\mu^a$  for each of the generators  $t^a$  of the group. Each of these fields defines then a field-tensor, namely

$$igF_{\mu\nu}^a t^a = [D_\mu, D_\nu] = ig(\partial_\mu A_\nu^a - \partial_\nu A_\mu^a + gf^{abc}A_\mu^b A_\nu^c)t^a, \quad (1.18)$$

thus

$$F_{\mu\nu}^a = \partial_\mu A_\nu^a - \partial_\nu A_\mu^a + gf^{abc}A_\mu^b A_\nu^c, \quad (1.19)$$

where the fact that the generators of the symmetry-group do not necessarily commute has been used explicitly.

The general Lagrangian now looks very similar to the one in eq. 1.13,

$$\mathcal{L} = \bar{\psi}(i\not{D})\psi - \frac{1}{4}F_{\mu\nu}^a F^{a\mu\nu} - m\bar{\psi}\psi. \quad (1.20)$$

---

<sup>4</sup> In the  $U(1)$  case the only generator of the symmetry group is the identity  $\mathbf{1}$ .

To see the fundamental difference between this and the abelian Lagrangian in eq. 1.13, the expression for the field-tensors, eq. 1.18, has to be substituted in the Lagrangian of eq. 1.20. While in the QED case the only interaction terms (terms with at least three fields) are the ones between the fermion fields and the gauge-fields, in the non-abelian case there are terms with three and even four gauge-fields. This indicates how the gauge-fields (and thus their quanta, the gauge-bosons) interact with each other through three- resp. four-gauge-field vertices.

## 1.2 The Glashow-Salam-Weinberg Model

In this section the theory that successfully describes the electro-weak interaction is introduced. It will be shown that this is achieved with a gauge theory based on a spontaneously broken  $SU(2) \times U(1)$  symmetry. The breaking of the symmetry is mediated by an additional scalar field. As a consequence of the existence of an additional, scalar boson-field, the so called *Higgs* field, is predicted.

### 1.2.1 Higgs Mechanism and Gauge-Boson Masses

In the previous section it has been shown how the local invariance of the Lagrangian under the transformations of some symmetry group  $G$  leads to massless gauge-boson fields. Mass terms for the gauge-fields are explicitly forbidden, so they have to be introduced by some more complicated mechanism. We study this first on the example of the  $SU(2)$  symmetry group.

Let  $\phi$  be a scalar field that transforms like a spinor under  $SU(2)$  transformations, i.e.

$$\phi(x) \rightarrow e^{i\alpha^i(x)\frac{\sigma^i}{2}} \phi(x), \quad (1.21)$$

with  $\sigma^i$  the Pauli matrices <sup>5</sup>. The covariant derivative is then

$$D_\mu \phi = \left( \partial_\mu - \frac{ig}{2} A_\mu^i \sigma^i \right) \phi. \quad (1.22)$$

Assume now that  $\phi$  acquires a non-vanishing vacuum-expectation value, i.e.  $\langle \phi \rangle \neq 0$ , as

$$\langle \phi \rangle = \frac{1}{\sqrt{2}} \begin{pmatrix} 0 \\ v \end{pmatrix}, \quad (1.23)$$

---

<sup>5</sup> The Pauli-matrices are

$$\sigma^1 = \begin{pmatrix} 0 & 1 \\ 1 & 0 \end{pmatrix}, \quad \sigma^2 = \begin{pmatrix} 0 & -i \\ i & 0 \end{pmatrix} \quad \text{and} \quad \sigma^3 = \begin{pmatrix} 1 & 0 \\ 0 & -1 \end{pmatrix}.$$

where the gauge-symmetry freedom has been used to restrict the non-vanishing part to the lower entry. The important part of the kinetic term for the scalar field  $\phi$ , which is the square of the covariant derivative term, becomes then

$$|D_\mu\phi|^2 = \frac{1}{8}g^2 \begin{pmatrix} 0 & v \\ v & \end{pmatrix} \sigma^i\sigma^j \begin{pmatrix} 0 \\ v \end{pmatrix} A_\mu^i A^{j\mu} + \dots \quad (1.24)$$

We symmetrize in  $i$  and  $j$ ,

$$|D_\mu\phi|^2 = \frac{1}{16}g^2 \begin{pmatrix} 0 & v \\ v & \end{pmatrix} \{\sigma^i, \sigma^j\} \begin{pmatrix} 0 \\ v \end{pmatrix} A_\mu^i A^{j\mu} + \dots \quad (1.25)$$

and use the anti-commutation relation for the Pauli-matrices  $\{\sigma^i, \sigma^j\} = 2\delta^{ij}$ . The mass terms for the gauge-bosons  $A^i$  is then

$$\mathcal{L}_{i,\text{mass}} = \frac{1}{2}m_A^2 A_\mu^i A^{i\mu} = \frac{g^2 v^2}{8} A_\mu^i A^{i\mu}, \quad (1.26)$$

thus all three gauge-bosons receive the mass

$$m_A = \frac{gv}{2}. \quad (1.27)$$

In order to end up with one massless gauge-boson (one gauge-boson, the photon, has to be massless for a successful theory), in addition to the  $SU(2)$  symmetry a  $U(1)$  symmetry has to be imposed. The scalar field is assigned the charge  $1/2$  under  $U(1)$ , thus the field transforms as

$$\phi \rightarrow e^{i\alpha^i \frac{\sigma^i}{2}} e^{i\beta \frac{1}{2}} \phi, \quad (1.28)$$

where the  $x$ -dependence has been suppressed everywhere. The scalar field  $\phi$  acquires the same vacuum-expectation value as in eq. 1.23. Using the definition from eq. 1.8 the covariant derivative of  $\phi$  becomes

$$D_\mu\phi = (\partial_\mu - \frac{ig}{2}A_\mu^i\sigma^i - \frac{ig'}{2}B_\mu)\phi, \quad (1.29)$$

where the third term comes from the transformation under the  $U(1)$  symmetry and the constants  $g$  and  $g'$  have been extracted in the term linear in  $\varepsilon$  in the expansion of the comparator, i.e.

$$U(x + \varepsilon\eta, x) = 1 - \frac{i\varepsilon\eta^\mu}{2} (gA_\mu^i(x)\sigma^i + g'B_\mu(x)) + \mathcal{O}(\varepsilon^2). \quad (1.30)$$

The part of the kinetic term for the field  $\phi$ ,  $|D_\mu\phi|^2$ , giving rise to the mass terms for the gauge-bosons, is

$$\begin{aligned} \mathcal{L}_{\text{mass}} &= \frac{1}{8} \begin{pmatrix} 0 & v \\ v & \end{pmatrix} (gA_\mu^i\sigma^i + g'B_\mu) (gA^{j\mu}\sigma^j + g'B^\mu) \begin{pmatrix} 0 \\ v \end{pmatrix} \\ &= \frac{v^2}{8} \left( g^2 ((A_\mu^1)^2 + (A_\mu^2)^2) + (-gA_\mu^3 + g'B_\mu)^2 \right), \end{aligned} \quad (1.31)$$

where we have explicitly used the definition of the Pauli-matrices. Note that the two fields  $A^3$  and  $B$  are entangled. To find the mass eigenstates the fields can be disentangled by defining the new fields

$$\begin{aligned} W_\mu^\pm &= \frac{1}{\sqrt{2}} (A_\mu^1 \mp iA_\mu^2), \\ Z_\mu &= \frac{1}{\sqrt{g^2 + g'^2}} (gA_\mu^3 - g'B_\mu) \quad \text{and} \\ A_\mu &= \frac{1}{\sqrt{g^2 + g'^2}} (g'A_\mu^3 + gB_\mu). \end{aligned} \quad (1.32)$$

The Lagrangian from eq. 1.31 then become

$$\mathcal{L}_{\text{mass}} = \frac{v^2}{8} \left( g^2 ((W_\mu^+)^2 + (W_\mu^-)^2) + (g^2 + g'^2) Z_\mu^2 \right), \quad (1.33)$$

and the new mass-eigenstate fields acquire the masses

$$m_{W^\pm} = \frac{gv}{2}, \quad m_Z = \frac{v}{2} \sqrt{g^2 + g'^2} \quad \text{and} \quad m_A = 0. \quad (1.34)$$

As desired the theory consists of three massive ( $W^\pm, Z$ ) and one massless ( $A$ ) field.

We now assume an additional fermion-field in an arbitrary representation  $t^a$  of  $SU(2)$  and charge  $Y$  under  $U(1)$  (hyper-charge). The covariant derivative of this field is

$$D_\mu = \partial_\mu - igA_\mu^a t^a - ig'B_\mu Y. \quad (1.35)$$

Rewriting this in the mass-eigenstate fields defined in eq. 1.32 and eq. 1.34 leads to

$$\begin{aligned} D_\mu = \partial_\mu - \frac{ig}{\sqrt{2}} (W_\mu^+ t^+ + W_\mu^- t^-) - \frac{i}{\sqrt{g^2 + g'^2}} Z_\mu (g^2 t^3 - g'^2 Y) - \\ \frac{igg'}{\sqrt{g^2 + g'^2}} A_\mu (t^3 + Y), \end{aligned} \quad (1.36)$$

where the operators  $t^\pm$ , defined as  $t^\pm = t^1 \pm it^2$ , are the familiar iso-spin creation and annihilation operators.

As the field  $A_\mu$  should be identified with the electromagnetic potential, its coupling should be the electro-magnetic coupling  $e$ , i.e.

$$e = \frac{gg'}{\sqrt{g^2 + g'^2}}, \quad (1.37)$$

and its quantum number the electric charge  $Q$ ,

$$Q = t^3 + Y. \quad (1.38)$$



To simplify further, the mixing of the fields  $A^3$  and  $B$  can be parametrized with the so-called *Weinberg-angle*  $\theta_w$  (or *Weak-Mixing-Angle*) as

$$\begin{pmatrix} Z \\ A \end{pmatrix} = \begin{pmatrix} \cos \theta_w & -\sin \theta_w \\ \sin \theta_w & \cos \theta_w \end{pmatrix} \begin{pmatrix} A^3 \\ B \end{pmatrix}, \quad (1.39)$$

with

$$\cos \theta_w = \frac{g}{\sqrt{g^2 + g'^2}} \quad \text{and} \quad \sin \theta_w = \frac{g'}{\sqrt{g^2 + g'^2}}. \quad (1.40)$$

The covariant derivative becomes then

$$D_\mu = \partial_\mu - \frac{ig}{\sqrt{2}} (W_\mu^+ t^+ + W_\mu^- t^-) - \frac{ig}{\cos \theta_w} Z_\mu (t^3 - \sin^2 \theta_w Y) - ie A_\mu Q, \quad (1.41)$$

and the couplings of the  $Z$  and  $A$  fields to the fermions are completely determined by their electric charge  $Q$  and the third component of the weak iso-spin  $t^3$ . In addition the relations

$$\begin{aligned} g &= \frac{e}{\sin \theta_w}, \\ m_W &= m_Z \cos \theta_w \end{aligned} \quad (1.42)$$

for the weak coupling constant  $g$  and the ratio of the masses of the gauge-bosons  $W$  and  $Z$  can be found.

## 1.2.2 Couplings To Fermions

It has been shown in several experiments (see e.g. [5]) that the W-bosons only couple to left-handed fermions. This leads to no complications in writing down the couplings of these fermions to the gauge-bosons. Since the kinetic term for the fermion-field can be decoupled into a left- and a right-handed field, the left- and right-handed fields can be treated separately by choosing different representations for each of them. To make sure that the right-handed fermions do not couple to the W-bosons, they can be assigned to the singlet representation of  $SU(2)$ , while the left-handed fields live in the doublet-representation<sup>6</sup>, i.e.

$$E_L = \begin{pmatrix} \nu_e \\ e \end{pmatrix}_L \quad \text{and} \quad e_R, \quad (1.43)$$

as well as

$$U_L = \begin{pmatrix} u \\ d \end{pmatrix}_L \quad \text{and} \quad u_R \quad \text{and} \quad d_R. \quad (1.44)$$

The extension to the other families is straight forward. The correct hyper-charges  $Y$  for each of the fields can be found using the charge-relation in eq. 1.38. They are summarized in Table 1.2. The kinetic energy terms in the Lagrangian for these fields, that define the

<sup>6</sup> The mixing between quark-generations is not discussed, since it is not important for this thesis.

	$Q$	$t^3$	$Y$
$\begin{pmatrix} \nu_e \\ e \end{pmatrix}_L$	0 -1	+1/2 -1/2	-1/2
$e_R$	-1	0	-1
$\begin{pmatrix} u \\ d \end{pmatrix}_L$	+2/3 -1/3	+1/2 -1/2	+1/6
$u_R$	+2/3	0	+2/3
$d_R$	-1/3	0	-1/3

Table 1.2: Charge, hyper-charge and third weak iso-spin component for the various fermion-fields in the GSW theory.

couplings to the gauge-bosons completely, are then

$$\mathcal{L}_{\text{kin}} = \bar{E}_L i \not{D} E_L + \bar{e}_R i \not{D} e_R + \bar{U}_L i \not{D} U_L + \bar{u}_R i \not{D} u_R + \bar{d}_R i \not{D} d_R. \quad (1.45)$$

As an example we derive the couplings for the up-quarks. The coupling terms for the up quark to the gauge-bosons are

$$\begin{aligned} \mathcal{L}_{\text{u,c}} = & \frac{g}{\sqrt{2}} (\bar{u}_L \gamma^\mu d_L W_\mu^+ + \bar{d}_L \gamma^\mu u_L W_\mu^-) + \\ & \frac{g}{\cos \theta_w} \left( \bar{u}_L \gamma^\mu \left( \frac{1}{2} - \frac{2}{3} \sin^2 \theta_w \right) u_L + \bar{u}_R \gamma^\mu \left( -\frac{2}{3} \sin^2 \theta_w \right) u_R \right) Z_\mu + \\ & e \bar{u} \gamma^\mu \frac{2}{3} u A_\mu. \end{aligned} \quad (1.46)$$

Using the projection operators onto the right- and left-handed currents, defined as

$$j_{R/L}^\mu = \bar{u} \gamma^\mu \left( \frac{1 \pm \gamma^5}{2} \right) u, \quad (1.47)$$

the full set of coupling terms is found to be

$$\begin{aligned} \mathcal{L}_{\text{u,c}} = & \frac{g}{\sqrt{2}} \left( \bar{u} \gamma^\mu \left( \frac{1 - \gamma^5}{2} \right) d W_\mu^+ + \bar{d} \gamma^\mu \left( \frac{1 - \gamma^5}{2} \right) u W_\mu^- \right) + \\ & \frac{g}{\cos \theta_w} \bar{u} \gamma^\mu \left( \frac{c_A - c_V \gamma^5}{2} \right) u Z_\mu + e \bar{u} \gamma^\mu \frac{2}{3} u A_\mu, \end{aligned} \quad (1.48)$$

where the coefficients for the axial-current  $c_A$  and the vector-current  $c_V$  are defined as

$$c_A = \frac{1}{2} - \frac{4}{3} \sin^2 \theta_w \quad \text{and} \quad c_V = \frac{1}{2}. \quad (1.49)$$

These coefficients can be computed for all the fermion-fields in a similar way. They are listed in Table 1.3. The resulting Feynman-rules for the couplings of fermions to the gauge-

	$c_A$	$c_V$
e	$-\frac{1}{2} + 2 \sin^2 \theta_w$	$-\frac{1}{2}$
$\nu_e$	$+\frac{1}{2}$	$+\frac{1}{2}$
u	$+\frac{1}{2} - \frac{4}{3} \sin^2 \theta_w$	$+\frac{1}{2}$
d	$-\frac{1}{2} + \frac{2}{3} \sin^2 \theta_w$	$-\frac{1}{2}$

Table 1.3: Coefficients for the axial- and the vector-currents for the various fermion-fields in the GSW theory.

$$\begin{aligned}
 & \text{Feynman rule for } Z_\mu: \quad \text{Vertex: } \frac{-ig}{2 \cos \theta_w} \gamma_\mu (c_A - c_V \gamma^5) \quad \text{Propagator: } \frac{-i}{p^2 - m_Z^2} \left( g^{\mu\nu} - \frac{p^\mu p^\nu}{p^2 - \xi m_Z^2} (1 - \xi) \right) \\
 & \text{Feynman rule for } W_\mu^\pm: \quad \text{Vertex: } \frac{-ig}{2\sqrt{2}} \gamma_\mu (1 - \gamma^5) \quad \text{Propagator: } \frac{-i}{p^2 - m_W^2} \left( g^{\mu\nu} - \frac{p^\mu p^\nu}{p^2 - \xi m_W^2} (1 - \xi) \right) \\
 & \text{Feynman rule for } A_\mu: \quad \text{Vertex: } -ieQ \gamma_\mu \quad \text{Propagator: } \frac{-ig^{\mu\nu}}{p^2 + i\epsilon}
 \end{aligned}$$

Figure 1.1: Feynman-rules for the couplings of fermions to the gauge-bosons in the GSW theory.

bosons are shown in the left part of Fig. 1.1. In the right part of Fig. 1.1 the propagator terms for the gauge-bosons are shown. They can e.g. be computed using path integral methods [1]. The parameter  $\xi$  is the so called gauge-fixing parameter. This parameter can in principle be chosen freely, the final 'physical' result of any calculation is independent of the specific choice.

### 1.2.3 Fermion Mass Terms and the Higgs Boson

A simple fermion mass term such as  $-m\bar{\psi}\psi$  cannot be used any more, since the left- and right-handed fields live in different representations of the gauge-group. In order to obtain the needed mass term, the fields  $E_L$ ,  $e_R$  and  $\phi$  can be contracted. Expanding  $\phi$  again

around its vacuum expectation value  $v$ , the fermion mass terms turn out to be

$$\begin{aligned}\mathcal{L}_{e,\text{mass}} &= -\lambda_e \bar{E}_L \phi e_R + \dots = \\ &= -\frac{1}{\sqrt{2}} \lambda_e v \bar{e}_L e_R + \dots,\end{aligned}\tag{1.50}$$

resulting in the mass for the electron of  $m_e = \frac{1}{\sqrt{2}} \lambda_e v$ . In a similar way mass terms for all the massive fermion-fields can be found. Note that by construction the neutrino-field stays massless (i.e. there is no coupling term to right-handed neutrinos). In addition the parameter  $\lambda_e$  is not constrained, leading to the possibility of acquiring different masses for each fermion type.

The scalar field  $\phi$  can be parametrized as <sup>7</sup>

$$\phi(x) = \frac{1}{\sqrt{2}} \begin{pmatrix} 0 \\ v + h(x) \end{pmatrix},\tag{1.51}$$

with the scalar, real-valued field  $h$  denoting the fluctuations of  $\phi$  around the vacuum expectation value  $v$ , i.e.  $\langle h \rangle = 0$ .

We have to define an explicit Lagrangian, that leaves the field  $\phi$  with a vacuum value  $\neq 0$ :

$$\mathcal{L}_\phi = |D_\mu \phi|^2 + \mu^2 \phi^\dagger \phi - \lambda (\phi^\dagger \phi)^2, \quad \text{with } \mu^2 < 0.\tag{1.52}$$

The potential  $V(\phi) = \mu^2 \phi^\dagger \phi - \lambda (\phi^\dagger \phi)^2$  has a minimum at

$$v = \left( \frac{\mu^2}{\lambda} \right)^{1/2} \neq 0,\tag{1.53}$$

and the terms involving the field  $h$  are

$$\begin{aligned}\mathcal{L}_h &= -\mu^2 h^2 - \lambda v h^3 - \frac{1}{4} \lambda h^4 = \\ &= -\frac{1}{2} m_h^2 h^2 - \sqrt{\frac{\lambda}{2}} m_h h^3 - \frac{1}{4} \lambda h^4.\end{aligned}\tag{1.54}$$

The quantum of the scalar field  $h$  is a scalar (boson), the *Higgs* boson, with mass

$$m_h = \sqrt{2\lambda} v.$$

Putting the expression from eq. 1.51 into the mass terms for the fermions one finds the couplings of the Higgs to the fermions,

$$\mathcal{L}_{hf} = -m_f \bar{f} f \left( 1 + \frac{h}{v} \right),\tag{1.55}$$

---

<sup>7</sup> We use the *unitarity gauge* to render the field  $\phi$  real in every point  $x$ .

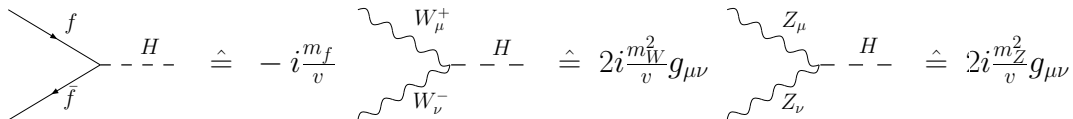


Figure 1.2: Feynman-rules for the couplings of fermions and gauge-bosons to the Higgs boson.

and finally in the covariant derivative term of  $\phi$  one finds the coupling terms of the gauge-bosons to the Higgs field,

$$\mathcal{L}_{hG} = \left( m_W^2 W^{\mu+} W_{\mu}^- + \frac{1}{2} m_Z^2 Z^{\mu} Z_{\mu} \right) \left( 1 + \frac{h}{v} \right)^2. \quad (1.56)$$

The Feynman rules for the coupling of the fermions and the gauge-bosons to the Higgs are shown in Fig. 1.2.

### 1.3 Quantum Chromo Dynamics (QCD)

Having discussed the weak and electro-magnetic interactions, we now turn to the strong interaction, responsible for the formation of hadrons. The success of the interpretation of the force-carriers as the quanta of the gauge-fields that had to be introduced in order to preserve the local gauge-invariance of the Lagrangian under a certain symmetry-group continuous for this interaction. The symmetry-group describing a theory that is consistent with experimental observations is the color- $SU(3)$  group and the corresponding quantum number is the *color* (conventionally labeled as *red*, *green* and *blue*). The (anti-)quarks  $q$  ( $\bar{q}$ ) can be assigned to the fundamental representation of  $SU(3)$ , thus the three combinations

$$\bar{q}^i q_i, \quad \varepsilon^{ijk} q_i q_j q_k \quad \text{and} \quad \varepsilon_{ijk} \bar{q}^i \bar{q}^j \bar{q}^k \quad (1.57)$$

are singlets under color- $SU(3)$  transformations and form stable particles. They can be identified as *Mesons* ( $\bar{q}^i q_i$ ) and *Baryons* ( $\varepsilon^{ijk} q_i q_j q_k, \varepsilon_{ijk} \bar{q}^i \bar{q}^j \bar{q}^k$ ).

#### 1.3.1 Group Structure of $SU(3)$

The general  $SU(3)$  transformation for the quark fields is

$$q^i \rightarrow (1 + i\alpha^a t^a + \mathcal{O}(\alpha^2)) q^i, \quad (1.58)$$

with  $t^a$  the generators of the symmetry group that obey the commutation relation

$$[t^a, t^b] = i f^{abc} t^c. \quad (1.59)$$

The coefficients  $f$  are again the (anti-symmetric) structure-constants of the symmetry-group.

The generators in the fundamental representation are  $d \times d$  hermitian matrices, with  $d = 3$  the dimension of the fundamental representation. The normalization of the matrices  $t^a$  in the fundamental representation is

$$\text{tr}[t^a t^b] = C \delta^{ab}, \quad \text{with } C = \frac{1}{2}. \quad (1.60)$$

The matrices in the adjoint representation (denoted by  $G$ ) are

$$(t_G^b)_{ac} = i f^{abc} \quad (1.61)$$

and the dimension of the adjoint representation for the group  $SU(N = 3)$  is given by

$$d(G) = N^2 - 1 = 8. \quad (1.62)$$

We find the useful *quadratic Casimir operator*  $C_2$  for the fundamental representation, defined as

$$t^a t^a = C_2, \quad (1.63)$$

using the relation

$$d C_2 = d(G) C \Rightarrow C_2 = \frac{N^2 - 1}{2N} = \frac{4}{3}. \quad (1.64)$$

Finally we find the *quadratic Casimir operator*  $C_2(G)$  and the normalization  $C(G)$  of the matrices in the adjoint representation as

$$C_2(G) = C(G) = N = 3. \quad (1.65)$$

### 1.3.2 QCD Lagrangian and Feynman Rules

We recall the general Lagrangian for non-abelian gauge theories from eq. 1.20 and define the QCD Lagrangian as

$$\mathcal{L}_{\text{QCD}} = \bar{\psi}(i\not{D})\psi - \frac{1}{4}(F_{\mu\nu}^a)^2 - m\bar{\psi}\psi + \mathcal{L}_{\text{gauge-fixing}} + \mathcal{L}_{\text{ghost}} \quad (1.66)$$

where we have added the so-called gauge-fixing term

$$\mathcal{L}_{\text{gauge-fixing}} = -\frac{1}{2\xi}(\partial^\mu A_\mu^a)^2 \quad (1.67)$$

and the ghost-term

$$\mathcal{L}_{\text{ghost}} = \bar{c}^a(\partial^\mu D_\mu^{ac})c^c \quad (1.68)$$

$$\begin{aligned}
 & \text{Quark-gluon vertex: } \text{quark} \rightarrow \text{quark} + \text{gluon}(a, \mu) \hat{=} ig\gamma^\mu t^a \\
 & \text{Quark-gluon vertex: } \text{quark}(b, \nu) + \text{gluon}(c, \rho) \rightarrow \text{quark}(a, \mu) + \text{gluon}(k) \hat{=} gf^{abc} \times \\
 & \quad [ g^{\mu\nu}(k-p)^\rho + g^{\nu\rho}(p-q)^\mu + g^{\rho\mu}(q-k)^\nu ] \\
 & \text{Gluon propagator: } \text{gluon} \rightarrow \text{ghost}(c) \rightarrow \text{gluon} \hat{=} \frac{-i}{k^2+i\epsilon} \left( g_{\mu\nu} - (1-\xi) \frac{k_\mu k_\nu}{k^2} \right) \\
 & \text{Four-gluon vertex: } \text{gluon}(b, \nu) + \text{gluon}(c, \rho) \rightarrow \text{gluon}(a, \mu) + \text{gluon}(d, \sigma) \hat{=} -ig^2 \times \\
 & \quad [ f^{abc} f^{cde} (g^{\mu\rho} g^{\nu\sigma} - g^{\mu\sigma} g^{\nu\rho}) + f^{ace} f^{bde} (g^{\mu\nu} g^{\rho\sigma} - g^{\mu\sigma} g^{\nu\rho}) \\
 & \quad + f^{ade} f^{bce} (g^{\mu\nu} g^{\rho\sigma} - g^{\mu\rho} g^{\nu\sigma}) ]
 \end{aligned}$$

Figure 1.3: Feynman rules for QCD.

in order to be able to define a meaningful gauge-boson propagator. The  $\xi$  in the gauge-fixing term is the gauge-fixing parameter and can be chosen arbitrarily. It turns out that the so called *Feynman-'t Hooft gauge* ( $\xi = 1$ ) is especially useful <sup>8</sup>.

Using the definition of the covariant derivative from eq. 1.17 and the field-strength from eq. 1.18 the Feynman rules for the couplings of the gauge-bosons to the quarks and themselves can be found in the non-linear part of the Lagrangian in eq. 1.66. They are shown (without the rules for the ghost-field  $c$ ), together with the propagator for the gauge-bosons (*gluons*), in Fig. 1.3.

### 1.3.3 The Running of the Coupling and Asymptotic Freedom

The calculation of amplitudes for perturbative field theories usually includes the calculation of loop-diagrams. Diagrams like these usually are divergent, when the undefined loop-momentum becomes very large. The diagrams are thus called *ultraviolet (UV) divergent*. To render these diagrams finite the so called *renormalization* technique can be used which 'factorizes' the divergences into the not-observable 'bare' parameters of the theory, such as the 'bare' masses of particles and the 'bare' coupling constant. Within this procedure the divergent terms (which usually appear as  $1/\epsilon$  poles in dimensional regularization) are removed by so called *counter-terms* at some specific scale, the renormalization scale  $\mu_R$ , and the theory is defined by the so called 'physical' parameters for the masses and the coupling. These quantities can be measured experimentally.

In general the choice of this scale is arbitrary. If any observable quantity is expanded to all orders in the coupling constant, the  $\mu_R$ -dependent terms have to cancel order by order. As an example <sup>9</sup> let us consider a dimensionless observable quantity  $R$ , that depends on

<sup>8</sup> Any observable quantity is independent of the choice of the gauge  $\xi$ .

<sup>9</sup> This example has been adapted from a lecture on QCD given by B. R. Webber at CERN in February 2008 [6].

an energy scale  $Q$ . Dimensional analysis yields that the observable quantity  $R$  can only depend on the ratio of the scales  $Q$  and  $\mu_R$ , and of course on the coupling constant  $\alpha_s$ , i.e.  $R(Q/\mu_R, \alpha_s)$ . The observable satisfies then the so called *Callan-Symanzik* equation,

$$\left( \mu_R \frac{\partial}{\partial \mu_R} + \beta(g) \frac{\partial}{\partial g} \right) R = 0, \quad (1.69)$$

with  $g$  the QCD coupling and  $\mu_R$  the renormalization scale. We can expand the beta-function  $\beta(g)$  in orders of the coupling,

$$\beta(g) = -\frac{g^3}{(4\pi)^2} b_0 + \mathcal{O}(g^5) = -\frac{g^3}{(4\pi)^2} \left( \frac{11}{3} C_2(G) - \frac{4}{3} n_f C \right) + \mathcal{O}(g^5). \quad (1.70)$$

In  $SU(3)$  the coefficient of the first term  $b_0$  becomes

$$b_0 = \left( 11 - \frac{2}{3} n_f \right), \quad (1.71)$$

where  $n_f$  is the number of light quarks (i.e. light compared to the scale  $Q$ ). We focus here on this term, the coefficients for the terms up to the order  $g^9$  are presently known.

Equation 1.69 implies that the scale dependence can be absorbed into a *running coupling constant*  $\alpha_s(Q)$  defined as

$$\alpha_s(Q) = \frac{\bar{g}^2}{4\pi} \quad (1.72)$$

where  $\bar{g}$  is the *renormalized coupling* defined by the so called *renormalization group equation* (RGE)

$$\frac{d}{d \log(Q/M)} \bar{g} = \beta(\bar{g}), \quad (1.73)$$

with the initial condition  $\alpha_s(\mu_R) = \alpha_s$ . As the RGE only determines the evolution of the coupling constant, its normalization has to be measured experimentally. This is done at a specific reference scale, conveniently chosen to be the Z-boson mass  $m_Z$ <sup>10</sup>. The value of  $\alpha_s$  reported by the *Particle Data Group* in 2006 is [3]

$$\alpha_s(m_Z) = 0.1176 \pm 0.0020. \quad (1.74)$$

This uncertainty of about  $\sim 2\%$  will propagate into all QCD predictions of order  $\alpha_s$ .

The solution of the RGE gives

$$\alpha_s(Q) = \frac{\alpha_s}{1 + \frac{\alpha_s b_0}{2\pi} \log(Q/M)}. \quad (1.75)$$

---

<sup>10</sup> The coupling constant is also dependent on the definition of the renormalization scheme. The most commonly used scheme is the *modified minimal subtraction scheme*  $\overline{\text{MS}}$ . We will implicitly refer all results to this scheme.



We can define the dimensional scale parameter  $\Lambda$  as

$$1 = \frac{g^2 b_0}{8\pi^2} \log(M/\Lambda) \quad (1.76)$$

in order to remove the dependence of the running coupling constant on the reference value  $\alpha_s$ . The running coupling becomes then

$$\alpha_s(Q) = \frac{2\pi}{b_0} \frac{1}{\log(Q/\Lambda)}. \quad (1.77)$$

Equation 1.77 is a remarkable result. First of all the qualitative result depends on the sign of the  $\beta$ -function, i.e. on the sign of its first coefficient  $b_0$ . If the  $\beta$ -function is negative ( $b_0$  is positive), the coupling constant decreases as  $\log^{-1}(Q)$  when  $Q$  becomes large. This effect is known as *asymptotic freedom* and appears in QCD as long as the number of light flavours is  $n_f < 17$ . The total number of known quark flavours is 6, and the number of light flavours for typical hadron-collider processes is 5. We can therefore safely argue that, if the typical process scale  $Q$  is large enough compared to  $\Lambda$ , the coupling constant is small and perturbative expansions of observable quantities lead to accurate results.

On the other hand, if  $Q$  becomes small, i.e.  $Q \rightarrow \Lambda$ , the coupling constant increases and the perturbative description breaks down. The value of  $\Lambda$  has experimentally been determined to  $\sim 200$  MeV, corresponding to a distance  $1/\Lambda$  of about the size of the smallest hadrons. In other words,  $\Lambda$  ( $1/\Lambda$ ) is the scale (distance) at which the strong interaction actually becomes strong.

### 1.3.4 Hadronic Processes and Parton Density Functions

With the Feynman rules above all necessary ingredients are known for the computation of any hard scattering parton-parton QCD process. Experimentally however it is not possible to examine such processes. A typical experiment involves the interaction of hadrons<sup>11</sup>, the bound states of quarks and gluons. The interactions occurring within the hadrons cannot be treated perturbatively, since the quark/gluon bound-states are established via low-momentum-transfer interactions. However, in high energy hadron collisions the hadrons can be treated as a loose cloud of approximately non-interacting particles (partons). The parton momenta are collinear to the hadron momentum and each of the constituents carries a fraction  $x$  of the hadron momentum (*Parton Model* [7]). The picture can be justified by the fact that a constituent of the hadron can only acquire a significant transverse momentum (with respect to the hadron momentum) through the exchange of a hard gluon. But this is highly suppressed since the QCD coupling becomes small for such large

---

<sup>11</sup> At the LHC these hadrons are protons.

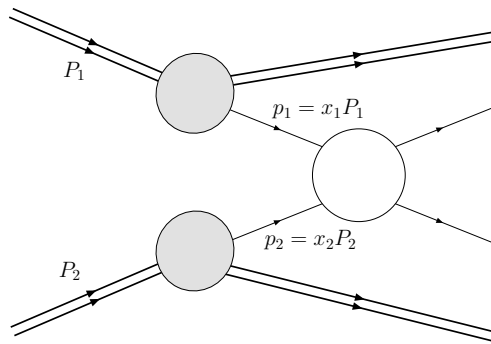


Figure 1.4: Schematic diagram for a hadron-hadron interaction at high energies. The interacting partons 'factorize' from the protons with momenta  $P_{1/2}$  and can be treated as free quarks/gluons with momenta  $p_{1/2} = x_{1/2} P_{1/2}$ .

momentum transfers. In other words, the inner-hadron interactions are soft and thus 'slow' (i.e. taking place at longer time scales) compared to the hard scattering process and can approximately be neglected.

Using this picture the following notation for hadron-hadron collisions can be introduced. The incoming hadrons have momenta  $P_{1/2}$ . Their momenta in the center-of-mass frame are assumed to be large enough compared to the hadron masses, such that latter can be neglected,  $P_{1/2}^2 = 0$  (this is the case at the LHC with a hadron-hadron center-of-mass energy of 14 TeV). The momenta of the interacting partons  $p_{1/2}$  are then, using the parton picture,

$$p_{1/2} = x_{1/2} P_{1/2}, \quad (1.78)$$

with  $x_{1/2} \in [0, 1]$  the fraction of the hadron momentum carried by the partons  $p_{1/2}$ <sup>12</sup>. The hadron-hadron center-of-mass energy squared is defined as

$$s = (P_1 + P_2)^2. \quad (1.79)$$

The parton-parton center-of-mass energy squared is then simply

$$\hat{s} = (p_1 + p_2)^2 = (x_1 P_1 + x_2 P_2)^2 = x_1 x_2 s. \quad (1.80)$$

A hadron-hadron collision process is schematically shown in Fig. 1.4. At leading order the hard scattering partons with momenta  $p_1$  and  $p_2$  interact without 'disturbance' (white circle) by the other partons (*spectator quarks*).

The only unresolved ingredient for the understanding of the parton momenta is the variable  $x$ . The distribution of this variable depends on the soft inner-hadron interactions

---

<sup>12</sup> Note, that since the hadrons are treated as massless, the partons are automatically massless as well, i.e.  $p_{1/2}^2 = 0$ .

and cannot be derived using perturbative QCD. The so called *Parton Distribution Function*  $f_f(x)$  (PDF) can be defined, where  $f_f(x)dx$  is the probability of finding a parton of type  $f$  (an (anti-)quark-flavour or a gluon) in the hadron that carries a fraction within  $[x, x + dx]$  of the hadron momentum. All the constituent partons together have to carry the total hadron momentum, i.e.

$$\sum_f \int_0^1 x f_f(x) dx = 1. \quad (1.81)$$

Other constraints are put on the PDFs by the quantum numbers of the hadrons. For example, in the case of protons the total expected number of up-quarks (down-quarks) is two (one), i.e.

$$\int_0^1 dx (f_u(x) - f_{\bar{u}}(x)) = 2 \quad \text{and} \quad \int_0^1 dx (f_d(x) - f_{\bar{d}}(x)) = 1. \quad (1.82)$$

More so called sum-rules exist for the electrical charge of the hadrons and other observables. These rules can be used to constrain the distributions using experimental deep-inelastic scattering data.

We now have all the ingredients in hand to define the hadronic cross-section for a process  $pp \rightarrow X$  as

$$\sigma(pp \rightarrow X) = \sum_{ff'} \int_0^1 dx_1 dx_2 f_f(x_1) f_{f'}(x_2) \hat{\sigma}(x_1, x_2, s), \quad (1.83)$$

with  $\hat{\sigma}$  the partonic hard scattering cross-section and the sum running over all parton-type-pairs  $ff'$  that contribute to the process.

### 1.3.5 Soft and Collinear Effects: Parton Evolution and Parton Shower

Above it has been assumed that the PDFs are independent of the scale of the hard scattering process  $Q$ . In the parton model picture this means that the structure of the proton looks the same, whatever the energy scale might be at which the proton is 'probed' (e.g. in deep inelastic scattering experiments (DIS)). However, this behavior, known as *Bjorken scaling*, is only true at leading order. The approximative character of the Bjorken scaling can be understood from the following picture. As the probing scale  $Q$  is increased, the before as point-like observed parton is resolved into several, softly interacting particles. As the number of constituent partons is increased, while the hadron momentum stays constant, each of the constituents has to carry less of the total momentum. This leads to an increase in the parton densities at low and a decrease of the densities at high  $x$  values. This scale dependence, known as the *breaking of the Bjorken scaling*, is experimentally observed.

This scale dependence arises obviously from the interactions within the hadrons during the scattering process, and is thus a higher-order correction to the leading order parton picture. The diagrams of these corrections contain singularities in the soft and collinear limit of the additional radiation. The large corrections due to these singular regions in the phase-space can be absorbed into the parton density functions using parton evolution, which by this procedure become scale dependent. The evolution of the parton densities with varying scale  $Q$  for the constituents of hadrons are described by the *Altarelli-Parisi equations* [8] as

$$\begin{aligned}
 \frac{d}{d \log Q} f_g(x, Q) &= \frac{\alpha_s(Q^2)}{\pi} \int_x^1 \frac{dz}{z} \left[ P_{qg}(z) \sum_f \left( f_f(x/z, Q) + f_{\bar{f}}(x/z, Q) \right) + P_{gg}(z) f_g(x/z, Q) \right] \\
 \frac{d}{d \log Q} f_f(x, Q) &= \frac{\alpha_s(Q^2)}{\pi} \int_x^1 \frac{dz}{z} [P_{qq}(z) f_f(x/z, Q) + P_{gq} f_g(x/z, Q)] \\
 \frac{d}{d \log Q} f_{\bar{f}}(x, Q) &= \frac{\alpha_s(Q^2)}{\pi} \int_x^1 \frac{dz}{z} [P_{q\bar{q}}(z) f_{\bar{f}}(x/z, Q) + P_{g\bar{q}} f_g(x/z, Q)],
 \end{aligned}
 \tag{1.84}$$

with the splitting functions

$$\begin{aligned}
 P_{qq}(z) &= \frac{4}{3} \left( \frac{1+z^2}{(1-z)_+} + \frac{3}{2} \delta(1-z) \right) \\
 P_{qg}(z) &= \frac{4}{3} \left( \frac{1+(1-z)^2}{z} \right) \\
 P_{gq}(z) &= \frac{1}{2} (z^2 + (1-z)^2) \\
 P_{gg}(z) &= 6 \left( \frac{1-z}{z} + \frac{z}{(1-z)_+} + z(z-1) + \left( \frac{11}{12} - \frac{n_f}{18} \right) \delta(1-z) \right),
 \end{aligned}
 \tag{1.85}$$

where the plus-distribution is defined as

$$\int_0^1 dx f(x) g(x)_+ = \int_0^1 dx (f(x) - f(1)) g(x).
 \tag{1.86}$$

The splitting functions  $P_{ab}(z)$  are directly related to the probability for the splitting of a parton  $a$  with momentum  $p$  into a parton  $b$  with longitudinal momentum  $zp$ . By using the above evolution equations to define the parton densities at some scale  $Q$  all the leading logarithmic terms introduced by soft and collinear radiation at higher orders are re-summed. A detailed derivation of the evolution equations can e.g. be found in [9].

The factorization approach from eq. 1.83 becomes scale dependent as well and the so called *factorization scale*,  $\mu_F$ , has to be introduced. The hadronic cross-section becomes

then

$$\sigma(\text{pp} \rightarrow X) = \sum_{ff'} \int_0^1 dx_1 dx_2 f_f(x_1, \mu_F) f_{f'}(x_2, \mu_F) \hat{\sigma}(x_1, x_2, s, \mu_F), \quad (1.87)$$

where the partonic cross-section  $\hat{\sigma}$  can also become factorization scale dependent. For LO cross-sections the partonic cross-section is typically independent of the factorization scale.

The above description is very important for computing inclusive observables such as cross-sections. However, it does not describe the kinematics of the final state particles properly. To do this a similar, alternative approach can be used, the *Parton Shower* approach. We just briefly describe the idea and refer the reader to the literature (e.g. [9]) for more details. The starting point is the definition of the so-called *Sudakov Form Factors*

$$\Delta_f(t) \equiv \exp \left[ - \sum_{f'} \int_{t_0}^t \frac{dt'}{t'} \int dz \frac{\alpha_s}{2\pi} \hat{P}_{f'f}(z) \right], \quad (1.88)$$

where  $\hat{P}_{f'f}(z)$  are the un-regularized splitting functions<sup>13</sup> and the substitution  $t \equiv Q^2$  has been applied. These form factors can be interpreted as the probability of a parton not to split when evolving from scale  $t_0$  to scale  $t$ . Together with the *Altarelli-Parisi Equations* they can be employed to define an iterative algorithm to radiate/split partons in a cascade up to some cut-off scale. After this procedure (*parton-shower*) the final-state consists of a multi-parton configuration and again, similarly as in the case of the PDFs, the leading logarithmically enhanced contributions of the higher-order corrections are included up to all orders.

The specific implementation of the algorithm can vary. We just mention those used in this thesis from the programs HERWIG [10] and PYTHIA [11]. HERWIG and PYTHIA are MC event generators that combine LO hard scattering amplitudes with such parton-shower algorithms. HERWIG uses a so called angular-ordered algorithm, that includes leading soft gluon enhancements to all orders. In the virtuality-ordered shower algorithm used in PYTHIA this is achieved via a veto technique.

### 1.3.6 Long Distance Effects: Hadronization

The formation of hadrons is a non-perturbative process. The hadronization takes place at low momentum transfer and long distances where the strong coupling is large. Therefore there are only phenomenological models available to describe the hadronization effects.

---

<sup>13</sup> In eq. 1.85 we used plus- and delta-distributions to regularize the splitting functions. This procedure is needed to regularize the singularities arising when  $z \rightarrow 0, 1$ . In the parton-shower approach the singularities are regularized using an explicit cut-off, i.e. a minimal energy transfer in the splitting is required, otherwise the radiation is unresolved and the parton did not split.

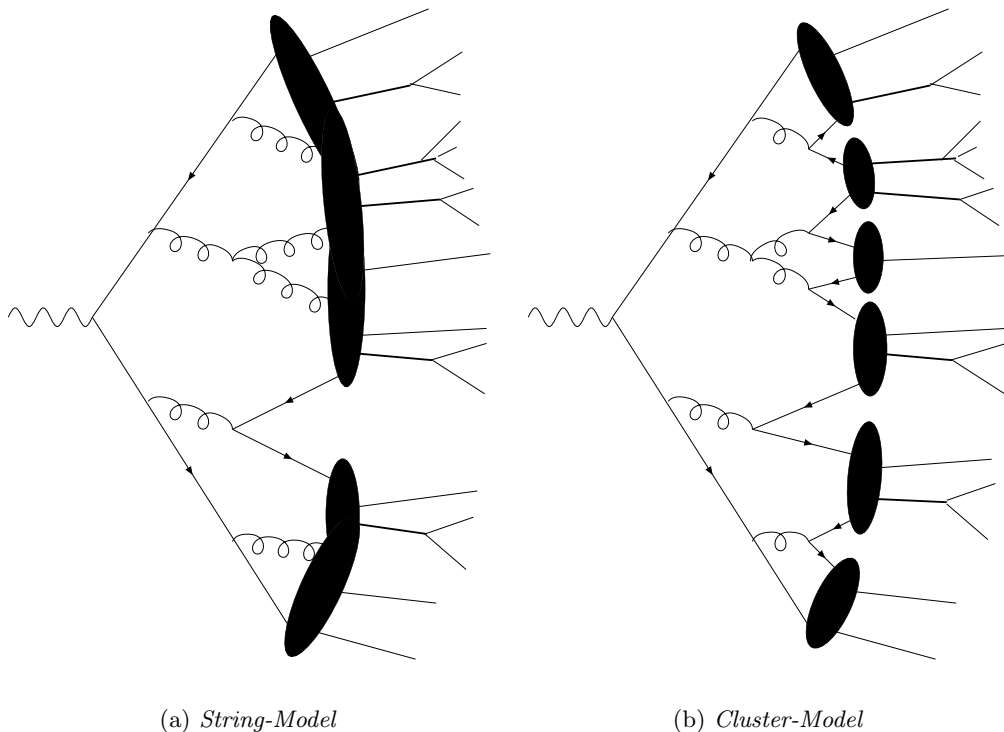


Figure 1.5: Schematic picture for the formation of hadrons from partons, in a  $q\bar{q}$  final state configuration after parton-shower, (a) for the *String-Model*, (b) for the *Cluster-Model*.

The commonly used models are the *String-Model*, used in PYTHIA, and the *Cluster-Model*, used in HERWIG.

The main idea of the *String-Model* is that, when an oppositely color-charged quark-anti-quark pair moves apart, the color-field between them can be described as a narrow ‘flux tube’ of uniform energy density (*string tension*). Gluons form so called kinks in these flux-tubes. At the end of the perturbative parton-shower colorless strings form between quark-anti-quark pairs (as shown in Fig. 1.5(a)). The motion of these strings is then described classically, with the possibility of breaking a string into a  $q\bar{q}$  pair, when the field energy in the string allows for it. These quarks are combined into the final-state hadrons, which, if not stable, proceed in decaying until a set of stable final-state hadrons is obtained.

In the *Cluster-Model* the quarks after the parton-shower are combined as quark-anti-quark pairs into clusters, where beforehand gluons at the end of the shower are forced to split into  $q\bar{q}$  pairs (illustrated in Fig. 1.5(b)). The clusters are then associated with so called “super-resonances”, that subsequently decay into the known set of hadronic

resonances.

A detailed description and comparison of these and other hadronization models can e.g. be found in [9].

### 1.3.7 Underlying Event and Multi-Parton Interactions

In hadron-hadron collisions there are additional effects that do not affect the hard scattering process. One of them is the *Underlying Event*, describing soft interactions between the spectator partons, i.e. the partons from the protons that are not involved in the hard scattering (cf. Fig. 1.4). Another effect is *Multi-Parton* interaction, where more than two of the constituent quarks of the protons undergo a hard scattering. There are several models available for these effects; we will explicitly use the JIMMY model [12] for the HERWIG generator in upcoming sections of this thesis.

## 1.4 Cross-Section and Decay-Width

For later usage, but without derivation, the formulas for the computation of cross-sections and decay widths from the  $S$ -matrix elements  $\mathcal{M}$  are shown here. For a detailed derivation we refer the reader to the literature, e.g. [1].

The cross-section for the scattering process  $A + B \rightarrow X$  is

$$\sigma = \frac{1}{4E_A E_B |v_A - v_B|} \int \left( \prod_f \frac{d^3 p_f}{(2\pi)^3 2E_f} \right) \times |\mathcal{M}|^2 (2\pi)^4 \delta^{(4)}(p_A + p_B - \sum p_f), \quad (1.89)$$

where  $E_{A/B}$  ( $v_{A/B}$ ) are the energies (velocities) of the incoming particles  $A$  and  $B$ , and  $p_f$ ,  $f \in X$ , are the momenta of all final state particles. The whole formula is Lorentz-invariant under boosts along the  $z$ -axis, i.e. the axis parallel to the collision axis of the particles  $A$  and  $B$ .

The formula for the decay width of the process  $A \rightarrow X$  is

$$\Gamma = \frac{1}{2E_A} \int \left( \prod_f \frac{d^3 p_f}{(2\pi)^3 2E_f} \right) \times |\mathcal{M}|^2 (2\pi)^4 \delta^{(4)}(p_A - \sum p_f). \quad (1.90)$$

This formula is not Lorentz-invariant (due to the factor of  $1/E_A$ ). In general the decay width of a particle is computed in its rest-frame, where  $E_A = m_A$ .

Quantity		Value	Standard Model
$m_t$	[GeV]	$172.7 \pm 0.29 \pm 0.6$	$172.7 \pm 2.8$
$m_W$	[GeV]	$80.450 \pm 0.058$	$80.376 \pm 0.017$
$m_Z$	[GeV]	$91.1876 \pm 0.0021$	$91.1874 \pm 0.0021$
$\Gamma_Z$	[GeV]	$2.4952 \pm 0.0023$	$2.4968 \pm 0.0011$
$\Gamma(\text{had})$	[GeV]	$1.7444 \pm 0.002$	$1.7434 \pm 0.0010$
$\Gamma(\text{inv})$	[MeV]	$499.0 \pm 1.5$	$501.65 \pm 0.11$
$\Gamma(\ell^+\ell^-)$	[MeV]	$83.984 \pm 0.086$	$83.996 \pm 0.021$
$\sigma_{\text{had}}$	[nb]	$41.541 \pm 0.037$	$41.467 \pm 0.009$

Table 1.4: Experimentally observed (Value) values for Standard Model parameters compared to the SM best fit predictions (Standard Model).  $\sigma_{\text{had}}$  is the hadronic cross-section in electron-positron annihilation with a center-of-mass energy corresponding to the Z boson mass. For details see [3], section *Electroweak model and constraints on new physics*.

## 1.5 Tests and Limitations of the Standard Model

The electro-weak theory described in section 1.2 together with QCD (section 1.3) form the so-called *Standard Model of Particle Physics* (SM). The predictions of these quantum field theories have been tested against a tremendous amount of experimental data and were found to be in excellent agreement. The predicted (Standard Model) and experimentally observed values (Value) for a selection of Standard Model parameters is shown in Table 1.4. The predictions for the masses of the W and Z bosons ( $m_W$ ,  $m_Z$ ) and the top-quark ( $m_t$ ) as well as the total ( $\Gamma_Z$ ) and the partial ( $\Gamma(\text{had})$ ,  $\Gamma(\text{inv})$ ,  $\Gamma(\ell^+\ell^-)$ ) widths of the Z boson agree with the Standard Model predictions. The last line in the table shows the values for the total hadronic cross-section in electron-positron annihilation with a center-of-mass energy corresponding to the Z mass  $m_Z$ . The numbers are taken from [3].

One of the most precisely known parameters is the *Landé-factor*  $g$ , related to the magnetic moment of the electron. Theoretical predictions and experimental measurements of this factor agree to eight significant digits. Together with the results of other experiments (e.g. measurements of the quantum Hall effect, neutron Compton wavelength etc.) it is understood that Quantum Electrodynamics (QED) is the most precisely known and most successful physical theory.

However, there are a few short-comings in the Standard model. One of them is the only fundamental missing piece, the Higgs boson. So far no experiment was able to find this particle, which is vital to the complete framework of the SM. It not only gives rise to the masses of the W and Z bosons (known as *electroweak symmetry-breaking*), but also serves as the origin of the masses for the fermions. From theoretical considerations and



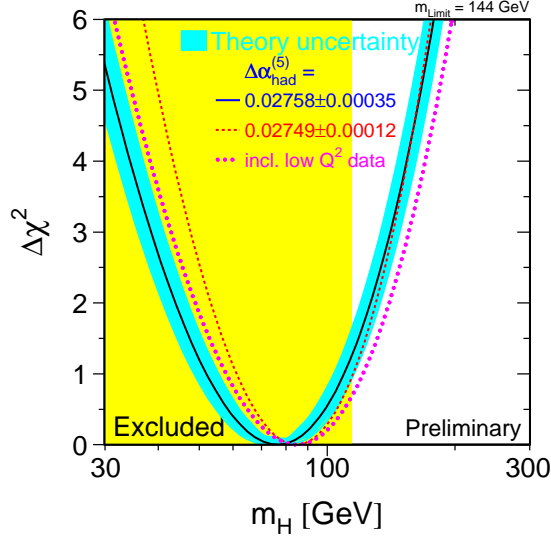


Figure 1.6: Figure taken from [16]. The plot shows the value  $\Delta\chi^2 = \chi^2 - \chi_{\min}^2$  as a function of the Higgs mass that is used in the fit of all high- $Q^2$  data available. The blue band shows an estimation of the theoretical error due to missing higher order corrections. The left (yellow) region labeled 'excluded' shows the region excluded by direct searches at 95% CL. The dashed curve is the result obtained using the evaluation of  $\Delta\alpha_{\text{had}}^{(5)}(m_Z)$  from [17]. The dotted curve includes also the low- $Q^2$  results.

measured electro-weak parameters an upper limit on the Standard Model Higgs mass can be set at  $m_H \leq 194 \text{ GeV}$  with 95% CL [3]. This prediction also includes the lower bound from direct searches of  $m_H \geq 114.4 \text{ GeV}$  at 95% CL [13]. The constraints on the Higgs boson mass arising from fitting all high- $Q^2$  data of the LEP [14] experiments [15] is shown in Fig. 1.6, taken from [16]. The upper band quoted there ( $m_H \leq 144 \text{ GeV}$ ) is increased to the value mentioned above when the direct search lower limit (denoted by the yellow region) is included.

Another unresolved issue is the so called *hierarchy problem*. As discussed above, theoretical considerations and experimental observations favour a Higgs boson mass of the order of  $\sim 100 \text{ GeV}$ . In order to achieve this the divergences in the quantum-corrections to the Higgs mass arising from radiative terms have to cancel very precisely. In other words, something 'protects' the Higgs mass from increasing. If there is no mechanism at hand to provide this protection the theory has to be fine-tuned up to the highest mass scales in order to keep the Higgs mass small.

The success of the unification of the weak and the electromagnetic interaction into a

spontaneously broken  $U(1) \times SU(2)$  gauge theory gives rise to the hope of a unification of QCD and the GSW theory at some larger scale. This would mean that the SM as described above is the low-energy effective theory of a unified gauge theory at some larger scale (also known as *Grand-Unified-Theory* (GUT) scale).

Further open questions are e.g. the origin of neutrino masses and dark matter (which has been proposed to explain e.g. the deviations of the rotational movement of galaxies from theoretical predictions).

There is a variety of proposed models that try to solve one or several of the above mentioned problems. A very popular model is *Super-Symmetry* (SUSY) [18], where additional particles, so called SUSY-partners for each of the SM particles are introduced (extension in the dimension of the spin-space). Other approaches introduce extra space-like dimensions (e.g. *Universal Extra Dimension* (UED) [19]) or additional color-like symmetries (*Technicolor* [20]).

Despite the success of the SM it has been agreed upon among a major part of the scientific community that there has to be some new physics beyond the SM, and that this new physics should show up around 1 TeV. The fact that almost all proposed models predict the existence of new particles, that should be observable at high-energy experiments such as the LHC [21] gives hope that the upcoming collider experiments at the LHC shed light into this new domain, where consequences of the new physics can be observed. This might either lead to a confirmation, or to an exclusion of one or more of the proposed models.

## Chapter 2

# SM Higgs Phenomenology at the Large Hadron Collider

### 2.1 Higgs Production and Decay Modes

#### 2.1.1 Production Processes and Cross-Sections

Using the theoretical framework described in chapter 1, the possible mechanisms that contribute to the SM Higgs boson production at the LHC can be derived. As the colliding particles are protons, the set of incoming particles is restricted to the set of constituents of the protons, namely to quarks  $q$ , anti-quarks  $\bar{q}$  and gluons  $g$ .

A possibility is the direct interaction of an incoming quark from one proton and an incoming anti-quark from the other proton. This process however does not contribute substantially to the Higgs production cross-section. The coupling of the Higgs boson to fermions depends linearly on the fermion-mass ( $-i\frac{m_f}{v}$ ), indicating that only heavy quarks (t, b) contribute to the production. However, the parton distribution functions for heavy quarks in the proton are very small. It can therefore be concluded that this production channel is completely negligible for any practical purpose.

A first relevant production mechanism is the so called *Higgs-Strahlung* process, shown in Fig. 2.1(a). The incoming quark/anti-quark pair produces a vector boson (either W or Z), which radiates a Higgs boson.

A further important process is the Higgs production in association with top-quarks (*Associated Production*), shown in Fig. 2.1(c). The incoming particles are gluons that annihilate into a  $t\bar{t}$ -pair.

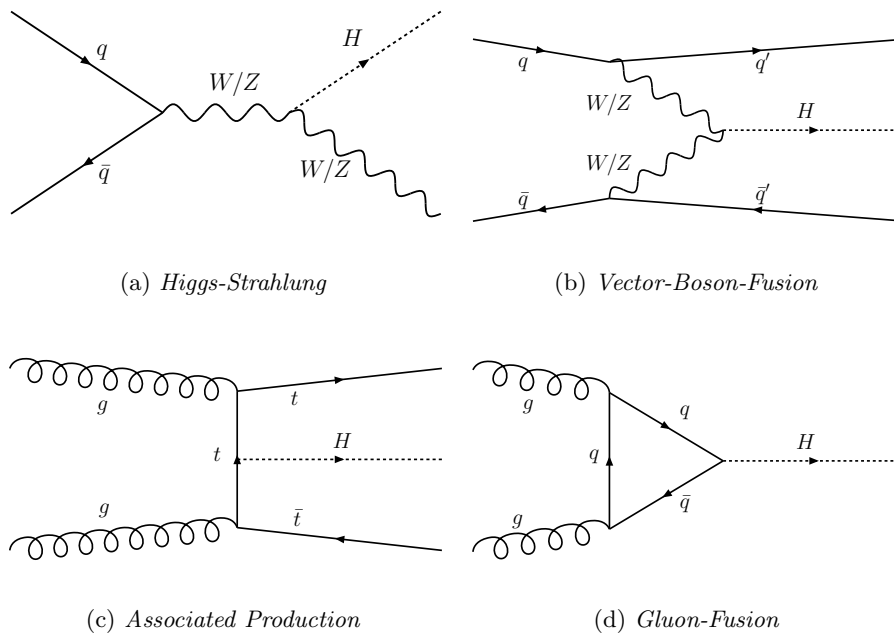


Figure 2.1: LO Feynman-diagrams for the Higgs production processes at hadron colliders.

The next process that contributes is the so-called *Vector-Boson-Fusion* process, shown in Fig. 2.1(b). In this process both incoming quarks radiate a vector boson (W or Z), which then fuse to a Higgs boson.

The last, and at the same time most important production mode is the *Gluon-Fusion* process, shown in Fig. 2.1(d). In this production process the incoming particles are gluons. Since the Higgs does not couple to the gluons directly (i.e. the gluons are massless gauge bosons), the Higgs production has to be mediated via a quark loop. Again the largest contribution to this process comes from diagrams including a heavy quark (b, t) in the loop. From first principles it is not obvious that this is the dominating Higgs production process at the LHC. One might even argue, that since the corresponding diagram includes a loop, the process might be suppressed (loop-suppressed) with respect to the VBF process. But the importance of the *Gluon-Fusion* process becomes clear when taking into account the PDFs of the protons at the appropriate scale. The parton-parton luminosities  $\mathcal{L}_{ff}$  as a function of the parton-parton invariant mass  $m_{ff}$  are shown in Fig. 2.2. They are defined as

$$\mathcal{L}_{ff}(m_{ff}) = \sum_{ff'} \int_0^1 dx_1 dx_2 f_f(x_1) f_{f'}(x_2) \delta(x_1 x_2 s - m_{ff}^2), \quad (2.1)$$

with  $f_f(x)$  the parton density in the proton of parton type  $f$  with fractional momentum  $x$

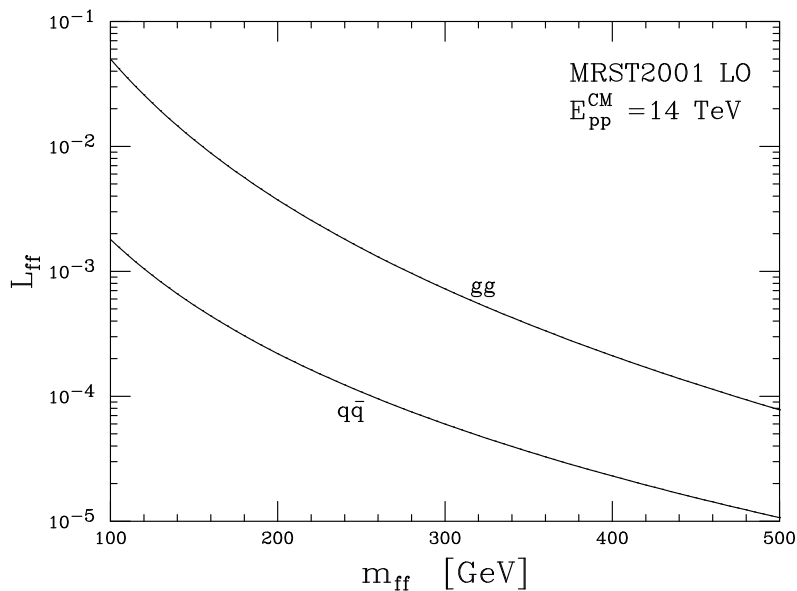


Figure 2.2: Parton-parton luminosities for proton-proton collisions at the LHC energy ( $E_{pp}^{\text{CM}} = 14 \text{ TeV}$ ) as a function of the parton-parton invariant mass with the MRST2001 LO PDF set. The two lines show the gluon-gluon (gg) and the quark-anti-quark ( $q\bar{q}$ ) luminosities.

(cf. section 1.3.6). The PDFs are taken from the MRST2001 LO set [24] and the proton-proton center-of-mass energy is  $\sqrt{s} = 14 \text{ TeV}$ . The two lines in Fig. 2.2 correspond to the gluon-gluon (gg) and the quark-anti-quark ( $q\bar{q}$ ) luminosities, where in the  $q\bar{q}$  case the sum runs over the pairs  $u\bar{u}$ ,  $d\bar{d}$  and  $s\bar{s}$ .

The first observation is that the gg luminosity exceeds the  $q\bar{q}$  luminosity by at least one order of magnitude over almost the whole range under investigation. Additionally, it has to be pointed out that with the exception of the *Gluon-Fusion* process all final states contain other (partly heavy) particles, so that the parton-parton invariant mass in general has to be larger than the Higgs mass in order to make the production possible. These facts show how the *Gluon-Fusion* process is preferred over the other Higgs production mechanisms.

The LO Higgs production cross-sections at LHC for the various production processes as a function of the Higgs mass are shown in Fig. 2.3. The cross-sections for the *Vector-Boson-Fusion* and the *Associated Production* have been computed using the dedicated programs VV2H [22] and HQQ [23]. The calculations for the *Higgs-Strahlung* and the *Gluon-Fusion* processes can be found in Appendix B.

The bands in Fig. 2.3 correspond to the variation of the factorization and renormalization scales  $\mu_R$  and  $\mu_F$ . They are varied simultaneously in the range  $[\mu/2, 2\mu]$ , with  $\mu$  some process dependent reference scale. For the *Higgs-Strahlung* processes it is either the mass

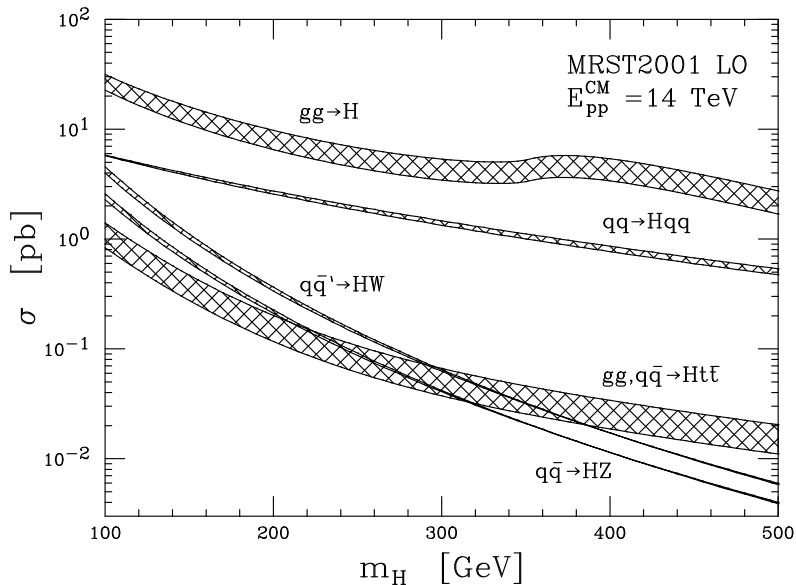


Figure 2.3: SM Higgs production cross-sections for the various processes as a function of the Higgs mass at the LHC. The bands indicate the uncertainty coming from the variation of the factorization scale  $\mu_F$  (normalization scale  $\mu_R$ ) in the range  $\mu/2 \leq \mu_{R/F} \leq 2\mu$ , where  $\mu$  is some process dependent reference scale.

of the  $W$ -boson  $m_W$  or the mass of the  $Z$ -boson  $m_Z$ , for the other processes it is the Higgs mass  $m_H$ . The cross-section variations under the variation of the scales is much smaller for the *Vector-Boson-Fusion* and the *Higgs-Strahlung* processes. Since the LO diagrams of these processes (cf. Fig. 2.1) are independent of the strong coupling, there is no  $\mu_R$  dependence. The other two processes are of order  $\alpha_s^2$ .

### 2.1.2 Decay Modes and Branching Ratios

A Higgs produced in any of the production channels described above will almost immediately decay into other particles. The direct decay products are again restricted to the set of particles that couple to the Higgs boson, i.e. fermions (quarks and leptons) and massive vector bosons ( $W$  and  $Z$ ). The branching ratio of the Higgs decay-mode  $X$  is defined as

$$BR(X) = \frac{\Gamma(H \rightarrow X)}{\sum_Y \Gamma(H \rightarrow Y)} = \frac{\Gamma(H \rightarrow X)}{\Gamma_{\text{tot}}(H)}, \quad (2.2)$$

where  $\Gamma(H \rightarrow X)$  is the partial width of the decay-mode  $H \rightarrow X$ , and  $\Gamma_{\text{tot}}(H)$  is the total width of the Higgs boson, i.e. the sum over the partial widths of all possible decay-modes

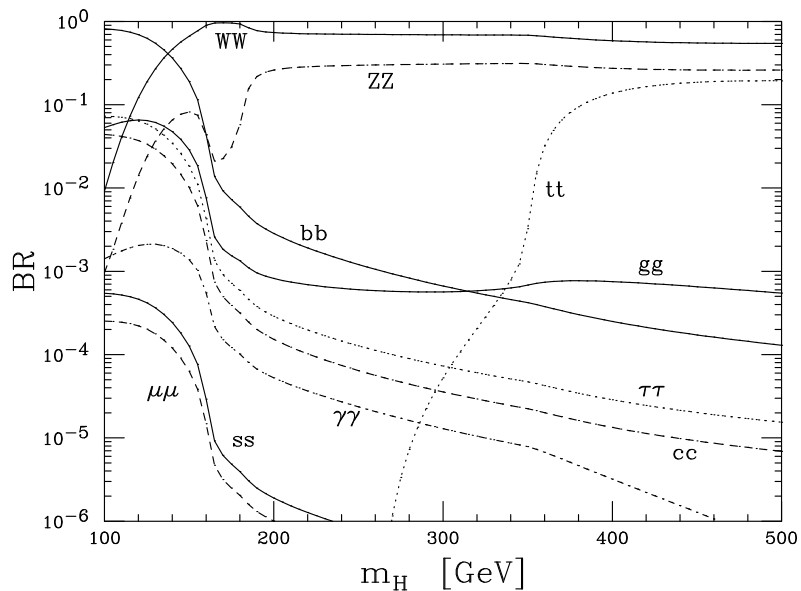


Figure 2.4: SM Higgs branching ratios for the various decay-modes as a function of the Higgs mass.

Y. Recalling the general formula for the partial width from section 1.4,

$$\Gamma(A \rightarrow X) = \frac{1}{2m_A} \int \left( \prod_{p_f \in X} \frac{d^3 p_f}{2E_f (2\pi)^3} \right) |\mathcal{M}(A \rightarrow X)|^2 (2\pi)^4 \delta^{(4)}(p_A - \sum p_f), \quad (2.3)$$

it becomes clear that the magnitude of the partial width, and thus the branching ratio, is dictated by the couplings appearing in the matrix element  $\mathcal{M}$  and the kinematic restrictions in  $\delta^{(4)}(p_A - \sum p_f)$ . The first of these arguments leads to the preferred decay of the Higgs boson into heavy fermions or vector bosons, the second argument forbids e.g. the decay of the Higgs into two top-quarks when it is lighter than about twice the top mass  $m_t$ .

Qualitatively the fermionic decay-modes are dominated by the decay into  $b\bar{b}$  for Higgs masses below and by  $t\bar{t}$  for Higgs masses above the top-pair threshold. As soon as the Higgs mass reaches the vector boson-pair threshold ( $m_H \sim 2 \times m_W$ ), these decay modes become dominant. There are two other decay modes; the decays into two gluons and into two photons. As discussed before, these gauge-bosons do not couple to the Higgs, thus these modes can only be mediated via a fermion- or a massive-vector-boson-loop.

The branching ratios for the different Higgs decay modes as a function of the Higgs mass are shown in Fig. 2.4. The numbers have been computed using the program HDECAY [25].

### 2.1.3 Towards Discovering the Higgs

We want to step back a moment and review the consequences implied by the previous observations for a possible discovery of the Higgs at a hadron-collider experiment. Over the whole mass range under investigation the cross-section of the *Gluon-Fusion* process is about one order of magnitude larger than the ones for the other production channels. In fact, provided that the search-strategy is inclusive enough, i.e. we do not apply any selection cuts that favour explicitly one of the production processes, they can be neglected completely.

More discussion is needed for the choice of the decay-mode, in which the Higgs boson is most likely observable. Naively the mode might be chosen that provides the largest branching ratio for each Higgs mass hypothesis. But this is not always the best choice, taking into account that in an actual experimental analysis the Higgs boson events need to be separated from the background events. For this goal it is desirable to choose the decay-mode with a signal as clean as possible. 'Clean' means that the final state particles detected in the experiment should be reliably identifiable, and their kinematic observables (e.g. charge, momentum, energy) can be measured precisely. How well a certain particle can be measured obviously depends to a large extent on the specific detector used in the experiment <sup>1</sup>. Nevertheless, a few general rules hold for all hadron-collider experiments running or under construction:

- Quarks and gluons undergo a shower-like radiation chain, hadronize and form jets. It is very difficult, if not even impossible, to determine the initial quark flavour of a jet. Even separating quark-jets from gluon-jets is very challenging and leads to a large fraction of misidentified jets. In addition, measuring kinematic observables of jets is not very precise and usually leads to bad momentum- and energy-resolutions [26].
- Charged leptons (electrons, muons) and photons can be identified reliably and have an energy/momentum-resolution at the order of a few percent or better.
- Neutrinos leave the experiment undetected.

Having these criteria in mind, it can be justified which of the various decay-modes are most promising for the different Higgs mass hypotheses.

- High mass region ( $m_H \gtrsim 200$  GeV)  
In this region the branching ratio into a pair of massive vector bosons is almost unity. The branching ratio into a pair of  $W$ -bosons is about a factor of 2 larger than

---

<sup>1</sup> It will be discussed in chapter 6 how this is done in the CMS experiment.



the one into a pair of  $Z$  bosons. In the case of the decay of the vector bosons into leptons (which provides the cleanest signal), the neutrinos coming from the  $W$ -decay will stay undetected, whereas the  $Z$ -channel allows for the full reconstruction of the Higgs momentum, and thus for the reconstruction of the invariant Higgs mass peak over the continuum background.

- Intermediate region ( $m_H \sim 170$  GeV)

The branching ratio of the Higgs decaying into a pair of  $W$ -bosons is almost unity. The impossibility of reconstructing the Higgs momentum completely due to the undetected neutrinos can be overcome by applying selection cuts, taking into account the spin-correlations of the system [27].

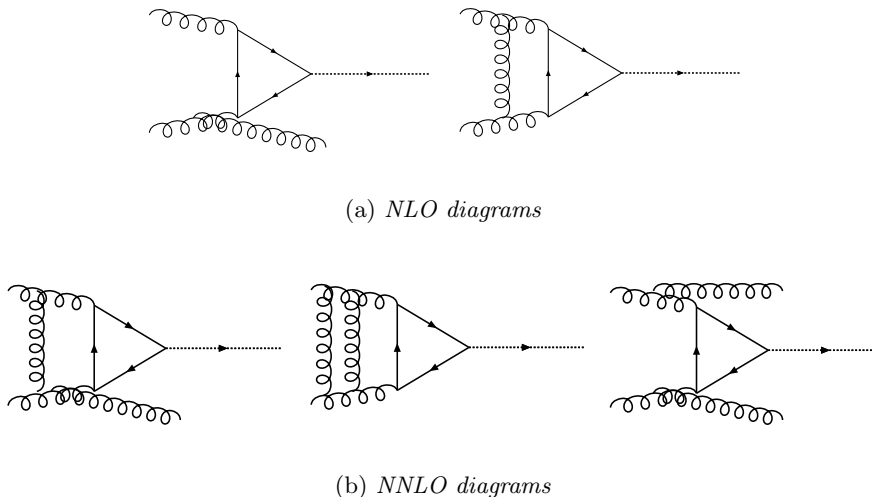
- Low mass region ( $m_H \lesssim 140$  GeV)

The decay-modes are dominated by  $b\bar{b}$ . Nonetheless the discovery of the Higgs in this mode is very difficult, due to the overwhelming QCD background. The most promising mode is the di-photon-mode. Although the branching ratio is small ( $\sim 10^{-3}$ ), the Higgs momentum can be fully determined, and thus the invariant Higgs mass peak can be reconstructed over the continuum  $\gamma\gamma$ -background.

## 2.2 Improving the Predictions: Higher Order QCD Effects

As shown above, the dominant Higgs production mechanism at the LHC is the *Gluon-Fusion* process. This implies that a high-precision calculation for the Higgs production cross-section for the *Gluon-Fusion* process is fundamental. When looking at Fig. 2.3 we find that the LO calculation is not sufficient. The scale-variation uncertainty amounts to  $\sim 30\%$  over the entire mass-range. In addition, the final-state particle configuration of the LO process consists of only the Higgs boson; there is no additional hadronic activity and the Higgs boson transverse momentum  $p_T^H$  is always zero; a clearly unrealistic prediction. In order to overcome these shortcomings higher order QCD effects have to be taken into account.

There are two approaches for including higher order QCD effects. The first one is the inclusion of Feynman-diagrams of higher orders in  $\alpha_s$ , thus including more terms of the perturbative expansion of the cross-section (fixed-order calculation). The second is the inclusion of the leading logarithmic terms in the  $\alpha_s$ -expansion up to all orders (resummation). Both approaches, as well as the combination of them will be discussed in the upcoming sections.

Figure 2.5: (N)NLO Feynman-diagrams for the process  $gg \rightarrow H$ .

### 2.2.1 Fixed-Order Calculation

In this section the production cross-section and kinematic observables of the Higgs boson in the *Gluon-Fusion* channel up to NNLO is discussed. Some Feynman-diagrams contributing to the process up to this order are shown Fig. 2.5. All virtual and real emission amplitudes have to be computed and suitably combined. The first inclusive and semi-inclusive NNLO calculations have been performed in [29]. However, in order to apply arbitrary cuts on the final-state particle phase space, a fully differential calculation is needed. The main difficulty of such an exclusive calculation is the structure of the singularities in the double-real-radiation amplitudes. While at NLO (single-real-radiation) subtraction methods [30] are well known and solve the complications arising from such singularities, a similar method could not be adapted to the double-real-radiation contribution for a long time<sup>2</sup>. An alternative solution has been developed in [32, 33]. In contrast to the subtraction method the extraction of singular regions in the phase-space is completely automated and the cancellation of the singularities is performed numerically. The authors of [32] apply this method (*Sector-Decomposition*<sup>3</sup>) to the *Gluon-Fusion* process in the Monte-Carlo program FEH1P [34].

The program FEH1P incorporates two approximations. The first is the *heavy-top-quark* approximation, which is valid as long as the Higgs is lighter than about twice the top

<sup>2</sup> Recently the counter-terms needed for the subtraction of the singularities in the double-real-radiation amplitudes were computed in [31].

<sup>3</sup> The *Sector-Decomposition* method is discussed in more detail in Appendix C.

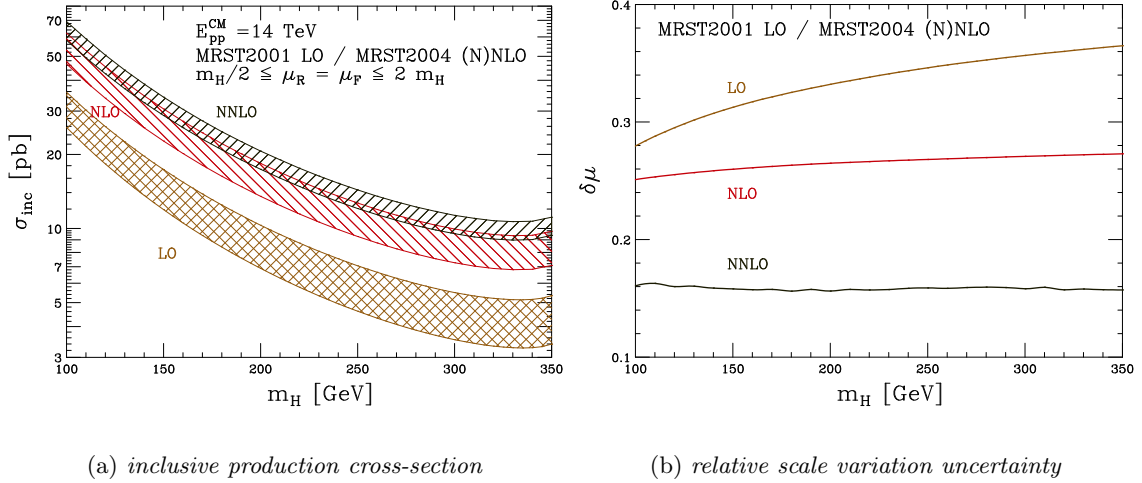


Figure 2.6: SM Higgs production cross-sections and relative scale variation at different orders of  $\alpha_s$  for the *Gluon-Fusion* channel as function of the Higgs mass.

mass ( $m_H \lesssim 2 \times m_t$ ). In this approximation the top-quark loop is contracted to a point-like vertex [35]. The second approximation consists in neglecting other quarks (i.e. the b-quark) in the loop contributing to the process. In what follows this program will be used for the computation of the fixed-order results of the  $pp \rightarrow H + X$  process through *Gluon-Fusion*.

We estimate the error introduced through these two approximations for the production of a Higgs with mass  $m_H = 165 \text{ GeV}$  using the program HiGLU [36], which computes the cross-section at NLO using the exact top mass dependence and the bottom-loop. The cross-section with the full top and bottom mass dependence is

$$\sigma_{\text{HiGLU}} = (24.56 \pm 0.01) \text{ pb.} \quad (2.4)$$

The NLO cross-section from FEHiP is

$$\sigma_{\text{FEHiP}} = (25.85 \pm 0.01) \text{ pb,} \quad (2.5)$$

leading to a relative error of

$$\Delta_{\text{b/t}} \simeq 5\%. \quad (2.6)$$

### 2.2.1.1 Inclusive Cross-Section

First the effects of the higher-order corrections to the inclusive  $pp \rightarrow H + X$  cross-section at the LHC are investigated. The cross-sections for the Higgs mass range from 100 to

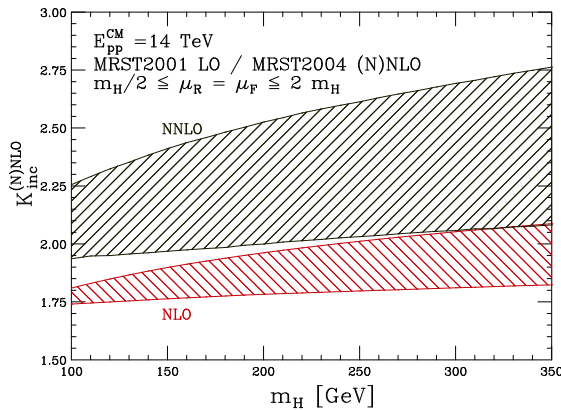


Figure 2.7: Inclusive  $K$ -factors at different orders of  $\alpha_s$  for the *Gluon-Fusion* channel as a function of the Higgs mass and the scale choice  $\mu$ .

350 GeV are shown in Fig. 2.6(a)<sup>4</sup>. The bands correspond to the simultaneous variation of the renormalization- and factorization-scale ( $\mu_R$ ,  $\mu_F$ ) in the range  $[\frac{m_H}{2}, 2m_H]$ . The statistical uncertainties from the numerical integration are negligible compared to the scale uncertainty, and therefore not shown.

The inclusive cross-section decreases with increasing Higgs mass (cf. Fig. 2.6(a)). While the LO- and the NLO-bands are separated, the NLO- and NNLO-bands overlap over the entire mass range, indicating a convergence of the series expanded in  $\alpha_s$ . In addition the scale uncertainty decreases when going from NLO to NNLO, while the LO and NLO scale uncertainties are of the same order. This can be seen more clearly in Fig. 2.6(b), where the relative scale variation  $\delta\mu$ , defined as

$$\delta\mu(m_H) := \frac{\sigma_{\text{inc}}(m_H, \mu = m_H/2) - \sigma_{\text{inc}}(m_H, \mu = 2m_H)}{\sigma_{\text{inc}}(m_H, \mu = m_H/2)}, \quad (2.7)$$

is shown. While the uncertainties in the LO (NLO) case range between 28% and 37% (25% and 28%), the uncertainty at NNLO is constant at  $\sim 16\%$ ; an improvement by a factor  $\geq 1.8$  ( $\geq 1.6$ ) compared to the LO (NLO) numbers.

The importance of the NNLO corrections can also be seen by the increase in the inclusive cross-section caused by them. To quantify the effects the inclusive  $K$ -factor can be defined as

$$K_{\text{inc}}^{(N)\text{NLO}}(m_H, \mu) = \frac{\sigma_{\text{inc}}^{(N)\text{NLO}}(m_H, \mu)}{\sigma_{\text{inc}}^{\text{LO}}(m_H, \mu)}, \quad (2.8)$$

where  $\mu := \mu_R = \mu_F$ . The corresponding distributions are shown in Fig. 2.7. The NLO  $K$ -factors range between 1.7 and 2.0, while the NNLO  $K$ -factors range between 2.0 and 2.7,

<sup>4</sup> The cross-sections are only shown up to a Higgs mass value of 350 GeV. For larger Higgs masses the *heavy-top-quark* approximation does not hold anymore.

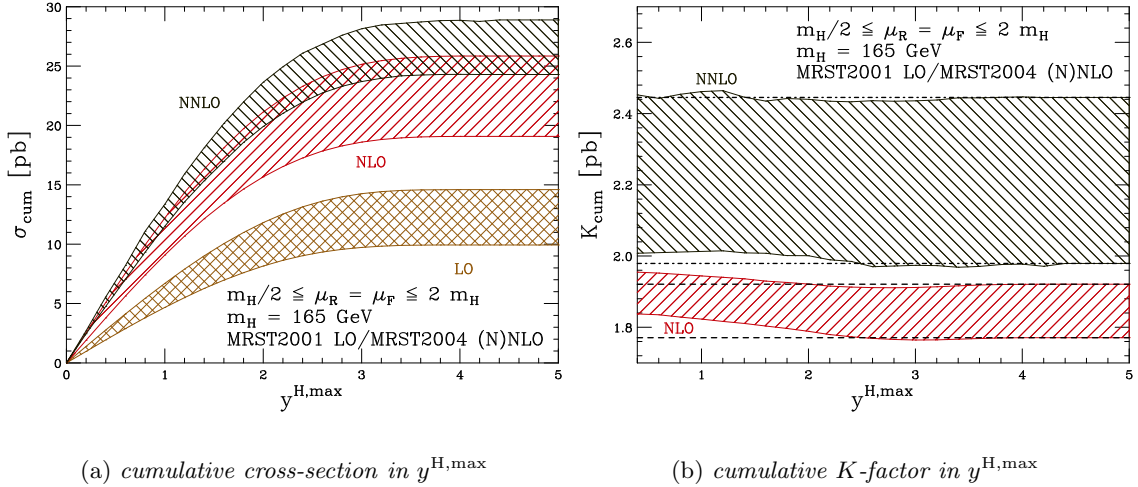


Figure 2.8: Cumulative cross-section (a) and  $K$ -factors (b) as a function of  $y^{H,\max}$  for a Higgs mass of  $m_H=165 \text{ GeV}$  for different orders in the perturbative calculation. The bands correspond to a scale variation in the range  $[m_H/2, 2 m_H]$ . The dashed lines in (b) display the inclusive  $K$ -factors.

depending on the Higgs mass  $m_H$  and the scale choice. It is worth noting that the increase in the variation of the  $K$ -factors with varying scale when going from NLO to NNLO does not originate from a larger scale uncertainty of the NNLO cross-section compared to NLO (in fact, the opposite is true). It comes from the definition of the  $K$ -factors in eq. 2.8, namely from the variation of the LO cross-section in the denominator. Even if the numerator would show no variation at all, the  $K$ -factors would still vary significantly.

In summary, while the absolute corrections are rather big, the scale variation uncertainty is reduced indicating the convergence of the perturbative expansion. It is interesting to see how further corrections affect this process. The leading logarithmic contributions at  $N^3\text{LO}$  have been calculated in [37]. The effect turns out to be  $\sim 5\%$  for the LHC and it can be safely assumed that corrections to the inclusive cross-section beyond NNLO can be neglected.

### 2.2.1.2 Higgs Transverse Momentum and Rapidity

Having seen the importance of the higher-order effects on the inclusive cross-sections, the effects on the kinematic variables of the Higgs boson can be studied. The Higgs kinematics is completely determined by its mass  $m_H$ , its transverse momentum  $p_T^H$  and its rapidity

$y^{\text{H}}$ , defined as

$$y^{\text{H}} = \frac{1}{2} \ln \left( \frac{E^{\text{H}} + p_z^{\text{H}}}{E^{\text{H}} - p_z^{\text{H}}} \right), \quad (2.9)$$

where  $E^{\text{H}}$  is the Higgs energy and  $p_z^{\text{H}}$  the  $z$ -component of the spatial Higgs momentum. We will focus here on the Higgs mass hypothesis  $m_{\text{H}} = 165$  GeV.

To quantify the higher-order effects on the kinematic variables, the cumulative cross-sections  $\sigma_{\text{cum}}$  in  $y^{\text{H}}$  and  $p_{\text{T}}^{\text{H}}$  are defined as

$$\sigma_{\text{cum}}(y^{\text{H},\text{max}}) = \int_{-y^{\text{H},\text{max}}}^{y^{\text{H},\text{max}}} \frac{\partial \sigma}{\partial y^{\text{H}}} dy^{\text{H}}, \quad (2.10)$$

and

$$\sigma_{\text{cum}}(p_{\text{T}}^{\text{H},\text{max}}) = \int_0^{p_{\text{T}}^{\text{H},\text{max}}} \frac{\partial \sigma}{\partial p_{\text{T}}^{\text{H}}} dp_{\text{T}}^{\text{H}}, \quad (2.11)$$

i.e. the differential cross-sections are integrated up to some cut-off value, simulating an experimental cut on the Higgs boson kinematics. Taking the cut-off to infinity results in the inclusive cross-section  $\sigma_{\text{inc}}$  as computed in section 2.2.1.1. The corresponding cumulative  $K$ -factors are defined as

$$K_{\text{cum}}^{(N)\text{NLO}}(X, \mu) = \frac{\sigma_{\text{cum}}^{(N)\text{NLO}}(X, \mu)}{\sigma_{\text{cum}}^{\text{LO}}(X, \mu)}, \quad (2.12)$$

with  $X \in \{p_{\text{T}}^{\text{H},\text{max}}, y^{\text{H},\text{max}}\}$ .

The distributions for  $y^{\text{H},\text{max}}$  are shown in Fig. 2.8. The cross-section (Fig. 2.8(a)) increases as the cut-off  $y^{\text{H},\text{max}}$  is increased, until the inclusive cross-section is reached. The cumulative  $K$ -factors are shown in Fig. 2.8(b). With the exception of the low- $y^{\text{H},\text{max}}$  region ( $\lesssim 2$ ) at NLO, the  $K$ -factors are constant and equal to the inclusive  $K$ -factors (shown as dashed lines in Fig. 2.8(b)). Apparently restricting the Higgs rapidity phase-space has no effect on the impact of the higher-order QCD corrections. This insensitivity of the  $K$ -factors to the restriction of the phase-space can not be regarded as a general rule. This will become apparent in the next variable,  $p_{\text{T}}^{\text{H},\text{max}}$ .

The distribution for the cumulative cross-section as a function of  $p_{\text{T}}^{\text{H},\text{max}}$  is shown in Fig. 2.9. While the restriction of the Higgs phase-space has no effect on the cross-section at LO (i.e. at LO the Higgs transverse momentum  $p_{\text{T}}^{\text{H}}$  is always 0), the cross-sections decrease rapidly at NLO/NNLO with decreasing cut-off  $p_{\text{T}}^{\text{H},\text{max}}$ . They even become negative for cut-offs of about 5 GeV (8 GeV) in the NLO (NNLO) case. This (unphysical) behavior for small  $p_{\text{T}}^{\text{H},\text{max}}$ -values can be understood in the context of the fixed-order calculation. As the Higgs transverse momentum  $p_{\text{T}}^{\text{H}}$  is restricted to small values, logarithmic terms of the

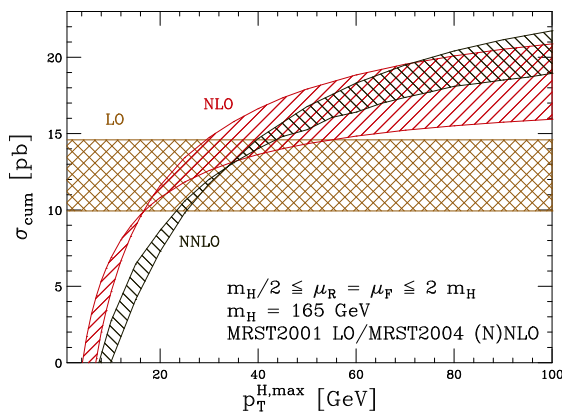


Figure 2.9: Cumulative cross-section as a function of  $p_T^{H,\max}$  for a Higgs mass of  $m_H=165$  GeV at different orders of the perturbative calculation. The bands correspond to a scale variation in the range  $[m_H/2, 2m_H]$ .

type  $\ln(p_T^H/Q)$ , with  $Q$  some typical scale for the process, become large and negative. In this regime re-summation of these logarithmic terms to all orders would be needed to render the cumulative cross-section predictions physically reliable. In other words, the effect shows how soft, multiple radiation becomes important in the low- $p_T^H$  phase-space region. But these radiative effects are not fully covered in the fixed-order calculation, where at most two partons are present in the final state.

In a previous section it has been discussed that the fixed-order inclusive cross-section can be regarded as a very precise prediction for the Higgs production through *Gluon-Fusion* at the LHC. Apparently, when restricting the Higgs phase-space to the low- $p_T^H$  region, this predictive power may break down. The question, up to which cut-off  $p_T^{H,\max}$  the fixed-order differential cross-section has to be integrated in order to render the resulting cumulative cross-section reliable, has to be posed. This is especially important if experimental cuts are imposed on the final state particles that restrict the Higgs phase-space to this region. The question will be answered in the upcoming section.

### 2.2.2 Re-Summation

After having discussed the prediction of fixed-order calculations up to NNLO, an alternative strategy for including higher-order QCD effects should be discussed. Instead of including the terms in the expansion of the cross-section at higher order in  $\alpha_s$ , one can try to include only the leading logarithmic terms, but to all orders in  $\alpha_s$ .

This so called re-summation can e.g. be implemented in a parton-shower algorithm, as

applied in the LO Monte-Carlo event generator HERWIG [10]<sup>5</sup>. The inclusive cross-section computed by HERWIG corresponds to a fixed-order LO cross-section. Additional hadronic activity is added to the event by the showering of the initial state partons, i.e. by either emitting gluons or/and by gluons splitting into  $q\bar{q}$ -pairs according to probabilities defined by the appropriate *Sudakov Form Factors* (cf. section 1.3.6). In order to compare the HERWIG results to the fixed-order calculation for variable renormalization and factorization scales, they are multiplied with the inclusive  $K$ -factor  $K^{\text{HW}}$ , defined as

$$K^{\text{HW}}(\mu) = \frac{\sigma_{\text{inc}}^{\text{LO}}(\mu)}{\sigma_{\text{inc}}^{\text{HW}}}, \quad (2.13)$$

with  $\sigma_{\text{inc}}^{\text{HW}}$  the inclusive cross-section predicted by HERWIG.

After this scaling the inclusive cross-section computed by HERWIG is equivalent to the fixed-order cross-section. The cumulative cross-sections obtained using the event generator HERWIG are defined as

$$\sigma_{\text{cum}}^{\text{HW}}(y^{\text{H,max}}, \mu) = K^{\text{HW}}(\mu) \times \int_{-y^{\text{H,max}}}^{y^{\text{H,max}}} \frac{\partial \sigma^{\text{HW}}}{\partial y^{\text{H}}} dy^{\text{H}}, \quad (2.14)$$

and

$$\sigma_{\text{cum}}^{\text{HW}}(p_{\text{T}}^{\text{H,max}}, \mu) = K^{\text{HW}}(\mu) \times \int_0^{p_{\text{T}}^{\text{H,max}}} \frac{\partial \sigma^{\text{HW}}}{\partial p_{\text{T}}^{\text{H}}} dp_{\text{T}}^{\text{H}}. \quad (2.15)$$

These distributions, computed with HERWIG and compared to the LO cumulative cross-sections from section 2.2.1.2, are shown in Fig. 2.10. As expected, the parton-shower has no effect on the Higgs rapidity distribution, while the  $p_{\text{T}}^{\text{H}}$  distribution changes substantially. Through the showering of the initial state partons, the Higgs boson can pick up transverse momentum, resulting in the shown cumulative  $p_{\text{T}}^{\text{H}}$  spectrum.

The Higgs transverse momentum prediction from the LO calculation obviously is not sufficient. As discussed before, at least one additional parton has to be present in the final state for the Higgs to receive some transverse momentum  $p_{\text{T}}^{\text{H}} > 0$ . In contrast to the HERWIG-approach, where the transverse momentum of the Higgs is uniquely generated through the multiple radiation of partons in the shower, at NLO one additional parton from the hard scattering process may be present in the final state, recoiling against the Higgs boson. Momentum conservation demands that this parton and the Higgs boson are always back-to-back in the plane transverse to the collision-axis, i.e.  $p_{\text{T}}^{\text{parton}} = p_{\text{T}}^{\text{H}}$ . From Fig. 2.9 it became clear that multiple, soft radiation effects are important in the low

---

<sup>5</sup> Here we use an unofficial version of HERWIG, updated for full spin-correlation effects in the decay products of the Higgs boson, kindly provided by Bryan Webber.



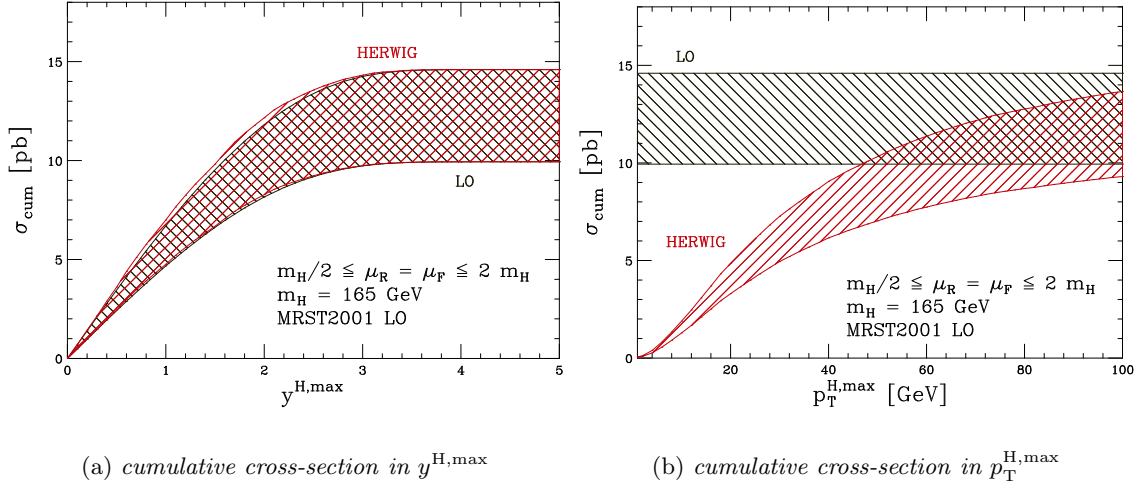


Figure 2.10: Cumulative cross-sections as functions of  $y^{H,\max}$  and  $p_T^{H,\max}$  for a Higgs mass of  $m_H=165$  GeV at LO. The bands correspond to a scale variation in the range  $[m_H/2, 2m_H]$ .

$p_T^H$  region. This importance can be demonstrated in more detail by comparing the NLO cumulative cross-section distribution with the distributions including these soft effects. In the course of this comparison we make use of two additional tools. The first one is a calculation of the Higgs boson transverse momentum spectrum  $p_T^H$  presented in [38] and implemented in the program HqT [39], where a matching technique is used to match the fixed NLO results to a re-summed calculation including the leading and next-to-leading logarithmic terms (NLL). The second tool is MC@NLO [40], which combines NLO hard scattering amplitudes with the parton shower algorithm of HERWIG, i.e. it re-sums the leading logarithmic terms up to all orders in  $\alpha_s$  and normalizes the inclusive cross-section to NLO [41]

At this point the normalization strategy pursued in this comparison has to be discussed. The tools used treat this issue differently. While, as discussed before, FEH<sub>IP</sub> uses the *heavy-top-approximation*, but re-scales the final result by the ratio of the cross-sections using the *exact-top-mass* dependence and the *heavy-top-approximation* at Born level, HqT does not perform this re-scaling, i.e. HqT computes cross-sections either in the bare *heavy-top-approximation*, or includes the full top mass dependence. In MC@NLO among two different strategies can be chosen. The first one is the *heavy-top-approximation*, the second one is using *exact-top-mass* dependence for the amplitudes at Born-level, and *infinite-top-mass* for the NLO amplitudes.

In addition, HqT does not compute inclusive cross-sections, but binned Higgs transverse

program	HiGLU	FEHiP	MC@NLO
$m_t$ dep.	<i>exact</i>	<i>mixed</i>	<i>mixed</i>
$\sigma_{\text{inc}}^{\text{NLO}}$ [pb]	$25.54 \pm 0.01$	$25.85 \pm 0.01$	$23.48 \pm 0.01$
$\Delta^{\text{rel}}$ [%]	-	+1.2	-8.1

Table 2.1: Inclusive NLO cross-sections for the *Gluon-Fusion* process computed using different top-mass-dependencies. The cross-sections are computed for a Higgs mass of  $m_H=165$  GeV and the scale choice  $\mu_R = \mu_F = m_H/2$  using MRST2004 NLO PDF sets. In this comparison the bottom-loop is not included.

momentum spectra. Since inclusive (cumulative) cross-sections should be compared, numerical integration tools have to be used to derive the cross-sections from the HqT-spectra. The tool used is the so called *trapezoidal rule*.

First the question should be answered, which of the above approaches gives the most-precise cross-section prediction compared to the full NLO *exact-top-mass* calculation. In order to do this the various cross-section predictions can again be compared to the program HiGLU [36]. The inclusive NLO cross-sections for the *Gluon-Fusion* process computed using the different programs are listed in Table 2.1. The last line shows the relative variation ( $\Delta^{\text{rel}}$ ) of each number with respect to the HiGLU prediction in percent, i.e.

$$\Delta^{\text{rel}} = \frac{\sigma_{\text{inc}}^{\text{NLO}}(X) - \sigma_{\text{inc}}^{\text{NLO}}(\text{HiGLU})}{\sigma_{\text{inc}}^{\text{NLO}}(\text{HiGLU})} \times 100 \%, \quad (2.16)$$

with  $X \in \{\text{FEHiP}, \text{MC@NLO}\}$ . The FEHiP number deviates by +1.2% compared to the *exact-top-mass* number, while the MC@NLO approach underestimates the inclusive cross-section by 8.1%. In principal all the following results could be normalized to the HiGLU prediction, but for consistency reasons <sup>6</sup> the FEHiP result is used as the default inclusive cross-section value; i.e. for all the following numbers and plots, whenever a number is labeled MC@NLO or HqT, we refer to the cross-section that is inclusively re-weighted to the FEHiP prediction.

Since HqT only computes Higgs transverse momentum spectra, and it has been concluded before that re-summation does not affect the Higgs rapidity spectrum significantly, the study can be restricted to the Higgs- $p_T$  cumulative cross-section. This distribution is shown in Fig. 2.11(a). While the distributions based on re-summed results agree over the whole spectrum (MC@NLO underestimates the cumulative cross-section slightly), the fixed NLO distribution fails, as expected, in the low- $p_T^H$  region. Only by integrating the fixed NLO distribution up to  $p_T^{H,\text{max}} \sim 50$  GeV the results become comparable, implying

<sup>6</sup> For the NNLO numbers used in the upcoming parts of this thesis, there are no *exact-top-mass* calculations available. Therefore the FEHiP prediction is used for the NLO numbers as well.

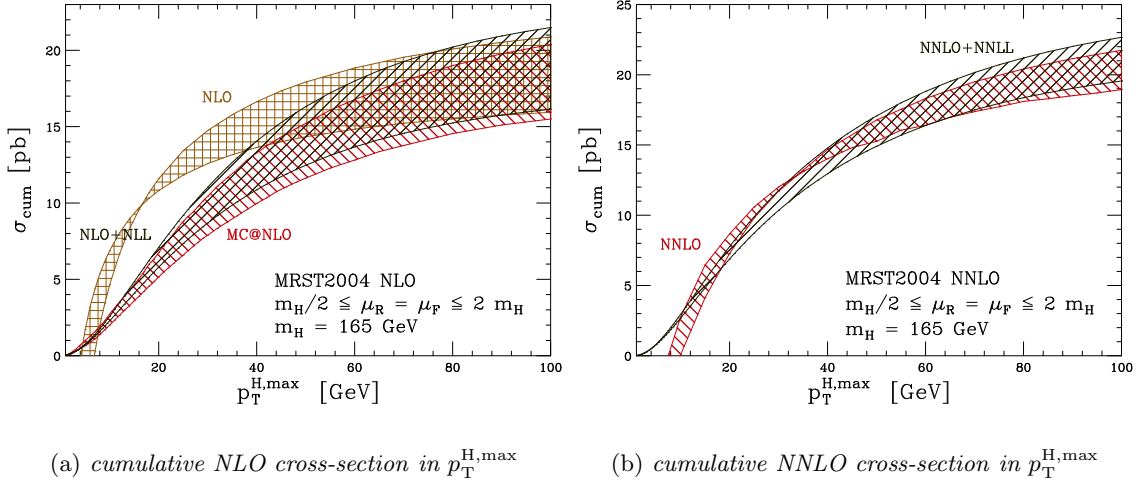


Figure 2.11: Cumulative cross-section as a function of  $p_T^{H,\max}$  for a Higgs mass of  $m_H=165$  GeV. The fixed-order cross-sections ((N)NLO) are compared to the re-summed spectra ((N)NLL) and the MC generator MC@NLO. The bands correspond to a scale variation in the range  $[m_H/2, 2m_H]$ .

that above this threshold effects of multiple soft radiation become very small. In a later section it will become clear how this leads to unreliable cross-section predictions by the fixed NLO calculation, when applying experimental cuts that restrict the Higgs phase space to the low- $p_T^H$  region.

Next the computation of the cross-sections at NNLO is considered. Since there is no parton-shower algorithm matched to NNLO hard scattering amplitudes, the distribution computed with FEH1P can only be compared to the NNLO+NNLL results from HQT. The corresponding  $p_T^{H,\max}$  cumulative cross-section distributions are shown in Fig. 2.11(b). Again the fixed-order prediction 'breaks down' in the very low  $p_T^{H,\max}$  region, but compared to the NLO case, both distributions agree much better down to a  $p_T^{H,\max}$  value of  $\sim 15$  GeV, indicating that the multiple soft radiation effects beyond NNLO are negligible already after integrating the fixed NNLO distribution up to about this threshold.

Next we investigate how well the two parton-shower event generators compare to the NNLO+NNLL distribution. For this the MC@NLO and HERWIG spectra in Figs. 2.11(a) and 2.10(b), respectively, are rescaled to the inclusive NNLO cross-section ( $R(\text{MC@NLO})$ ,  $R(\text{HERWIG})$ ). The distributions are shown in Fig. 2.12. All distributions agree, with MC@NLO slightly under-, and HERWIG slightly overestimating the cumulative cross-section. It can be concluded that the rescaled parton-shower MC predictions (especially in the case of MC@NLO) reproduce the 'best' prediction (NNLO+NNLL) reliably.

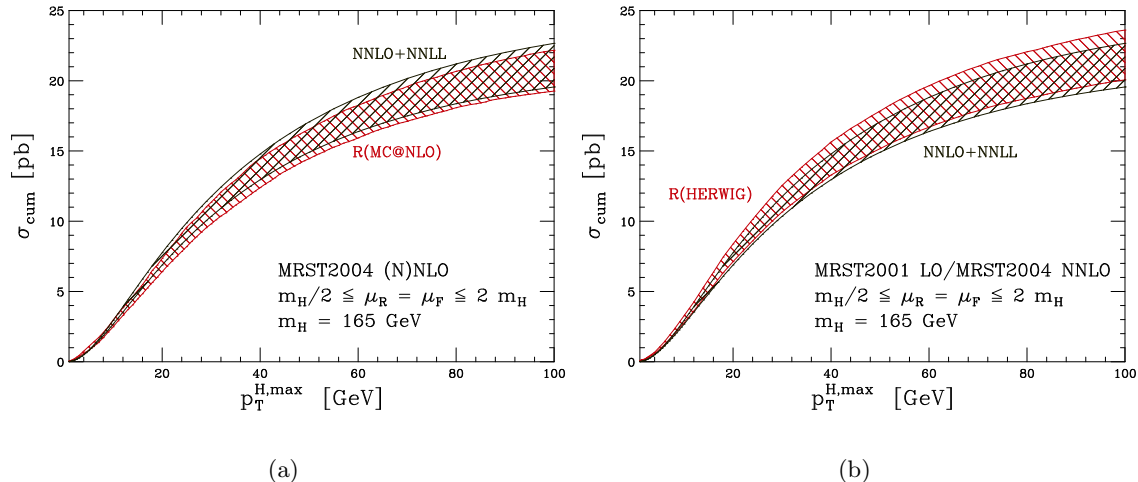


Figure 2.12: Cumulative cross-section as a function of  $p_T^{H,\max}$  for a Higgs mass of  $m_H=165$  GeV. The re-summed spectra ((N)NLO+(N)NLL) are compared to the rescaled HERWIG (a) and MC@NLO (b) predictions. The bands correspond to a scale variation in the range  $[m_H/2, 2m_H]$ .

### 2.3 Higher Order QCD Effects and Event Generators: The Re-Weighting Technique

In order to perform a realistic simulation of the events at hadron-collider experiments, it is desirable to generate Monte-Carlo events that can be passed through a detector simulation. In principle such events can be generated using a parton-shower algorithm as implemented in HERWIG or PYTHIA [11]. The short-coming of these generators is that they incorporate LO hard scattering amplitudes <sup>7</sup> with showering algorithms; however, above it has been observed that higher order QCD effects have a significant impact on the Higgs production through *Gluon-Fusion* at the LHC. In this section it is discussed how the results from fixed-order QCD calculations can be incorporated into such event generators. The technique explained below has been developed in the context of this and a previous thesis (by Giovanna Davatz). Results of this work have been published in [42].

<sup>7</sup> An exception to this is MC@NLO, which matches NLO hard scattering amplitudes with the parton-shower algorithm in HERWIG.

### 2.3.1 The Re-Weighting Procedure

The cross-section for the process  $pp \rightarrow \{p_i\}$ , generated by the generator  $G$  is

$$\sigma^G(\mathcal{O}) = \int d\Pi f^G(\{p_i\}) \mathcal{O}(\{p_i\}), \quad (2.17)$$

where the events  $f^G$  are integrated over the phase-space variables  $d\Pi$  of all final state particles  $i$  and  $\mathcal{O}$  is a selection function<sup>8</sup> of the final state particle kinematics  $p_i$ . The events then correspond to phase-space points weighted with the appropriate process amplitudes. The simplest observable is the inclusive cross-section  $\sigma_{\text{inc}}^G$  corresponding to  $\mathcal{O} = 1$ , i.e.

$$\sigma_{\text{inc}}^G \equiv \sigma^G(1) = \int d\Pi f^G(\{p_i\}). \quad (2.18)$$

The relation between the events  $f^G$  and the cross-section  $\sigma^G$  is therefore

$$f^G = \frac{d\sigma^G(1)}{d\Pi}. \quad (2.19)$$

The events  $f^G$  can be re-weighted with a function  $K^G$  ( $K$ -factors),

$$f^G \rightarrow f^{R(G)} = f^G K^G \quad (2.20)$$

and the re-weighted cross-section defined as

$$\sigma^{R(G)}(\mathcal{O}) = \int d\Pi f^G(\{p_i\}) K^G(\{p_i\}) \mathcal{O}(\{p_i\}) = \int d\Pi f^{R(G)}(\{p_i\}) \mathcal{O}(\{p_i\}). \quad (2.21)$$

The function  $K^G$  is determined by requiring the re-weighted cross-section  $\sigma^{R(G)}$  to reproduce a given reference cross-section  $\sigma^{\text{ref}}$  for a given selection function  $\mathcal{O}$ , i.e.

$$\sigma^{R(G)}(\mathcal{O}) = \sigma^{\text{ref}}(\mathcal{O}). \quad (2.22)$$

#### 2.3.1.1 Inclusive Re-Weighting

The simplest case is inclusive re-weighting, where it is required that the re-weighted inclusive cross-section  $\sigma_{\text{inc}}^{R(G)}$  matches some inclusive higher-order (HO) cross-section. In the above formalism this reads

$$\sigma_{\text{inc}}^{R(G)} \equiv \sigma^{R(G)}(1) = \sigma_{\text{inc}}^{\text{HO}}. \quad (2.23)$$

Combining eq. (2.21) and eq. (2.23) and solving the resulting equation for  $K^G$ , assuming that the re-weighting-function  $K^G$  is constant, leads to

$$K^G = \frac{\sigma_{\text{inc}}^{\text{HO}}}{\sigma_{\text{inc}}^G}. \quad (2.24)$$

This is the already familiar definition of the inclusive  $K$ -factor (cf. eq. (2.8)).

---

<sup>8</sup>  $\mathcal{O}$  either accepts or rejects events according to the kinematic configuration of the final state particles; i.e.  $\mathcal{O} \in \{0, 1\}$ .

### 2.3.1.2 Differential Re-Weighting

In general the selection function  $\mathcal{O}$ , and thus  $K^G$ , can be arbitrary functions of a set of kinematic variables of the final state particles  $p_i$ . As an example, the operator  $\delta(x - X)$  can be chosen for  $\mathcal{O}$ , with  $X$  some specific value for the kinematic variable  $x$ . Substituting this into relation (2.21) leads to

$$\sigma^{R(G)}(\mathcal{O}) = \int d\Pi dx \frac{d\sigma^G}{d\Pi dx} K^G(x) \delta(x - X) = \left. \frac{d\sigma^G}{dx} \right|_{x=X} K^G(X), \quad (2.25)$$

where relation (2.19) has been used for the definition of the events  $f^G$ . The reference cross-section can be rewritten in a similar way, i.e.

$$\sigma^{\text{ref}}(\mathcal{O}) = \int dx \frac{d\sigma^{\text{ref}}}{dx} \delta(x - X) = \left. \frac{d\sigma^{\text{ref}}}{dx} \right|_{x=X}. \quad (2.26)$$

Demanding the selection-function to be true for all possible values  $X$ , the relation for the differential  $K$ -factors as a function of the variable  $X$  becomes

$$K(X) = \left( \left. \frac{d\sigma^{\text{ref}}}{dx} \right|_{x=X} \right) \times \left( \left. \frac{d\sigma^G}{dx} \right|_{x=X} \right)^{-1}. \quad (2.27)$$

In this way the generated (multi-)differential cross-section can be matched to any (multi-)differential reference cross-section.

In practice it is not (always) possible to find both, generated and reference, differential cross-sections. Therefore the cross-section cannot be re-weighted point-wise as described in (2.27). The differential re-weighting procedure can be approximated by a bin-wise-integrated re-weighting procedure, choosing

$$\mathcal{O}_j = \begin{cases} 1, & \text{if } x \in [X_j, X_{j+1}] \\ 0, & \text{otherwise,} \end{cases} \quad (2.28)$$

with some specific binning  $X^j$  of the variable  $x$ . In this way the  $K$ -factors turn out to be bin-wise constant functions,

$$K_j^G \equiv K^G(x \in [X_j, X_{j+1}]) = \frac{\Delta\sigma_j^{\text{ref}}}{\Delta\sigma_j^G}, \quad (2.29)$$

with

$$\Delta\sigma_j^{\text{ref}} := \int_{X_j}^{X_{j+1}} dx \frac{d\sigma^{\text{ref}}}{dx} \quad \text{and} \quad \Delta\sigma_j^G := \int_{X_j}^{X_{j+1}} dx \frac{d\sigma^G}{dx}. \quad (2.30)$$

	HERWIG	MC@NLO	FEHiP	
			NLO	NNLO
$\sigma_{\text{inc}}$ [pb]	$8.66 \pm 0.07$	$23.48 \pm 0.01$	$25.85 \pm 0.01$	$28.90 \pm 0.08$
$K_{\text{inc}}^{\text{NLO}}$	$2.985 \pm 0.024$	$1.101 \pm 0.001$	-	-
$K_{\text{inc}}^{\text{NNLO}}$	$3.337 \pm 0.029$	$1.231 \pm 0.003$	-	-

Table 2.2: Cross-sections and inclusive  $K$ -factors for the various event generators for a Higgs mass of  $m_H = 165$  GeV.

### 2.3.2 Re-Weighting the *Gluon-Fusion* Process

The procedure described above can now be applied to the *Gluon-Fusion* process at the LHC. The events generated with HERWIG and MC@NLO are re-weighted in two different ways:

1. inclusive re-weighting,
2. differential re-weighting in  $p_T^H$ .

The Higgs mass hypotheses used are  $m_H=165$  GeV ( $m_H=120$  GeV) for the inclusive (differential) re-weighting. As reference cross-sections the FEHiP predictions with the scale choice  $\mu_F = \mu_R = m_H/2$  are used. The cross-sections and the inclusive  $K$ -factors for the two MC event generators are listed in Table 2.2. While the NLO  $K$ -factor for MC@NLO exclusively originates from the different treatment of the top quark mass dependence (cf. section 2.2.2), the large HERWIG  $K$ -factors represent the fact that HERWIG computes cross-sections basically at LO.

#### 2.3.2.1 Re-Weighting in $p_T^H$

In section 2.2.1.2 the effects of higher-order QCD corrections on the Higgs transverse momentum spectrum have been shown. These effects can be incorporated into the MC event generators by computing the bin-wise constant,  $p_T^H$  dependent  $K$ -factors according to formula (2.29). In this case the formulas (2.30) become

$$\Delta\sigma_j^G = \int_{p_{T,j}^H}^{p_{T,j+1}^H} dp_T^H \frac{d\sigma^G}{dp_T^H} \equiv \sigma_{\text{cum}}^G(p_{T,j+1}^H) - \sigma_{\text{cum}}^G(p_{T,j}^H), \quad (2.31)$$

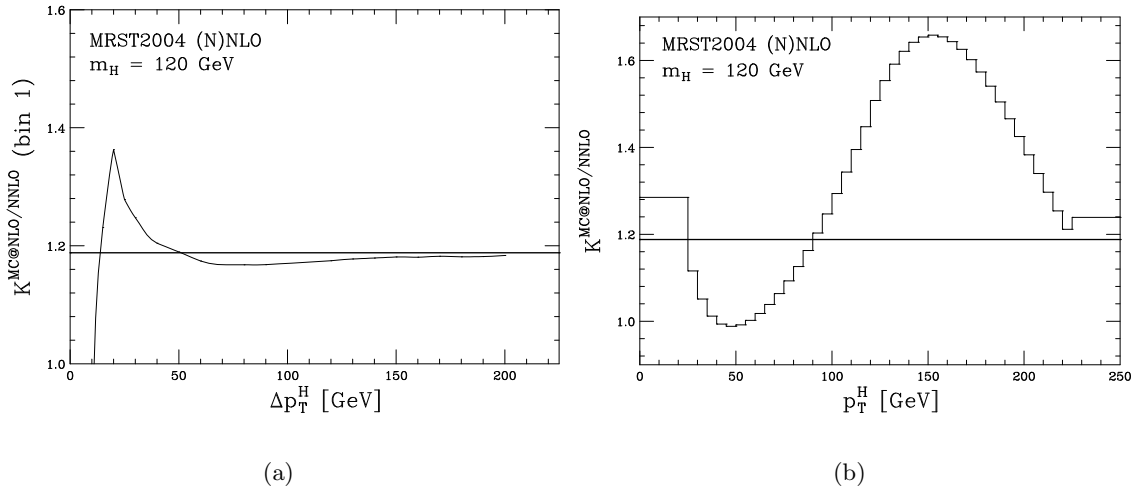


Figure 2.13: (a)  $K$ -factor for re-weighting MC@NLO to the fixed NNLO  $p_T^H$  spectrum as a function of the width of the first bin  $\Delta p_T^H$ . (b) Differential  $K$ -factors for the re-weighting of MC@NLO events to the fixed NNLO  $p_T^H$  spectrum.

where the definition of the cumulative cross-section in  $p_T^H$  from equation (2.11) has been used. The  $p_T^H$ -differential  $K$ -factors for re-weighting the events from generator  $G$  to the reference spectrum obtained at some higher order (HO) are therefore

$$K_j^{G/\text{HO}} = \frac{\sigma_{\text{cum}}^{\text{HO}}(p_{T,j+1}^H) - \sigma_{\text{cum}}^{\text{HO}}(p_{T,j}^H)}{\sigma_{\text{cum}}^G(p_{T,j+1}^H) - \sigma_{\text{cum}}^G(p_{T,j}^H)}. \quad (2.32)$$

The definition of an appropriate binning requires some discussion. On the one hand it is desirable to keep the binning as narrow as possible to ensure that the differential effects are captured, on the other hand it has been shown in Fig. 2.9 how the predictions of fixed-order perturbation theory for the cumulative  $p_T^H$  spectrum become unreliable in the low  $p_T^{\text{H,max}}$  region. We therefore have to perform some sort of matching, i.e. in the low  $p_T^H$  region the differential behavior of the MC generator should be used, while in the large  $p_T^H$  regime the MC generator events should be re-weighted to the fixed-order distribution.

The matching can be controlled by the choice of the size of the first bin,  $\Delta p_T^H$ . The upper bound of this first bin should be set to a value, from which on the fixed-order perturbative spectrum can be trusted. There is no criterion that provides a recipe for the 'right' choice for this bin size. To justify a reasonable choice it is useful to investigate how the  $K$ -factor in this first bin changes, when increasing the bin size. This is shown in Fig. 2.13(a). For very small bin sizes  $\Delta p_T^H$  the  $K$ -factor is negative, reflecting the missing contributions of the multiple soft radiation terms in the fixed-order calculation. With increasing bin-size



the  $K$ -factor increases as well, until it reaches its maximum at  $\sim 25$  GeV. From there on the  $K$ -factor decreases and finally reaches the inclusive  $K$ -factor (represented by the solid, horizontal line) in the limit  $\Delta p_T^H \rightarrow \infty$ .

The lowest point in the spectrum where the  $K$ -factor of the first bin equals the inclusive  $K$ -factor ( $\sim 20$  GeV) specifies the  $p_T^{H,\text{max}}$  value for which the  $p_T^H$ -cumulative cross-sections of the fixed NNLO calculation and the inclusively re-weighted MC generators are equal (cf. 2.12). Previously this point has been defined as the one from which on the perturbative fixed-order result can be trusted.

From these observations it seems natural to define the size of the first bin in such a way, that its  $K$ -factor is close to the inclusive  $K$ -factor. If a smaller first bin is chosen (i.e. the  $K$ -factor in the first bin is smaller than the inclusive  $K$ -factor), a regime is entered where the differential spectrum at fixed-order cannot be trusted. In the case of a larger first bin (i.e. the  $K$ -factor in the first bin is larger than the inclusive  $K$ -factor) important differential information might be lost.

A less delicate, but for practical purposes not less important point is the choice of when to stop the differential re-weighting. In practice it is not reasonable to evolve the differential  $K$ -factors to infinity, therefore a cut-off value for  $p_T^H$  has to be defined, from which on the same  $K$ -factor is assigned to all the events (we define this as the cut-off-bin). This  $K$ -factor is then computed as the ratio of the differences between the inclusive and the cumulative cross-sections up to this point. The cut-off value should be chosen such that the cut-off is 'smooth', i.e. slightly changing the cut-off affects the  $K$ -factors around this cut-off only mildly. This can be achieved by choosing it in such a way, that the  $K$ -factor for the cut-off-bin is close to the  $K$ -factor in the bin just before the cut-off bin.

In the example discussed here ( $m_H = 120$  GeV), the first bin-size is chosen to be 25 GeV and the cut-off at  $p_T^H = 200$  GeV. The range between these values is partitioned into bins of 5 GeV width. To compute the  $K$ -factors (eq. 2.32) the cumulative cross-sections for the generators  $G$  and the fixed-order calculation (FEHiP) have to be computed. This is not done at every bin-edge  $p_{T,j}^H$ , but only for a certain set of points. The cumulative cross-sections can be parametrized as functions of  $p_T^H$ .

The obtained, bin-wise constant  $K$ -factors for re-weighting MC@NLO events to the NNLO  $p_T^H$  spectrum for a Higgs mass of 120 GeV are shown in Fig. 2.13(b). The differential  $K$ -factors range between 1.0 and 1.7. Starting at  $\sim 1.3$  the  $K$ -factors decrease with increasing  $p_T^H$  until they reach a minimum at  $\sim 50$  GeV before increasing again. The maximum is reached at  $\sim 150$  GeV.

### 2.3.2.2 Multi-Differential Re-Weighting

In addition to the Higgs transverse momentum  $p_T^H$  other variables can be considered. The Higgs rapidity  $y^H$  might be of special interest here. The double differential re-weighting of the Higgs boson process in the *Gluon-Fusion* channel has been discussed in detail in [42]. It has been shown that the additional inclusion of a Higgs rapidity dependence of the  $K$ -factors has a small impact on measured cross-sections. Therefore this approach will not be pursued in the progress of this thesis.

### 2.3.3 Limitations of the Re-Weighting Technique

The accuracy of the cross-section prediction using the re-weighting technique depends strongly on the measured quantity, i.e. on the specific choice of  $\mathcal{O}$  in formula 2.17. In order to achieve perfect agreement between the re-weighted and the reference cross-sections, the  $K$ -factors have to be computed point-wise differentially in all the variables that  $\mathcal{O}$  depends on. If for example the measured cross-section is the inclusive cross-section ( $\mathcal{O} = 1$ ), inclusive  $K$ -factors are sufficient. If  $p_T^H$ -spectra are measured, the  $K$ -factors become  $p_T^H$ -dependent and so on.

In general the measured cross-section depends on a variety of cuts on several (correlated) kinematic variables of the final state particles. It is not always feasible, and sometimes impossible, to compute the  $K$ -factors differentially in all these variables. Nevertheless, a simplified approach might be sufficient in describing the  $K$ -factors. For example, if the cuts probe only the Higgs transverse momentum spectrum, it is sufficient to use  $p_T^H$ -dependent  $K$ -factors.

From this it becomes clear that the differential approach discussed above is sufficient as long as only the Higgs kinematics is probed by the cuts, and the phase space of the potential partons (hadronic activity) in the final state is not restricted. As soon as cuts on these partons are imposed, the approximative character of the re-weighting might have a non-negligible impact.

## 2.4 Conclusions of this Chapter

In this chapter it has been shown that the higher-order QCD corrections for the Higgs production in the *Gluon-Fusion* channel are large, but also Higgs boson kinematics dependent. The correct treatment of the corrections is very dependent on the observable to be measured. In general this observable (i.e. a cross-section after the application of certain

experimental cuts that restrict the phase-space) depends on a variety of (correlated) kinematic variables of the final-state particles. The discussed re-weighting technique might serve to incorporate the higher-order corrections into MC event generators in an effective manner.

In addition it turned out that the fixed-order calculations are unreliable when the Higgs boson phase-space is restricted to the low  $p_{\text{T}}^{\text{H}}$  region, i.e. below 50 GeV at NLO and below 20 GeV at NNLO.

In the next two chapters we discuss the two specific decay modes  $\text{H} \rightarrow \gamma\gamma$  and  $\text{H} \rightarrow \text{WW} \rightarrow \ell\nu\ell\nu$ , where typical sets of experimental cuts will be applied. It will be discussed how the higher-order effects can be adequately incorporated into these processes.



## Chapter 3

# Higgs in the '*light*' Mass Range: The Di-Photon Channel

As a first example for the decay of the Higgs boson into detectable particles we consider the decay into two photons,  $H \rightarrow \gamma\gamma$ . As discussed in section 2.1.3 this is the most promising discovery channel in the low Higgs mass region ( $m_H \sim 120$  GeV). The experimental signature of the final state is rather simple, consisting of a photon-pair with invariant mass  $m_{\gamma\gamma} = m_H$ .

The typical experimental selection cuts in this mode are [43, 44, 34]:

- The absolute value of the pseudo-rapidity  $|\eta_{\gamma_{1,2}}|$  of each of the two photons must be smaller than 2.5. This corresponds to the coverage in polar angle of a detector such as ATLAS or CMS.
- One of the two photons must have a transverse energy above 40 GeV, while the other photon is required to have a transverse energy above 25 GeV.
- In order to exclude events with considerable hadronic activity around the final state photons, as for example can be expected in background events with quark-photon fragmentation, the photons must be isolated, i.e. the additional energy in a cone  $\Delta R = \sqrt{\Delta\eta^2 + \Delta\phi^2} < 0.4$  around each photon must not exceed 15 GeV.

After this selection the invariant mass of the photon-pair can be reconstructed and the Higgs mass-peak over the continuum  $\gamma\gamma$ -background extracted.

The cross-sections,  $\sigma_{\text{acc}}$ , after these selection cuts are computed using the various methods discussed in the previous chapter (fixed-order, re-summation, re-weighting) for several

$m_H$ [GeV]	$\Gamma_H$ [GeV]	$BR(H \rightarrow \gamma\gamma)$
110	$0.284 \times 10^{-2}$	$0.198 \times 10^{-2}$
120	$0.348 \times 10^{-2}$	$0.227 \times 10^{-2}$
130	$0.481 \times 10^{-2}$	$0.229 \times 10^{-2}$
140	$0.791 \times 10^{-2}$	$0.198 \times 10^{-2}$
150	$1.645 \times 10^{-2}$	$0.141 \times 10^{-2}$

Table 3.1: Higgs width  $\Gamma_H$  and branching ratio for the decay into two photons computed using HDECAY [25] for five different Higgs mass hypotheses.

'light' Higgs mass hypotheses and the uncertainties induced by varying the renormalization and factorization scales are studied.

The continuum  $\gamma\gamma$ -background is then generated using the full NLO program DIPHOX [45] and discuss the qualitative impact of the higher-order QCD corrections on the significance of a Higgs boson signal at the various mass hypotheses under consideration.

The results of this chapter have been published in [44]

### 3.1 Fixed-Order Cross-Sections

First the inclusive cross-sections and  $K$ -factors for five different Higgs mass hypotheses between 110 and 150 GeV are computed. The Higgs widths  $\Gamma_H$  and branching ratios  $BR(H \rightarrow \gamma\gamma)$  according to HDECAY [25] are listed in Table 3.1. The inclusive cross-sections for the five Higgs masses are shown in Fig. 3.1(a).

We compute the cross-sections after the selection cuts described above ( $\sigma_{acc}$ ) with the fixed-order program FEHiP, which has the Higgs decay into photons included. The cross-sections are shown in Fig. 3.1(b) and the corresponding cut-efficiencies, defined as

$$\varepsilon^{(N)NLO}(m_H, \mu) := \frac{\sigma_{acc}^{(N)NLO}(m_H, \mu)}{\sigma_{inc}^{(N)NLO}(m_H, \mu)}, \quad (3.1)$$

in Fig. 3.2(a). The efficiencies with respect to the scale-variation are very stable in both, the NLO and the NNLO case. Furthermore the efficiencies are significantly increasing with increasing Higgs mass, which can be explained by the larger probability of a heavier Higgs boson to decay into high- $p_T$  photons. Nevertheless, the difference in the efficiencies at NLO and NNLO is not completely negligible, i.e. the event rejection rate is slightly larger at NNLO than at NLO.

Although the effect is very small we want to investigate it a little further. The origin of this difference might be the isolation criterion in the selection cuts. Since at NNLO there

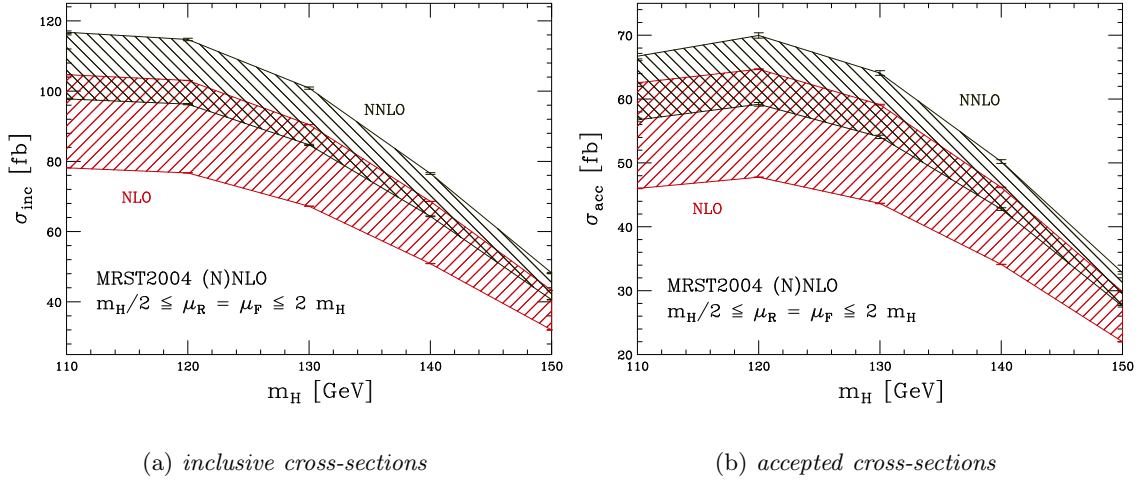


Figure 3.1: Inclusive and accepted cross-sections in the  $H \rightarrow \gamma\gamma$  channel for different Higgs mass hypotheses.

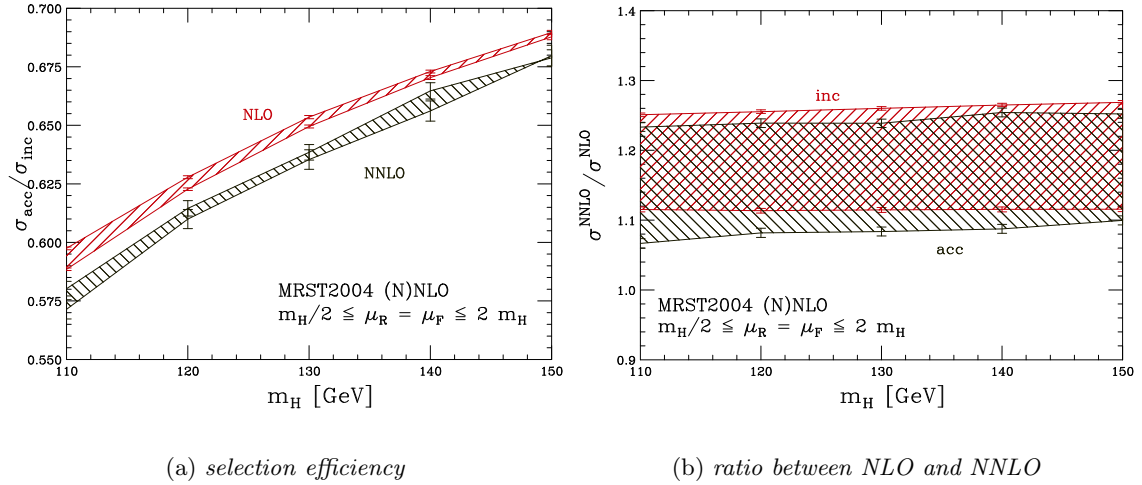


Figure 3.2: Selection efficiencies for and ratio between the NLO and the NNLO calculation in the  $H \rightarrow \gamma\gamma$  channel for several Higgs mass hypotheses.

are up to two partons present in the final state, whereas at NLO there is only one parton, the fraction of non-isolated photons at NNLO is larger than at NLO. This is illustrated by computing the NLO and NNLO accepted cross-sections with removed isolation criterion for a Higgs mass of  $m_H = 120$  GeV. The cross-sections and efficiencies are

$$\begin{aligned}
 \sigma_{\text{acc}}^{\text{NLO}}(\mu = m_H/2) &= (65.27 \pm 0.06) \text{ fb} &\Rightarrow \varepsilon^{\text{NLO}} &= 0.634 \pm 0.001 \\
 \sigma_{\text{acc}}^{\text{NNLO}}(\mu = m_H/2) &= (71.33 \pm 0.59) \text{ fb} &\Rightarrow \varepsilon^{\text{NNLO}} &= 0.622 \pm 0.005,
 \end{aligned}
 \tag{3.2}$$

$\mu_F = \mu_R$	$m_H/2$		$2m_H$	
Generator	HERWIG	MC@NLO	HERWIG	MC@NLO
$m_H$	110 GeV			
$\sigma_{\text{inc}}^{\text{NLO}}$ [fb]	104.69 $\pm$ 0.03		78.16 $\pm$ 0.02	
$\sigma_{\text{inc}}^{\text{NNLO}}$ [fb]	116.76 $\pm$ 0.37		97.77 $\pm$ 0.20	
$K_{\text{inc}}^{\text{NLO}}$	2.880	1.066	2.150	1.060
$K_{\text{inc}}^{\text{NNLO}}$	3.212	1.189	2.690	1.326
$m_H$	120 GeV			
$\sigma_{\text{inc}}^{\text{NLO}}$ [fb]	103.02 $\pm$ 0.03		76.71 $\pm$ 0.02	
$\sigma_{\text{inc}}^{\text{NNLO}}$ [fb]	114.71 $\pm$ 0.34		96.30 $\pm$ 0.20	
$K_{\text{inc}}^{\text{NLO}}$	2.896	1.067	2.157	1.068
$K_{\text{inc}}^{\text{NNLO}}$	3.225	1.188	2.708	1.341
$m_H$	130 GeV			
$\sigma_{\text{inc}}^{\text{NLO}}$ [fb]	90.48 $\pm$ 0.03		67.22 $\pm$ 0.02	
$\sigma_{\text{inc}}^{\text{NNLO}}$ [fb]	100.85 $\pm$ 0.32		84.70 $\pm$ 0.17	
$K_{\text{inc}}^{\text{NLO}}$	2.905	1.079	2.158	1.071
$K_{\text{inc}}^{\text{NNLO}}$	3.238	1.203	2.719	1.350
$m_H$	140 GeV			
$\sigma_{\text{inc}}^{\text{NLO}}$ [fb]	68.62 $\pm$ 0.02		50.88 $\pm$ 0.02	
$\sigma_{\text{inc}}^{\text{NNLO}}$ [fb]	76.54 $\pm$ 0.24		64.36 $\pm$ 0.12	
$K_{\text{inc}}^{\text{NLO}}$	2.909	1.083	2.157	1.077
$K_{\text{inc}}^{\text{NNLO}}$	3.245	1.208	2.729	1.363
$m_H$	150 GeV			
$\sigma_{\text{inc}}^{\text{NLO}}$ [fb]	43.24 $\pm$ 0.01		32.00 $\pm$ 0.01	
$\sigma_{\text{inc}}^{\text{NNLO}}$ [fb]	48.24 $\pm$ 0.15		40.60 $\pm$ 0.08	
$K_{\text{inc}}^{\text{NLO}}$	2.914	1.089	2.157	1.083
$K_{\text{inc}}^{\text{NNLO}}$	3.251	1.215	2.736	1.374

Table 3.2: Inclusive cross-sections from fixed-order calculations and  $K$ -factors for the various event generators for the process  $pp \rightarrow H \rightarrow \gamma\gamma$ . The numbers are listed for the two scale choices  $\mu = m_H/2$  and  $\mu = 2m_H$ .

leading to a relative difference in the efficiencies of

$$\frac{\varepsilon^{\text{NLO}} - \varepsilon^{\text{NNLO}}}{\varepsilon^{\text{NLO}}} = (1.89 \pm 0.78) \%, \quad (3.3)$$

compared to  $(2.85 \pm 0.41) \%$  for the numbers including the isolation criterion. From this it can be concluded that about 1/3 of the difference in the efficiency can be explained by



the distinctive partonic structure of the final states at NLO and NNLO. The rest has to originate from the different kinematic properties of the Higgs boson.

It is not obvious how the differences in the Higgs kinematics affect the efficiencies. In general we expect that a harder  $p_T^H$  spectrum also produces harder photons, leading to an increase in the efficiency. But the selection cuts, though they seem simple at first sight, are complicated enough not to allow the direct derivation of the restrictions on the Higgs boson phase-space. However, since the differences are very small, we will not pursue this issue further.

## 3.2 Re-Weighted Cross-Sections

Having discussed the effects of QCD at some fixed higher order on the measurable cross-section after selection cuts for the  $H \rightarrow \gamma\gamma$  channel, we turn to the MC generators (HERWIG, MC@NLO), which produce events that eventually can be passed through some detector simulation. In section 2.3 we discussed how QCD corrections can be incorporated into these event generators using re-weighting techniques. The first approach considered is inclusive re-weighting. In its course the events from the generators are re-weighted with  $K$ -factors that are the ratio of the inclusive reference cross-sections  $\sigma^{(N)NLO}$  and the ones computed using the generator,  $\sigma^G$ . The  $K$ -factors for the different Higgs masses and scale choices are listed in Table 3.2. The errors for the  $K$ -factors in the Table are suppressed; they are all of the order of 1%. Then the selection cuts as described at the beginning of this chapter are imposed on these events and the resulting accepted cross-sections  $\sigma_{acc}^{R(G)}$  computed. The cross-sections, together with those obtained at fixed-order from the previous section, are listed in Table 3.3.

For all the Higgs masses and both scale choices the differences between the re-weighted HERWIG and the re-weighted MC@NLO results are smaller than the statistical error. We conclude that the presence of the additional parton from the hard scattering process in MC@NLO with respect to HERWIG has no effect on the efficiency. We want to compare the efficiencies of the re-weighted MC generators to the ones from the fixed-order calculations. The selection efficiencies for MC@NLO, NLO and NNLO are shown in Fig. 3.3. Over the whole mass range the MC@NLO efficiency is larger than the NLO and the NNLO efficiency. Again, we want to see what happens when we switch off the isolation criterion. The numbers for NLO and MC@NLO are then

$$\begin{aligned} \sigma_{acc}^{NLO}(\mu = m_H/2) &= (65.27 \pm 0.06) \text{ fb} \quad \Rightarrow \quad \varepsilon^{NLO} = 0.634 \pm 0.001 \quad \text{and} \\ \sigma_{acc}^{R(G)}(\mu = m_H/2) &= (65.00 \pm 0.21) \text{ fb} \quad \Rightarrow \quad \varepsilon^{R(G)} = 0.631 \pm 0.002, \end{aligned} \quad (3.4)$$

with  $G = \text{MC@NLO}$ . Without the isolation the MC@NLO and NLO results agree perfectly. This is somehow surprising. Since in the parton-shower of MC@NLO many more

$\mu_F = \mu_R$	$m_H/2$		$2m_H$	
Generator	HERWIG	MC@NLO	HERWIG	MC@NLO
$m_H$	110 GeV			
$\sigma_{\text{acc}}^{\text{NLO}}$ [fb]	$62.55 \pm 0.06$		$46.00 \pm 0.04$	
$\sigma_{\text{acc}}^{\text{NNLO}}$ [fb]	$66.72 \pm 0.43$		$56.73 \pm 0.28$	
$\sigma_{\text{acc}}^{R(G)/\text{NLO}}$ [fb]	$62.29 \pm 0.16$	$62.02 \pm 0.24$	$46.50 \pm 0.12$	$46.71 \pm 0.17$
$\sigma_{\text{acc}}^{R(G)/\text{NNLO}}$ [fb]	$69.47 \pm 0.17$	$69.17 \pm 0.35$	$58.18 \pm 0.15$	$58.42 \pm 0.24$
$m_H$	120 GeV			
$\sigma_{\text{acc}}^{\text{NLO}}$ [fb]	$64.68 \pm 0.06$		$47.77 \pm 0.04$	
$\sigma_{\text{acc}}^{\text{NNLO}}$ [fb]	$69.97 \pm 0.42$		$59.18 \pm 0.29$	
$\sigma_{\text{acc}}^{R(G)/\text{NLO}}$ [fb]	$64.58 \pm 0.16$	$64.96 \pm 0.24$	$48.10 \pm 0.12$	$48.53 \pm 0.17$
$\sigma_{\text{acc}}^{R(G)/\text{NNLO}}$ [fb]	$71.92 \pm 0.17$	$72.32 \pm 0.34$	$60.39 \pm 0.15$	$60.92 \pm 0.25$
$m_H$	130 GeV			
$\sigma_{\text{acc}}^{\text{NLO}}$ [fb]	$59.13 \pm 0.06$		$43.66 \pm 0.04$	
$\sigma_{\text{acc}}^{\text{NNLO}}$ [fb]	$64.08 \pm 0.37$		$54.08 \pm 0.26$	
$\sigma_{\text{acc}}^{R(G)/\text{NLO}}$ [fb]	$59.43 \pm 0.14$	$59.38 \pm 0.21$	$44.15 \pm 0.10$	$44.41 \pm 0.14$
$\sigma_{\text{acc}}^{R(G)/\text{NNLO}}$ [fb]	$66.24 \pm 0.15$	$66.19 \pm 0.32$	$55.63 \pm 0.13$	$55.95 \pm 0.21$
$m_H$	140 GeV			
$\sigma_{\text{acc}}^{\text{NLO}}$ [fb]	$46.18 \pm 0.04$		$34.11 \pm 0.04$	
$\sigma_{\text{acc}}^{\text{NNLO}}$ [fb]	$50.22 \pm 0.29$		$42.78 \pm 0.21$	
$\sigma_{\text{acc}}^{R(G)/\text{NLO}}$ [fb]	$46.51 \pm 0.10$	$46.86 \pm 0.16$	$34.48 \pm 0.08$	$34.62 \pm 0.11$
$\sigma_{\text{acc}}^{R(G)/\text{NNLO}}$ [fb]	$51.88 \pm 0.11$	$52.27 \pm 0.24$	$43.63 \pm 0.10$	$43.79 \pm 0.16$
$m_H$	150 GeV			
$\sigma_{\text{acc}}^{\text{NLO}}$ [fb]	$29.82 \pm 0.04$		$22.01 \pm 0.04$	
$\sigma_{\text{acc}}^{\text{NNLO}}$ [fb]	$32.79 \pm 0.19$		$27.56 \pm 0.13$	
$\sigma_{\text{acc}}^{R(G)/\text{NLO}}$ [fb]	$30.14 \pm 0.06$	$30.11 \pm 0.10$	$22.31 \pm 0.05$	$22.40 \pm 0.07$
$\sigma_{\text{acc}}^{R(G)/\text{NNLO}}$ [fb]	$33.63 \pm 0.07$	$33.59 \pm 0.15$	$28.30 \pm 0.06$	$28.42 \pm 0.10$

Table 3.3: (Re-weighted) accepted cross-sections after standard selection cuts in the  $pp \rightarrow H \rightarrow \gamma\gamma$  channel for various event generators and the fixed-order calculation.

partons are created, one might expect that the influence of the isolation would rather decrease the efficiency compared to the fixed-order result. This apparently is not the case. Apparently the shower rather spreads the energy of the additional partons over a larger region of space, leading to an increase in the efficiency.

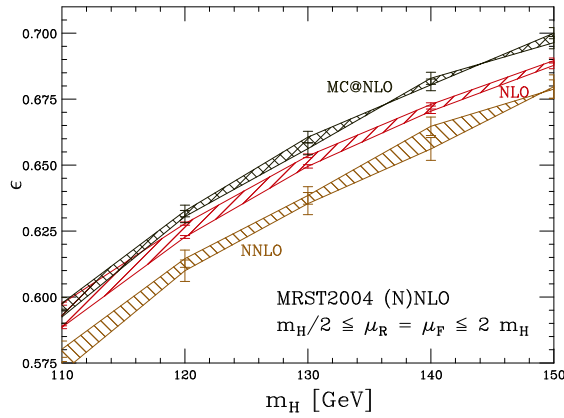


Figure 3.3: Selection efficiencies for the fixed-order calculations (NLO, NNLO) and the program MC@NLO.

In the next step the NNLO efficiencies are compared to the ones obtained with the MC event generators. It has become clear that the efficiency is somewhat sensitive to the Higgs kinematics. It can therefore be assumed that if the NNLO Higgs kinematics is reproduced within the event generators, the efficiencies would agree to a better precision. We will do this using the differential re-weighting technique in  $p_T^H$  discussed in section 2.3.1.2. The efficiency for the differentially re-weighted MC@NLO events is

$$\sigma_{\text{acc}}^{R(\text{MC@NLO})}(\mu = m_H/2) = (72.39 \pm 0.24) \text{ fb} \quad \Rightarrow \quad \varepsilon^{R(\text{MC@NLO})} = 0.631 \pm 0.002. \quad (3.5)$$

Apparently the result does not change at all within statistical errors. In (3.5) only the statistical error is shown, but not the uncertainties introduced in the re-weighting procedure (finite-size binning, fitting, etc.). However, these errors are expected to be at least at the order of the efficiency differences between NNLO and MC@NLO.

### 3.3 Kinematic Distributions

In the last section it has been concluded that the higher order QCD corrections are accurately described by using inclusive re-weighting techniques. In this section we consider more complicated variables than the cross-sections after cuts, namely the mean transverse momentum

$$p_T^m := \frac{p_T^{\gamma 1} + p_T^{\gamma 2}}{2}, \quad (3.6)$$

and the absolute value of the pseudo-rapidity difference of the two photons

$$y^* := \frac{|\eta^{\gamma 1} - \eta^{\gamma 2}|}{2}, \quad (3.7)$$

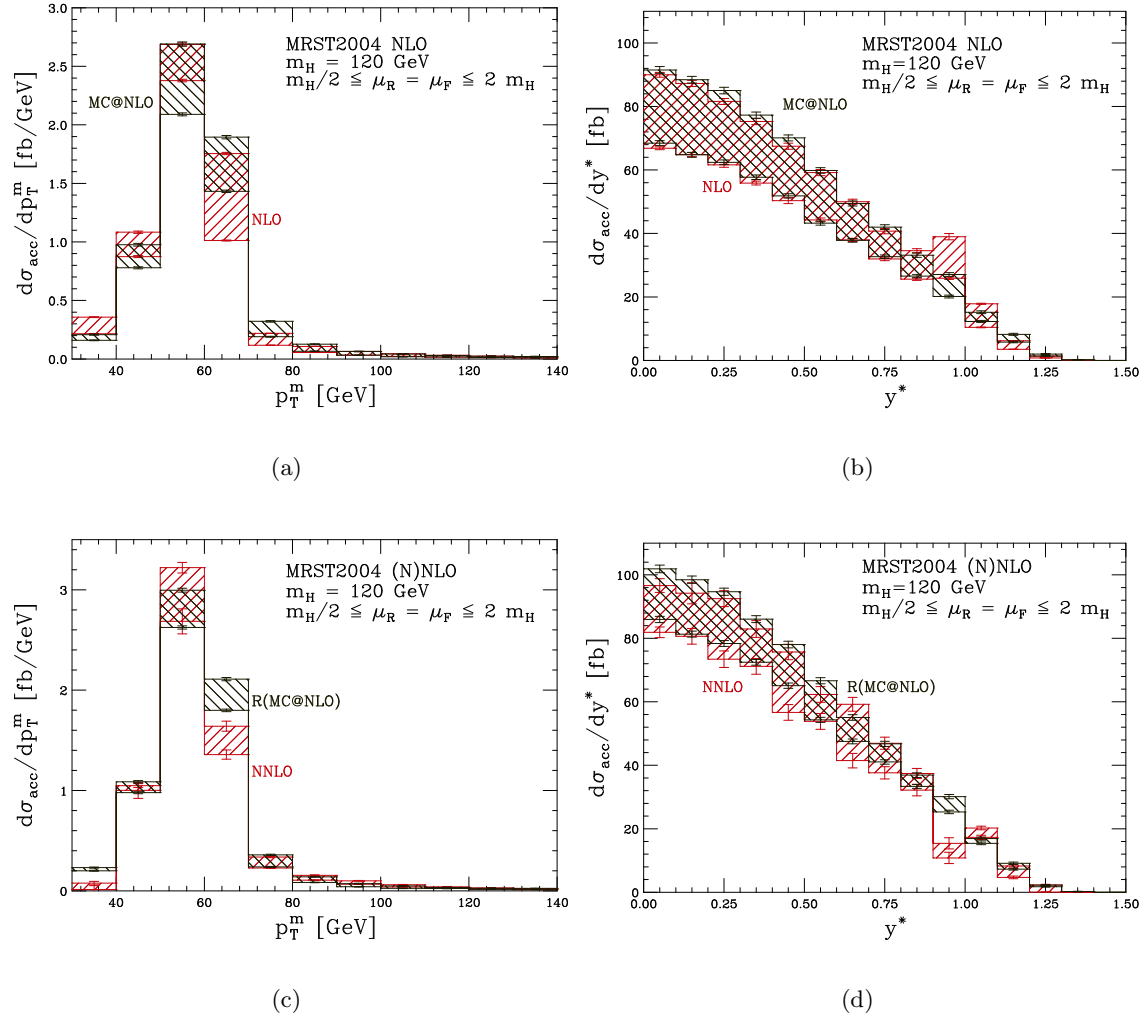


Figure 3.4: Comparison between fixed-order (N)NLO and (re-weighted) MC@NLO predictions for the mean transverse momentum  $p_T^m$  and the pseudo-rapidity difference  $y^*$  for photons coming from the decay of a Higgs boson with mass  $m_H=120$  GeV. The bands correspond to a variation of the renormalization and the factorization scales  $\mu_R$  and  $\mu_F$  in the range  $[m_H/2, 2m_H]$ .

where the pseudo-rapidity  $\eta$  is defined as

$$\eta = \ln \left( \cot \left( \frac{\theta}{2} \right) \right) \quad (3.8)$$

with  $\theta$  the polar angle of the particle with respect to the incoming particle direction (beam-line). Note that for massless particles the pseudo-rapidity corresponds to the rapidity defined in eq. 2.9. These variables are particularly interesting because they have been considered to serve for a further discrimination of the signal against the background [43].

$\mu_F = \mu_R$	$m_H/2$			$2 m_H$		
	$\sigma_{\text{acc}}$ [fb]	$S$	$n_{\text{sig}}$	$\sigma_{\text{acc}}$ [fb]	$S$	$n_{\text{sig}}$
$m_H$	120 GeV					
NLO	64.68	1940	6.00	47.77	1433	4.44
NNLO	69.97	2099	6.50	59.18	1775	5.50

Table 3.4: Expected number of signal events and statistical significance for an integrated luminosity of  $30 \text{ fb}^{-1}$ .

The distributions for  $p_T^m$  and  $y^*$  after the application of the selection cuts computed at fixed NLO and with MC@NLO are shown in the first two plots of Fig. 3.4. The second two plots show comparisons between NNLO and MC@NLO, inclusively re-weighted to NNLO. The deviations around  $p_T^m \sim 60 \text{ GeV}$  arise from large perturbative corrections, since the  $p_T^m$ -spectrum is zero above this value at LO. The same is true for the  $y^*$ -distribution around  $y^* \sim 1$ . Around these kinematic boundaries re-summation of large logarithms would be necessary. Besides these effects the distributions agree.

### 3.4 Prompt Di-Photon Background and Signal Significance

After studying the signal cross-sections in detail we conclude this section by estimating the impact of the higher order QCD corrections on the signal significance, defined as

$$n_{\text{sig}} := \frac{S}{\sqrt{B + (\Delta B)^2}}, \quad (3.9)$$

where  $S$  and  $B$  are the number of signal and background events expected for a certain integrated luminosity, and  $\Delta B$  is the absolute uncertainty on the number of expected background events.

In a real experiment the background would be measured from data by extrapolating the  $\gamma\gamma$ -background from the side-bands into the signal-region. We define the signal region as the  $\pm 2 \text{ GeV}$  window around the Higgs mass. The estimated number of background events will therefore not suffer from theoretical uncertainties. In order to being able to make a qualitative statement on the expected signal significance we estimate the  $\gamma\gamma$ -background cross-section using the NLO program DIPHOX [45] with one scale choice (i.e.  $\mu_R = \mu_F = m_{\gamma\gamma}/2$ ) and the default PDF set MRST2004 NLO. We assume a relative uncertainty on this background of 1%. This uncertainty has been shown to be a good estimate for the measurement of the  $\gamma\gamma$ -background from the signal side-band region [26]. The Higgs mass is set to  $m_H = 120 \text{ GeV}$  and an integrated luminosity of  $30 \text{ fb}^{-1}$  is assumed.

The cross-section for the  $\gamma\gamma$ -background in the  $(120 \pm 2)$  GeV mass window obtained with DIPHOX after the selection cuts is

$$\sigma_{\text{acc}}^{\text{DIPHOX}} = 0.9244 \text{ pb} \quad \Rightarrow \quad B = 27732. \quad (3.10)$$

The denominator in the significance (3.9) becomes then

$$\sqrt{B + (\Delta B)^2} = \sqrt{27732 + (0.01 \times 27732)^2} \simeq 323. \quad (3.11)$$

The resulting signal-significances, using the accepted cross-sections at NLO and NNLO from Table 3.3 are listed in Table 3.4. Since the number of signal events  $S$ , and thus the signal significance are linearly dependent on the signal cross-section, it is no surprise, that the significances behave in the same way as the cross-sections. While the significance increases when going from NLO to NNLO, the relative scale uncertainty is reduced.

### 3.5 Conclusions of this Chapter

In this chapter we have used the fully differential program FEH1P to compute the expected cross-section for the  $H \rightarrow \gamma\gamma$  process after imposing a set of typical experimental cuts. It turned out that the selection efficiencies for fixed NLO and NNLO, as well as for the parton shower MC event generator MC@NLO are very similar, leading to the conclusion that inclusive re-weighting of the MC@NLO events to the NNLO prediction results in a reliable prediction for the expected cross-section.

Remaining, small differential effects could not be covered by a differential re-weighting in the Higgs transverse momentum  $p_{\text{T}}^H$ . It is expected that even if full, point-wise differential re-weighting would resolve these differences, finite-bin-size effects may still leads to some discrepancies. In addition, more complicated observables  $(p_{\text{T}}^m, y^*)$  have been investigated. It has been shown that fixed-order calculations cannot reliably predict the entire distributions of these variables, since re-summation of logarithmic terms is needed.

## Chapter 4

# Higgs in the '*intermediate*' Mass Range: The W-Pair Channel

In this section we study the cross-section for the Higgs decaying in the WW-mode. As shown in Fig. 2.4 the branching-ratio of the SM Higgs boson into a pair of W-bosons is almost unity for Higgs masses around the W-pair threshold  $m_H \sim 160 \text{ GeV}$ ; using this channel for the observation of the Higgs in this specific mass-region is therefore favourable. The W-bosons decaying into leptons produce neutrinos which cannot be detected in a real experiment, thus no Higgs invariant mass peak can be reconstructed. The separation of the signal events over the large background has therefore for a long time been considered as very difficult.

In 1996, Dittmar and Dreiner [27] studied the effects of spin correlations and the mass of the resonant and non-resonant WW system. For signal events they observed that the opening angle  $\phi_{\ell\ell}$  between the leptons in the plane transverse to the beam axis tends to be smaller than the corresponding angle for the background processes; in addition, the transverse momentum spectrum of the charged leptons is sensitive to the Higgs-boson mass. In order to reduce the large top-pair background, which is characterized by strong jet activity, they proposed to reject events with jets of large transverse momentum. Using these cuts it has been shown [48] that the background can be sufficiently suppressed against the signal in order to use this decay-mode as a discovery channel for a SM Higgs in this mass range.

The results of this chapter have been published in [46] and [47].

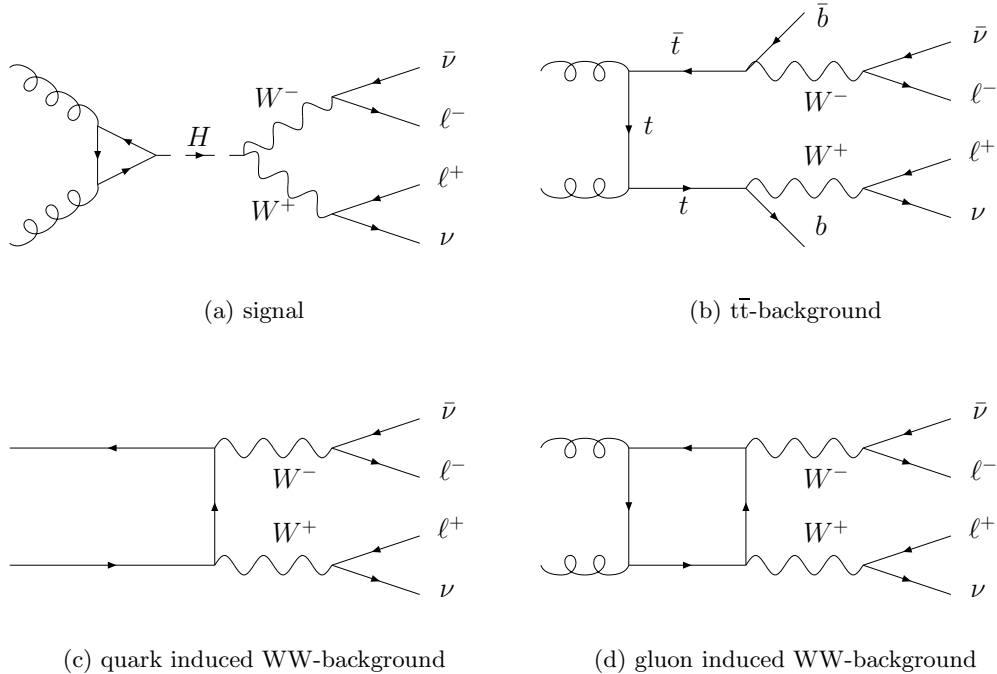


Figure 4.1: Feynman diagrams for the signal and the main background processes for the  $H \rightarrow WW$  process.

## 4.1 Final State Signature and Background Processes

The LO diagrams for the signal and the main background processes are shown in Fig. 4.1. All processes produce four leptons via a W-boson pair. The two neutrinos leave the experiment undetected, the only observable final-state particles are the charged leptons, either electrons or muons<sup>1</sup>, and potential hadronic activity, either originating from initial state radiation or the t-decays in the  $t\bar{t}$  process. There is no constraint on the lepton-flavour combination for the two charged leptons, but charge-conservation demands that the leptons carry opposite electric charge.

Qualitatively one can assume that any process leading to a pair of oppositely charged leptons accompanied by missing transverse energy, especially any process producing a pair of W-bosons, will contribute to the background. Those shown in Fig. 4.1 are the dominating ones. Technically the square of diagram 4.1(d) is of order  $\alpha_s^2$ ; of the same order as the NNLO corrections to the process in diagram 4.1(c). The contribution of the gluon-induced WW background is therefore suppressed compared to those induced by quarks. However, the different spin-structure of the initial states leads to a relative increase

<sup>1</sup> We neglect the contribution of the W bosons decaying into  $\tau$ -leptons.



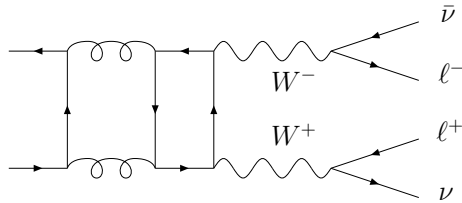


Figure 4.2: Diagram contributing to the NNLO corrections for the quark induced WW background.

process	$\sigma_{\text{inc}}^{\text{NLO}}$ [pb]
$qq \rightarrow WW \rightarrow e^+ \nu e^- \bar{\nu}$	1.4
$gg \rightarrow WW \rightarrow e^+ \nu e^- \bar{\nu}$	0.05
$t\bar{t} \rightarrow WW b\bar{b} \rightarrow e^+ \nu e^- \bar{\nu} b\bar{b}$	11.9
background	13.4
signal	0.3

Table 4.1: Inclusive cross-sections for the most important background-processes for the SM Higgs search in the WW-decay mode compared to the signal cross-section.

of the gluon induced process after the application of experimental selection cuts [27]. In order to be fully consistent at this order of perturbation theory, it would be desirable to include the NNLO diagrams for the quark induced process. Especially the diagram shown in Fig. 4.2, combined with diagram 4.1(c), contributes to the cross-section at the same order of  $\alpha_s$  and has, similarly to diagram 4.1(d), a gluon-like spin structure in the initial state. Unfortunately, such a calculation is not available at the moment.

In Table 4.1 the magnitudes of the signal and the background cross-sections at NLO are compared for one lepton-flavour combination. The sum of the background cross-sections exceeds the signal cross-section by a factor of  $\sim 40$ , indicating again that only very restrictive cuts will help to increase the signal over background ratio significantly. The cross-sections for the  $t\bar{t}$  and the quark induced WW background have been computed using MC@NLO. The gluon induced WW cross-section has been computed using the dedicated program GG2WW, version 2.4.0 [49].

The selection cuts applied on the final-state particles are summarized here:

1. the charged leptons should have a transverse momentum of  $p_{\text{T}}^{\ell} > 25 \text{ GeV}$  and a pseudo-rapidity  $|\eta|$  smaller than 2;
2. these leptons must be isolated from hadrons; the hadronic energy within a cone of  $R = 0.4$  around each lepton must not exceed 10% of the corresponding lepton

- transverse momentum;
3. the di-lepton mass should fall into the range  $12 \text{ GeV} < m_{\ell\ell} < 40 \text{ GeV}$ , where the lower cut reduces potential backgrounds from  $b$ -resonances;
  4. the missing energy in the event,  $E_{\text{T}}^{\text{miss}}$ , has to exceed  $50 \text{ GeV}$ ;
  5. the opening angle  $\phi_{\ell\ell}$  between the two leptons in the transverse plane should be smaller than  $45^\circ$ ;
  6. there should be no jet with a transverse momentum  $p_{\text{T}}^{\text{jet}}$  larger than  $25 \text{ GeV}$  in the central detector region  $|\eta^{\text{jet}}| < 2.5$  and
  7. the harder <sup>2</sup> lepton is required to have  $30 \text{ GeV} < p_{\text{T}}^{\ell, \text{max}} < 55 \text{ GeV}$ .

We will refer to these cuts as the *partonic signal cuts* throughout this thesis. The cuts do not correspond exactly to, but are strongly motivated by those initially proposed in [27]. In addition, these cuts are an adaptation to parton-level of the experimental cuts applied in earlier Higgs discovery studies performed using full detector simulation [48].

Two of the kinematic variables used in the cuts listed above have to be specified in some more detail. The first remark concerns the calculation of the missing transverse energy. We compute  $E_{\text{T}}^{\text{miss}}$  directly from the four-momenta of the final state neutrinos. This can obviously not be done in a real experiment. The second remark concerns the definition of the jets used in cut number 6. If not explicitly stated otherwise, we use a  $k_{\text{T}}$ -algorithm [50] in the  $E$ -scheme with cone parameter  $R = 0.4$ .

## 4.2 Fixed Order Results

In order to compute the fixed-order cross-sections up to NNLO for the process  $pp \rightarrow \text{H} \rightarrow \text{WW} \rightarrow \ell\nu\ell\nu$  in the *Gluon-Fusion* channel, the corresponding decay matrix-element had to be included into the program FEHiP. In addition, the numerical integration strategy had to be adapted to ensure adaptive convergence of the integration. We present the details of these procedures in Appendix D. Note that this is the first fully differential calculation at NNLO for a process with such a complicated final-state structure.

In Table 4.2 we show the inclusive cross-sections computed with our improved program for a Higgs mass hypothesis of  $m_{\text{H}} = 165 \text{ GeV}$ . We use the parton distribution set MRST2001LO for the calculation of the LO cross-section and the MRST2004(N)NLO sets for the higher orders. The renormalization and factorization scales  $\mu_{\text{R}}$  and  $\mu_{\text{F}}$  are varied

---

<sup>2</sup> By the 'harder' lepton we refer to the one with larger transverse momentum  $p_{\text{T}}$ .

$\sigma_{\text{inc}}$ [fb]	LO	NLO	NNLO
$\mu = m_{\text{H}}/2$	$152.63 \pm 0.06$	$270.61 \pm 0.25$	$301.23 \pm 1.19$
$\mu = 2m_{\text{H}}$	$103.89 \pm 0.04$	$199.76 \pm 0.17$	$255.06 \pm 0.81$

Table 4.2: Inclusive cross-sections for the process  $pp \rightarrow \text{H} \rightarrow \text{WW} \rightarrow \ell\nu\ell\nu$  at different orders of perturbative QCD and two scale choices  $\mu = \mu_{\text{R}} = \mu_{\text{F}}$ .

simultaneously in the range  $[m_{\text{H}}/2, 2m_{\text{H}}]$  and according to HDECAY [25] the width of the Higgs boson with mass  $m_{\text{H}} = 165 \text{ GeV}$  is  $\Gamma_{\text{H}} = 0.25 \text{ GeV}$ . Finally, the W-boson mass is set to  $m_{\text{W}} = 80.41 \text{ GeV}$  and its width to  $\Gamma_{\text{W}} = 2.06 \text{ GeV}$ . These are the default values for all upcoming studies.

The  $K$ -factors for the inclusive cross-section,

$$K_{(\text{N})\text{NLO}}(\mu) = \frac{\sigma_{(\text{N})\text{NLO}}(\mu)}{\sigma_{\text{LO}}(\mu)},$$

range from 1.77 to 1.92 at NLO and from 1.97 to 2.45 at NNLO, depending on the scale choice. The numbers reflect the same behavior as the cross-sections without the Higgs decay into a pair of W-bosons. This is not surprising since the decay in the inclusive case corresponds to nothing but a multiplication of the Higgs production cross-section with the branching ratio for the full decay.

#### 4.2.1 Differential Distributions

In chapter 2 it has been observed that the higher-order calculations affect the inclusive cross-section as well as differential distributions. In chapter 3 it was found that the corrections after the application of experimental cuts can appear to be very 'inclusive-like' if the cuts select phase-space regions democratically, i.e. the  $K$ -factors after the selection cuts are very similar to the inclusive  $K$ -factors. This behavior can not be regarded as a general property of higher order corrections. The amplitude of the higher-order process, and thus the higher-order corrections, depend strongly on the phase-space region selected. For example, if the cuts favour the low  $p_{\text{T}}^{\text{H}}$  region, we expect that the  $K$ -factors after the application of these cuts differ significantly from the inclusive  $K$ -factors (cf. section 2.2.1.2).

In order to understand the higher-order corrections after the application of the selection cuts we study all the kinematic observables constrained by the cuts separately. We do this by computing the cumulative cross-sections (cf. section 2.2.1.2) as

$$\sigma_{\text{cum}}(X^{\text{cut}}, \mu) = \int_{0(X^{\text{cut}})}^{X^{\text{cut}}(\infty)} \frac{\partial\sigma(\mu)}{\partial X} dX, \quad (4.1)$$

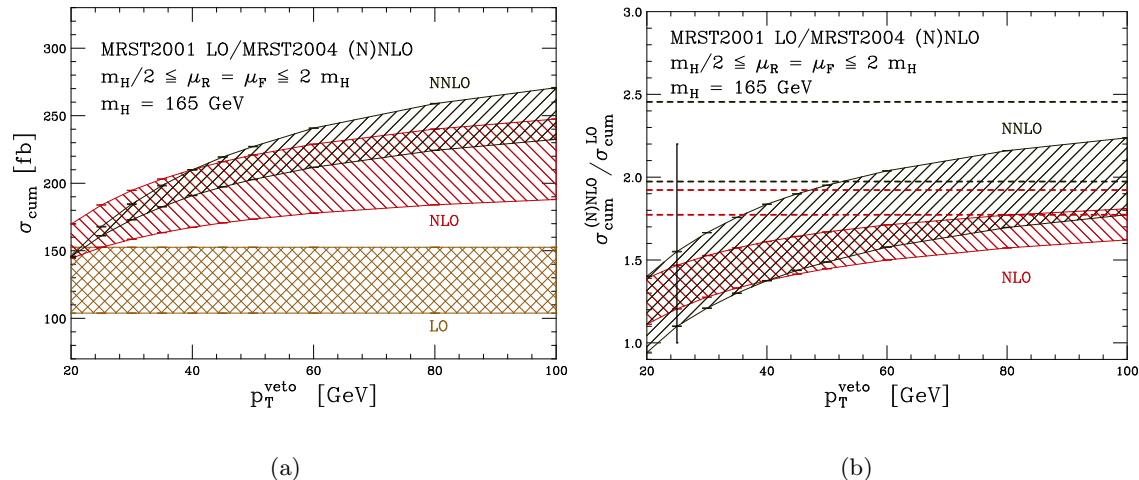


Figure 4.3: (a) The cross-section for  $H \rightarrow WW \rightarrow \ell\nu\ell\nu$ , vetoing events with jets in the central region  $|\eta^{\text{jet}}| < 2.5$  and  $p_T^{\text{jet}} > p_T^{\text{veto}}$ . (b) The  $K$ -factor as a function of  $p_T^{\text{veto}}$ . The dashed horizontal lines correspond to the NLO and NNLO  $K$ -factors for the inclusive cross-section. The vertical solid line denotes the value of  $p_T^{\text{veto}}$  in the *partonic signal cuts* of section 4.1.

where  $X$  denotes some final-state kinematic variable and  $X^{\text{cut}}$  is an upper limit on the variable that mimics a cut at this value. Alternatively, the cut value  $X^{\text{cut}}$  may also denote the lower boundary of the integration region in eq. 4.1 and the upper boundary is taken to  $\infty$  (denoted as the integration boundaries in brackets).

In Fig. 4.3 the effect of the veto on jets with transverse momentum  $p_T^{\text{jet}} > p_T^{\text{veto}}$  (see also [51, 33]) is considered. Events are vetoed if they contain jets in the central detector region  $|\eta^{\text{jet}}| < 2.5$ . We observe that the relative magnitude of the NLO and NNLO contributions depends strongly on  $p_T^{\text{veto}}$ . The NNLO cross-section increases more rapidly than at NLO by relaxing the veto. Figure 4.3 demonstrates that the large NLO and NNLO corrections must be attributed to contributions from jets with large, rather than small, transverse momentum.

In order to reduce the  $pp \rightarrow t\bar{t}$  background, a small value for  $p_T^{\text{veto}}$  is required. As  $p_T^{\text{veto}}$  is decreased, the scale uncertainty at NNLO decreases as well. Around a veto-value of  $p_T^{\text{veto}} = 20 \text{ GeV}$  the difference of the cross-section at  $\mu = 2m_H$  and  $\mu = m_H/2$  changes sign. In this kinematic region logarithmic contributions,  $\log(p_T^{\text{veto}}/m_H)$  from soft radiation beyond NNLO should also be examined [51]. We will do this in section 4.3 of this thesis. However, the small scale uncertainty at NNLO and the small magnitude of the corrections suggest that such logarithms have a mild effect.

In Fig. 4.4 the cross-section is shown after the requirement that the transverse momen-

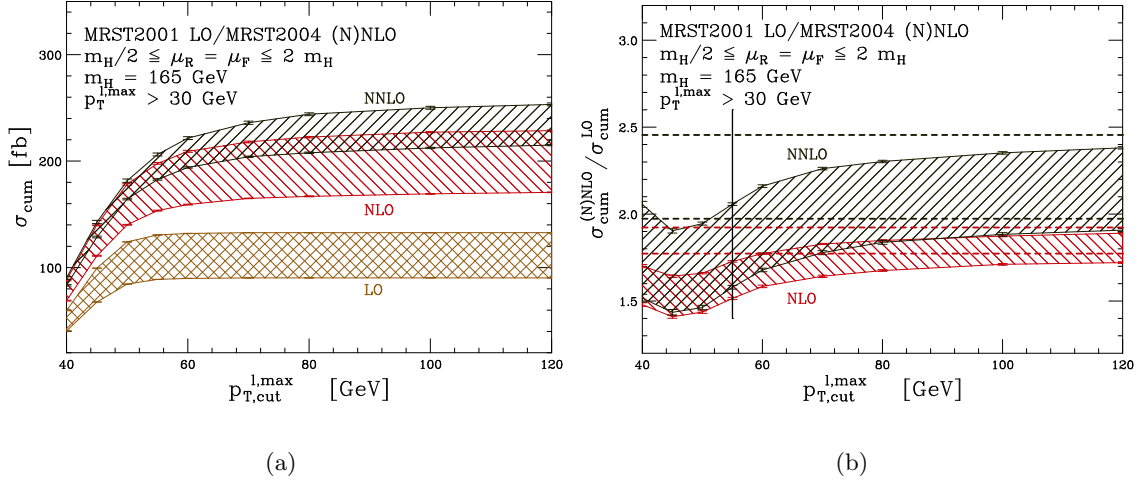


Figure 4.4: (a) The cross-section for events where the hardest visible lepton has transverse momentum  $30 \text{ GeV} < p_T^{\ell, \max} < p_{T, \text{cut}}^{\ell, \max}$ . (b) The  $K$ -factor as a function of  $p_{T, \text{cut}}^{\ell, \max}$  (no other cut is applied). The dashed horizontal lines correspond to the NLO and NNLO  $K$ -factors for the inclusive cross-section. The vertical solid line denotes the value of  $p_{T, \text{cut}}^{\ell, \max}$  in the *partonic signal cuts* of section 4.1.

tum of the hardest visible lepton is restricted to the interval  $30 \text{ GeV} < p_T^{\ell, \max} < p_{T, \text{cut}}^{\ell, \max}$ . The value chosen for the upper boundary of the allowed region in the selection cuts is  $p_{T, \text{cut}}^{\ell, \max} = 55 \text{ GeV}$ . At LO, only  $\sim 1\%$  of the hardest visible leptons have a transverse momentum of  $p_T^{\ell, \max} > 55 \text{ GeV}$ . However, at NLO (NNLO) about  $\sim 13$  ( $19$ )% of the events lie above this cut. Thus the choice  $p_{T, \text{cut}}^{\ell, \max} = 55 \text{ GeV}$  removes regions of phase-space that are only populated at NLO and NNLO. We observe that the NLO and NNLO  $K$ -factors are smaller below this cut. In addition, the scale uncertainty drops below  $12\%$  at NNLO, while the corresponding scale uncertainty for the inclusive cross-section is  $17\%$ .

A powerful discriminating variable between the signal and the  $pp \rightarrow WW$  background is the opening angle  $\phi_{\ell\ell}$  between the two charged leptons in the plane transverse to the beam axis. In Fig. 4.5 the cumulative cross-section for events with  $\phi_{\ell\ell} < \phi_{\ell\ell}^{\text{cut}}$  is shown. The NLO and especially the NNLO corrections are significantly larger for small angular cuts  $\phi_{\ell\ell}^{\text{cut}}$ . For  $\phi_{\ell\ell}^{\text{cut}} = 40^\circ$  the NNLO  $K$ -factor is  $\sim 2.27$  ( $2.70$ ) for  $\mu = m_H/2$  ( $2m_H$ ). The corresponding  $K$ -factor for the inclusive cross-section is  $\sim 1.97$  ( $2.45$ ). The NNLO scale uncertainty for  $\phi_{\ell\ell}^{\text{cut}} = 40^\circ$  is  $18.5\%$ , while for the inclusive cross-section it is  $\sim 17\%$ . Thus the envisaged cut at  $\phi_{\ell\ell}^{\text{cut}} = 45^\circ$  enhances contributions with large perturbative corrections.

The decay of the W bosons produces large missing transverse energy  $E_T^{\text{miss}}$ . In Fig. 4.6 the cumulative cross-section for  $E_T^{\text{miss}} > E_T^{\text{miss, cut}}$  is shown. At leading order there are no contributions from  $E_T^{\text{miss}} > m_W$ . This region of phase-space requires that the Higgs

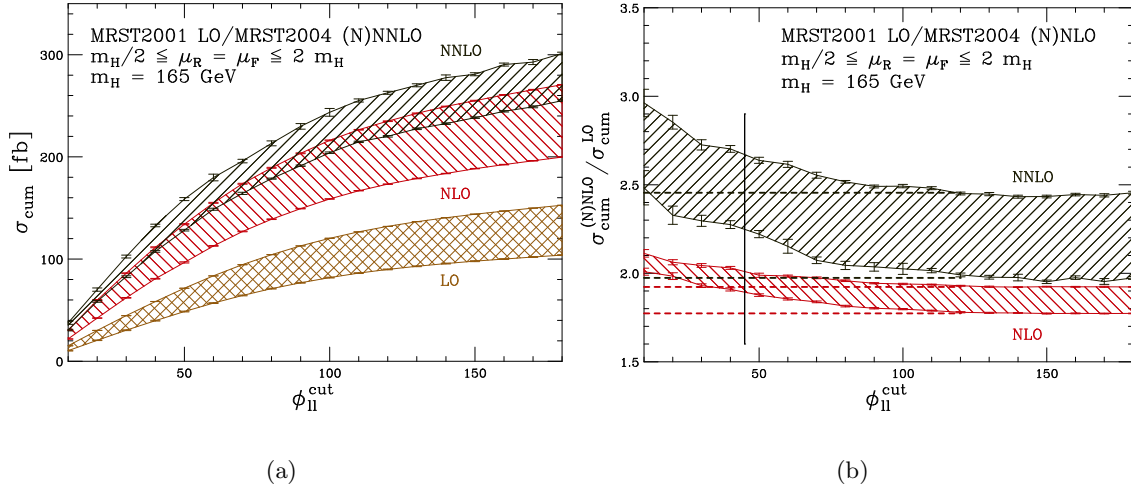


Figure 4.5: (a) The cross-section for visible leptons with an angle on the transverse plane  $\phi_{\ell\ell} < \phi_{\ell\ell}^{\text{cut}}$ . (b) The  $K$ -factor as a function of  $\phi_{\ell\ell}^{\text{cut}}$  (no other cut is applied). The dashed horizontal lines correspond to the NLO and NNLO  $K$ -factors for the inclusive cross-section. The vertical solid line denotes the value of  $\phi_{\ell\ell}^{\text{cut}}$  in the *partonic signal cuts* of section 4.1.

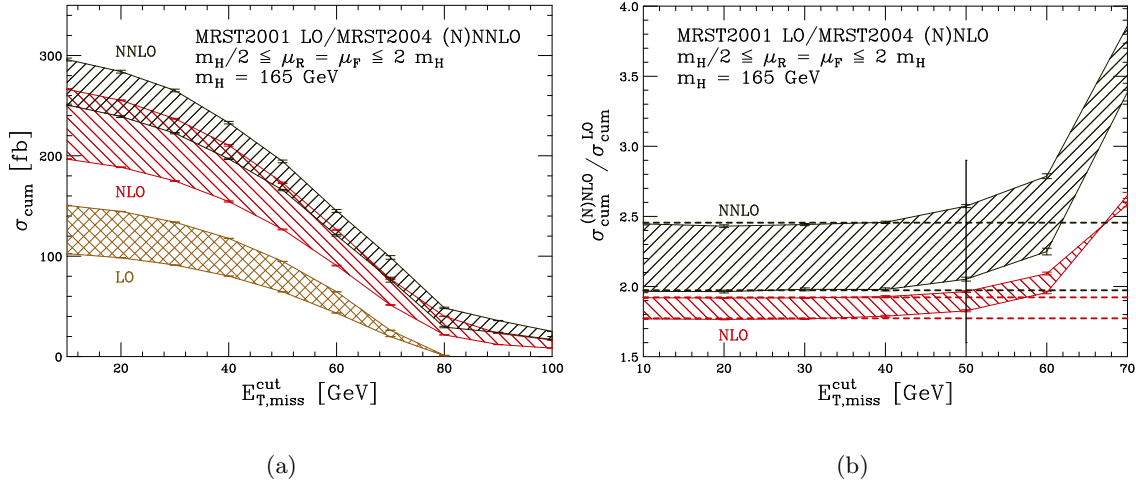


Figure 4.6: (a) The cross-section for events with missing transverse energy  $E_{T,\text{miss}}^{\text{miss}} > E_{T,\text{miss}}^{\text{miss,cut}}$ , where  $E_{T,\text{miss}}^{\text{miss}}$  is computed as the transverse momentum of the neutrino pair. (b) The  $K$ -factor as a function of  $E_{T,\text{miss}}^{\text{miss,cut}}$  (no other cut is applied). The dashed horizontal lines correspond to the NLO and NNLO  $K$ -factors for the inclusive cross-section. The vertical solid line denotes the value of  $E_{T,\text{miss}}^{\text{miss,cut}}$  in the *partonic signal cuts* of section 4.1.

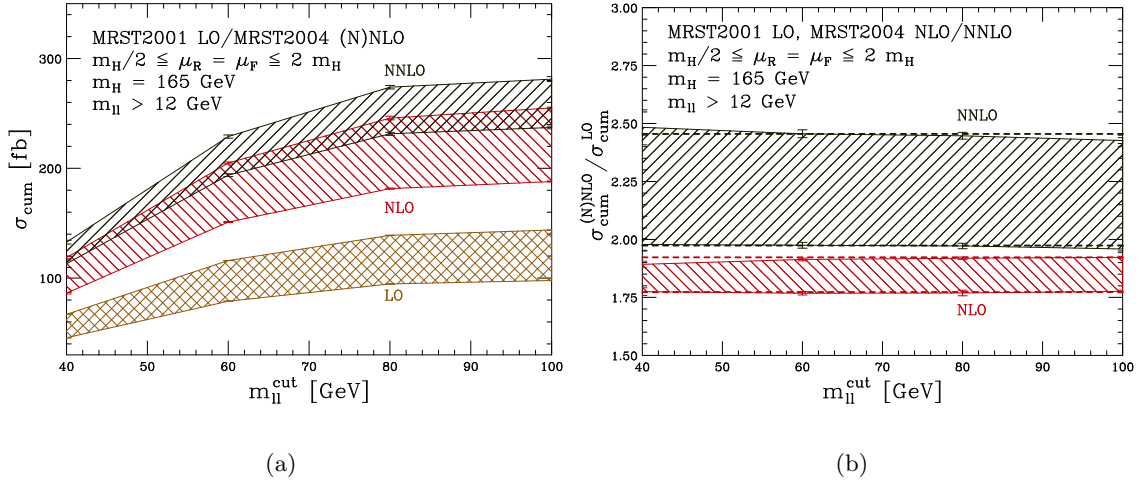


Figure 4.7: (a) The cross-section for events with charged lepton-pair invariant mass  $12 \text{ GeV} < m_{\ell\ell} < m_{\ell\ell}^{\text{cut}}$ . (b) The  $K$ -factor as a function of  $m_{\ell\ell}^{\text{cut}}$  (no other cut is applied). The dashed horizontal lines correspond to the NLO and NNLO  $K$ -factors for the inclusive cross-section.

system is boosted by additional radiation at NLO and NNLO. The contribution from  $E_T^{\text{miss}} > 80 \text{ GeV}$  for  $\mu = m_H/2$  amounts to 0.7% at LO,  $\sim 14\%$  at NLO and  $\sim 16\%$  at NNLO. The scale variation for this region of phase-space is 60% at NLO (essentially LO) and 49% at NNLO (essentially NLO). By requiring very large missing transverse energy, the significance of the above phase-space region is enhanced; the  $K$ -factors tend to increase with respect to the inclusive cross-section.

In Fig. 4.7 the cumulative cross-section is shown as a function of the cut on the invariant mass in the interval  $12 \text{ GeV} < m_{\ell\ell} < m_{\ell\ell}^{\text{cut}}$ . The cross-section has a perturbative convergence with  $K$ -factors and scale variation very similar to those for the inclusive cross-section for all choices of  $m_{\ell\ell}^{\text{cut}}$ .

We have now studied the kinematic behavior of the cross-section through NNLO for all variables which are subject to significant experimental cuts in order to optimize the signal to background ratio. It was found that the cuts discussed above can change individually the  $K$ -factors and the behavior of the cross-section under scale-variation. It is not obvious how the simultaneous application of all the cuts will affect the cross-section. This will be studied in the next section.

## 4.2.2 Signal Cross-Section at the LHC

In Table 4.3 the cross-sections after applying all the *partonic signal-cuts* are listed. The

$\sigma_{\text{acc}}$ [fb]	LO	NLO	NNLO
$\mu = m_{\text{H}}/2$	$21.002 \pm 0.021$	$22.47 \pm 0.11$	$18.45 \pm 0.54$
$\mu = m_{\text{H}}$	$17.413 \pm 0.017$	$21.07 \pm 0.11$	$18.75 \pm 0.37$
$\mu = 2 m_{\text{H}}$	$14.529 \pm 0.014$	$19.50 \pm 0.10$	$19.01 \pm 0.27$

Table 4.3: Cross-section after applying all the *partonic signal cuts* of section 4.1 at different orders of perturbative QCD.

$\sigma_{\text{acc}}$ [fb]	$\mu_{\text{F}} = m_{\text{H}}/4$	$\mu_{\text{F}} = m_{\text{H}}/2$	$\mu_{\text{F}} = m_{\text{H}}$	$\mu_{\text{F}} = 2 m_{\text{H}}$
$\mu_{\text{R}} = m_{\text{H}}/4$	$17.89 \pm 0.27$	$18.27 \pm 0.29$	$18.97 \pm 0.29$	$19.01 \pm 0.27$
$\mu_{\text{R}} = m_{\text{H}}/2$	$18.68 \pm 0.90$	$18.33 \pm 0.40$	$18.75 \pm 0.37$	$19.87 \pm 0.42$
$\mu_{\text{R}} = m_{\text{H}}$	$18.84 \pm 0.60$	$18.45 \pm 0.54$	$17.52 \pm 0.93$	$18.10 \pm 0.63$
$\mu_{\text{R}} = 2 m_{\text{H}}$	$16.82 \pm 0.94$	$18.40 \pm 1.00$	$16.06 \pm 0.94$	$15.45 \pm 0.98$

Table 4.4: NNLO cross-sections for the *partonic signal cuts* and independent variation of the renormalization scale  $\mu_{\text{R}}$  and the factorization scale  $\mu_{\text{F}}$ .

NLO and NNLO  $K$ -factors are small in comparison to the corresponding  $K$ -factors for the inclusive cross-section. The relative magnitude of the NLO and NNLO corrections with respect to LO is similar to the observed  $K$ -factors in Fig. 4.3 for a jet-veto value around  $\sim 20$  GeV. The scale variation is also small at NNLO (it compares to the statistical error of our numerical integration); this is again similar to the pattern observed in Fig. 4.3 for small values of the jet-veto cut. Remarkably, for the scale choice of  $\mu = m_{\text{H}}/2$  the NNLO cross-section is even smaller than the corresponding LO cross-section.

The cross-sections in Table 4.3 for the *partonic signal cuts* demonstrate a much better perturbative behaviour than the inclusive cross-section. However, it cannot be concluded yet that we have obtained a very precise prediction for the signal cross-section, since the small  $K$ -factors and scale variations may be accidental. We have computed the average transverse momentum of the Higgs boson to be  $\langle p_{\text{T}}^{\text{H}} \rangle_{\text{cuts}} \sim 15$  GeV at NNLO for  $\mu_{\text{F}} = \mu_{\text{R}} = m_{\text{H}}/2$ . The corresponding average without selection cuts is  $\langle p_{\text{T}}^{\text{H}} \rangle \sim 48$  GeV. Logarithms of the type  $\log(p_{\text{T}}^{\text{H}}/m_{\text{H}})$  could therefore have a more significant impact after the cuts than for the inclusive cross-section.

However, the results for the variation of the renormalization and factorization scales in Table 4.3 do not indicate the existence of such large logarithmic corrections. To investigate this aspect in more detail, the cross-sections with the *partonic signal cuts* applied for independent variation of  $\mu_{\text{R}}$  and  $\mu_{\text{F}}$  in the interval  $[m_{\text{H}}/4, 2 m_{\text{H}}]$  are computed and shown in Table 4.4. The largest scale variation in this interval is  $\sim 10\%$ . The corresponding scale variation for the inclusive cross-section in the smaller interval  $[m_{\text{H}}/2, 2 m_{\text{H}}]$  is  $\sim 16\%$  (cf. section 2.2.1.1). The NNLO result has a remarkable stability under the variation of



the renormalization and factorization scales, indicating that the numerical coefficients of the higher-order logarithmic terms should be small. We want to verify this assumption in the next section.

### 4.3 Re-Summation Effects

In the previous section it has been shown that the higher-order QCD corrections affect the distributions of kinematic observables restricted by the *partonic signal cuts*. While the individual observables show different behavior, the cross-section after applying all the cuts becomes very stable under the variation of the renormalization and factorization scales. We noticed how the cuts restrict the Higgs phase-space to the low  $p_T^H$  region and discussed how multiple soft and collinear radiation might become important.

In section 2.2.1.2 it was found that the Higgs transverse momentum spectrum is sensitive to these effects in the low- $p_T^H$  region. We also noticed that, if the spectrum is integrated over a large enough region, these radiation effects become negligible and the fixed-order calculation should be reliable. We found that at NLO this region is defined at  $p_T^{H,\max} \sim 50$  GeV, while at NNLO the result becomes comparable to the computation including re-summation of leading logarithmic terms already by integrating up to a value of  $p_T^{H,\max} \sim 20$  GeV.

#### 4.3.1 Differential Distributions

We want to extend the study of the soft radiation effects to the variables that undergo a selection cut for the  $H \rightarrow WW$  process. We list these variables again:

1.  $m_{\ell\ell}$ , the invariant mass of the charged lepton pair;
2.  $\phi_{\ell\ell}$ , the angle between the two charged leptons in the plane transverse to the beam axis;
3.  $p_T^{\ell,\max}$ , the transverse momentum of the harder lepton;
4.  $E_T^{\text{miss}}$ , the missing transverse energy and
5.  $p_T^{\text{veto}}$ , the maximum transverse momentum for jets with  $|\eta_{\text{jet}}| < 2.5$ .

We compare the NNLO fixed-order cumulative cross-sections from section 4.2.1 with the inclusively re-weighted distributions predicted by MC@NLO; neither hadronization nor the underlying event have been considered. Again, the factorization and renormalization

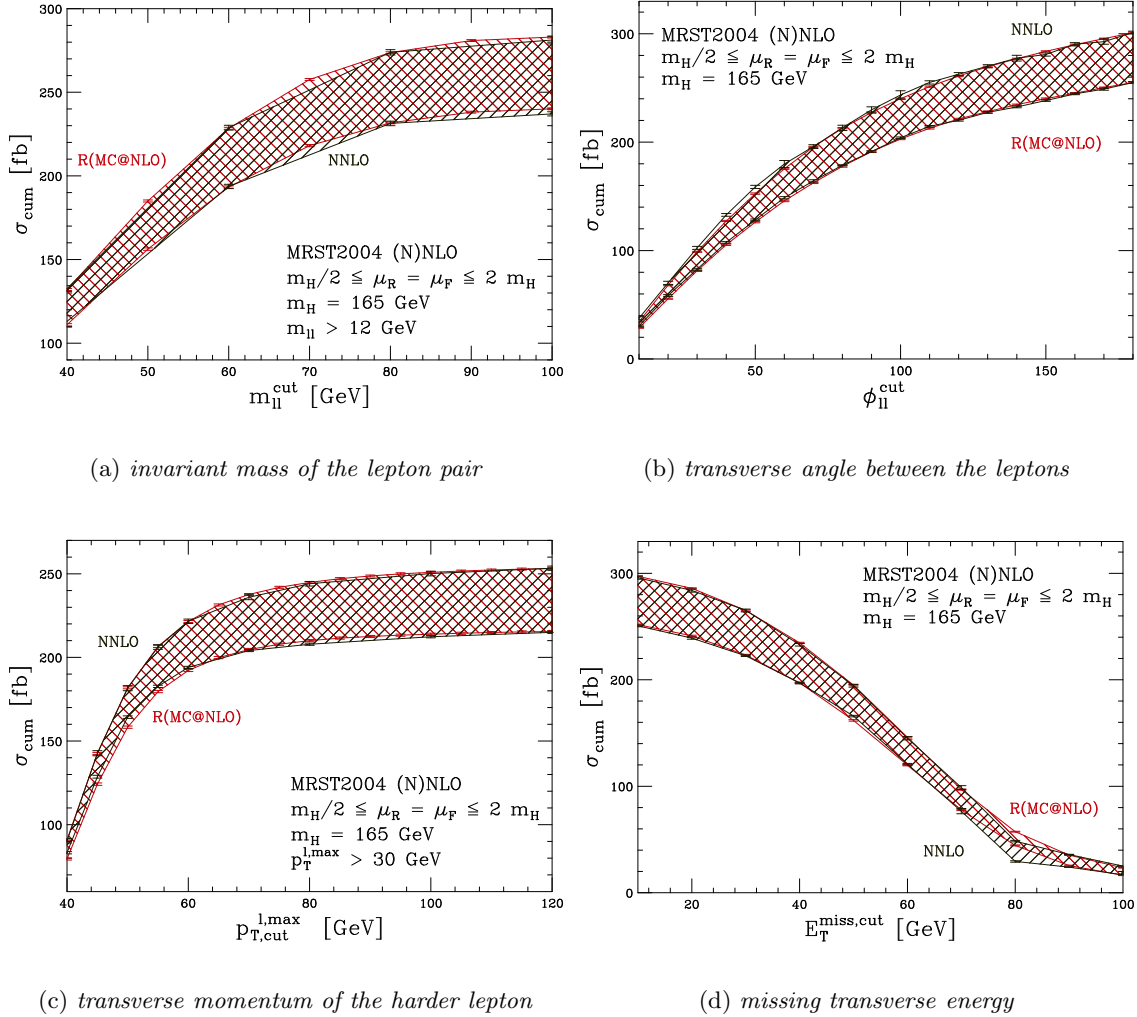


Figure 4.8: Comparison of the cumulative cross-sections for the leptonic kinematic variables that undergo a selection cut, for fixed-order (NNLO) and inclusively re-weighted MC@NLO ( $R(\text{MC@NLO})$ ).

scales are varied simultaneously in the range  $[m_H/2, 2m_H]$ . The distributions are shown in Fig. 4.8 and Fig. 4.9.

The agreement for the purely leptonic variables (1. – 4. in the list) is remarkable. The only small difference can be seen in the  $E_T^{\text{miss}}$  distributions at a value of about 80 GeV, where, as explained before, the NNLO fixed-order results are nominally of NLO, since at LO the maximum missing transverse energy is limited by the mass of the W boson. It is therefore not surprising that the soft and collinear radiation effects lead to rather large corrections in this phase-space region.

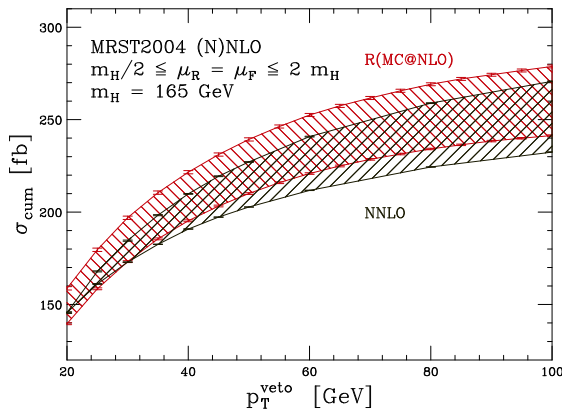


Figure 4.9: Comparison of the cumulative cross-section for the jet-veto between fixed-order (NNLO) and inclusively re-weighted MC@NLO ( $R(\text{MC@NLO})$ ).

For the jet-veto distribution (Fig. 4.9) such a perfect agreement can not be expected. In fact the jet-veto cut is naturally the selection cut that is most sensitive to the hadronic structure of the final state. However, especially in the region of the envisaged cut of 25 GeV, the agreement is very good. Therefore this agreement confirms the picture observed in section 2.2.1.2. We want to point out that a comparison of fixed-order NLO with MC@NLO would not result in a good agreement. It has been discussed that a jet-veto at 25 GeV corresponds to a  $p_T^{\text{H,max}}$  value of exactly 25 GeV and that the cumulative cross-section in  $p_T^{\text{H}}$  at NLO does not agree with the re-summed spectrum (cf. Fig. 2.11(a)).

### 4.3.2 Signal Cross-Section

In Table 4.5 the cross-sections after applying all *partonic signal cuts* are listed. In addition to the  $k_T$  algorithm we have used the SISCone algorithm [52], implemented in the FASTJET package [53]. The jet radius in the azimuth-rapidity plane was set to  $R = 0.4$  and the merging parameter for the SISCone algorithm to  $f = 0.5$ <sup>3</sup>. Formally the two algorithms yield identical results for the fixed-order calculation up to NLO.

In the first part of the Table we show the results obtained using a fixed LO computation and the LO+parton-shower event generator HERWIG. We find a much larger fixed order result than when a parton shower is added. At fixed LO all events have a Higgs boson with zero transverse momentum, and the jet-veto rejects none of the events (cf. section 2.2.1.2). In contrast, HERWIG generates a large fraction ( $\sim 50\%$ ) of events with  $p_T^{\text{jet}} > p_T^{\text{veto}}$ .

<sup>3</sup>The merging parameter  $f$  defines, how much two separate proto-jets need to overlap in order to be merged into one jet.

$\sigma_{\text{acc}}$ [fb] jet algorithm	$\mu = m_H/2$		$\mu = 2 m_H$	
	SISCone	$k_T$	SISCone	$k_T$
LO	21.00 $\pm$ 0.02		14.53 $\pm$ 0.01	
HERWIG	11.16 $\pm$ 0.04	11.59 $\pm$ 0.04	7.60 $\pm$ 0.03	7.89 $\pm$ 0.03
NLO	22.40 $\pm$ 0.06		19.52 $\pm$ 0.05	
MC@NLO	17.42 $\pm$ 0.08	18.42 $\pm$ 0.08	13.60 $\pm$ 0.06	14.39 $\pm$ 0.06
$R^{\text{NLO}}$ (HERWIG)	19.79 $\pm$ 0.07	20.56 $\pm$ 0.07	14.61 $\pm$ 0.05	15.17 $\pm$ 0.05
NNLO	18.18 $\pm$ 0.43	18.45 $\pm$ 0.54	18.76 $\pm$ 0.31	19.01 $\pm$ 0.27
$R^{\text{NNLO}}$ (MC@NLO)	19.33 $\pm$ 0.09	20.43 $\pm$ 0.09	17.24 $\pm$ 0.07	18.24 $\pm$ 0.07
$R^{\text{NNLO}}$ (HERWIG)	22.02 $\pm$ 0.08	22.88 $\pm$ 0.08	18.65 $\pm$ 0.07	19.38 $\pm$ 0.07

Table 4.5: Cross-sections after the *partonic signal cuts* are applied for different perturbative approximations. The statistical integration errors are shown explicitly. The MC@NLO and HERWIG cross-sections are evaluated with 1000000 generated events.

In the second part of Table 4.5 we show the results obtained using a fixed NLO computation, the event generator MC@NLO and the inclusively to NLO re-weighted event generator HERWIG ( $R(\text{HERWIG})$ ). The NLO result is quite different from the one obtained with MC@NLO. However, this is no surprise since we already discussed that the fixed NLO result is not expected to predict the cross-section reliably compared to the re-summed calculation.

In the last part of Table 4.5 we show the results obtained using a fixed NNLO computation and the results from MC@NLO and HERWIG, rescaled to the NNLO total cross-section. The NNLO result and the rescaled MC@NLO are consistent. We do not expect the same scale variation behavior, cf. Fig. 4.9. In fact, the scale uncertainty of the re-weighted MC@NLO result corresponds to the inclusive NNLO scale uncertainty, while for the fixed NNLO calculation the scale variation leads to a reduced uncertainty (cf. section 4.2.2).

We remind the reader that for all the results of this section MC@NLO and HERWIG have been used at parton level, i.e. neither hadronization nor underlying event effects are considered. We observe that the  $k_T$ -algorithm gives larger cross-sections than the SISCone algorithm for MC@NLO and HERWIG; as mentioned before, the results for the two algorithms are very similar at fixed order through NNLO (within our numerical integration precision). Additionally MC@NLO gives slightly smaller values for the cross-sections than HERWIG. Again this has been observed in the Higgs transverse momentum spectra presented in section 2.2.2, where we have found that HERWIG slightly over-estimates the cumulative cross-section in  $p_T^H$ .

## 4.4 Jet Algorithm, Hadronization & the Underlying Event

So far we have neglected any hadronization and underlying event (UE) effects. This was necessary in order to compare the MC event generator results with the fixed-order calculations (where the inclusion of hadronization and UE is not possible). To finalize this part we want to understand how the cross-section after the selection cuts is affected by the hadronization and the UE. This is achieved by using the MC event generator MC@NLO and the assumption that these effects and the hard-scattering process factorize in such a way, that the conclusions can be adopted to our most precise result, obtained at fixed NNLO.

First we want to argue why this approach should be valid to a good approximation. The hadronization procedure does not take place in the perturbative regime. Any hadronization model is a phenomenological description of the formation of hadrons from quarks. This should be roughly independent of the hard-scattering process, thus the only effect we expect from the hadronization is a change of the sub-structure in the momentum-flow of the final-state particles. If we assume a hermetic detector able to collect all the final-state energy, the over-all momentum of all final-state particles should not change upon the inclusion of hadronization effects.

The effect of the underlying event can be seen as an addition of hadronic activity in the final state due to multi-parton- and beam-remnant-interaction. Again, these effects should be independent of the hard-scattering process to a good approximation.

Both effects have no impact on the leptonic final state configuration, with the exception of the isolation criterion, which turned out to have a minor impact. We therefore expect that the impact on the cross-section after the selection cuts is dominated by their effect on the jet-veto through the jet-structure. As appropriate variable to observe any effect we thus choose the cumulative cross-section in  $p_T^{\text{veto}}$ , after the application of all other *partonic signal cuts*.

We are interested in the effects of changing the jet-algorithm parameter  $R$ . In Fig. 4.10 we plot the cumulative cross-section of MC@NLO as a function of the  $p_T^{\text{veto}}$  value for the  $k_T$  and the SISCone algorithm with jet-radii  $R = 0.4$  and  $R = 0.7$ . We find that for small values of the jet-veto parameter the choice of the jet clustering method is more significant. For a jet-veto at  $p_T^{\text{veto}} = 25$  GeV the choice of jet-algorithm changes the cross-section by  $\sim 6\%$  with MC@NLO. A similarly large variation of  $\sim 7\%$  is observed when we vary the jet-radius from  $R = 0.4$  to  $R = 0.7$ . For a jet veto value larger than about  $p_T^{\text{veto}} \simeq 40$  GeV the sensitivity of the cross-section to the choice of the jet-algorithm or the jet-radius falls below  $\sim 2 - 3\%$ .

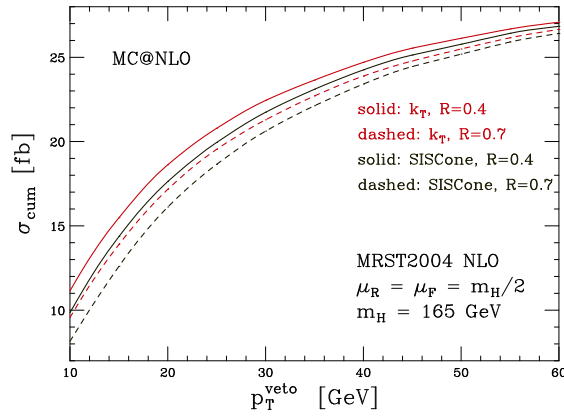


Figure 4.10: Comparison between the SISCone and  $k_T$  algorithm for different values of the allowed maximum jet transverse energy (jet-veto). All other *partonic signal cuts* are applied.

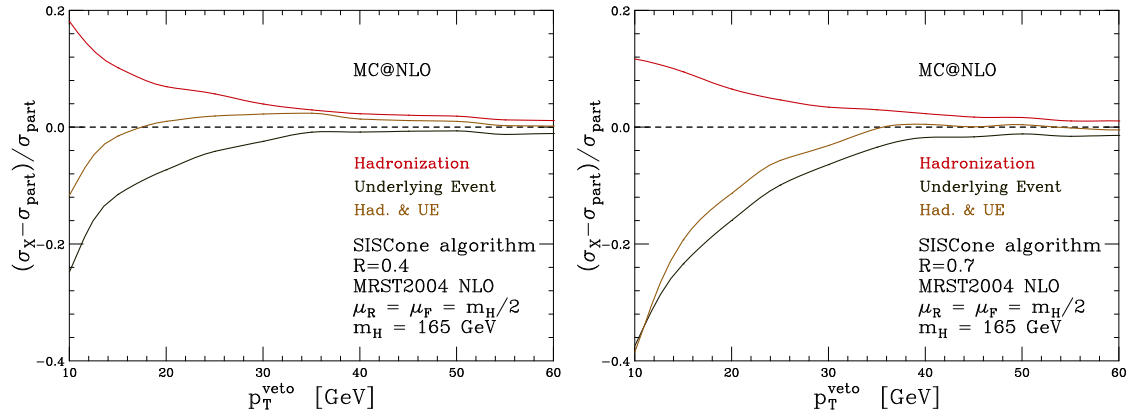


Figure 4.11: Difference of the cross-section after *partonic signal cuts* including the underlying event and hadronization models, with respect to the partonic cross-section. The cross-section is shown as a function of the jet-veto value for the SISCone clustering algorithm.

We now study the effect of hadronization as it is modeled in HERWIG and of the underlying event as implemented in JIMMY [12]. In Fig. 4.11 we present the relative difference of the cross-section with respect to the partonic cross-section when the hadronization and/or the underlying event are switched on. Here we use the SISCone algorithm with a merging parameter  $f = 0.5$  and two values for the jet-radius  $R = 0.4$  (left) and  $R = 0.7$  (right). We apply all the *partonic signal cuts* with the exception of the jet-veto. Of interest are values of the jet-veto between 25 and 40 GeV, which are envisaged for the Higgs boson search.

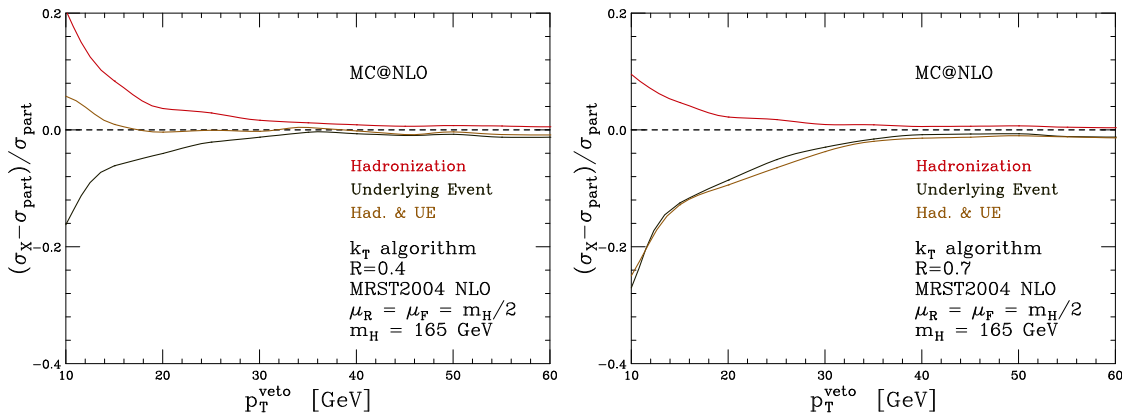


Figure 4.12: Difference of the cross-section after *signal cuts* including the underlying event and hadronization models, with respect to the partonic cross-section. The cross-section is shown as a function of the jet-veto value for the  $k_T$  clustering algorithm.

Qualitatively we anticipate that the hadronization and the underlying event change the partonic cross-section with opposite signs, as outlined in [54]. Hadronization reduces the average  $p_T$  of (gluonic) jets by roughly  $\delta p_T^{\text{jet}} \sim (1 \text{ GeV})/R$ . The underlying event increases the jet  $p_T^{\text{jet}}$  by roughly  $\delta p_T^{\text{jet}} \sim R^2 \times (5 \text{ GeV})$  at the LHC. The slope of the partonic cumulative cross-section in  $p_T^{\text{veto}}$  is large for small values of the jet-veto (cf. Fig. 4.9). The shifts  $\delta p_T^{\text{jet}}$  from hadronization and the underlying event can therefore induce significant changes to the cross-section. A jet-veto after hadronization corresponds to a looser effective jet-veto at the parton level. We therefore anticipate the cross-section to increase by switching on the hadronization model. Similarly, we anticipate a decrease of the cross-section due to the underlying event.

These trends can be verified in Fig. 4.11. A smaller jet-radius increases the impact of hadronization and decreases the impact of the underlying event. The two effects are not linearly additive. However, we find that a cancellation between the two effects, which varies according to the jet-radius, takes place. For a jet veto  $p_T^{\text{veto}} = 25 \text{ GeV}$  and  $R = 0.4$ , the hadronization shift is about  $\sim +7\%$  and the underlying event shift is  $\sim -4\%$ . For a larger  $R = 0.7$ , the two shifts are  $+5\%$  and  $-10\%$ , respectively.

In Fig. 4.12 the effects of hadronization and the underlying event are shown for the  $k_T$  algorithm. We find the same qualitative features as for the SISCone algorithm. However, we note that the  $k_T$ -algorithm shows an overall reduced sensitivity.

## 4.5 Conclusions of this Chapter

In this chapter we have studied the QCD corrections up to NNLO for the  $H \rightarrow WW \rightarrow \ell\nu\ell\nu$  cross-section at the LHC. We observed that these corrections have a significant impact on the inclusive cross-section (the inclusive  $K$ -factor at NNLO is  $\sim 2$ ) while the scale uncertainty is reduced compared to LO and NLO, indicating a convergence of the perturbative series.

Furthermore all the kinematic observables that undergo experimental cuts in a typical Higgs search in this channel have been studied in detail. It was observed that these cuts affect the  $K$ -factors in very different ways, either increasing or decreasing the  $K$ -factors. However, the cross-section after applying all envisaged cuts shows a remarkable stability under the variation of the renormalization and the factorization scales and the corresponding  $K$ -factors are of the order of one.

It was observed how specific cuts (i.e. the jet-veto) restrict the Higgs boson phase-space to the low transverse momentum region, where the re-summation of large logarithms might be needed in order to render the prediction reliable. To investigate this we compared the fixed (N)NLO predictions for the transverse momentum spectrum of the Higgs to the parton-shower MC event generators HERWIG and MC@NLO, as well as to the re-summed spectrum at (N)NLO+(N)NLL. It was observed that while the fixed NLO prediction is not reliable, unless the Higgs  $p_T$  spectrum is integrated up to  $p_T^H \sim 50$  GeV, the fixed NNLO calculation agrees with the re-summed spectra already after integrating up to  $p_T^H \sim 20$  GeV.

In order to understand the effects of the multiple radiation on the cross-section after applying the cuts, all the variables restricted by these cuts have been studied. The agreement for all the variables in the range of the envisaged cuts is very good. From all these observations it can be concluded that the fixed NNLO prediction for the cross-section after applying all the cuts is a very precise prediction.

Finally, effects of hadronization and the underlying event have been studied using different jet algorithms. It turned out that the effects are of the order of 5 – 10 % and might even cancel each other to a large amount under certain circumstances.



## Part II

# The Compact Muon Solenoid (CMS) Experiment at the LHC



## Chapter 5

# Experimental Apparatus

Over the last decades collider experiments have given tremendous insight into particle physics and the general structure of the matter making up the universe. While over the years the technical obstacles to build larger and more powerful particle accelerators have been overcome, dedicated experiments have been able to test the Standard Model of Particle Physics to a very accurate level for many of its main predictions. Among others we emphasize the discovery of the W and Z bosons in 1983 by the experiments UA1 and UA2 [55] at the Super-Proton-Synchrotron (SPS) at CERN and the top-quark discovery [56] in 1993 at the Tevatron-collider at Fermilab (USA).

The potential and the limitations for a collider experiment to measure physical quantities or discover particles are dictated by the specific accelerator and detector designs. On the accelerator side we distinguish between two main classes; the linear accelerators, where particles are accelerated on a linear distance up to their final collision energy, and the synchrotron accelerators, where particles are accelerated on a circle. On the detector side we distinguish between two main classes of experiments, the fixed-target experiments, where incoming particles are scattered on a fixed, typically solid, liquid or gaseous block of target matter, and the collider experiments, where two incoming particle-beams are colliding head-on.

The two main quantities characterizing such an apparatus are the center-of-mass energy  $E_{\text{CM}}$  of the colliding particles and the luminosity  $\mathcal{L}$ , which is defined as

$$\mathcal{L} = \Phi_a \times N_b, \quad (5.1)$$

where  $\Phi_a$  is the incoming particle current and  $N_b$  is the number of target particles in a fixed target experiment. In a collider experiment the luminosity is defined as

$$\mathcal{L}_{\text{col}} = \frac{N_a N_b j v / U}{A}, \quad (5.2)$$

with  $N_a$  ( $N_b$ ) the number of particles per bunch in beam  $a$  (beam  $b$ ),  $j$  the number of particle bunches per beam-type,  $U$  the circumference of the synchrotron,  $v$  the velocity of the particles and  $A = 4\pi\sigma_x\sigma_y$  the beam area at the interaction point ( $\sigma_x, \sigma_y$  are the Gaussian-shape distributions of the particle beam in vertical and horizontal direction).

The number of scattering reactions in the time-interval  $t_2 - t_1$  for the process  $X \rightarrow Y$  can then be computed as

$$N(X \rightarrow Y) = \int_{t_1}^{t_2} \sigma(X \rightarrow Y) \mathcal{L} dt = \sigma(X \rightarrow Y) \times \mathcal{L}_{\text{int}}, \quad (5.3)$$

where we used that the cross-section  $\sigma(X \rightarrow Y)$  is constant over time and defined the integrated luminosity for the time-interval  $t_2 - t_1$ ,  $\mathcal{L}_{\text{int}}$ . The center-of-mass energy  $E_{\text{CM}}$  influences which processes are possible in the experiment. Finally, the type of the incoming particles constrains the possible scattering reactions as well.

Each of the above mentioned collider/experiment strategies have their characteristic advantages and short-comings. While for fixed target experiments it is e.g. rather simple to increase the luminosity by increasing the fixed-target-density, collider experiments have advantageous energetic behavior, i.e. with the same beam-energy much higher center-of-mass energies can be reached compared to fixed-target experiments.

On the accelerator side a linear geometry is favourable because of its rather simple architecture and the fact that linearly accelerated charged particles do not lose energy due to synchrotron radiation,

$$\Delta E_{\text{syn}} = \frac{4\pi\alpha}{3R} \beta^3 \gamma^4, \quad \text{with } \beta = \frac{v}{c} \quad \text{and} \quad \gamma = \frac{E}{mc^2}, \quad (5.4)$$

where  $\alpha$  is the fine structure constant and  $R$  is the radius of the accelerator. On the other hand, the needed distance to accelerate a particle to a desired collision-energy becomes quickly large in a linear accelerator. In addition, in a circular geometry (synchrotron) there is the possibility for several experiments running simultaneously, since there can be more than one collision point for the particles beams. In a linear acceleration geometry this is more complicated.

Most modern high-energy physics collider experiments are installed at synchrotron accelerators. The limitations in terms of possible center-of-mass collision energies are mainly given by the energy loss of the particles through synchrotron radiation in eq. 5.4. As an example, the maximum center-of-mass energy reachable at the LEP collider running at CERN between 1989 and 2000 was  $\sim 209$  GeV. Beyond this threshold the additional energy added to accelerate the colliding electrons and positrons was almost completely radiated off, and no further net acceleration could be achieved. The energy-loss through

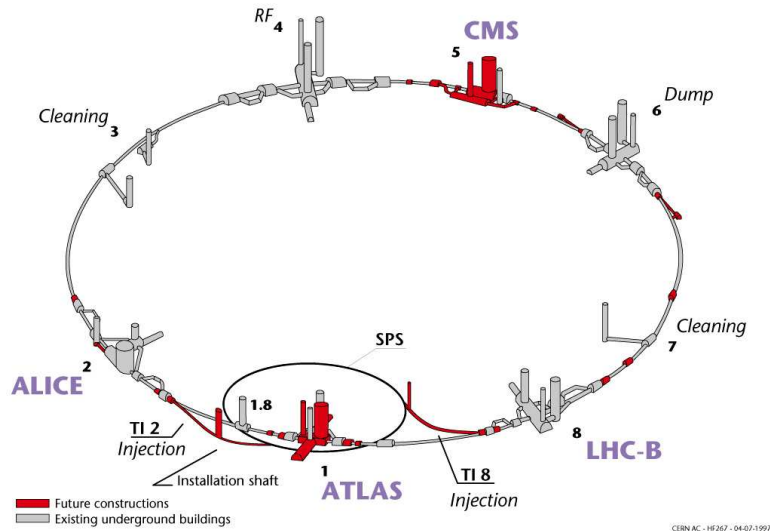
**Layout of the LEP tunnel including future LHC infrastructures.**

Figure 5.1: Layout of the LHC tunnel including the four experiments LHC-B, ALICE, ATLAS and CMS.

radiation depends on two adjustable parameters, first on the synchrotron radius  $R$  and second on the colliding particle mass  $m$ , i.e. higher center-of-mass energies can be reached by either increasing the radius  $R$  or by using heavier particles in the collision. Since it was natural to reuse the LEP tunnel, the second option was favored by replacing the colliding electrons from LEP by heavier particles, e.g. by protons.

The last crucial characteristics of a collider experiment is the type of colliding particles. These particles can be fundamental particles, i.e. particles that are not built-up by more fundamental particles in the Standard Model. In this case the complete collision momenta of the reaction are known if the beam parameters are determined. If the colliding particles are compound objects, e.g. protons or heavy ions, then the interacting partons carry only a fraction of the total hadron momentum. Finally, the charge combination of the colliding particles puts technical requirements on the acceleration machinery. If the particles have e.g. same sign charges, one magnetic field is not enough to keep both particle beams on the circular orbit.

## 5.1 The Large Hadron Collider

The Large Hadron Collider (LHC) [21] is a proton-proton synchrotron with a circumference of 27 km located at the European Organization for Nuclear Research (CERN) near

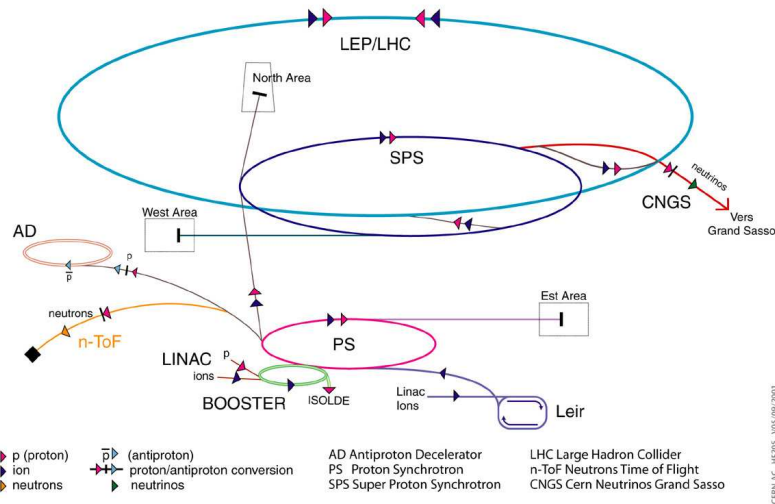
**Accelerator chain of CERN (operating or approved projects)**

Figure 5.2: Accelerator chain at CERN.

Geneva, Switzerland. The operational start is scheduled for the year 2008, the nominal center-of-mass energy of 14 TeV should be reached in 2009.

The LHC accelerator ring is installed in the former LEP tunnel at CERN. There will be four experiments, namely ALICE (A Large Ion Collider Experiment) [57], LHC-b [58], ATLAS (A Toroidal LHC Apparatus) [59] and CMS (Compact Muon Solenoid) [60]. The LHC infrastructure with the main accelerator ring and the four experiments is shown in Fig. 5.1. While the two detectors CMS and ATLAS are multipurpose experiments, LHC-b is dedicated to the study of b-physics and ALICE to heavy-ion collisions.

In order to keep protons with 7 TeV energy on the circular orbit a magnetic field of about 8.3 T is needed. This magnetic field is provided by 1232 superconducting dipole magnets, each with a length of 14.3 m, operating at a temperature of 1.9 K. Additional 400 quadrupole-magnets are installed to focus the proton beams [21].

Before accelerating the beams to their final energy, the LHC ring is fed with protons at an energy of 450 GeV by the accelerator chain shown in Fig. 5.2. Both beam-pipes of the LHC accelerator are filled with 2808 bunches of  $1.1 \times 10^{11}$  protons each. The bunches are separated by about 7 m. After filling, the radio-frequency-cavities (indicated as RF in Fig. 5.1) are used to accelerate the protons up to the nominal 7 TeV. This fill- and ramping-time is expected to be at the order of one hour. When the protons have reached their nominal energy, the beams can be used for collision-reactions at the four interaction points until the beam-quality has dropped below some useful value. The “physics” time for one fill is estimated to be around 20 hours. The design peak luminosity for the LHC is

$10^{34} \text{ cm}^{-2} \text{ s}^{-1}$ . In the beginning of the LHC operation the luminosity will be lower. The stated start-up luminosity (also referred to as 'low luminosity run') is  $2 \times 10^{33} \text{ cm}^{-2} \text{ s}^{-1}$ .

During the collisions phase there will be a bunch-crossing at the interaction points every 25<sup>th</sup> nano-second, which corresponds to a bunch-collision rate of 40 MHz. At the design luminosity up to 20 inelastic proton-proton collision are expected for each of these proton-bunch-crossings. Thus the resulting event-rate per second of  $\sim 0.8 \times 10^9$  poses strong requirements on the radiation hardness, the granularity and the response-time of the detectors running under these circumstances.

## 5.2 The Compact Muon Solenoid Experiment

One of the four experiments hosted at the LHC is the multi-purpose detector CMS (Compact Muon Solenoid). Its design proposal [61] included the following emphases:

1. a very good and redundant muon system,
2. the best possible electromagnetic calorimeter (ECAL) consistent with 1),
3. a high quality central tracking consistent with 1) and 2),
4. a financially affordable detector.

The specific design goals were mainly motivated by the search for the SM Higgs boson in a wide mass range, where excellent lepton measurements, as well as very good photon energy resolutions are needed.

In the CMS detector these goals are achieved using a compact geometry, where all tracking and calorimetry is located inside a very strong, super-conducting solenoid magnet with field-strength of 4 T, but actually operated at 3.8 T. In the central detector part (barrel) the only detector components outside of the solenoid are the iron return-yokes including the muon-system and a small part of the hadronic calorimeter, discussed later. A schematic drawing of the CMS detector is shown in Fig. 5.3. The detector has a length of about 22 m, a diameter of about 15 m and a total weight of over 12000 tonnes.

We will briefly describe the various detector subsystems in the upcoming sections. For more detailed information we refer to the various Technical Design Reports [62] and a recent publication describing the CMS detector as built [63].

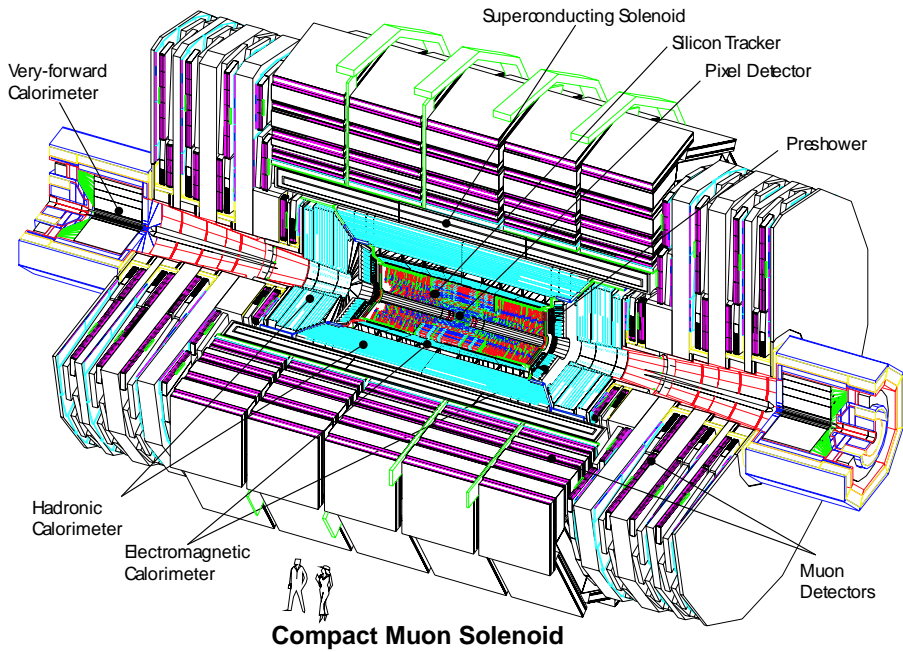


Figure 5.3: The Compact Muon Solenoid (CMS) Experiment at the LHC.

### 5.2.1 Central Tracking

The purpose of the central tracking system is to measure the position and the momentum of charged particles, as well as the vertex reconstruction. The tracking system is the innermost part of the CMS detector. It consists of the pixel and the silicon-strip detectors and will take a volume of a length of about 5.4 m and a diameter of about 2.4 m. Together with the strong ( $\sim 4T$ ) magnetic field induced by the super-conducting solenoid magnet the tracking system allows for a very accurate measurement of the momenta of charged particles.

The central part of the tracking system is the pixel detector, shown in Fig. 5.4. It consists of three layers in the barrel and two end-cap discs on both sides. The square pixel shape is  $(150 \times 150) \mu\text{m}^2$ . The more than 15000 readout chips give about 44 million readout channels.

Outside of the pixel detector the silicon-strip detector is installed. In the barrel it consists of four (six) inner (outer) layers. On each side of the inner layers three end-cap mini-discs are installed. The end-cap silicon-strips consist of nine additional discs. The schematic longitudinal view of a quarter of the silicon-strip detector is shown in Fig. 5.5.

The expected momentum resolution for the tracking system is  $\Delta p_T/p_T^2 \simeq 0.015\%$  in the central region  $|\eta| < 1.6$  and  $\Delta p_T/p_T^2 \simeq 0.06\%$  for  $|\eta| \sim 2.5$ .



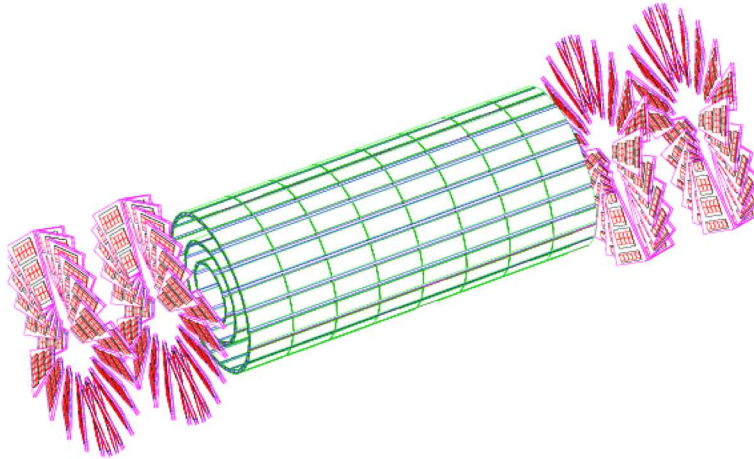


Figure 5.4: Schematic drawing of the CMS Pixel Detector.

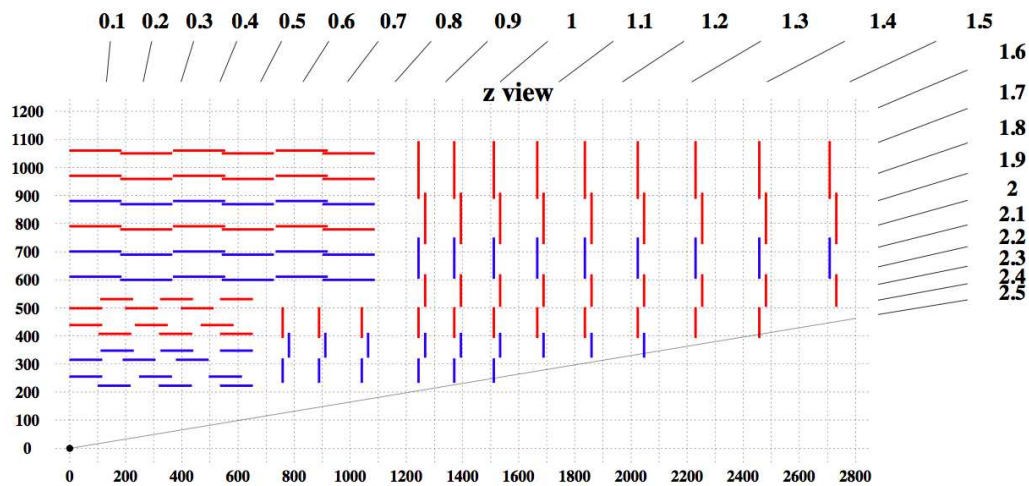


Figure 5.5: Schematic transverse view of the silicon-strip detector layers.

### 5.2.2 The Electromagnetic Calorimeter (ECAL)

Around the tracking detector, still completely within the magnet, the electromagnetic calorimeter (ECAL) is placed. It again consists of a barrel and two end-cap parts. The

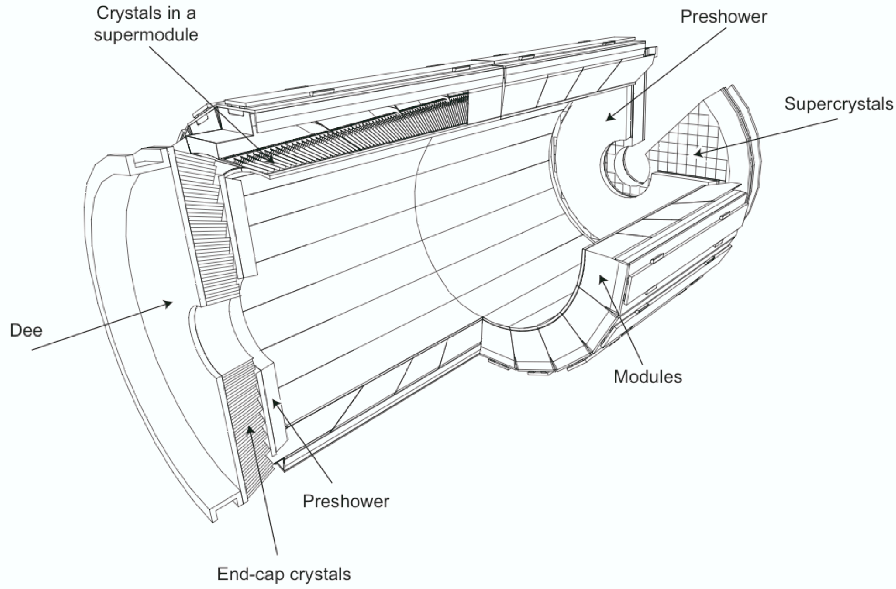


Figure 5.6: Schematic view of the ECAL detector of CMS.

active material of the ECAL are scintillating lead-tungstate crystals, each with a front-face area of about  $(2.2 \times 2.2) \text{ cm}^2$  ( $(2.5 \times 2.5) \text{ cm}^2$ ) and a length of 23 cm (25 cm) in the barrel  $|\eta| < 1.4$  (end-cap  $2.5 > |\eta| > 1.4$ ) region. A schematic view of the ECAL is shown in Fig. 5.6.

The advantage of the lead-tungstate material over other scintillating crystals (such as BGO-crystals) is the short light decay time (within only 15 ns about 60% of the light is emitted) combined with its radiation hardness and its high density, allowing for a compact ECAL design. This is especially important for installing the ECAL (as well as the HCAL) within the superconducting magnet.

A disadvantage is the relatively small light yield, which requires a strong amplification of the signal. In the barrel this is achieved by equipping each crystal with two avalanche photo-diodes (APD). Due to the higher radiation expected, in the end-caps the signal collection and amplification is realized by vacuum photo-triodes (VPT).

In the barrel the crystals are organized in 36 super-modules, each consisting of 1700 crystals. Eighteen of these super-modules form an ECAL barrel ring, concentric around the beam pipe. The crystals are oriented in such a way, that they face three degrees away from the center of the detector (collision point) to minimize the probability of a particle passing through the inactive material between the crystals. The end-cap crystals are organized in four so-called 'Dee's', each consisting of about 5000 crystals, again tilt by three degrees away from the central interaction point.

The length of the crystals corresponds to about 26 interaction lengths, such that an electron of 35 GeV deposits 97% of its energy in a cluster of  $5 \times 5$  crystals. The energy resolution of the ECAL is designed to be well below 1% for electron/photon energies above  $\sim 30$  GeV, which is e.g. needed for the discovery of a light Higgs boson in the  $H \rightarrow \gamma\gamma$  channel.

The resolution of the ECAL can be parametrized as (see e.g. [64])

$$\frac{\sigma_E}{E} = \frac{a}{\sqrt{E}} \oplus \frac{b}{E} \oplus c. \quad (5.5)$$

where  $a$  is the stochastic term,  $b$  the noise and  $c$  the constant term. The stochastic term arises mainly from fluctuations in the shower containment and photo-statistics. The noise term  $b$  reflects the electronic and the pile-up noise. The design goal for these parameters is  $a = 2.7\%$ ,  $b < 200$  MeV and  $c = 0.5\%$ , leading to the demanded over-all resolution of less than 1%. Testbeam data taken in 2004 showed that the ECAL sub-detector is able to reach this design resolution.

### 5.2.3 The Hadronic Calorimeter (HCAL)

The last detector sub-system inside the super-conducting magnet is the hadronic calorimeter (HCAL). Its purpose is the measurement of the energy of hadrons and ultimately particle jets as well as the hermetic coverage of the detector in order to be able to measure the missing transverse energy.

The active parts of the HCAL are plastic scintillator tiles, which alternate with brass tiles. The purpose of the brass tiles is the absorption of the energy of the incoming particles, while the scintillators collect the energy as blue scintillation light. This light is wavelength shifted into blue light, which is collected by an optical fiber readout system and transported to the photo-diodes transforming the light into an electronic signal.

In the barrel the HCAL is cylinder with a length of 9 m and a diameter of 2 m – 3 m, covering a pseudo-rapidity range of  $|\eta| < 1.48$ . The end-caps, covering a range of  $1.48 < |\eta| < 3.0$ , have a thickness of 1.8 m and a radius of about 3 m. To provide a maximum hermetic coverage, so called forward calorimeters are installed at the distance of 11 m on both sides of the interaction point, increasing the covered range up to  $|\eta| = 5$ .

The granularity of the detector is chosen such that highly boosted jets from the decays of W bosons can still be separated. This is achieved by a division into single readout channels (so called Calo-Towers) of size  $\Delta\eta \times \Delta\phi = 0.087 \times 0.087$ . Within such a region all the energy collected is summed up.

While in the high- $\eta$  regions the thickness of the HCAL corresponds to about 10 nuclear interaction lengths, which is sufficient to collect all of the hadronic energy accurately, in the central region ( $\eta \sim 0$ ) the thickness of about 80 cm corresponds only to about 5 nuclear interaction lengths. To remedy this shortcoming one additional scintillator layer is installed outside of the magnet, the so-called hadron outer calorimeter, which covers a range up to  $|\eta| = 1.4$ . Including this sub-detector, the thickness of the HCAL corresponds to at least 10 nuclear interaction lengths over the whole pseudo-rapidity region  $|\eta| < 5$ .

The expected intrinsic resolution of the HCAL for the reconstruction of jets with transverse energy of  $E_T^{\text{jet}} \sim 100 \text{ GeV}$  is about 14%, varying strongly with the energy from  $\sim 50\%$  for jets with transverse energy of  $E_T^{\text{jet}} \simeq 20 \text{ GeV}$  down to  $< 10\%$  for  $E_T^{\text{jet}} > 200 \text{ GeV}$  [65].

#### 5.2.4 The Muon System

The muon system (together with the iron flux-return yokes) is the outer-most detector sub-system of CMS. Its purpose is to identify and measure muons to a high precision, one of the main design goals of CMS. The muon system takes advantage of three different technologies, the Drift Tubes (DT) in the barrel ( $|\eta| < 1.2$ ), Cathode Strip Chambers (CSC) in the end-caps ( $0.9 < |\eta| < 2.4$ ) and Resistive Plate Chambers (RPC) in both, barrel and end-caps. A schematic longitudinal view of a quarter of the CMS muon system is shown in Fig. 5.7.

The size of a typical DT chamber in the barrel is  $(2 \times 2 \times 0.4) \text{ m}^3$ . The drift tubes consist of aluminum cathodes and stainless steel anode-wires. They are filled with an Argon-Carbon-Dioxide mixture (Ar – CO<sub>2</sub>). Each DT chamber contains twelve layers of drift tubes grouped into three super-layers, where the first and the third super-layer measure the coordinate of the passing muon in the transverse plane ( $\phi$ ) and the second super-layer determines the coordinate in the longitudinal direction ( $z$ ). With this an angular resolution of about 1 mrad is obtained in the transverse plane. The total barrel muon-system consists of  $\sim 250$  DT chambers with more than 20000 individual channels.

In the end-cap region CMS relies on the CSC technology, where the cathodes are divided into strips. The CSC are proportional drift chambers with gold-plated anode wires perpendicular to the cathode strips. The chambers are filled with an Ar – CO<sub>2</sub> – CF<sub>4</sub> gas mixture and are arranged in concentric rings around the beam pipe. The resolution varies with the distance to the interaction point, from  $\sim 75 \mu\text{m}$  (inner-most) to  $\sim 150 \mu\text{m}$  (outer-most). The CMS end-cap muon system is made of 540 CSCs.

In addition to the DTs and the CSCs the muon-system is equipped with RPCs. This very fast responding system is used by the trigger and allows thus a good understanding

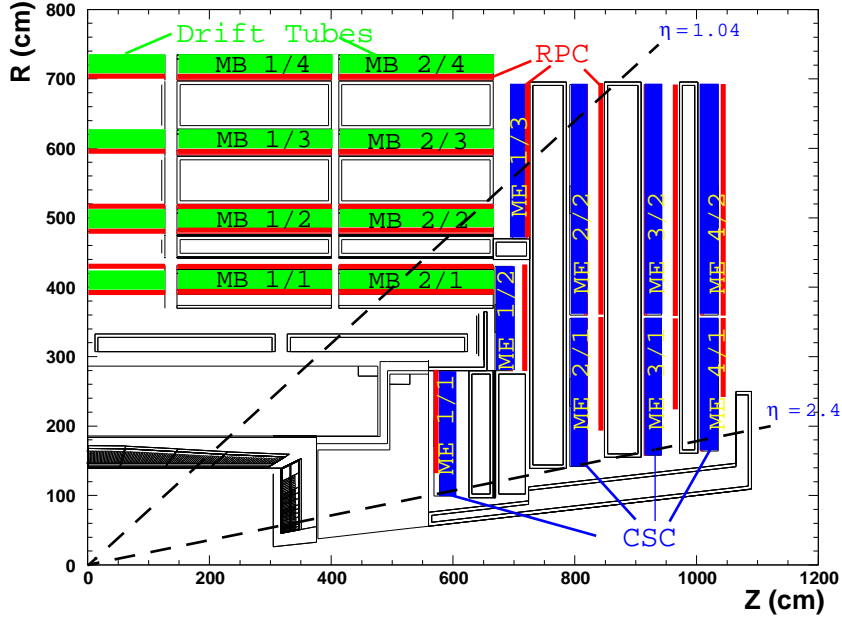


Figure 5.7: Schematic longitudinal view of the muon system of the CMS detector.

of the muon trigger efficiency. An RPC consists of two parallel phenolic resin plates separated by a gas gap and a conductive graphite layer forming the electrodes. In the inner barrel region each DT is accompanied by two layers of RPCs, in all other regions each muon-system layer contains one RPC layer.

The expected momentum resolution using the combined information of the muon system is  $\sim 1\%$  ( $\sim 2\%$ ) for muons with momenta  $p \sim 10$  GeV around  $|\eta| \simeq 0$  ( $|\eta| \simeq 2$ ). This resolution increases with increasing momentum of the muons up to  $\sim 4.5\%$  ( $\sim 7.0\%$ ) for muons with momenta  $p \sim 1000$  GeV [65].

### 5.2.5 The Trigger System

At LHC design luminosity about  $0.8 \times 10^9$  interaction-events per second are expected in the CMS experiment. Assuming a data size of  $\sim 1$  MB per event this would lead to a total of  $\sim 800$  TB of data per second to store. There is no information system that can handle this huge amount of data in such a short time. The main purpose of the trigger system is thus the reduction of the event data to a feasible rate of potentially interesting events. The maximum data rate is  $\sim 100$  MB per second, that can be coped with by the data acquisition system (DAQ).

The data reduction is achieved in two separate steps. The first, completely hardware

driven system is the so-called Level 1 trigger (L1). At this stage the most relevant quantities for the trigger-decision are computed roughly based on the fast information obtainable from the muon system and the calorimetry. The main quantities characterizing an event are computed, e.g. the transverse momentum and isolation of the four hardest objects (muons, electrons, photons, jets as well as missing transverse energy). Threshold cuts on these quantities allow to reduce the data rate to  $\sim 50 - 100$  kHz.

If the event data passed these L1 selections, the whole detector data is read out and processed by the Higher Level Trigger (HLT), containing the Level 2 and 3 (L2 & L3) trigger steps. Due to the rate reduction more information can be processed for this trigger selection. For example, at Level 2 part of the tracker information is included. The data reduction rate of L2 is  $\sim 10$ . At L3 the full tracker information is available and the full event can be reconstructed. The L3 reduction rate is  $\sim 100$ , resulting in a final event rate of  $\sim 100$  Hz.

# Chapter 6

## Physics Object Reconstruction

In this Chapter we describe the physics object reconstruction within the CMS analysis and software framework `CMSSW` [66]. The input of the reconstruction is the digitized detector response of each of the detector subsystems. The reconstruction is divided into the two steps of 'low level' and 'high level' object reconstruction<sup>1</sup>. We will not distinguish between these two steps, but directly enter the reconstruction of the 'high level' objects and explain some details for the underlying 'low level' object reconstruction where needed.

We want to emphasize that the physics object reconstruction is an ongoing development. All the details explained below are specific for the software release version `CMSSW_1_3` used in the last Chapter of this thesis. In other, especially more recent software releases some details such as thresholds and intrinsic cuts, but also reconstruction strategies might change significantly.

Also we will not discuss all the 'high level' objects reconstructed in the standard `CMSSW` reconstruction procedure. We will focus exclusively on the objects used in the physics analysis described in the next chapter of this thesis.

### 6.1 Track Finding

We start the discussion of the reconstruction with the 'low level' objects of the tracks. They will be needed for the reconstruction of the electrons and muons, which are 'higher level' objects, as well as for their isolation. The track reconstruction is divided into four steps, as shown in Fig. 6.1.

---

<sup>1</sup> 'Low level' objects are typically tracks and collected calorimetry information. 'High level' objects are for example muons and jets.

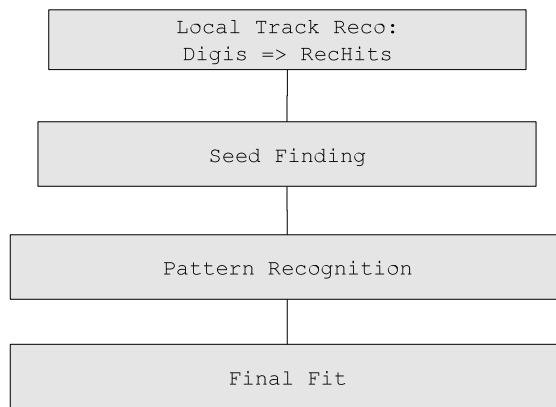


Figure 6.1: Track reconstruction flow within CMSSW.

The initial information is given by the digitized responses of the pixel and the tracking detectors described in section 5.2.1. In the first step, the local reconstruction, these digitized responses are converted into `RecHits`, i.e. into reconstructed hits in the tracker<sup>2</sup>. In the second step, the `RecHits` are used to find a seed for the reconstruction of the track. In the third step these seeds are used in a pattern recognition algorithm to find a track candidate, which, in the fourth step, are fitted to give the final track object. We will briefly describe each of these steps in the following, for more details see e.g. [67].

### 6.1.1 Local Reconstruction

The digitized output of the detector has to be translated into `RecHits` by clustering together strips (in the silicon-strip detector) or pixels (in the pixel detector). This is done by first finding a seed strip (pixel), which has to fulfill that the signal over noise ratio ( $S/N$ ) is larger than some threshold. Typical values for these thresholds are  $S/N > 3$  for the silicon and  $S/N > 6$  for the pixel detector. Then adjacent strips (pixels) are added to this seed forming a cluster when they themselves fulfill a threshold criterion (i.e.  $S/N > 2$  for strip and  $S/N > 5$  for the pixel detector). The positions of resulting clusters are then determined and they serve as the bases for the further reconstruction.

### 6.1.2 Seed Finding

The seeds for the track finding are basically pairs of `RecHits` from the local reconstruction. This is done by looking for compatible hits in different layers of the tracker. Here compatible means that they fulfill the beam-constraint, i.e. they point to the interaction point.

<sup>2</sup> In what follows the tracker means always both, the pixel and the silicon-strip detector.



Alternatively to the beam constraint a third hit can be used to define a seed. These seed hits then define the initial track trajectory for the further processing. The pixel detector is especially useful for the seed finding since it provides an excellent position measurement.

### 6.1.3 Pattern Recognition

The pattern recognition is based on a combinatorial Kalman filter method. The algorithm starts at a seed layer and includes the information of the successive detector layers. This is done by first deciding which layers are compatible with the seed trajectory, which is then extrapolated to this layer with the hypothesis of a charged particle in a magnetic field including information on the material the trajectory has to pass through, i.e. taking into account multiple scattering and possible energy loss. If a hit is found in the envisaged layer, it is added to the trajectory and track parameters are recalculated including this new information. There might be several hits compatible with the extrapolation. If this is the case all possibilities are pursued further, each building a single track candidate. The 'no-hit' possibility is also included, taking into account the fact that the particle might have left no hit in the layer. Therefore after each layer the track parameters are known to a better precision. This procedure is repeated until either the outermost layer of the tracker is reached or some 'stop condition' is satisfied.

From the above construction ambiguities can arise. The same track can e.g. be reconstructed starting from different seeds, or a given seed may lead to more than one track. These ambiguities have then to be resolved in order to avoid double counting of tracks. Which of the 'over-laying' tracks is chosen to be removed is basically decided on the number of hits and on the  $\chi^2$  of the fit.

### 6.1.4 Final Fit

Finally the tracks found in step three are re-fitted. This is again done using a Kalman filter. It is initialized at the layer of the innermost hit. Then the fit proceeds in an iterative way through the layers, estimating the track parameters again. After having reached the outer-most layer a second filter is used to run again from the outer-most layer inwards.

Using all the above procedure it has been shown that the track reconstruction efficiency is about 98% for muons with transverse momentum between 1 and 100 GeV in the region  $|\eta| < 2$  [67]. It has to be pointed out that these numbers (as well as all the efficiencies stated later in this chapter) were computed using an older CMS software framework (ORCA). However, the results do not change significantly (especially not get worse) for the CMSSW framework. We will refer to the tracks reconstructed according to this procedure as the `ctfWithMaterialTracks`.

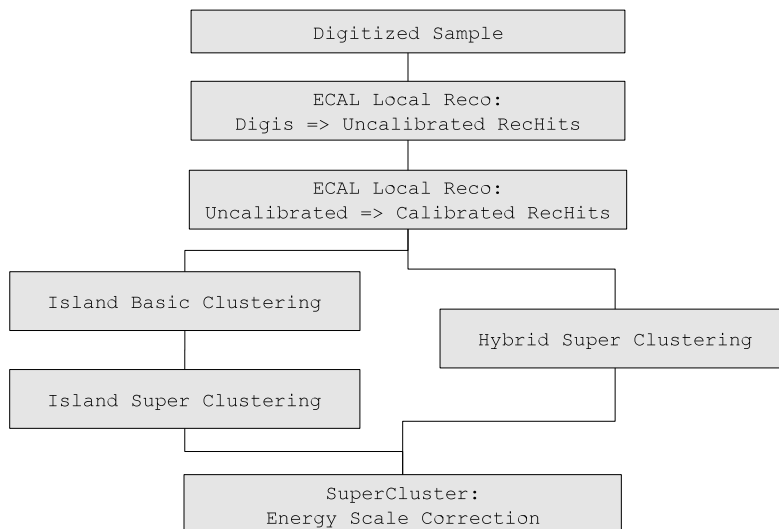


Figure 6.2: ECAL stand-alone reconstruction flow.

## 6.2 Electron Reconstruction

The electron reconstruction starts from the `SuperCluster`, which is the product of the ECAL stand-alone reconstruction. A single electron deposits approximately 94% (97%) of its energy in a  $3 \times 3$  ( $5 \times 5$ ) crystal cluster. Information from the pixel detector and the tracker is added to construct the final electron objects, the `PixelMatchGsfElectrons`.

### 6.2.1 ECAL Stand-Alone Reconstruction

The ECAL stand-alone reconstruction flow is shown in Fig. 6.2. The purpose of this so called *Super-Clustering* is the collection of the bremsstrahlung photons, which are emitted by an electron and spread in  $\phi$ , to improve the estimate for the initial electron energy.

The starting point is the digitized ECAL detector response, which in a first step is translated into so called `Uncalibrated RecHits`, basically corresponding to uncalibrated energy deposits for each ECAL crystal. After the application of calibration constants (`Calibrated RecHits`), the actual clustering of crystals is performed. There are two different clustering algorithms used; the `Island` algorithm in the end-caps of the ECAL, the `Hybrid` algorithm [68] in the barrel. The final step is the application of an energy dependent energy calibration factor, obtained either from test-beam or by using in-situ method such as Z decays [26].

It has been shown that using the procedure described below for the ECAL stand-alone

reconstruction, an efficiency of more than 99% for electrons with  $p_T \geq 7 \text{ GeV}$  can be reached [67].

### 6.2.1.1 Island Clustering

The starting point is a so called seed crystal defined as a crystal with a locally maximum energy deposit. Then the neighboring crystals around this seed-crystal are scanned and added to the cluster if they fulfill the following requirements:

- the crystal contains a `RecHit` with positive energy (well above the noise level);
- the crystal has not been assigned to another cluster and
- the crystal added previously (in the same direction) has a higher energy.

After all the `RecHits` with positive energy have been assigned to a `BasicCluster`, these `BasicClusters` are merged into so called `SuperClusters`. The procedure is very similar to the clustering of the `RecHits` into `BasicCluster`. The seed is a locally maximal energetic `BasicCluster`, and other nearby clusters are added to the `SuperCluster` following the recipe above.

### 6.2.1.2 Hybrid Super Clustering

This algorithm, only applicable in the barrel of the ECAL, takes into account the knowledge of the shower-shape of the energy-deposits in the ECAL. A charged particle bending in the magnetic field will deposit its energy spread over a small range in  $\eta$  but a larger range in  $\phi$  because of bremsstrahlung in the plane orthogonal to the magnetic field. The starting point is again a `RecHit` with a local maximum energy deposit. After this a bar of  $1 \times 5$  `RecHits` ( $1 \times 3$  if the energy of the  $1 \times 3$ -bar is smaller than  $1 \text{ GeV}$ ) is built around the seed `RecHit`. Then, around this basic bar, additional  $1 \times 5$  ( $1 \times 3$ ) bars are added to the `SuperCluster` in  $\phi$ -direction, until the energy deposited in the next bar is lower than some cut-off, e.g.  $0.1 \text{ GeV}$ . In contrast to the `Island` algorithm, the `Hybrid` algorithm directly generates `SuperClusters`.

## 6.2.2 Pixel Matching and Track Fitting

Since electrons (positrons) are charged particles they should, in addition to the energy deposit in the ECAL, leave a reconstructable track. The basics of finding these tracks follow roughly the procedure discussed in section 6.1. However, for the finding of an

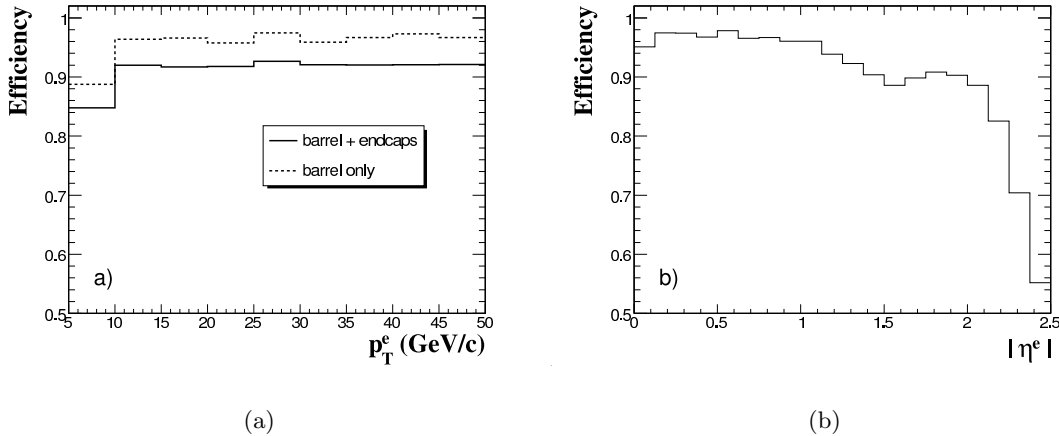


Figure 6.3: Electron reconstruction efficiency as function of (a) the electron transverse momentum  $p_T$  and (b) the electron pseudo-rapidity. The figures are taken from [67].

appropriate seed the calorimetry information is helpful. This is done by matching the `SuperCluster` with hits in the pixel detector. Looking for seed hits in the pixel detector is advantageous here, since the energy-weighted `SuperCluster` position corresponds to the impact point of an electron that would not have radiated off any energy before reaching the ECAL. Since most of the material budget lies after the pixel detector, most of the electrons have not radiated significantly before reaching the pixel detector.

For this matching hits in the pixel detector are predicted by extrapolating the electron trajectory on the basis of the information of the `SuperCluster` to the pixel layers. A first seed `Rechit` is then looked for in a relatively wide  $\Delta\phi$ ,  $\Delta z$  window around this prediction. If a compatible hit is found, its information is used to update the trajectory prediction of the electron track. This trajectory then drives the search for a second seed hit in analogy to the seed finding described in section 6.1. It has been shown that the pixel finding efficiency for electrons with  $p_T = 10 \text{ GeV}$  is about 90%, averaged over the full ECAL range [67]. The two pixel hits found then serve as seeds for the further track finding. However, for electrons the Kalman-filter described above is not adequate for the pattern recognition. Due to the highly non-Gaussian fluctuations because of bremsstrahlung off the electrons, a nonlinear filter, the Gaussian-sum-filter (GSF) [69] is used, which describes the propagation of the electrons in the magnetic field much better. The track found (if it exists) is called the `GSF-track`. Together with the `SuperCluster`, this forms the electron candidate referred to as the `PixelMatchGsfElectron`. If no compatible track is found, the object typically is a photon candidate.

We show the electron reconstruction efficiencies as a function of the electron transverse

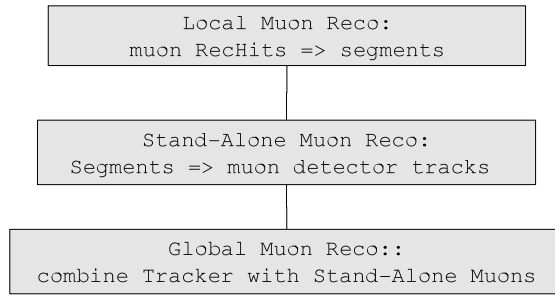


Figure 6.4: Muon reconstruction chain.

momentum  $p_T$  in Fig. 6.3(a) and as a function of the pseudo-rapidity  $\eta$  in Fig. 6.3(b). The reconstruction efficiency is above 90% everywhere, except for very low  $p_T$  ( $p_T < 10$ ), very high  $\eta$  ( $\eta > 2$ ) and the barrel-endcap transition region ( $\eta = 1.4$ ) [67]. Again these plots and numbers were computed using the ORCA framework. However, the general behavior holds for the used version of CMSSW as well.

## 6.3 Muon Reconstruction

The muon reconstruction is divided into three step, shown in Fig. 6.4. First the digitized detector response is combined into so called segments. In the second step (stand-alone muon reconstruction) these segments serve for the finding of muon trajectories in the muon system only (muon detector tracks). In the last step these tracks are combined with information from the tracker to give the final muon candidates.

### 6.3.1 Stand-Alone Muon Reconstruction

The starting point are the `RecHits` in the drift tubes (DT) in the barrel, the cathode strip chamber (CSC) in the end-caps and the resistive plate chambers (RPC) in both barrel and end-caps. The hits from the DT and the CSC are combined into so called segments. This is done in a similar manner as the pattern recognition in the tracker. Hits in the inner-most muon chambers serve as seed for the extrapolation of the trajectory into the outer layers using again Kalman-filter techniques. The precise strategy varies, depending on if a hit is found in a DT or a CSC. In the propagation of the trajectory from layer to layer potential energy loss in the material, effects of multiple scattering and a non-uniform magnetic field are taken into account. Similar to the track finding, the track parameters are updated after each step. The procedure ends when the outer-most layer of the muon system is reached. Then a back-fitting (from outer-most to inner-most) is done and finally

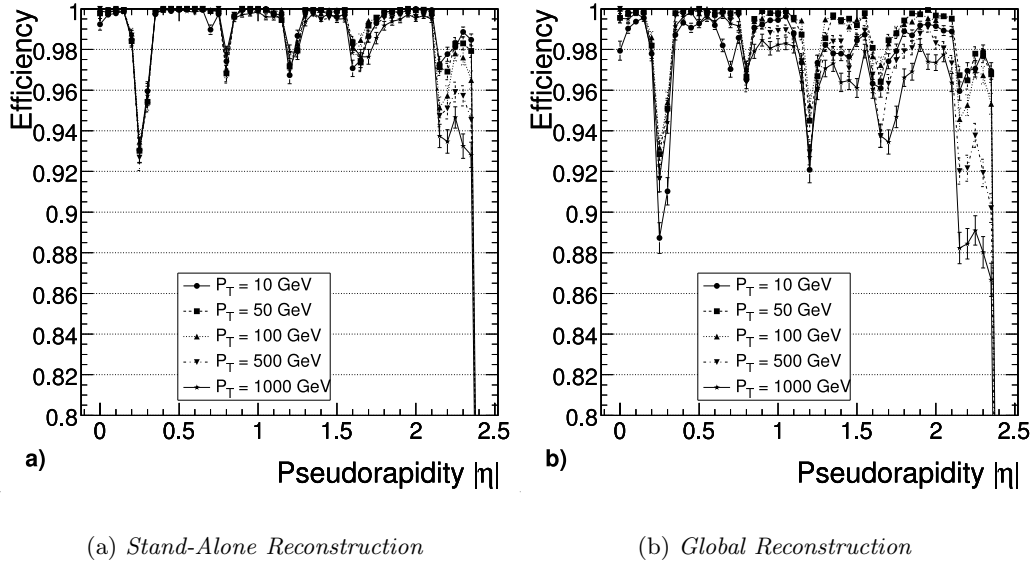


Figure 6.5: Muon reconstruction efficiency as a function of the pseudo-rapidity  $\eta$ , in (a) using the stand-alone and in (b) the global muon reconstruction. The Figures are taken from [67].

the trajectory of the muon candidate can be extrapolated to the interaction point. The tracks found in this procedure are the `StandAloneMuons`.

The stand-alone muon reconstruction efficiency as a function of the pseudo-rapidity for different muon momenta is shown in Fig. 6.5(a). With the exception of the detector transition regions the efficiency is  $\sim 99\%$  [67].

### 6.3.2 Global Muon Reconstruction

In the last step of the muon reconstruction the information from the tracker is used. Similar to the case of electrons the stand-alone muons can be used to find seeds for the pattern recognition in the tracker. Here the two hits forming the seed have to come from two different layers. To find the initial tracker trajectory parameters, an additional beam-spot constraint is applied. Then the procedure for finding the tracks follows the steps described in section 6.1, where again a Kalman-filter is used. Finally several refitting procedures are applied in order to have an accurate momentum reconstruction for the muons. The collection of resulting muon candidates is referred to as the `GlobalMuons`-collection.

The global muon reconstruction efficiency is shown in Fig. 6.5(b). The efficiency is  $\sim 95-99\%$  over the whole pseudo-rapidity range, again with the exception of the detector

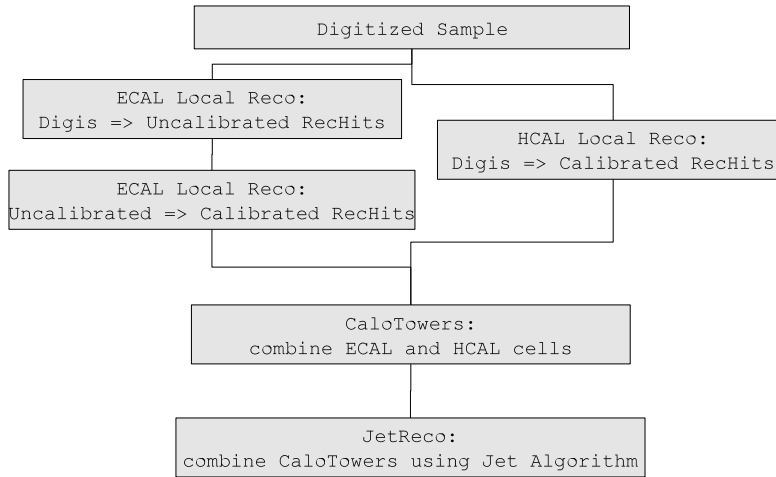


Figure 6.6: Jet reconstruction flow within CMSSW.

transition regions.

## 6.4 Jet Reconstruction

The reconstruction flow for jets with CMSSW is shown in Fig. 6.6. The starting point are the digitized hadronic (HCAL) and electromagnetic (ECAL) calorimeter responses. From these the ECAL `RecHits` and the HCAL `RecHits` are constructed independently, corresponding to the energy deposits in a single crystal (ECAL `RecHits`) or an HCAL cell (HCAL `RecHits`). In the next steps these `RecHits` are combined into so called `CaloTowers`, which correspond to the combination of the hadronic and the electromagnetic energy deposited in a calorimetry region defined by the HCAL granularity.

The `CaloTowers` are reconstructed as follows. For all the HCAL `RecHits` the sum of the ECAL `RecHit` energies is computed by summing up the energies in all the crystals corresponding to the calorimeter region defined by the HCAL `RecHit`-cell. The hadronic (electromagnetic) energy of this `CaloTower` is then set to the corresponding HCAL `RecHit`-energy (sum of the ECAL `RecHit`-energies) if they are above a certain threshold. The energy thresholds used for the reconstruction of the `CaloTowers` are summarized in Table 6.1. There HB, HE and HO denote cells in the hadronic-barrel, the hadronic-endcap and the hadronic outer-barrel calorimeter; EB and EE stand for the electromagnetic barrel and endcap calorimeter respectively. The total energy of the `CaloTower` is the sum of the hadronic and the electromagnetic energy in that cell.

After having found all the `CaloTowers` in the event, they can be combined into jets using any jet-algorithm. For the purpose of the clustering the `CaloTowers` are treated as

Energy thresholds [GeV]				
HB	HO	HE	$\Sigma$ EB	$\Sigma$ EE
0.9	1.1	1.4	0.2	0.45

Table 6.1: Energy thresholds used for the reconstruction of the `CaloTowers`.  $\Sigma$  denotes the sum over 25 crystals, corresponding to one HCAL tower.

massless particles with energies defined by the `CaloTower`-energies and directions defined by the positions of the center of the `CaloTowers` and the interaction point. In this thesis the preferred jet-algorithm is the  $k_T$ -jet-algorithm [50] in the  $E$ -scheme. For the following analysis we use the algorithm parameter  $R = 0.6$ . We refer to the jets found with this algorithm as the `caloJets_Fastjet6`-collection.



## Chapter 7

# Higgs Search in the WW Channel with the CMS Experiment

In chapter 4 the effects of higher order QCD corrections up to NNLO for the  $H \rightarrow WW$  signal after selection cuts at the LHC have been studied at parton level. It was found that the fixed (N)LO calculations do not result in a reliable prediction, since the effects of multiple soft and collinear radiation are important in the phase-space region selected by the cuts (cf. Table 4.5, section 4.3.2). At fixed NNLO these additional radiation effects appear to be negligible and the uncertainty from varying the renormalization and factorization scales  $\mu_R$  and  $\mu_F$  is reduced. Moreover, the cross-sections obtained with parton-shower MC models (MC@NLO and HERWIG), inclusively re-weighted to NNLO, agree very well with this fixed-order prediction.

However, the cross-sections listed in Table 4.5 will not be measured directly in the real experiment. Selection cuts and detector effects, such as cracks in the calorimeters etc., will reduce the measured event rate. In this chapter we investigate these effects, and show how they can be factorized from the hard scattering process such that the partonic cross-sections from chapter 4 can be propagated into a prediction for the experimentally measured event rate. This expected rate can then be used for the computation of the signal significance or exclusion limits at the LHC.

To do this, the study is divided as follows: First event samples for the various background and the signal processes are generated using MC event generators. Then these events are passed through the CMS detector simulation. From the simulated detector response the final state particles are reconstructed using the procedures discussed in chapter 6. After this a set of *experimental selection cuts* will be defined, transporting the *partonic signal cuts* from section 4.1 into an experimental environment. We then study the effect of

these selection cuts on the signal cross-section and compare the results with the partonic predictions from section 4, including systematic, statistical and theoretical uncertainties.

In addition, the cross-sections for the most important background processes after the selection cuts will be estimated. Finally these numbers are used to compute the signal significance and the exclusion-power of the CMS experiment for a Higgs mass hypothesis of  $m_H = 165$  GeV.

## 7.1 Analysis Strategy

The strategy for finding or excluding the Higgs boson in the WW channel pursued here relies on counting the total number of events that pass the selection cuts. Even though there are differences in some kinematic distributions between the signal and the background (e.g. transverse momenta of the leptons, angle between the leptons etc), at low luminosities it is hardly possible to resolve this differences due to the lack of statistics. However, for higher integrated luminosities the usage of this information can lead to an improvement in the expected signal significances and exclusion limits. It has been shown in [70] that especially for the determination of the Higgs boson mass, if an excess is observed, such variables can be useful. We do not pursue this approach here, but point out that all our conclusions can principally be adapted to such an analysis.

For the estimation of the expected discovery power of the CMS experiment the *expected signal significance*  $\langle \text{sig} \rangle$  will be calculated. The expected significance defines the probability that the background only would give equal or more events than are expected to be observed if the signal is present. The probabilities are calculated including all systematic and theoretical uncertainties (which will be discussed in detail below) following the recipe in [72].

The exclusion limit will be computed using the *Modified Frequentist Approach*. The signal confidence level is defined as

$$CL_S = \frac{CL_{S+B}}{CL_B}, \quad (7.1)$$

where  $CL_{S+B}$  ( $CL_B$ ) is the confidence level for the *signal+background* (*background only*) hypothesis. Again we follow the detailed description of the statistical method in [72].

## 7.2 Event Sample Production and Cross-Sections

All the samples used are produced within the CMS software framework CMSSW [66] release version CMSSW\_1.3. The background processes included in the study, together

process	$\sigma_{\text{NLO}}$ [pb]	generator
qq $\rightarrow$ WW	114.3	PYTHIA/MC@NLO
t $\bar{t}$	840	TopRex [73]
Z/ $\gamma^*$ $\rightarrow$ $\ell\ell$	5600	PYTHIA
ZZ	15.3	PYTHIA
WZ	49.9	PYTHIA
gg $\rightarrow$ WW $\rightarrow$ $l\nu l\nu$	0.48	—
Wtb $\rightarrow$ WW $b\bar{b} \rightarrow$ $l\nu l\nu$	3.4	—
gg $\rightarrow$ H $\rightarrow$ WW $\rightarrow$ $l\nu l\nu$ $m_{\text{H}} = 165$ GeV	2.44, $\mu = m_{\text{H}}/2$ 1.80, $\mu = 2m_{\text{H}}$	PYTHIA/MC@NLO

Table 7.1: Processes used in the H $\rightarrow$ WW study, together with their NLO cross-sections and the MC event generator used to produce the samples.

with their cross-sections, are listed in the first part of Table 7.1. Where no decay is specified the cross-section corresponds to the inclusive process;  $\ell$  denotes the sum over all combinations of e,  $\mu$  and  $\tau$ . The processes gg  $\rightarrow$  WW and Wtb could not be simulated for this study. Their contribution to the background after the selection cuts will be estimated using the results of [26].

All the samples are produced using the LO event generators PYTHIA [11] and TopRex[73] and are inclusively re-weighted to the NLO cross-sections <sup>1</sup>. An exception to this is the WW sample, which is re-weighted differentially in the  $p_{\text{T}}$  of the WW-pair to the MC@NLO prediction.

The last lines in the table show the signal cross-sections for a Higgs mass hypothesis of  $m_{\text{H}}=165$  GeV for the two scale choices  $\mu = m_{\text{H}}/2$  and  $\mu = 2m_{\text{H}}$ . Similarly to the WW process, the signal events are re-weighted differentially in the transverse momentum of the Higgs ( $p_{\text{T}}^{\text{H}}$ ) to the MC@NLO spectrum. For the inclusive cross-section we use here the fixed NLO prediction, i.e. in the remainder of this thesis, all signal cross-sections labeled (N)NLO denote the MC@NLO numbers inclusively re-weighted to the fixed (N)NLO cross-section.

### 7.3 Object Identification and Selection Cuts

Before the selection cuts can be applied the final state objects have to be defined from the detector response. This procedure leads to some small modifications of the selection cuts as well, since e.g. the missing transverse energy cannot be computed directly from the

<sup>1</sup> The re-weighting techniques have been discussed in detail in section 2.3.

neutrino momenta. We will therefore define a set of *experimental signal cuts* that translate the *partonic signal cuts* from section 4 into an experimental environment.

For convenience the *partonic signal cuts* from chapter 4 are listed here:

### Partonic Signal Cuts

1. Both charged leptons should have a transverse momentum  $p_T^\ell > 25 \text{ GeV}$  and be in the central detector region  $|\eta| < 2.0$ ;
2. these leptons must be isolated from hadrons; the hadronic energy within a cone of  $R = 0.4$  around each lepton must not exceed 10% of the corresponding lepton transverse momentum;
3. the di-lepton mass should be in the range  $12 \text{ GeV} < m_{\ell\ell} < 40 \text{ GeV}$ ; the lower cut reduces contaminations from b-resonances;
4. the missing transverse energy  $E_T^{\text{miss}}$  in the event should exceed 50 GeV;
5. the opening angle  $\phi_{\ell\ell}$  between the two leptons in the plane transverse to the beam-pipe should be smaller than  $45^\circ$ ;
6. there should be no jet with transverse momentum larger than 25 GeV in the central detector region  $|\eta^{\text{jet}}| < 2.5$  and
7. the harder lepton is required to have a transverse momentum in the range  $30 \text{ GeV} < p_T^{\ell, \text{max}} < 55 \text{ GeV}$ .

The first step is the selection and identification of all important final state objects. This selection will reduce the number of events with two identified leptons compared to the partonic study, where naturally all leptons 'pass' the selection criteria. The objects to identify are

- the charged, isolated leptons (electrons and muons),
- the jets and
- the missing transverse energy.

#### 7.3.1 Electron Identification

The starting point of the electron identification is the `PixelMatchGsfElectron` collection described in section 6.2. The analysis is very sensitive to lepton misidentification since

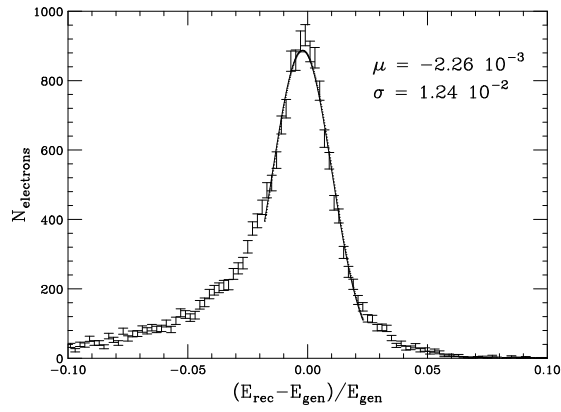


Figure 7.1: Energy resolution for reconstructed and identified, isolated electrons coming from a Higgs with mass  $m_H=165$  GeV.

such misidentification increases the background and uncertainty of the expected event rate dramatically. Therefore we have to make sure that the misidentification rate is as small as possible, while keeping the reconstruction efficiency high. To achieve this the following criteria are imposed on the electron candidates [74]:

- The energy deposition in the hadronic calorimeter ( $H$ ) should be small compared to the energy deposited in the electromagnetic calorimeter ( $E$ ), i.e.  $H/E < 0.05$ .
- The GSF-track and the associated SuperCluster have to match within
  1.  $|\eta^{\text{track}} - \eta^{\text{SC}}| < 0.005$ ,
  2.  $|\phi^{\text{track}} - \phi^{\text{SC}}| < 0.02$  and
  3.  $E^{\text{SC}}/p^{\text{track}} > 0.8$ ,

where  $\eta$  is the pseudo-rapidity,  $\phi$  the angle in the transverse plane,  $E$  the energy and  $p$  the total spatial momentum of the **track** or the **SuperCluster** (SC), respectively.

One of the most powerful cuts against the contamination of background events is the isolation. The isolation for the electrons is defined as:

- The sum of the transverse energies of all tracks within a cone of  $R = 0.2$  around the electron track divided by the SuperCluster transverse energy  $E_T^{\text{SC}}$  has to be smaller than 0.05. The sum runs over all `ctfWithMaterialTracks` that satisfy
  1.  $p_T^{\text{track}} > 0.9$  GeV and
  2.  $|z^{\text{track}} - z^{\text{electron}}| < 0.2$  cm, where  $z$  is the longitudinal position of the track extrapolated to the beam-pipe.

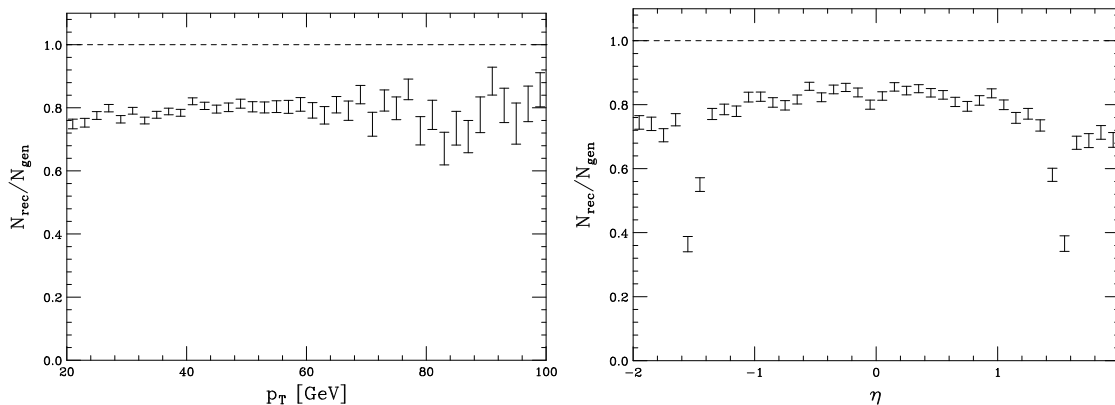


Figure 7.2: Electron reconstruction/identification efficiency as a function of the electron transverse momentum  $p_T$  and the pseudo-rapidity  $\eta$ .

To avoid counting the track of the electron-candidate in this sum, the transverse momentum of the electron `GSF-track` is subtracted.

We label these criteria as the *isolated electron identification*, and they will (partly) replace points 1 and 2 of the *partonic signal cuts* in the case of electrons.

It is important to understand how well the detector is able to measure the energies of the electrons of interest, namely the ones satisfying  $p_T^\ell > 20$  GeV and  $|\eta| < 2.0$ . The relevant observable is the *energy resolution*  $\rho_E$ , defined as

$$\rho_E = \frac{E_{\text{rec}} - E_{\text{gen}}}{E_{\text{gen}}}, \quad (7.2)$$

where  $E_{\text{rec}}$  is the reconstructed and  $E_{\text{gen}}$  the generated energy of the electron. The corresponding distribution for electrons coming from the decay of a Higgs with  $m_H=165$  GeV is shown in Fig. 7.1. The distribution is not symmetric around the maximum, indicating a slightly larger fraction of underestimated electron-energies compared to overestimated ones. This tail originates from the fact that electrons tend to radiate photons, that are not entirely collected in the `SuperCluster`, carrying away a fraction of the initial electron momentum. The peak region can be fitted with a Gaussian function to obtain the mean  $\mu = -2.26 \times 10^{-3}$  and the standard deviation  $\sigma = 1.24 \times 10^{-2}$ . It can be concluded that the energy of the electrons passing the *isolated electron identification* are measured with an accuracy of  $\sim 1.2\%$ .

The second and more severe difference with respect to the partonic study is the reconstruction efficiency of the electrons, defined as

$$\varepsilon_{\text{rec}} = \frac{N_{\text{rec}}}{N_{\text{gen}}}, \quad (7.3)$$

where  $N_{\text{rec}}$  denotes the number of electrons reconstructed and identified and  $N_{\text{gen}}$  is the number of generated electrons at parton level. Again the electrons of interest are the ones satisfying  $p_{\text{T}} > 20 \text{ GeV}$  and  $|\eta| < 2.0$ . As the selection efficiency is constant in the selected phase-space region to a good approximation, it will factorize from the hard scattering process and all the other selection cuts.

The reconstruction efficiencies for the electrons from the decay of a Higgs with a mass of  $m_{\text{H}}=165 \text{ GeV}$  as functions of the electron transverse momentum  $p_{\text{T}}$  and the electron pseudo-rapidity  $\eta$  are shown in Fig. 7.2. With the exception of the barrel-endcap transition region around  $|\eta| = 1.4$ , the efficiency is  $\sim 78 \%$  and does not vary as a function of  $p_{\text{T}}$  and  $\eta$ .

To compute these efficiencies the PYTHIA sample for the signal was used, which consists of  $\sim 50000$  events in total. For completeness we quote the overall electron reconstruction efficiency as

$$\varepsilon_{\text{rec}} = \frac{19808}{25395} \simeq 0.78, \quad (7.4)$$

i.e. 78% of all the electrons within  $p_{\text{T}} > 20 \text{ GeV}$  and  $|\eta| < 2.0$  generated in the signal sample are reconstructed and identified by the above criteria.

### 7.3.2 Muon Identification

The starting point for the muon identification is the `globalMuons` collection (cf. section 6.3). Since muons are essentially the only particles leaving hits in the muon chambers of the detector, the misidentification of other particles as muons is expected to be very small. The only additional selection criterion is therefore the isolation. The isolation of muons is defined as:

- The sum of the transverse momenta of all `ctfWithMaterialTracks` within a cone of radius  $R = 0.3$  around the muon track has to be smaller than  $2 \text{ GeV}$ . The sum runs over all tracks that satisfy
  1.  $p_{\text{T}}^{\text{track}} > 0.9 \text{ GeV}$ ,
  2.  $|z^{\text{track}} - z^{\text{muon}}| < 0.2 \text{ cm}$  and
  3. number of hits in the tracker,  $\#_{\text{hits}} > 5$ .

In order to make sure that the transverse momentum of the muon-track is excluded, tracks within a radius of  $R = 0.01$  around the muon-track are not included in this sum.

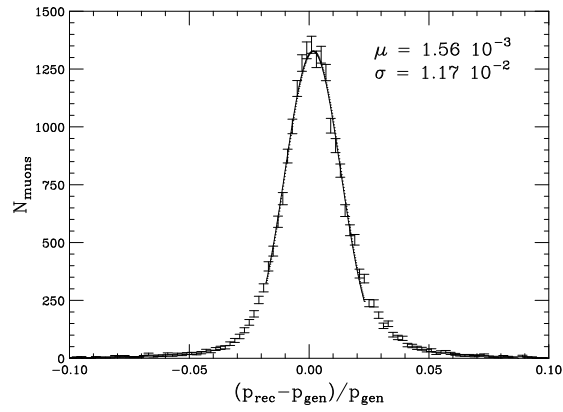


Figure 7.3: Momentum resolution for reconstructed and identified, isolated muons coming from a Higgs with mass  $m_H=165$  GeV.

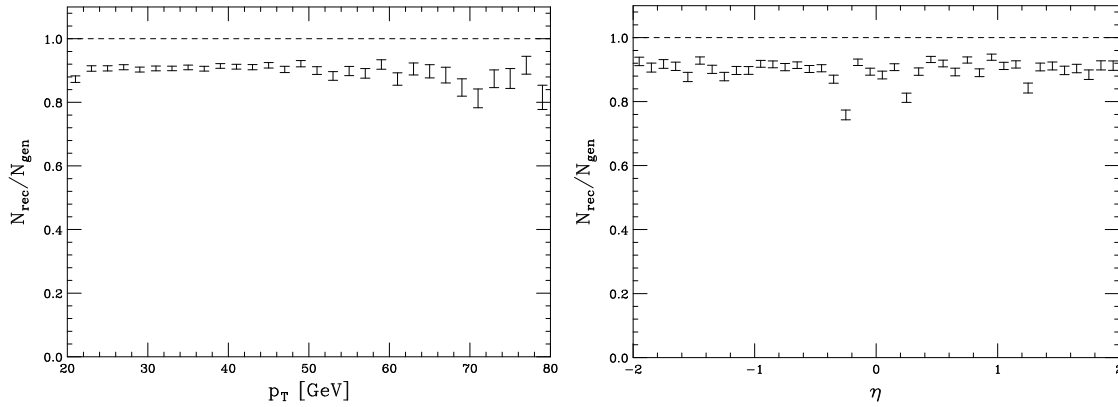


Figure 7.4: Muon reconstruction efficiency as a function of the muon transverse momentum  $p_T$  and pseudo-rapidity  $\eta$  for the  $m_H=165$  GeV signal sample.

These criteria, together with the *isolated electron identification* from section 7.3.1, are referred to as the *isolated lepton identification* in the upcoming sections.

The momentum resolution for the muons is computed as

$$\rho_p = \frac{p_{\text{rec}} - p_{\text{gen}}}{p_{\text{gen}}}, \quad (7.5)$$

for muons satisfying  $p_T > 20$  GeV and  $|\eta| < 2.0$ . The corresponding distribution is shown in Fig. 7.3. The Gaussian fit yields a mean of  $\mu = 1.56 \times 10^{-3}$  and a standard deviation of  $\sigma = 1.17 \times 10^{-2}$ , indicating that the momenta of the selected muons are measured with an error of  $\sim 1.2\%$ .

The reconstruction efficiencies as functions of the muon transverse momentum and pseudo-rapidity are shown in Fig. 7.4. Again the efficiencies are approximately constant



and the over-all reconstruction efficiency is

$$\varepsilon_{\text{rec}} = \frac{21884}{24277} \simeq 0.90. \quad (7.6)$$

### 7.3.3 Leptonic Selection Variables

The selection criteria for the *experimental signal cuts* replacing points 1 and 2 as well as the purely leptonic selection criteria 3, 5 and 7 of the *partonic signal cuts* can now be defined as:

#### Experimental Signal Cuts

1. Events are accepted if there are at least two leptons satisfying the *isolated lepton identification* criteria with  $p_{\text{T}} > 25 \text{ GeV}$  and  $|\eta| < 2.0$ ;
2. the di-lepton mass should be in the range  $12 \text{ GeV} < m_{\ell\ell} < 40 \text{ GeV}$ ;
3. the opening angle  $\phi_{\ell\ell}$  between the two leptons in the plane transverse to the beam-pipe should be smaller than  $45^\circ$  and
4. the harder <sup>2</sup> lepton is required to have a transverse momentum in the range  $30 \text{ GeV} < p_{\text{T}}^{\ell, \text{max}} < 55 \text{ GeV}$ .

The energy/momentum has been shown to be measured accurately for the leptons in the selected phase-space region (defined by cut 1 in the list above) and the reconstruction efficiencies for these leptons are constant to a good approximation. These efficiencies should thus factorize from the hard scattering process and the other leptonic selection cuts (cuts 2, 3 and 4 in the list). This factorization can be tested by a comparison with the partonic predictions from chapter 4. To do this the partonic distributions obtained with MC@NLO are first multiplied by 9, which corresponds to including all possible final-state lepton combinations of e,  $\mu$  and  $\tau$  <sup>3</sup>, and then by the event selection efficiency obtained using the fully simulated signal sample. This efficiency is shown in Table 7.2. The total scaling factor  $f_{\text{scale}}$  is then

$$f_{\text{scale}} = 9 \times \varepsilon_{\text{lep}} = 9 \times 0.183 = 1.647. \quad (7.7)$$

We have to specify in some more detail the treatment of the final states including  $\tau$  leptons in this approach. The  $\tau$  leptons are not directly observed in the experiment. To a significant fraction, they decay leptonically, resulting in a similar final state signature as

---

<sup>2</sup> By the 'harder' lepton we refer to the one with larger transverse momentum  $p_{\text{T}}$ .

<sup>3</sup> All the results in chapter 4 were computed for one such lepton combination.

$m_H = 165 \text{ GeV}$	$N_{\text{events}}$	$\sigma_{\text{NLO}} \text{ [fb]}, \mu = m_H/2$
total	89844	2440
accepted	16481	447
$\varepsilon_{\text{lep}}$	0.183	

Table 7.2: Number of events passing the *isolated lepton identification* criteria and corresponding NLO cross-sections.

the other leptonic W decay modes. The kinematic distributions of the muons and electrons from these  $\tau$  decays can not be expected to be identical to the distributions for the prompt<sup>4</sup> electrons and muons; in fact they are much softer since a significant fraction of the momentum is carried away by the additional neutrino. In the partonic study of chapter 4 the decay of  $\tau$  leptons in final states was not discussed at all. However, in the simulated MC sample these decay modes are included. The efficiency in Table 7.2 has therefore to be understood as the combination of the *isolated lepton identification* efficiencies and the branching ratio of the  $\tau$  leptons into electrons and muons. The fraction of events containing at least one electron or muon from a  $\tau$  decay is  $f_\tau \simeq 28\%$ , using a branching ratio for a  $\tau$  decaying into an electron or a muon of  $BR(\tau \rightarrow e, \mu) \simeq 0.35$  [3]. These decay modes thus contribute significantly to the total event rate and cannot be neglected. By applying the scaling factor from eq. 7.7 it is assumed that the effects of the contribution of the final states including  $\tau$  leptons factorize. We do not explicitly prove this approach here, but keep in mind that it might lead to disagreements between the partonic predictions from chapter 4 and the full simulation of the signal sample.

The cumulative distributions for the purely leptonic variables (invariant mass  $m_{\ell\ell}$ , the angle  $\phi_{\ell\ell}$  and the transverse momentum of the harder lepton  $p_T^{\ell, \text{max}}$ ) from the scaled partonic study (MC@NLO) and the full simulation (CMSSW) can now be compared<sup>5</sup>. The distributions for the scale choice  $\mu = m_H/2$  are shown in the left part of Fig. 7.5. On the right side the ratios of the cumulative cross-sections obtained with the detector study (CMSSW) and the partonic study (MC@NLO) are shown. The agreement between the distributions for all three variables is good. The only significant difference can be seen for very small opening angles  $\phi_{\ell\ell}$ . The origin of the difference might be related to the isolation requirement or the fact, that the differential re-weighting of the PYTHIA sample to the Higgs transverse momentum distribution fails to describe the  $\phi_{\ell\ell}$  spectrum reliably in the very small opening angle region (cf. Fig. 4.5 in section 4.2.1). Since the envisaged cut is at  $45^\circ$ , where the distributions agree, this effect can be neglected.

This agreement for the distributions indicates that the adopted factorization-approach

<sup>4</sup> We define the prompt electrons and muons as the ones coming from the decay of a W boson of the Higgs decay.

<sup>5</sup> See section 2.2.1.2 for the definition of the cumulative cross-section.

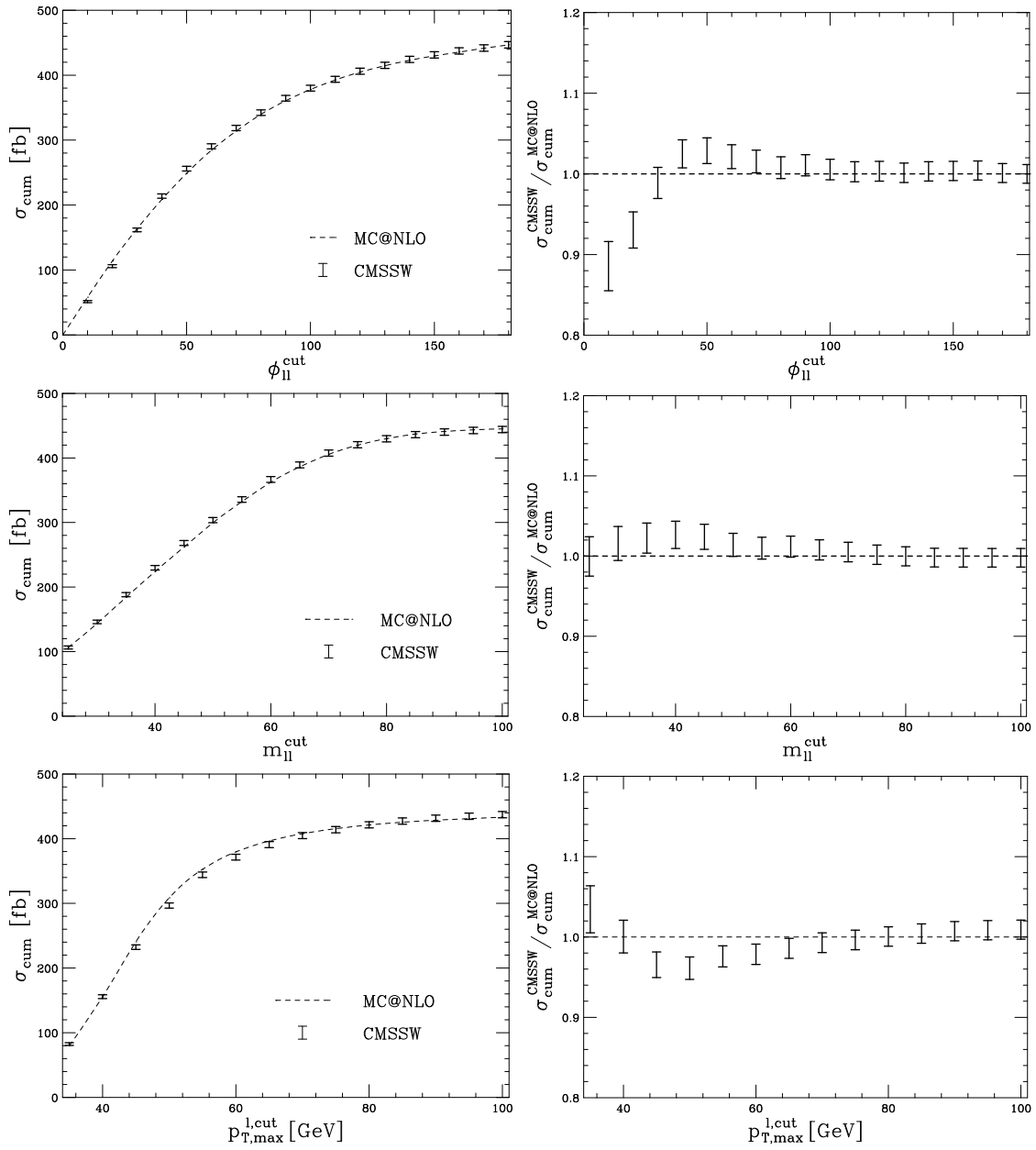


Figure 7.5: Cumulative cross-sections for the leptonic selection variables  $\phi_{\ell\ell}$ ,  $m_{\ell\ell}$  and  $p_{T,\text{max}}^{l,\text{cut}}$  compared for the study including detector effects (CMSSW) and the partonic predictions (MC@NLO).

is valid to a sufficient amount of precision.

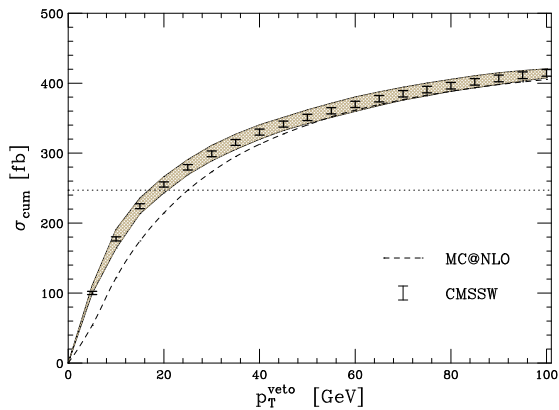


Figure 7.6: Cumulative cross-section as a function of  $p_T^{\text{veto}}$ . The band corresponds to a variation of the JES in the range 0.9 – 1.1.

### 7.3.4 Jet Identification and Jet Veto

Having discussed in detail the leptonic selection criteria we now turn to the identification of jets and the corresponding selection cut, the jet-veto. The measurement of the energy of a jet is experimentally very difficult. It is expected that the raw energy of the jets reconstructed within the CMSSW framework underestimate the true jet-energy by a factor of about 1.5 in the low  $p_T^{\text{jet}}$  region. This factor, known as the jet energy scale (JES), is energy- and detector-region-dependent and has to be determined experimentally. To avoid the problem of the determination of the JES the raw transverse energy of the jet without any further corrections can be considered. However, the uncertainty in the JES will contribute to the final systematic uncertainties.

The starting point for the jet identification is the uncorrected `caloJetsFastjet6` collection, that contains all jets clustered using a  $k_T$  algorithm with cone-size  $R = 0.6$ <sup>6</sup>. The only additional requirement is a cut on the so-called  $\alpha$ -parameter defined as

$$\alpha^{\text{jet}} = \frac{\sum p_T^{\text{track}}}{E_T^{\text{jet}}}, \quad (7.8)$$

where the sum runs over all `ctfWithMaterialTracks` satisfying

1. the track is within the jet, i.e.  $\Delta R(\text{track} - \text{jet}) < 0.6$ ;
2. the transverse momentum  $p_T^{\text{track}} > 2 \text{ GeV}$  and
3. the number of hits in the tracker is  $\#_{\text{hist}} > 5$ .

<sup>6</sup> The default choice of the cone-size in chapter 4 was  $R = 0.4$ .

For a real jet  $\alpha^{\text{jet}}$  should be close to 0.66, since on average 2/3 of the particles in a jet are electrically charged. To reduce the fraction of fake jets, e.g. jets from the underlying event, we impose a lower cut of 0.2 on this parameter for jets with transverse energy  $E_{\text{T}}^{\text{jet}} < 20 \text{ GeV}$ . Then the identified jets consist of all `caloJets_Fastjet6-jets` satisfying

- $p_{\text{T}}^{\text{jet}} > 20 \text{ GeV}$  and  $|\eta^{\text{jet}}| < 2.5$  or
- $p_{\text{T}}^{\text{jet}} < 20 \text{ GeV}$ ,  $|\eta^{\text{jet}}| < 2.5$  and  $\alpha^{\text{jet}} > 0.2$ .

The cumulative distribution as a function of the jet-veto value  $p_{\text{T}}^{\text{veto}}$  should be compared to the partonic distribution obtained with MC@NLO, similarly to the leptonic cut variables in section 7.3.3. However, a similarly good agreement can not be expected for this variable. The comparison is shown in Fig. 7.6. To simulate a miss-estimation of the JES by  $\pm 10\%$  it is varied between 0.9 and 1.1, i.e. the reconstructed raw jet transverse energy is multiplied by a factor of 0.9 and 1.1, respectively. The variation of the cumulative cross-section under this variation of the JES is shown as the band in Fig. 7.6.

It can be seen how a certain  $p_{\text{T}}^{\text{veto}}$  in the partonic case corresponds to a veto at a lower value of  $p_{\text{T}}^{\text{veto}}$  in the case of the full detector simulation. To keep the jet-veto efficiency close to the partonic study we apply a veto on the raw jet energy at  $p_{\text{T}}^{\text{veto}} = 15 \text{ GeV}$ , which corresponds roughly to a veto-value of  $p_{\text{T}}^{\text{veto}} = 25 \text{ GeV}$  in the partonic simulation (indicated by the dotted line in Fig. 7.6). However, this change in the cut variable will change the over-all selection efficiency after all cuts are applied.

### 7.3.5 Missing Transverse Energy

There are different ways for the reconstruction of the missing transverse energy from the experimental data. In order to avoid large corrections (i.e. due to the JES and muon corrections), and thus systematic uncertainties, the strategy should be kept as simple as possible.

In the partonic study the missing transverse energy has been computed directly from the neutrino momenta. Obviously this can not be done in an experimental environment. In the case where no hadronic activity is present in the final state, i.e. the final state consists of only the identified leptons, the missing transverse energy corresponds exactly to the transverse energy of the lepton pair. Since a jet-veto is imposed, the hadronic activity in the final state is small. This method for computing the missing transverse energy is therefore justifiable. The resolution of the missing transverse energy reconstruction is then basically dictated by the momentum resolution of the lepton reconstruction, which is very good for the selected leptons as shown in sections 6.2 and 6.3.

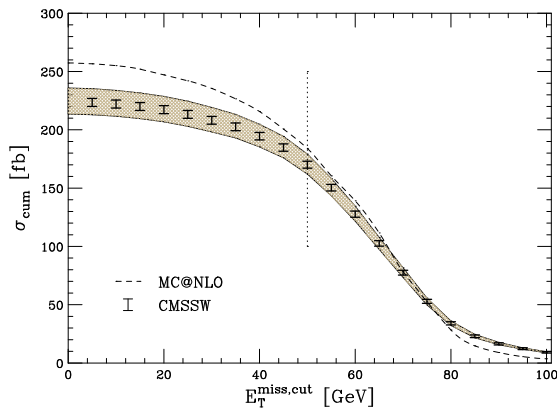


Figure 7.7: Cumulative cross-section as a function of the missing transverse energy with the jet-veto applied. The band corresponds to a variation of the JES in the range 0.9–1.1.

The comparison of the cumulative cross-sections as functions of the minimum missing transverse energy  $E_T^{\text{miss,cut}}$  between the partonic study (MC@NLO) and the full simulation (CMSSW) is shown in Fig. 7.7, where in addition to the selection of the leptons the jet-veto cut as described in the previous section at  $p_T^{\text{veto}} = 15 \text{ GeV}$  (full simulation) and  $p_T^{\text{veto}} = 25 \text{ GeV}$  (partonic study) has been imposed. The band corresponds again to a variation of the JES in the range 0.9 – 1.1.

For very low cut values the difference is dominated by the efficiency difference of the jet-veto. With increasing cut-value the cross-sections come closer, and especially in the intermediate region, around the nominal value of  $E_T^{\text{miss,cut}} = 50 \text{ GeV}$  (denoted by the dotted line) the agreement is good.

It will become clear later that the cut on the missing transverse energy has almost no effect after the application of all other cuts. This can be understood from the fact that the demand for two sufficiently hard leptons ( $p_T^\ell > 25 \text{ GeV}$ ), that are close to each other in the transverse plane ( $\phi_{\ell\ell} < 45^\circ$ ), with little additional hadronic activity (jet-veto) automatically produces large missing transverse energy.

## 7.4 Accepted Cross-Section and Uncertainties

The whole set of *experimental signal cuts* can now be defined:

### Experimental Signal Cuts

1. Events are accepted if there are two leptons (electrons or muons) satisfying the *isolated lepton identification* criteria with  $p_T > 25 \text{ GeV}$  and  $|\eta| < 2.0$ ;

cut	$m_H = 165 \text{ GeV}$	$\sigma_{\text{NLO}}$ [fb]		$\varepsilon$ [%]	
		$\mu = m_H/2$	$\mu = 2 m_H$		
	total	2440	1880	—	
1	lepton selection	350.4 $\pm$ 4.2	259.0 $\pm$ 3.1	14.4 $\pm$ 0.2	(14)
2	$\phi_{\ell\ell} < 45^\circ$	192.7 $\pm$ 3.1	142.4 $\pm$ 2.3	7.91 $\pm$ 0.13	(55)
3	$12 \text{ GeV} < m_{\ell\ell} < 40 \text{ GeV}$	135.3 $\pm$ 2.7	100.0 $\pm$ 2.0	5.56 $\pm$ 0.11	(70)
4	$p_T^{\text{veto}} = 15 \text{ GeV}$	63.2 $\pm$ 1.8	46.7 $\pm$ 1.3	2.60 $\pm$ 0.07	(47)
5	$E_T^{\text{miss}} > 50 \text{ GeV}$	62.9 $\pm$ 1.8	46.5 $\pm$ 1.3	2.58 $\pm$ 0.07	(100)
6	$30 \text{ GeV} < p_T^{\ell, \text{max}} < 55 \text{ GeV}$	52.5 $\pm$ 1.7	38.8 $\pm$ 1.2	2.15 $\pm$ 0.07	(83)

Table 7.3: Cross-sections for the signal process  $H \rightarrow \text{WW}$  with the two scale choices  $\mu = m_H/2$  and  $\mu = 2 m_H$  after each of the *experimental signal cut*, as well as the total (in brackets relative) selection efficiencies.

2. the opening angle  $\phi_{\ell\ell}$  between the two leptons in the plane transverse to the beam-pipe should be smaller than  $45^\circ$ ;
3. the di-lepton mass should be in the range  $12 \text{ GeV} < m_{\ell\ell} < 40 \text{ GeV}$ ;
4. there should be no jet passing the *jet identification* criteria in the central detector region ( $|\eta^{\text{jet}}| < 2.5$ ) with transverse energy larger than  $15 \text{ GeV}$ ;
5. the missing transverse energy computed as the vector sum of the selected lepton momenta should be larger than  $50 \text{ GeV}$  and
6. the harder lepton is required to have a transverse momentum in the range  $30 \text{ GeV} < p_T^{\ell, \text{max}} < 55 \text{ GeV}$ .

The NLO signal cross-sections after each cut for the two scale choices  $\mu = m_H/2$  and  $\mu = 2 m_H$ <sup>7</sup> are listed in Table 7.3. In the right column the selection efficiency in percent with respect to the total cross-section (in brackets with respect to the cross-section after the previous cut) are shown. The quoted errors are the statistical errors, amounting to  $\Delta_{\text{MCstat}} = 3.2\%$  for the final numbers. These errors are only dependent on the sample size used to determine the efficiencies and could thus be reduced by using a larger sample. The generated Higgs sample corresponds to about 80'000 re-weighted events. The over-all selection efficiency is 2.15%. We find a reduction compared to the partonic study from section 4.2 by a factor of  $\sim 3$ . A main part of this difference comes from the lepton-identification efficiency, which is naturally 100% at parton-level, and the inclusion of the  $\tau$  final state configurations. This can be confirmed by computing the partonic MC@NLO cross-sections for both scale choices including this lepton-identification

<sup>7</sup> We vary again the factorization and the renormalization scales simultaneously  $\mu = \mu_R = \mu_F$ .

efficiency. The resulting cross-sections are

$$\begin{aligned} f_{\text{scale}} \times \sigma_{\text{acc}}^{\text{MC@NLO}}(\mu = m_{\text{H}}/2) &= 55.95 \pm 0.79 \text{ fb} \quad \text{and} \\ f_{\text{scale}} \times \sigma_{\text{acc}}^{\text{MC@NLO}}(\mu = 2m_{\text{H}}) &= 43.66 \pm 0.58 \text{ fb.} \end{aligned} \quad (7.9)$$

The remaining difference between these numbers and the numbers from Table 7.3 can be explained by the differences in the cumulative cross-section for the jet-veto in Fig. 7.6. It can again be seen that the partonic picture, neglecting underlying event, hadronization and detector effects up to the lepton identification, gives a very accurate description of the selection efficiency.

#### 7.4.1 Systematic Uncertainty

To estimate the uncertainty introduced by the jet energy scale the cross-sections after all selection cuts are computed varying the JES between 0.9–1.1. The numbers for  $\mu = m_{\text{H}}/2$  are

$$\begin{aligned} \sigma_{\text{acc}}^{\text{NLO}}(\text{JES} = 0.9) &= 55.0 \pm 1.7 \text{ fb} \quad \text{and} \\ \sigma_{\text{acc}}^{\text{NLO}}(\text{JES} = 1.1) &= 50.2 \pm 1.6 \text{ fb.} \end{aligned} \quad (7.10)$$

The relative uncertainty on the cross-section caused by the variation of the JES is thus  $\Delta_{\text{JES}} = 4.7\%$ .

As the leptons are measured very accurately, the only additional (non-theoretical) uncertainty we add is the one from the lepton identification. We estimate this uncertainty to be  $\Delta_{\text{lep-id}} = 5\%$  [26]. Since the missing transverse energy is computed from the leptons, no additional uncertainty has to be included for this variable. Assuming the MC statistical uncertainty the lepton-identification and the JES uncertainties are not correlated, the total non-theoretical systematic uncertainty is

$$\Delta_{\text{sys}} = \sqrt{\Delta_{\text{lep-id}}^2 + \Delta_{\text{MCstat}}^2 + \Delta_{\text{JES}}^2} = 7.6\%. \quad (7.11)$$

#### 7.4.2 Theoretical Uncertainty

In addition to the systematic uncertainties from the experimental procedures theoretical uncertainties have to be included. One of them comes from the variation of the factorization and the renormalization scales. We define the mean expected cross-section  $\langle \sigma_{\text{acc}}^{\text{NLO}} \rangle$  and the scale uncertainty  $\Delta_{\text{scale}}$  as

$$\langle \sigma_{\text{acc}}^{\text{NLO}} \rangle = \frac{\sigma_{\text{acc}}^{\text{NLO}}(\mu = m_{\text{H}}/2) + \sigma_{\text{acc}}^{\text{NLO}}(\mu = 2m_{\text{H}})}{2} = 45.7 \text{ fb} \quad (7.12)$$



and

$$\Delta_{\text{scale}}^{\text{NLO}} = \frac{\sigma_{\text{acc}}^{\text{NLO}}(\mu = m_{\text{H}}/2) - \sigma_{\text{acc}}^{\text{NLO}}(\mu = 2m_{\text{H}})}{\sigma_{\text{acc}}^{\text{NLO}}(\mu = m_{\text{H}}/2) + \sigma_{\text{acc}}^{\text{NLO}}(\mu = 2m_{\text{H}})} = 15.1\%. \quad (7.13)$$

It has been shown in section 4.2.2 how the NLO cross-section is unreliable and how the scale uncertainty is reduced by going to NNLO predictions. We therefore re-weight the NLO predictions from Table 7.3 inclusively to the NNLO cross-section. The mean expected NNLO cross-section is then

$$\langle \sigma_{\text{acc}}^{\text{NNLO}} \rangle = \frac{\sigma_{\text{acc}}^{\text{NNLO}}(\mu = m_{\text{H}}/2) + \sigma_{\text{acc}}^{\text{NNLO}}(\mu = 2m_{\text{H}})}{2} = 53.9 \text{ fb}. \quad (7.14)$$

with a scale uncertainty of  $\Delta_{\text{scale}}^{\text{NNLO}} = 8.0\%$ .

It has to be pointed out that there is no theoretical motivation for the treatment of the uncertainty from the scale variation as Gaussian distributed around the mean of the cross-sections for the scale choices  $\mu = m_{\text{H}}/2$  and  $\mu = 2m_{\text{H}}$ . In order to estimate the uncertainty more precisely the scales should be varied independently and over a larger region<sup>8</sup>. However, the description above serves as a practical treatment of these uncertainties and allows to visualize the importance of the higher-order corrections up to NNLO.

There are other theoretical uncertainties that have to be included, namely the uncertainties on the value of  $\alpha_s$  and on the parton distribution functions. The uncertainty on the strong coupling constant  $\alpha_s$  is about 2% (cf. section 1.3.3). This uncertainty propagates into the final cross-section estimation (at LO as  $\Delta_{\alpha_s^2} \simeq 4\%$ ). The estimation of the uncertainty from varying the PDFs is more complicated. A rough estimate can be computed by comparing the accepted cross-section at parton level from MC@NLO with the alternative PDF set CTEQ6M [76] for a scale choice of  $\mu = m_{\text{H}}/2$ . The resulting cross-section is

$$\sigma_{\text{acc}}^{\text{NLO}}(\text{CTEQ6M}) = 58.95 \pm 0.82 \text{ fb}. \quad (7.15)$$

The uncertainty from this variation is then

$$\Delta_{\text{PDF}} = \frac{\sigma_{\text{acc}}^{\text{NLO}}(\text{CTEQ6M}) - \sigma_{\text{acc}}^{\text{NLO}}(\text{MRST2004NLO})}{\sigma_{\text{acc}}^{\text{NLO}}(\text{MRST2004NLO})} \simeq 5\%. \quad (7.16)$$

Finally one should include the uncertainties from the *infinite-top-mass* approximation and the neglecting of the b-loop in the *Gluon-Fusion*-process. These uncertainties have been computed at an earlier stage of this thesis (section 2.2.1) as  $\Delta_{\text{b/t}} = 5\%$ .

---

<sup>8</sup> Such a study has been performed in section 4.2.2 for the NNLO cross-sections, where it was found that the uncertainty is stable within a larger variation range for the scales.

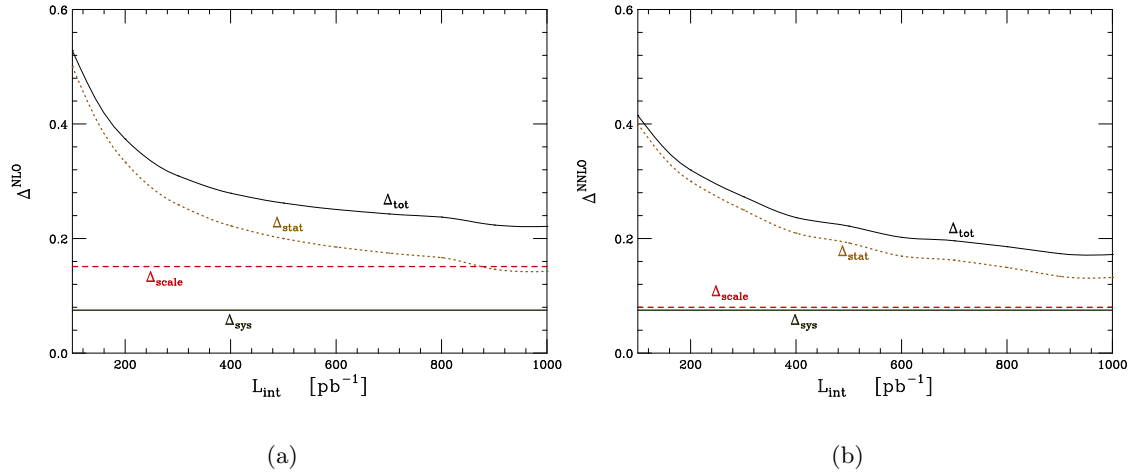


Figure 7.8: Comparisons of the various relative uncertainties at NLO (a) and NNLO(b).

Assuming that all these theoretical uncertainties are approximately uncorrelated<sup>9</sup> we can add them up to the total theoretical uncertainty (excluding the scale uncertainty) of

$$\Delta_{\text{theo}} = \sqrt{\Delta_{\alpha_s}^2 + \Delta_{\text{PDF}}^2 + \Delta_{b/t}^2} = 8.1\%. \quad (7.17)$$

### 7.4.3 Comparison of the Uncertainties

We can now compare the systematic and the scale uncertainty with the statistical uncertainty as a function of the integrated luminosity  $\mathcal{L}_{\text{int}}$ . The statistical uncertainty is computed using exact Poisson statistics with the mean values defined in eq. 7.12 (NLO) and eq. 7.14 (NNLO). The comparison is shown in Fig. 7.8, on the left using the NLO and on the right the NNLO scale uncertainty. The total uncertainty is defined as

$$\Delta_{\text{tot}} = \sqrt{\Delta_{\text{sys}}^2 + \Delta_{\text{stat}}^2 + \Delta_{\text{scale}}^2}. \quad (7.18)$$

In both cases the uncertainties are dominated by the statistical uncertainty for low luminosities. In the NLO case the scale uncertainty is larger than the statistical uncertainty for integrated luminosities of more than  $\sim 850 \text{pb}^{-1}$ . In the NNLO case the scale uncertainty is at the level of the systematic uncertainty and the total uncertainty is dominated by statistical effects over the whole luminosity range under investigation.

<sup>9</sup> Especially in the case of the uncertainty on  $\alpha_s$  and the PDFs this is an approximation. In addition, the uncertainties on  $\alpha_s$  and the PDFs are correlated with the scale uncertainty.

## 7.5 Background Event-Rates

To compute the signal significance and the exclusion limits the number of background events after the selection cuts has to be found. In a real experiment this number should be estimated as much as possible from data independently from Monte Carlo simulation. A way to do this is to measure the background events in some signal-free phase-space and then to extrapolate this number into the signal-region.

Such side-band phase-space regions have been proposed for the WW- and the  $t\bar{t}$ - background in [48], i.e. the WW-background can be estimated in the high-invariant mass region  $m_{\ell\ell} > 60 \text{ GeV}$  with larger opening angle  $\phi_{\ell\ell} < 140^\circ$ ; the  $t\bar{t}$ -background can be measured in the phase-space region where two identified jets are required in the central detector region.

The extrapolation of the expected background events into the signal region relies typically on the selection efficiency ratio between the signal-region and the normalization-region computed using MC simulation methods. We do not discuss this here, but compute the number of background events in the signal-region simply by using the MC simulation and quoting a total systematic uncertainty on these numbers of  $\Delta_{\text{sys}} = 20 \%$ . This number has been shown to be a reliable estimate for the uncertainties introduced through the side-band-extrapolation technique [26].

We estimate the cross-section for the background processes from Table 7.1 imposing the *experimental signal cuts* from section 7.4. For the Drell-Yan background  $Z/\gamma^* \rightarrow \ell\ell$  none of the 1.2 million simulated events survive the selection cuts. Thus we can only give an upper limit on this background cross-section as

$$\sigma_{\text{acc}}^{\text{NLO}}(Z/\gamma^* \rightarrow \ell\ell) < 3 \text{ fb.} \quad (7.19)$$

This value is rather large. It corresponds to the cross-section value if one of the events would remain after the cuts and is thus highly dominated by the statistics. We expect that using higher statistics samples, the value is decreased by at least one order of magnitude. We therefore do not include this background for the further study. The cross-sections after every selection cut (in brackets the selection efficiency with respect to the cross-section after the previous cut) for the other four simulated background-processes are shown in Table 7.4.

As expected, the dominating background-processes after the selection are the WW-continuum ( $\sim 11 \text{ fb}$ ) and the  $t\bar{t}$ -process ( $\sim 17 \text{ fb}$ ). For the WW-background the spin-structure of the initial-state particles renders the angular cut ( $\phi_{\ell\ell}$ ) particularly restrictive (6%), for the  $t\bar{t}$ -process the jet-veto (2.2%) and the angular cut (15%) have the largest

		$\sigma_{\text{NLO}}$ [fb]			
cut	process	WW		t $\bar{t}$	
	total	114300		840000	
1	lepton selection	1566	$\pm 97$ (1.4 %)	19416	$\pm 77$ (2.3 %)
2	$\phi_{\ell\ell} < 45^\circ$	93.2	$\pm 17.0$ (6.0 %)	2864	$\pm 30$ (15 %)
3	$12 \text{ GeV} < m_{\ell\ell} < 40 \text{ GeV}$	38.7	$\pm 12.2$ (42 %)	1186	$\pm 19$ (41 %)
4	$p_{\text{T}}^{\text{veto}} = 15 \text{ GeV}$	13.0	$\pm 1.9$ (34 %)	25.9	$\pm 2.8$ (2.2 %)
5	$E_{\text{T}}^{\text{miss}} > 50 \text{ GeV}$	12.9	$\pm 1.9$ (99 %)	25.6	$\pm 2.8$ (99 %)
6	$30 \text{ GeV} < p_{\text{T}}^{\ell, \text{max}} < 55 \text{ GeV}$	10.9	$\pm 1.8$ (84 %)	16.7	$\pm 2.3$ (65 %)
	$\varepsilon_{\text{tot}}$	$(9.6 \pm 1.6) \times 10^{-5}$		$(2.0 \pm 0.3) \times 10^{-5}$	
cut	process	WZ		ZZ	
	total	49900		15300	
1	lepton selection	843	$\pm 14$ (1.7 %)	514	$\pm 11$ (3.4 %)
2	$\phi_{\ell\ell} < 45^\circ$	57.2	$\pm 3.8$ (6.8 %)	34.5	$\pm 2.8$ (6.7 %)
3	$12 \text{ GeV} < m_{\ell\ell} < 40 \text{ GeV}$	5.27	$\pm 1.15$ (9.2 %)	3.70	$\pm 0.92$ (11 %)
4	$p_{\text{T}}^{\text{veto}} = 15 \text{ GeV}$	2.51	$\pm 0.79$ (48 %)	0.92	$\pm 0.46$ (24 %)
5	$E_{\text{T}}^{\text{miss}} > 50 \text{ GeV}$	2.51	$\pm 0.79$ (100 %)	0.92	$\pm 0.46$ (100 %)
6	$30 \text{ GeV} < p_{\text{T}}^{\ell, \text{max}} < 55 \text{ GeV}$	1.76	$\pm 0.66$ (70 %)	0.46	$\pm 0.33$ (50 %)
	$\varepsilon_{\text{tot}}$	$(3.5 \pm 1.3) \times 10^{-5}$		$(3.0 \pm 2.1) \times 10^{-5}$	

Table 7.4: NLO cross-sections for the various background processes after the selection cuts. In brackets the efficiencies for each single cut.

impact. The contamination from the other two processes (WZ, ZZ) is mainly reduced through the angular cut ( $\sim 7\%$ ) and the restrictions on the invariant mass of the lepton pair  $m_{\ell\ell}$  ( $\sim 10\%$ ).

The two additional background processes Wtb and  $gg \rightarrow WW$  could not be simulated for this study. Their contribution to the total background is estimated using the numbers from an earlier study [26], where very similar cuts have been imposed. The ratio of Wtb/t $\bar{t}$  events after the selection cuts has been computed to  $\sigma(\text{Wtb})/\sigma(\text{t}\bar{\text{t}}) = 0.14$ . The expected cross-section after the selection cuts is thus estimated as

$$\sigma_{\text{acc}}^{\text{NLO}}(\text{Wtb}) = 2.34 \text{ fb.} \quad (7.20)$$

The ratio of the gluon-induced and the quark-induced WW background has been estimated to be 31%. The estimation for the  $gg \rightarrow WW$  cross-section after the selection is therefore

$$\sigma_{\text{acc}}^{\text{NLO}}(gg \rightarrow WW) = 3.38 \text{ fb.} \quad (7.21)$$

The total cross-section for the background-processes included is then

$$\sigma_{\text{acc}}^{\text{NLO}}(\text{background}) = (35.5 \pm 7.1) \text{ fb,} \quad (7.22)$$

where the aforementioned total systematic uncertainty of 20% has been assumed.

Using all of the above, the mean expected signal over background ratio after selection cuts can be computed. In this calculation the systematic and the scale uncertainties on the signal cross-section (we neglect the additional theoretical uncertainties discussed at the end of section 7.4) as well as the total uncertainty on the background of 20% are included. The ratios using the NLO and the NNLO signal predictions are

$$\begin{aligned} S/B_{\text{NLO}} &= 1.29 \pm 0.33 \quad \text{and} \\ S/B_{\text{NNLO}} &= 1.52 \pm 0.34. \end{aligned} \tag{7.23}$$

Due to the higher NNLO cross-section the ratio increases by  $\sim 18\%$  when going from NLO to NNLO.

## 7.6 Expected Signal Significance and Exclusion Limit

The estimated signal and background cross-sections can now be used to compute the expected signal significance and exclusion limit for the CMS experiment. For the computation of these quantities we follow the strategy presented in [72] using exact Poisson statistics and include the uncertainties discussed above.

The signal significance, if  $d$  events are observed, can be defined as

$$\text{sig}(d) \equiv 1 - CL_{\text{B}}(d), \tag{7.24}$$

where  $CL_{\text{B}}(d)$  is the *background only* confidence level for  $d$  events observed. This confidence level is

$$CL_{\text{B}}(d) = \sum_{d' < d} p(d', B), \tag{7.25}$$

with  $p(d, B)$  the Poisson probability for observing  $d$  events if  $B$  events are expected. Similarly the *signal+background* confidence level can be defined as:

$$CL_{\text{S+B}}(d) = \sum_{d' < d} p(d', S + B). \tag{7.26}$$

The confidence level for the exclusion is

$$CL_{\text{S}} = \frac{CL_{\text{S+B}}}{CL_{\text{B}}}. \tag{7.27}$$

A *'five (two) sigma discovery'* is defined as the situation when  $1 - CL_{\text{B}}(d)$  is smaller than  $5.7 \times 10^{-7}$  (0.0455). As *'excluding the signal at 95% (99%) confidence level'* we refer to the situation when  $CL_{\text{S}}$  is smaller than 0.05 (0.01).

Using the definitions above the *mean expected signal significance*  $\langle 1 - CL_B \rangle$  if the signal is present and the *mean expected exclusion limit*  $\langle CL_S \rangle$  in the absence of a signal can be computed as

$$\begin{aligned} \langle 1 - CL_B \rangle &= \sum_d p(d, S + B) \left( 1 - \sum_{d' < d} CL_B(d') \right) \quad \text{and} \\ \langle CL_S \rangle &= \sum_d p(d, B) CL_S(d), \end{aligned} \tag{7.28}$$

where the values are averaged by summing the weighted results for all possible outcomes  $d$  of the experiment. Analytically the sums in eq. 7.28 run over an infinite number of terms. For practical purposes the sums can be truncated when the total probability reaches 99.99%, i.e. as soon as

$$\begin{aligned} \sum_d p(d, B) &\geq 0.9999 \quad \text{or respectively} \\ \sum_d p(d, S + B) &\geq 0.9999. \end{aligned} \tag{7.29}$$

In addition to the *mean expected* values the *most probable expected* values of the signal significance  $1 - CL_B(d^*)$  and the exclusion limit  $CL_S(d^*)$  can be computed, where  $d^*$  denotes the most probable number of expected events in the *signal+background* (signal significance) and the *background only* (exclusion limit) hypotheses.

The uncertainties used are the following. For the background it is 20%. For the signal we include the systematic, the theoretical and scale uncertainty, resulting in a total uncertainty of  $\sim 18\%$  for the NLO and  $\sim 13\%$  for the NNLO case. We use the (N)NLO signal predictions from section 7.4 and the background estimates  $B$  from section 7.5.

We show the mean (solid) and the most probable (dashed) expected signal significance in Fig. 7.9(a) as a function of the integrated luminosity for the NLO and the NNLO cross-sections. The dotted lines correspond to the  $5\text{-}\sigma$  ( $2\text{-}\sigma$ ) discovery line. The discontinuities in the dashed lines originate from the discrete possibilities for the outcome of the experiment. The figure shows the improvement for the expected exclusion limit and the signal significance by using the NNLO numbers, in both the mean and the most probable case. While at NLO a  $2\text{-}\sigma$  discovery can be made on average after collecting data corresponding to an integrated luminosity of  $\sim 200 \text{ pb}^{-1}$ , at NNLO this can already be reached with an integrated luminosity of  $\sim 120 \text{ pb}^{-1}$ . In the most probable case at NNLO a  $5\text{-}\sigma$  discovery is possible for  $\mathcal{L}_{\text{int}} \simeq 700 \text{ pb}^{-1}$ . At NLO this threshold is reached in the most probable case after  $\mathcal{L}_{\text{int}} \simeq 1.1 \text{ fb}^{-1}$  (not shown in the plot). In an earlier study using similar selection cuts [26] this value has been estimated to be  $\mathcal{L}_{\text{int}} \simeq 0.9 \text{ fb}^{-1}$ , which compares well with the prediction presented here. In general it can be observed how an average experiment would

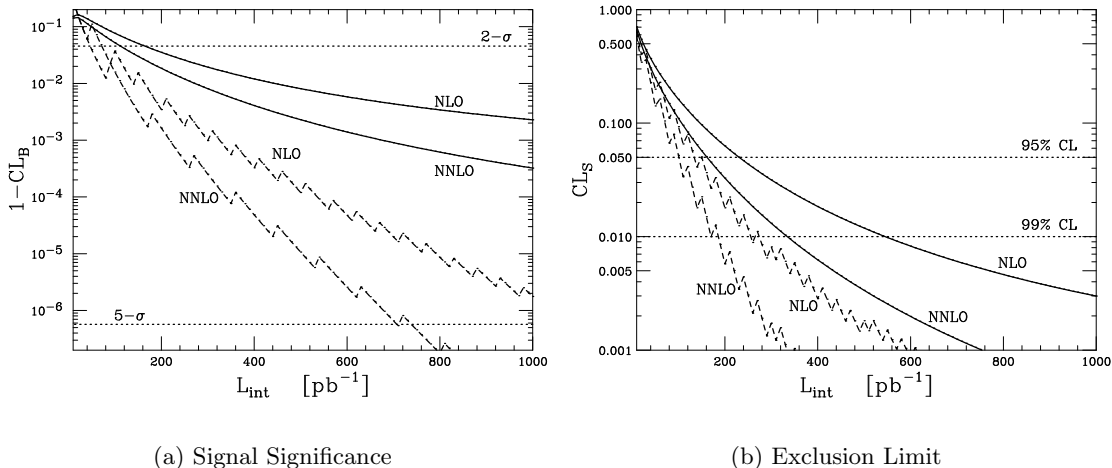


Figure 7.9: Expected mean (solid line) and most probable (dashed line) signal significance (a) and exclusion limit (b) for the CMS experiment as a function of the integrated luminosity. The Higgs mass is set to  $m_H=165$  GeV and both, the NLO and the NNLO signal cross-section predictions, are compared.

do much 'worse' than the most probable one, indicating that estimating the discovery potential from the most probable experiment is highly optimistic.

A similar picture can be observed for the exclusion limit, shown in Fig. 7.9(b). Solid lines again denote the mean and dashed lines the most probable exclusion limits for both, NLO and NNLO predictions. The dotted lines denote here the 95% (99%) exclusion confidence levels, i.e. in a hypothetically infinite number of real experiments, a statement like *'the signal is not present in the data'* would be true in 95% (99%) of the cases when a confidence level  $CL_S$  of 0.05 (0.01) is measured. Again, the increase in the expected signal cross-section from NLO to NNLO affects the exclusion limit. While at NNLO on average  $\sim 600 \text{ pb}^{-1}$  are needed to exclude a signal at 99% confidence level, at NNLO this mark is reached for an integrated luminosity of  $\sim 350 \text{ pb}^{-1}$ . In the most probable cases these values are reduced to  $300 \text{ pb}^{-1}$  ( $200 \text{ pb}^{-1}$ ) in the NLO (NNLO) case. Again these values have to be roughly doubled to estimate the performance of an average experiment.

## 7.7 Conclusions of this Chapter

In this chapter the  $H \rightarrow WW \rightarrow l\nu l\nu$  cross-section for a Higgs mass hypothesis of  $m_H = 165$  GeV has been computed using full CMS detector simulation. It has been shown how the effects of the experimental lepton reconstruction can be factorized from the hard

scattering process, if the lepton reconstruction efficiencies are approximately constant in the selected phase-space region. Thus the cumulative cross-sections in the leptonic selection variables can be compared to the partonic predictions and agree very well. The only complication is the jet-veto cut, since partonic and experimental jets are defined in a different way. However, as long as the experimental jet-veto efficiency is not much smaller than the partonic one, it can be safely argued that the higher-order QCD effects behave in the same way as in the partonic case, if the veto value is large enough that effects of multiple soft and collinear radiation can be neglected (cf. chapter 4).

Differential re-weighting of the signal events to the MC@NLO Higgs transverse momentum spectrum and subsequent inclusive re-weighting to the NNLO cross-section results in a very reliable prediction for the experimentally measured cross-section and the expected event rate. We used this cross-section, together with an estimate for the background event rate, to compute the signal significance in the *signal+background* and the exclusion limit in the *background only* hypotheses, including the most important theoretical and systematic uncertainties. It could be shown that the effect of the NNLO corrections has indeed a non-negligible impact and it can be concluded that, if the simulated lepton reconstruction efficiencies are reliable, a signal can either be observed or excluded with high confidence after the collection of data corresponding to an integrated luminosity of less than  $1 \text{ fb}^{-1}$ , in agreement with earlier studies performed.



# Conclusions

The discovery of the Higgs boson is the missing piece in the otherwise very well confirmed *Standard Model of Particle Physics*. Searches for this crucial ingredient for the understanding of electro-weak symmetry breaking have been performed at all high energy particle collider experiments, so far with negative outcome.

A new generation of experiments at the *Large Hadron Collider* (LHC) at CERN will give access to a new energy domain within a foreseeable time. While physics beyond the Standard Model is expected to become visible at these new energy scales, the discovery of the Higgs boson is still one of the main goals of these experiments. As for other searches the strategy relies heavily on simulations and theoretical calculations of the envisaged discovery process. For a discovery, and especially for any exclusion, it is absolutely vital to have very precise predictions as well as a good understanding of the uncertainties. For example, an over-estimation of the expected Higgs cross-section may lead to a 'false' exclusion, since not enough signal events are observed in the experimental data.

The thesis presented here discusses in unprecedented detail the phenomenology of a Higgs boson produced in the so called *Gluon-Fusion* channel at the LHC. First, the fully differential program FEHiP, that includes higher order QCD effects up to next-to-next-to-leading order (NNLO), is used to study the effects of these QCD corrections on the kinematics of the Higgs boson itself. While the corrections have been known to be important in the inclusive case, it was found that they vary significantly between different Higgs phase-space regions. In the very low Higgs transverse momentum region it was observed that the fixed-order calculation might break down and re-summation of large logarithmic terms be necessary. This assumption is tested against calculations including these terms, either through re-summation ((N)NLO+(N)NLL) or through a parton-shower algorithm (HERWIG, MC@NLO). It was found that while at NLO the Higgs transverse momentum spectrum has to be integrated up to a value of  $\sim 50$  GeV for a Higgs boson of mass  $m_H = 165$  GeV in order to render the logarithmic terms arising from multiple soft and collinear radiation negligible, at NNLO this is already achieved for a value of  $\sim 20$  GeV. Furthermore it is discussed how the Higgs-kinematics dependent corrections can be incorporated into MC event generators using differential re-weighting techniques.

Then the program FEHiP is used to investigate the higher order QCD effects in the specific decay mode  $H \rightarrow \gamma\gamma$ , after a typical set of experimental selection cuts are applied. It is found that the corrections behave very 'inclusive-like' and differential re-weighting is not needed to render the prediction for the cross-section more reliable. On the other hand some variables were found not to be reliably predictable by fixed-order calculations up to NNLO.

In the next step FEHiP was extended to include the decay mode  $H \rightarrow WW \rightarrow \ell\nu\ell\nu$ , the most promising discovery channel for a Higgs boson with mass  $m_H \sim 2m_W$ . In order to extract the signal events over the large background a set of very restrictive cuts has to be applied. The effects of the higher order QCD corrections on each variable restricted by the selection cuts has been studied in detail, again comparing to the predictions of the parton-shower programs HERWIG and MC@NLO. While the perturbative behavior of the variables was found to be very sensitive to the size of the allowed phase-space region, the comparisons to the parton-shower programs showed a very good agreement. To make a prediction for the expected cross-section at an experiment like CMS, all the selection cuts have been applied at parton-level. It was found that the  $K$ -factors after these cuts differ dramatically from the inclusive  $K$ -factors. The  $K$ -factors of  $\sim 2$  in the inclusive case are reduced to  $\sim 1$  after the selection cuts are applied, again demonstrating the strong phase-space dependence of the higher order QCD corrections. On the other hand the variation of the cross-section under the variation of the renormalization and factorization scales is strongly reduced after the cuts, indicating a very good convergence of the perturbative expansion. From these observations it is concluded that the NNLO prediction for the cross-section after the application of the cuts is very precise (at the order of 10%).

Finally, the phenomenology discussed before was used in a simulation of the search for the Higgs in the  $H \rightarrow WW$  channel with the *Compact Muon Solenoid* (CMS) experiment. Detector effects on the expected cross-section were discussed and it was argued that they can be treated as factorizable from the hard scattering process to a good approximation, if the specific lepton reconstruction efficiencies are constant in the envisaged phase-space region. Using this approach together with an estimation of the most important background processes, the expected mean and most probable signal significances (in the *signal+backgrounds* hypothesis) and exclusion limits (in the *background only* hypothesis) were computed using standard statistical methods. It was found that, using the NNLO predictions for the Higgs cross-section with  $m_H=165$  GeV, the CMS experiment, in the most probable case, will have to collect  $\sim 800 \text{ pb}^{-1}$  of data for a  $5\text{-}\sigma$  discovery and  $\sim 350 \text{ pb}^{-1}$  for an exclusion at 99% confidence level. An average experiment can discover the Higgs boson at a  $2\text{-}\sigma$  level after collection data that corresponds to  $\mathcal{L} \sim 150 \text{ pb}^{-1}$  and exclude its existence at 95% confidence level for  $\mathcal{L} \sim 200 \text{ pb}^{-1}$ .

Part III

Appendix



# Appendix A

## Dirac Algebra

The Dirac algebra is defined via the anti-commutation relation

$$\{\gamma^\mu, \gamma^\nu\} \equiv \gamma^\mu \gamma^\nu + \gamma^\nu \gamma^\mu = 2g^{\mu\nu} \times \mathbf{1}_{n \times n}, \quad (\text{A.1})$$

where  $g$  is the metric of an  $n$ -dimensional vector-space. We are interested in the 4-dimensional Minkowski-space, i.e. the relativistic 3-space + 1-time dimensional vector-space with metric

$$g^{\mu\nu} = \begin{pmatrix} 1 & 0 & 0 & 0 \\ 0 & -1 & 0 & 0 \\ 0 & 0 & -1 & 0 \\ 0 & 0 & 0 & -1 \end{pmatrix}. \quad (\text{A.2})$$

The so called *Weyl* or *chiral* representation of the Dirac algebra in this vector-space is

$$\gamma^0 = \begin{pmatrix} 0 & \mathbf{1}_{2 \times 2} \\ \mathbf{1}_{2 \times 2} & 0 \end{pmatrix}; \quad \gamma^j = \begin{pmatrix} 0 & \sigma^j \\ -\sigma^j & 0 \end{pmatrix}, \quad (\text{A.3})$$

with  $\sigma^i$  the Pauli-matrices

$$\sigma^1 = \begin{pmatrix} 0 & 1 \\ 1 & 0 \end{pmatrix}, \quad \sigma^2 = \begin{pmatrix} 0 & -i \\ i & 0 \end{pmatrix} \quad \text{and} \quad \sigma^3 = \begin{pmatrix} 1 & 0 \\ 0 & -1 \end{pmatrix}. \quad (\text{A.4})$$

It is convenient to define a 5<sup>th</sup> matrix  $\gamma^5$  as

$$\gamma^5 \equiv i\gamma^0\gamma^1\gamma^2\gamma^3\gamma^4 = \begin{pmatrix} -\mathbf{1}_{2 \times 2} & 0 \\ 0 & \mathbf{1}_{2 \times 2} \end{pmatrix}. \quad (\text{A.5})$$

We summarize (without proof) the trace-theorems for products of these matrices as

$$\begin{aligned}\mathrm{tr}(1) &= 4 \\ \mathrm{tr}(\text{any odd \# of } \gamma\text{'s}) &= 0 \\ \mathrm{tr}(\gamma^\mu \gamma^\nu) &= 4g^{\mu\nu} \\ \mathrm{tr}(\gamma^\mu \gamma^\nu \gamma^\rho \gamma^\sigma) &= 4(g^{\mu\nu} g^{\rho\sigma} - g^{\mu\rho} g^{\nu\sigma} + g^{\mu\sigma} g^{\nu\rho}) \\ \mathrm{tr}(\gamma^5) &= 0 \\ \mathrm{tr}(\gamma^\mu \gamma^\nu \gamma^5) &= 0 \\ \mathrm{tr}(\gamma^\mu \gamma^\nu \gamma^\rho \gamma^\sigma \gamma^5) &= -4i\varepsilon^{\mu\nu\rho\sigma}.\end{aligned}\tag{A.6}$$

## Appendix B

# Higgs Production Cross-Sections

In this appendix the calculations for the Higgs production at the LHC via the *Higgs-Strahlung* and the *Gluon-Fusion* process are presented. The cross-section for a hadron collider process can be written (cf. section 1.4) as

$$\sigma = \int_0^1 dx_1 dx_2 \sum_{i,j} f_i(x_1) f_j(x_2) \hat{\sigma}^{i,j}(x_1, x_2), \quad (\text{B.1})$$

where we sum over all partons in the colliding hadrons,  $f_i(x_k)$  is the parton density for partons of type  $i$  in the hadron at momentum fraction  $x_k$ ,

$$p_k = x_k P_k, \quad (\text{B.2})$$

with  $P_{1,2}$  the four-momenta of hadrons 1 and 2, which collide at a with center-of-mass energy  $s = (P_1 + P_2)^2$ .

The partonic cross-section  $\hat{\sigma}$  is

$$\hat{\sigma} = \frac{1}{2E_1 2E_2 |v_1 - v_2|} \int \left( \prod \frac{d^4 p_f}{(2\pi)^3} \delta(m_f^2 - p_f^2) \right) |\mathcal{M}|^2 (2\pi)^4 \delta^{(4)}(p_1 + p_2 - \sum p_f), \quad (\text{B.3})$$

where the integration goes over the phase-space of all final state particles  $p_f$  with masses  $m_f$ ,  $E_i$  ( $v_i$ ) is the energy (velocity) of the incoming parton  $p_i$ ,  $i \in \{1, 2\}$  in the laboratory rest-frame. For the computation of the  $S$ -matrix element  $\mathcal{M}$  the Feynman-rules described in chapter 1 are used.

Using formula (B.2) and the fact that the incoming partons (as well as the hadrons) can be treated as massless ( $|v_1 - v_2| = 2$ ), the prefactor in (B.3) and the invariant mass of the parton-pair become

$$\frac{1}{2E_1 2E_2 |v_1 - v_2|} = \frac{1}{2x_1 x_2 s} \quad \text{and} \quad (p_1 + p_2)^2 = x_1 x_2 s. \quad (\text{B.4})$$

## B.1 N-Body Phase-Space

First the phase-spaces for the final-state multiplicities needed below are computed. The phase-space integral for the  $n$ -body phase-space is

$$\int d\Pi_n = \int \left( \prod_n \frac{d^4 p_f}{(2\pi)^3} \delta(m_f^2 - p_f^2) \right) (2\pi)^4 \delta^{(4)}(Q - \sum_n p_f), \quad (\text{B.5})$$

where  $Q$  is the sum of all initial state four-momenta. The integral above is Lorentz-invariant, thus it can be computed in any frame, i.e. in the rest-frame of the momentum  $Q$ , where  $Q = (E_{\text{CM}}, \vec{0})$ , with  $E_{\text{CM}}$  the center-of-mass energy of all incoming particles.

### B.1.1 1-Body Phase-Space

The evaluation of the 1-body phase-space is trivial,

$$\int d\Pi_1 = \int \frac{d^4 p}{(2\pi)^3} \delta(m^2 - p^2) (2\pi)^4 \delta^{(4)}(Q - p) = (2\pi) \delta(m^2 - Q^2), \quad (\text{B.6})$$

with  $m$  the mass of the final-state particle.

### B.1.2 2-Body Phase-Space

The 2-body phase-space is

$$\int d\Pi_2 = \int \frac{d^4 p_1 d^4 p_2}{(2\pi)^6} \delta(m_1^2 - p_1^2) \delta(m_2^2 - p_2^2) (2\pi)^4 \delta^{(4)}(Q - p_1 - p_2). \quad (\text{B.7})$$

First both mass-constraint  $\delta$ -functions are integrated out. This leads to

$$\begin{aligned} \int d\Pi_2 &= \int \frac{d^3 \vec{p}_1 d^3 \vec{p}_2}{4E_1 E_2 (2\pi)^2} \delta^{(4)}(Q - p_1 - p_2) \\ &= \int \frac{d^3 \vec{p}_1 d^3 \vec{p}_2}{4E_1 E_2 (2\pi)^2} \delta^{(3)}(-\vec{p}_1 - \vec{p}_2) \delta(E_{\text{CM}} - E_1 - E_2) \\ &= \int \frac{d^3 \vec{p}_1}{4E_1 E_2 (2\pi)^2} \delta(E_{\text{CM}} - E_1 - E_2), \end{aligned} \quad (\text{B.8})$$

where the remaining  $\delta$ -function has been split into the energy and the spatial momentum part. The energies  $E_1$  and  $E_2$  are then

$$E_1 = \sqrt{m_1^2 + \vec{p}_1^2} \quad \text{and} \quad E_2 = \sqrt{m_2^2 + \vec{p}_1^2}. \quad (\text{B.9})$$



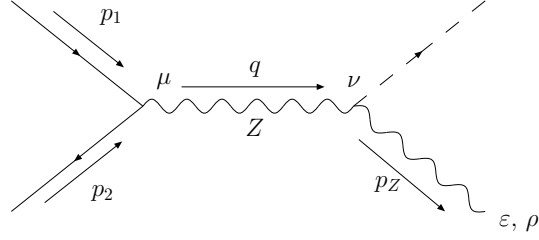


Figure B.1: Feynman-diagram for the LO Higgs-Strahlung process.

Using spherical coordinates and integrating over the last  $\delta$ -function the phase-space integral becomes

$$\begin{aligned} \int d\Pi_2 &= \int \frac{d\Omega}{16\pi^2} \frac{d|\vec{p}_1| |\vec{p}_1|^2}{E_1 E_2} \delta(E_{\text{CM}} - E_1 - E_2) = \int \frac{d\Omega}{16\pi^2} \frac{|\vec{p}_1|}{(E_1 + E_2)} \\ &= \frac{\sqrt{(Q^2 - (m_1 - m_2)^2)(Q^2 - (m_1 + m_2)^2)}}{8\pi Q^2}, \end{aligned} \quad (\text{B.10})$$

where  $E_{\text{CM}}^2$  has been replaced by  $Q^2$ . In the case of two massless particles this becomes simply

$$\int d\Pi_2 = \frac{1}{8\pi}. \quad (\text{B.11})$$

## B.2 Higgs-Strahlung Channel

The Feynman-diagram for the *Higgs-Strahlung* process in association with a Z-boson is shown in Fig. B.1. The matrix element for this process is

$$\begin{aligned} i\mathcal{M} &= \bar{v}^s(p_2) \frac{ig}{2\cos\theta_w} \gamma^\mu (c_A - c_V \gamma^5) u^r(p_1) \left( \frac{-i}{q^2 - m_Z^2} \right) \left( g_{\mu\nu} - \frac{q_\mu q_\nu}{m_Z^2} \right) 2i \frac{m_Z^2}{v} g^{\nu\rho} \varepsilon_\rho^*(p_Z) \\ &= A \times \bar{v}^s(p_2) \gamma^\mu (c_A - c_V \gamma^5) u^r(p_1) \times G_\mu^\rho \varepsilon_\rho^*(p_Z), \end{aligned} \quad (\text{B.12})$$

where *unitarity gauge* has been used for the gauge-boson propagator. The pre-factor  $A$  is defined as

$$A = \frac{2ig m_Z^2}{2v \cos\theta_w (q^2 - m_Z^2)} \quad (\text{B.13})$$

and the tensor  $G_\mu^\rho$  as

$$G_\mu^\rho = \left( g_{\mu\nu} - \frac{q_\mu q_\nu}{m_Z^2} \right) g^{\nu\rho}. \quad (\text{B.14})$$

The amplitude of the process, averaged over all incoming spin-states  $s, r$  and summed over all final state Z polarization states, is then

$$\frac{1}{4} \sum_{\text{pol}} \sum_{s,r} |\mathcal{M}|^2 = \frac{|A|^2}{4} \times \sum_{s,r} [u_c^r(p_1) \bar{u}_d^r(p_1) v_f^s(p_2) \bar{v}_a^s(p_2)] \times \gamma_{ab}^\mu (c_A - c_V \gamma^5)_{bc} (c_A + c_V \gamma^5)_{de} \gamma_{ef}^\alpha G_\mu^\rho G_\alpha^\sigma \times \sum_{\text{pol}} \varepsilon_\rho^*(p_Z) \varepsilon_\sigma(p_Z). \quad (\text{B.15})$$

We now use the identities for the sum over the spin-states of the external fermions <sup>1</sup>

$$\sum_s u^s(p) \bar{u}^s(p) = \sum_s v^s(p) \bar{v}^s(p) = p_\mu \gamma^\mu \equiv \not{p}, \quad (\text{B.16})$$

to obtain

$$\begin{aligned} \frac{1}{4} \sum_{\text{pol}} \sum_{s,r} |\mathcal{M}|^2 &= \frac{|A|^2}{4} \left( (\not{p}_1)_{cd} (\not{p}_2)_{fa} \gamma_{ab}^\mu (c_A - c_V \gamma^5)_{bc} (c_A + c_V \gamma^5)_{de} \gamma_{ef}^\alpha G_\mu^\rho G_\alpha^\sigma \sum_{\text{pol}} \varepsilon_\rho^*(p_Z) \varepsilon_\sigma(p_Z) \right) \\ &= \frac{|A|^2}{4} \text{tr} \left[ \gamma^\beta \gamma^\mu (c_A - c_V \gamma^5) \gamma^\delta (c_A + c_V \gamma^5) \gamma^\alpha \right] p_{1\delta} p_{2\beta} G_\mu^\rho G_\alpha^\sigma \sum_{\text{pol}} \varepsilon_\rho^*(p_Z) \varepsilon_\sigma(p_Z). \end{aligned} \quad (\text{B.17})$$

The trace can be evaluated using the identities from Appendix A. There are four different terms contributing, namely

$$\begin{aligned} t_1 &= + c_A^2 \text{tr} \left[ \gamma^\beta \gamma^\mu \gamma^\delta \gamma^\alpha \right], \\ t_2 &= - c_A c_V \text{tr} \left[ \gamma^\beta \gamma^\mu \gamma^5 \gamma^\delta \gamma^\alpha \right], \\ t_3 &= + c_A c_V \text{tr} \left[ \gamma^\beta \gamma^\mu \gamma^\delta \gamma^5 \gamma^\alpha \right], \\ t_4 &= - c_V^2 \text{tr} \left[ \gamma^\beta \gamma^\mu \gamma^5 \gamma^\delta \gamma^5 \gamma^\alpha \right]. \end{aligned} \quad (\text{B.18})$$

Closer investigation shows that the trace-structures of  $t_2$  and  $t_3$  (using  $\{\gamma^5, \gamma^\mu\} = 0$ ) as well as of  $t_1$  and  $t_4$  (using  $(\gamma^5)^2 = 1$ ) are the same. The sum of all four terms is therefore

$$t^{\beta\mu\delta\alpha} \equiv \sum t_i = (c_A^2 + c_V^2) \text{tr} \left[ \gamma^\beta \gamma^\mu \gamma^\delta \gamma^\alpha \right] - 2c_A c_V \text{tr} \left[ \gamma^\beta \gamma^\mu \gamma^\delta \gamma^\alpha \gamma^5 \right]. \quad (\text{B.19})$$

This then becomes

$$t^{\beta\mu\delta\alpha} = 4(c_A^2 + c_V^2) (g^{\beta\mu} g^{\delta\alpha} - g^{\beta\delta} g^{\mu\alpha} + g^{\beta\alpha} g^{\mu\delta}) + 8i c_A c_V \varepsilon^{\beta\mu\delta\alpha}. \quad (\text{B.20})$$

---

<sup>1</sup> These are only valid if the fermions are massless. Otherwise there is a contribution of the mass to the identities and they are no longer equal for the fermion- and the anti-fermion-spinors. For our purposes we can treat all incoming quarks as massless.

The last unresolved ingredient in eq. B.17 is the sum over the polarization states. In the unitarity-gauge <sup>2</sup> this is simply

$$\sum_{\text{pol}} \varepsilon_\rho^*(p_Z) \varepsilon_\sigma(p_Z) = -g_{\rho\sigma} + \frac{p_{Z\rho} p_{Z\sigma}}{m_Z^2}. \quad (\text{B.21})$$

After putting everything together the result for the amplitude reads

$$\frac{1}{4} \sum_{\text{pol}} \sum_{s,r} |\mathcal{M}|^2 = \frac{|A|^2}{4} t^{\beta\mu\delta\alpha} p_{1\delta} p_{2\beta} G_\mu^\rho G_\alpha^\sigma \left( -g_{\rho\sigma} + \frac{p_{Z\rho} p_{Z\sigma}}{m_Z^2} \right). \quad (\text{B.22})$$

Inserting momentum-conservation ( $q = p_1 + p_2$ ) and using the algebraic manipulation tool FORM [77] to contract all the Lorentz-indices, the result is reduced to

$$\begin{aligned} \frac{1}{4} \sum_{\text{pol}} \sum_{s,r} |\mathcal{M}|^2 &= \frac{g^2 m_Z^4}{v^2 \cos^2 \theta_w ((p_1 + p_2)^2 - m_Z^2)^2} (c_A^2 + c_V^2) 2 p_1 \cdot p_2 \\ &= \frac{g^2 m_Z^4}{v^2 \cos^2 \theta_w ((p_1 + p_2)^2 - m_Z^2)^2} (c_A^2 + c_V^2) (p_1 + p_2)^2, \end{aligned} \quad (\text{B.23})$$

where it has been used that the incoming quarks can be treated as massless ( $p_i^2 = 0$ ).

At this point it makes sense to discuss which modifications eq. B.23 would undergo if the Higgs boson was produced in association with a W instead of a Z. Obviously the masses in the propagator and in the coupling to the Higgs become  $m_W$ . In addition the coupling constant  $\frac{g}{\cos \theta_w}$  is replaced by  $\frac{g}{\sqrt{2}}$ . Finally, the W couples exclusively to left-handed fermions, i.e.  $c_A = c_V = 1$ . With these modifications in mind, we will derive the cross-section for the Higgs production in association with a W at the end of this section.

The total inclusive partonic cross section for this process, using equations B.23, B.3, B.4 and B.10, reads

$$\begin{aligned} \hat{\sigma}_{qq \rightarrow \text{HZ}}(y) &= \frac{g^4}{64\pi} \times \frac{m_Z^2 (c_A^2 + c_V^2)}{m_W^2 \cos^2 \theta_w} \times \\ &\frac{m_Z^2}{y^2} \left( 1 - \frac{(m_H - m_Z)^2}{y} \right)^{\frac{1}{2}} \left( 1 - \frac{(m_H + m_Z)^2}{y} \right)^{\frac{1}{2}} \left( 1 - \frac{m_Z^2}{y} \right)^{-2}, \end{aligned} \quad (\text{B.24})$$

where it has been defined that  $y = x_1 x_2 s$  and used that  $1/v^2 = g^2/(4m_W^2)$ .

In the case of W-production in association with the Higgs the result is

$$\begin{aligned} \hat{\sigma}_{qq \rightarrow \text{HW}}(y) &= \frac{g^4}{64\pi} \times \\ &\frac{m_W^2}{y^2} \left( 1 - \frac{(m_H - m_W)^2}{y} \right)^{\frac{1}{2}} \left( 1 - \frac{(m_H + m_W)^2}{y} \right)^{\frac{1}{2}} \left( 1 - \frac{m_W^2}{y} \right)^{-2}. \end{aligned} \quad (\text{B.25})$$

---

<sup>2</sup> We could have used any other gauge. The final results are the same, but in other gauges we would need to include the *Goldstone-boson* emission diagrams. In the unitarity-gauge the *Goldstone-boson*-propagator vanishes.

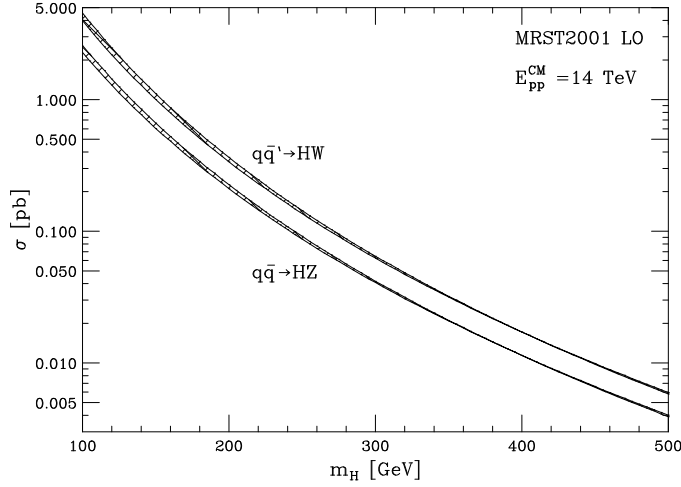


Figure B.2: Cross-sections for the Higgs-Strahlung process at the LHC as a function of the Higgs mass. The bands correspond to an uncertainty of the variation of the factorization scale  $\mu_R$ .

In order to obtain hadronic cross-sections the partonic formulas have to be integrated over the PDFs according to eq. B.1. We only consider the light quarks  $u$  and  $d$  in the proton. For the production with a  $Z$ -boson we need the quark combinations  $u\bar{u}$  and  $d\bar{d}$  and for the production in association with  $W$ -bosons the combinations  $u\bar{d}$  and  $d\bar{u}$  are relevant. The cross-section of eq. B.24 can be split into the two possible flavour channels by using the values for  $c_A$  and  $c_V$  from Tab. 1.3. This leads to

$$\hat{\sigma}_{u\bar{u}\rightarrow\text{HZ}} = \hat{\sigma}_{qq\rightarrow\text{HZ}} \quad \text{with} \quad (c_A^2 + c_V^2) = \frac{1}{2} - \frac{4}{3} \sin^2 \theta_w + \frac{16}{9} \sin^4 \theta_w \quad (\text{B.26})$$

and

$$\hat{\sigma}_{d\bar{d}\rightarrow\text{HZ}} = \hat{\sigma}_{qq\rightarrow\text{HZ}} \quad \text{with} \quad (c_A^2 + c_V^2) = \frac{1}{2} - \frac{2}{3} \sin^2 \theta_w + \frac{4}{9} \sin^4 \theta_w. \quad (\text{B.27})$$

The hadronic cross-sections are then

$$\sigma_{qq\rightarrow\text{HZ}} = 2 \int_0^1 dx_1 dx_2 [f_u(x_1) f_{\bar{u}}(x_2) \hat{\sigma}_{u\bar{u}\rightarrow\text{HZ}}(x_1 x_2 s) + f_d(x_1) f_{\bar{d}}(x_2) \hat{\sigma}_{d\bar{d}\rightarrow\text{HZ}}(x_1 x_2 s)] \quad (\text{B.28})$$

for  $Z$ -boson production and

$$\sigma_{qq\rightarrow\text{HW}} = 2 \int_0^1 dx_1 dx_2 [f_u(x_1) f_{\bar{d}}(x_2) + f_d(x_1) f_{\bar{u}}(x_2)] \hat{\sigma}_{qq\rightarrow\text{HW}}(x_1 x_2 s) \quad (\text{B.29})$$

for  $W$ -boson production. We want to point out that the PDFs are implicitly dependent on the factorization scale  $\mu_R$ .

These cross-sections can now be computed using any standard numerical integration technique. We will use here a VEGAS MC program PVEGAS [78]. For the PDFs we use the MRST2001 LO set [24] from the LHAPDF package [80], and we vary the factorization scale between  $m_{W/Z}/2$  and  $2m_{W/Z}$ . The center-of-mass energy is 14 TeV. The resulting cross-sections as a function of the Higgs mass are shown in Fig. B.2. The bands correspond to the uncertainty from the variation of the factorization scale.

## B.3 *Gluon-Fusion Channel*

### B.3.1 Matrix Element

Using the Feynman-diagram in Fig. B.3 one finds

$$i\mathcal{M}^{\mu\nu} = (-1) \int \frac{d^d k}{(2\pi)^d} \times \text{Tr} \left[ \left( -\frac{im}{v} \right) \frac{i(\not{k}' + m)}{k'^2 - m^2} i g_s t^a \gamma^\mu \frac{i(\not{k} + m)}{k^2 - m^2} i g_s t^b \gamma^\nu \frac{i(\not{k}'' + m)}{k''^2 - m^2} \right], \quad (\text{B.30})$$

with  $m$  the mass of the quark in the loop and  $v$  the Higgs vacuum-expectation value. Due to the fermion loop a factor of  $-1$  has to be applied, and we have to integrate over the undetermined loop momentum  $k$  (see e.g. [1]). In addition dimensional regularization is used to find a finite amplitude at the end of the calculation by taking the limit  $d \rightarrow 4$ .

Slightly rewriting this leads to

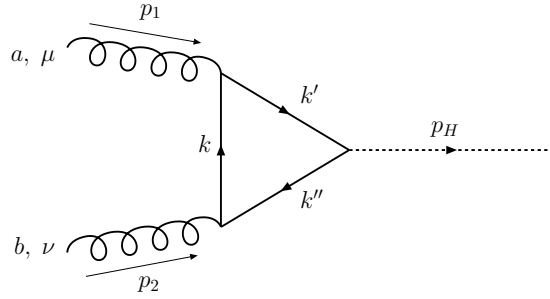
$$i\mathcal{M}_{\mu\nu} = \frac{g_s^2 m}{v} \text{Tr} [t^a t^b] \int \frac{d^d k}{(2\pi)^d} \frac{1}{(k'^2 - m^2)(k^2 - m^2)(k''^2 - m^2)} \times \text{Tr} [(\not{k}' + m) \gamma^\mu (\not{k}_\beta + m) \gamma^\nu (\not{k}'' + m)], \quad (\text{B.31})$$

with the color-factor  $\text{Tr} [t^a t^b] = C \delta^{ab}$  and  $C = 1/2$ . The momenta in the loop are

$$\begin{aligned} k' &= k + p_1 \\ k'' &= k - p_2. \end{aligned} \quad (\text{B.32})$$

The denominator of the integrand can be Feynman-parametrized like

$$\begin{aligned} \frac{1}{D} &= \frac{1}{(k'^2 - m^2)(k^2 - m^2)(k''^2 - m^2)} \\ &= \int_0^1 dx dy dz \delta(x + y + z - 1) \frac{2}{(x(k'^2 - m^2) + y(k^2 - m^2) + z(k''^2 - m^2))^3}. \end{aligned} \quad (\text{B.33})$$


 Figure B.3: Feynman-diagram for the LO *Gluon-Fusion* process.

Using identities from eq. B.32 and integrating over  $y$  (using  $y = 1 - x - z$ ), one finds

$$\frac{1}{D} = \int_0^1 dx \int_0^{1-x} dz \frac{2}{(k^2 + 2k \cdot (xp_1 + zp_2) - m^2)^3}, \quad (\text{B.34})$$

where all terms including  $p_i^2 = 0$  (massless gluons) have been discarded.

Shifting the integration variable  $k$  to

$$\ell = k + xp_1 - xp_2 \quad \Rightarrow \quad k = \ell + zp_2 - xp_1 \quad (\text{B.35})$$

gives a denominator of

$$\frac{1}{D} = \int_0^1 dx \int_0^{1-x} dz \frac{2}{(\ell^2 + 2xzp_1p_2 - m^2)^3}. \quad (\text{B.36})$$

Finally, substituting  $z' = z/(1-x)$  results in

$$\frac{1}{D} = \int_0^1 dx \int_0^1 dz' \frac{2(1-x)}{(\ell^2 + 2z'x(1-x)p_1p_2 - m^2)^3}. \quad (\text{B.37})$$

The numerator in eq. B.31 is

$$N^{\mu\nu} = \text{Tr} [(\not{k}' + m) \gamma^\mu (\not{k} + m) \gamma^\nu (\not{k}'' + m)]. \quad (\text{B.38})$$

We perform the trace over the fermion-line using eq. B.32 and the commutation rules for the Dirac matrices from eq. A.6. Notice, that since in the denominator the  $\ell$ -dependent term only depends only on the 4-length of  $\ell$ , all terms linear in  $\ell$  in the numerator will vanish after integrating from  $-\infty$  to  $\infty$ . We can discard them immediately, and find

$$\begin{aligned} N^{\mu\nu} = & 4m [4\ell^\mu \ell^\nu - g^{\mu\nu} \ell^2 + (4x^2 - 2x)p_1^\mu p_1^\nu \\ & + (-2z' + 4z'^2 + 2xz' - 8xz'^2 + 4x^2z'^2)p_2^\mu p_2^\nu \\ & + (-1 + 2z' + 2x - 6xz' + 4x^2z')p_1^\mu p_2^\nu \\ & + (1 - 4xz'(1-x))p_1^\nu p_2^\mu \\ & + g^{\mu\nu} (m^2 - (1 - 2xz'(1-x))p_1 \cdot p_2)] \end{aligned} \quad (\text{B.39})$$

The matrix total element reads now

$$i\mathcal{M}^{\mu\nu} = \frac{4g_s^2 m^2}{v} \delta^{ab} \int_0^1 dx dz' \int \frac{d^d \ell}{(2\pi)^d} \frac{(1-x)(4\ell^\mu \ell^\nu - g^{\mu\nu} \ell^2 + X^{\mu\nu})}{(\ell^2 + 2z'x(1-x)p_1 p_2 - m^2)^3}, \quad (\text{B.40})$$

with  $X^{\mu\nu}$  all the terms in the brackets of (B.39) that do not depend on  $\ell$ . We change from Minkowski- to Euclidean-metric by Wick-Rotation and set  $\ell_E^0 = i\ell^0$ , with  $\ell_E$  the new integration variable in 4-dimensional Euclidean space. We find then

$$i\mathcal{M}^{\mu\nu} = \frac{-4ig_s^2 m^2}{v} \delta^{ab} \int_0^1 dx dz' \int \frac{d^d \ell_E}{(2\pi)^d} \frac{(1-x)((1-4/d)\ell_E^2 g^{\mu\nu} + X^{\mu\nu})}{(\ell_E^2 + \Delta)^3}, \quad (\text{B.41})$$

where we it has been used that  $\ell^\mu \ell^\nu = \frac{1}{d} \ell^2 g^{\mu\nu}$ , and

$$\Delta = m^2 - 2z'x(1-x)p_1 \cdot p_2. \quad (\text{B.42})$$

The integration over euclidean space can now be performed (see e.g. [1]). For the  $\ell_E$ -independent part  $X^{\mu\nu}$  we find

$$\int \frac{d^d \ell_E}{(2\pi)^d} \frac{(1-x)X^{\mu\nu}}{(\ell_E^2 + \Delta)^3} = \frac{1}{(4\pi)^{d/2}} \frac{\Gamma(3-d/2)}{\Gamma(3)} \frac{(1-x)X^{\mu\nu}}{\Delta^{3-d/2}}. \quad (\text{B.43})$$

The integration over the first part of eq. B.41 gives

$$\begin{aligned} \int \frac{d^d \ell_E}{(2\pi)^d} \frac{(1-x)\ell_E^2}{(\ell_E^2 + \Delta)^3} \left(1 - \frac{4}{d}\right) g^{\mu\nu} &= \frac{1}{(4\pi)^{d/2}} \frac{\Gamma(2-d/2)}{\Gamma(3)} \frac{(1-x)d}{\Delta^{2-d/2}} \frac{d}{2} \left(1 - \frac{4}{d}\right) g^{\mu\nu} \\ &= \frac{1}{(4\pi)^{d/2}} \frac{\Gamma(3-d/2)}{\Gamma(3)} \frac{(1-x)}{\Delta^{3-d/2}} (-\Delta g^{\mu\nu}), \end{aligned} \quad (\text{B.44})$$

where in the last step we used the relation  $x\Gamma(x) = \Gamma(x+1)$ . Now both terms B.43 and B.44 are finite. We can set  $d=4$ , use  $\Gamma(1)/\Gamma(3) = 1/2$  and find

$$i\mathcal{M}^{\mu\nu} = \frac{-ig^2 m^2}{8\pi^2 v} \delta^{ab} \int_0^1 dx dz' \frac{(1-x)}{\Delta} (-\Delta g^{\mu\nu} + X^{\mu\nu}), \quad (\text{B.45})$$

with

$$Y^{\mu\nu} := -\Delta g^{\mu\nu} + X^{\mu\nu} = (4z'x(1-x) - 1)(g^{\mu\nu} p_1 \cdot p_2 - p_1^\nu p_2^\mu) + Z^{\mu\nu}. \quad (\text{B.46})$$

Here  $Z^{\mu\nu}$  stands for all the remaining terms in  $Y^{\mu\nu}$ . We do not explicitly list them all, since we will argue in a moment that all those terms will vanish, once taking a suitable gauge for the initial state gluon-polarization states. Notice the manifestly transverse character of the first part of  $Y^{\mu\nu}$ .

In order to find the amplitude we have to multiply this with the polarization vectors of the incoming gluons and average over these polarization states. The sum over the transverse polarization states together with the fact that the gluons are massless makes all the terms in  $Z^{\mu\nu}$  zero, and we end up with

$$\frac{1}{4} \sum_{\text{pol}} |\mathcal{M}|^2 = \frac{1}{9} \frac{(p_1 + p_2)^2 g_s^4}{v^2 \pi^4} \left( \int_0^1 dx dz \frac{(1-x)(-1+4xz(1-x))}{1-xz(1-x)\tau} \right)^2, \quad (\text{B.47})$$

with

$$\tau \equiv \frac{(p_1 + p_2)^2}{m^2}. \quad (\text{B.48})$$

For now we define the Feynman-parameter integral as

$$F(\tau) = \int_0^1 dx dz \frac{(1-x)(-1+4xz(1-x))}{1-xz(1-x)\tau}, \quad (\text{B.49})$$

and we will explicitly solve it in section B.3.2.

Using the 1-body phase-space from eq. B.6 the total cross-section becomes

$$\sigma_{\text{gg} \rightarrow \text{H}} = \frac{2}{9} \frac{\alpha_s^2 g_w^2}{\pi s} \frac{m_{\text{H}}^2}{m_{\text{W}}^2} \int dx f_g(x) f_g \left( \frac{m_{\text{H}}^2}{xs} \right) \frac{1}{x} \left| \sum_q F(\tau_q) \right|^2, \quad (\text{B.50})$$

where, in addition, the definition of the Higgs vacuum expectation value has been used. The functions  $f_g$  are the gluon density functions in the proton,  $\tau_q = m_{\text{H}}^2/m_q^2$ ,  $\alpha_s = g_s^2/4\pi$  and we sum over all possible quark types  $q$  in the loop. Notice, that the renormalization scale dependency only enters via the strong coupling constant, which will be evaluated as  $\alpha_s(\mu_{\text{R}})$ . The factorization scale dependency comes from the PDFs.

### B.3.2 Evaluation of the Feynman Integral

The only unresolved ingredient in formula B.50 are the Feynman-parameter integrals. We solve them using di-logarithms defined as

$$Li_2(x) = - \int_0^1 dt \frac{\log(1-xt)}{t} \quad (\text{B.51})$$

and the useful identities

$$\begin{aligned} Li_2(1-x) &= Li_2(1) - Li_2(x) - \log(1-x) \log(x) \quad \text{and} \\ Li_2(1/x) &= -Li_2(x) + 2Li_2(-1) - \frac{1}{2} \log^2(-x). \end{aligned} \quad (\text{B.52})$$



The Feynman-parameter integral is

$$F(\tau) = \int dx dz \frac{(1-x)(-1+4xz(1-x))}{1-xz(1-x)\tau} = \int dx dz \frac{-4}{\tau} X \left( \frac{\tau/4-1}{1-z\Omega} + 1 \right), \quad (\text{B.53})$$

where we have used the substitutions  $X = (1-x)$  and  $\Omega = \tau x X$ . The integration of the second part in the brackets is trivial;

$$I_1 \equiv \int dx dz \frac{-4}{\tau} (1-x) = -\frac{2}{\tau}. \quad (\text{B.54})$$

For the first part we introduce the additional substitution  $\tilde{z} = 1 - z\Omega$  to find

$$\begin{aligned} I_2 &\equiv \int dx dz \frac{-4}{\tau} X \frac{\tau/4-1}{1-z\Omega} = \int_0^1 dx \frac{1}{\Omega} \int_1^{1-\Omega} d\tilde{z} \frac{4X(\tau/4-1)}{\tilde{z}} \\ &= \frac{\tau-4}{\tau} \int_0^1 dx \frac{\log(1-\tau x(1-x))}{x}. \end{aligned} \quad (\text{B.55})$$

We define the variables

$$\rho_{\pm} = \frac{\tau \pm \sqrt{\tau^2 - 4\tau}}{2\tau} \quad (\text{B.56})$$

which satisfies

$$1 - x(1-x)\tau = \tau(x - \rho_+)(x - \rho_-) \quad (\text{B.57})$$

and find

$$\begin{aligned} I_2 &= \frac{\tau-4}{\tau} \int dx \left( \frac{\log(\tau)}{x} + \frac{\log(x - \rho_+)}{x} + \frac{\log(x - \rho_-)}{x} \right) \\ &= \frac{\tau-4}{\tau} \int dx \left( \frac{\log(\tau)}{x} + \frac{\log(-\rho_+)}{x} + \frac{\log(-\rho_-)}{x} + \frac{\log(1-x/\rho_+)}{x} + \frac{\log(1-x/\rho_-)}{x} \right) \end{aligned} \quad (\text{B.58})$$

The sum of the first three terms in the integrand vanishes using  $\rho_+\rho_- = 1/\tau$ . We are then left with

$$I_2 = \frac{\tau-4}{\tau} \int dx \left( \frac{\log(1-x/\rho_+)}{x} + \frac{\log(1-x/\rho_-)}{x} \right). \quad (\text{B.59})$$

We can rewrite this using the definition of the Di-Logs in eq. B.51 and the identities B.52 as

$$I_2 = \frac{\tau-4}{\tau} \left( -4Li_2(-1) + Li_2(1) + \frac{1}{2}(\log^2(-\rho_+) + \log^2(-\rho_-)) - \log(\rho_+)\log(\rho_-) \right), \quad (\text{B.60})$$

with the values  $Li_2(1) = \pi^2/6$  and  $Li_2(-1) = -\pi^2/12$ .

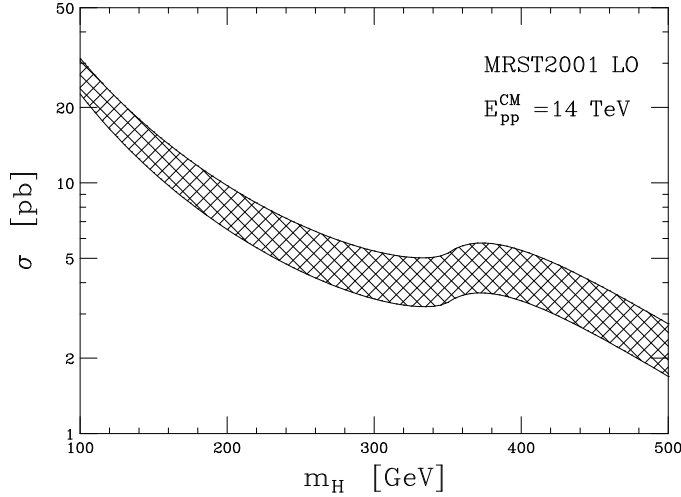


Figure B.4: LO cross-sections for the *Gluon-Fusion* process at the LHC as a function of the Higgs mass. The bands correspond to an uncertainty from the variation of the factorization and renormalization scales  $\mu_R$  and  $\mu_B$ .

If we assume  $\tau$  to be real valued, i.e.  $\tau \geq 4$ , then we can use analytic continuation of the logarithm to find  $\log(-\rho_{\pm}) = \log(\rho_{\pm}) \pm i\pi$ <sup>3</sup>. The integral becomes then

$$I_2 = \frac{\tau - 4}{2\tau} \left[ \log\left(\frac{\rho_+}{\rho_-}\right) - i\pi \right]^2 = \frac{\tau - 4}{2\tau} \left[ \log\left(\frac{1 + \sqrt{1 - 4/\tau}}{1 - \sqrt{1 - 4/\tau}}\right) - i\pi \right]^2. \quad (\text{B.61})$$

In the case of the  $\rho_{\pm}$  being complex, i.e.  $\tau < 4$ , we can use the same analytic continuation, and we find

$$I_2 = \frac{\tau - 4}{2\tau} \left[ \log\left(\frac{1 + i\sqrt{4/\tau - 1}}{1 - i\sqrt{4/\tau - 1}}\right) - i\pi \right]^2 = \frac{\tau - 4}{2\tau} \times 4 \arcsin^2\left(\sqrt{\frac{\tau}{4}}\right). \quad (\text{B.62})$$

The final result for the Feynman-parameter integral reads

$$F(\tau) = -\frac{2}{\tau} + \frac{\tau - 4}{2\tau} \times \left\{ \begin{array}{ll} \left[ \log\left(\frac{1 + \sqrt{1 - 4/\tau}}{1 - \sqrt{1 - 4/\tau}}\right) - i\pi \right]^2, & \text{if } \tau \geq 4 \\ 4 \arcsin^2\left(\sqrt{\frac{\tau}{4}}\right), & \text{if } \tau < 4. \end{array} \right\} \quad (\text{B.63})$$

### B.3.3 Cross-Section at the LHC

Using formulas eq. B.50 and eq. B.63 we can now use numerical integration techniques to find the LO cross-section at the LHC. We only consider the top and the bottom quarks in

<sup>3</sup> The differences in the sign for the imaginary term  $i\pi$  arises from the fact that  $\rho_+ = 1 - \rho_-$ , i.e. the imaginary parts of the two variables  $\rho_+$  and  $\rho_-$  have always opposite sign. By approaching the negative real axis this causes that the two variables to circle the origin in opposite direction.

the loop and set the masses to  $m_b = 4.2 \text{ GeV}$  and  $m_t = 175 \text{ GeV}$ . We use the MRST2001 LO PDF set [24] and vary the renormalization and factorization scales simultaneously between half and double the Higgs mass  $m_H$ . The resulting cross-sections for various Higgs mass hypotheses are shown in Fig. B.4.



# Appendix C

## Sector Decomposition

The parameter integrals in the higher order correction terms in the perturbative expansion of quantum field theories typically contain ultraviolet (UV) and infrared (IR) divergences. These divergences generally inhibit the direct numerical evaluation of such integrals. The treatment of these divergences becomes more and more complicated with increasing order.

For the UV divergences subtraction methods have been developed, that have been proven to be valid to all orders in perturbation theory [81]. Concerning the IR (soft and collinear) divergences a similar scheme could not be established so far. The so called *Sector Decomposition* method serves here as a constructive method to isolate these divergences, in principle to all orders in perturbation theory. The algorithm, based on the decomposition of the parameter phase-space into sectors in which the divergences factorize, can be used for the treatment of IR as well as UV divergences arising in loop- and phase-space integrals. Especially, but not exclusively, it has been proven to be useful to compute differential quantities in NNLO perturbative QCD [82, 75].

An extensive discussion of the *Sector Decomposition* method can be found in [83]. In the following we elaborate a simple example visualizing the main ideas behind the method.

Consider the two-dimensional parameter integral

$$I = \int_0^1 dx dy x^{-1-\varepsilon} y^{-\varepsilon} (x + (1-x)y)^{-1} \quad (\text{C.1})$$

on the unit square, shown in the first step of Fig. C.1. The integrand has a singular region when both  $x$  and  $y$  go to zero, i.e. the singularities are overlapping. The singularities can be factorized by decomposing the integral  $I$  as

$$I = \int_0^1 dx dy x^{-1-\varepsilon} y^{-\varepsilon} (x + (1-x)y)^{-1} (\Theta(x-y) + \Theta(y-x)), \quad (\text{C.2})$$

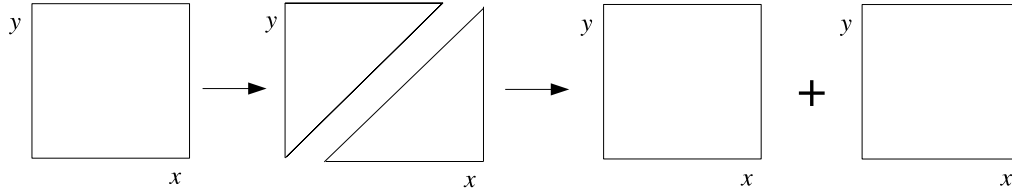


Figure C.1: Example for the Sector-Decomposition algorithm: Splitting of the integration area in order to factorize overlapping singularities in  $(x, y) = (0, 0)$ .

with  $\Theta(x)$  the step function defined as

$$\Theta(x) = \begin{cases} 1, & \text{if } x \geq 0 \\ 0, & \text{if } x < 0 \end{cases} . \quad (\text{C.3})$$

Now the integral is

$$I = \int_0^1 dx \int_0^x dy x^{-1-\varepsilon} y^{-\varepsilon} (x + (1-x)y)^{-1} + \int_0^1 dy \int_0^y dx x^{-1-\varepsilon} y^{-\varepsilon} (x + (1-x)y)^{-1} . \quad (\text{C.4})$$

This decomposition into two triangular sectors is shown in step 2 in Fig. C.1. The sectors are then remapped to the unit squares by substituting  $y \rightarrow y/x$  in the first and  $x \rightarrow x/y$  in the second sector (step 3 in Fig. C.1). The integral is then

$$S_1 + S_2 \equiv I = \int_0^1 dx dy x^{-1-2\varepsilon} y^{-\varepsilon} (1 + (1-x)y)^{-1} + \int_0^1 dx dy x^{-1-\varepsilon} y^{-1-2\varepsilon} (1 + (1-y)x)^{-1} . \quad (\text{C.5})$$

The singularities are now factorized in both sectors and the denominators take a constant value  $> 0$  on the entire unit square.

The  $1/\varepsilon$  poles can be extracted by Taylor-expanding around  $\varepsilon = 0$  using

$$x^{-1+\kappa\varepsilon} = \frac{1}{\kappa\varepsilon} \delta(x) + \sum_{n=0}^{\infty} \frac{(\kappa\varepsilon)^n}{n!} \left[ \frac{\log^n x}{x} \right]_+ . \quad (\text{C.6})$$

The plus-distribution is defined by its action on a test function  $f(x)$  according to

$$\int_0^1 dx f(x) [g(x)]_+ = \int_0^1 dx (f(x) - f(0))g(x) . \quad (\text{C.7})$$

The sectors become then

$$S_1 = \int_0^1 dx dy \left( \frac{1}{-2\varepsilon} \delta(x) + \sum_{n=0}^{\infty} \frac{(-2\varepsilon)^n}{n!} \left[ \frac{\log^n x}{x} \right]_+ \right) \times \left( \sum_{n=0}^{\infty} \frac{(-2\varepsilon)^n}{n!} \log^n y \right) d(x, y) \quad (\text{C.8})$$

and

$$S_2 = \int_0^1 dx dy \left( \frac{1}{-\varepsilon} \delta(x) + \sum_{n=0}^{\infty} \frac{(-\varepsilon)^n}{n!} \left[ \frac{\log^n x}{x} \right]_+ \right) \times \quad (C.9)$$

$$\left( \frac{1}{-2\varepsilon} \delta(y) + \sum_{n=0}^{\infty} \frac{(-2\varepsilon)^n}{n!} \left[ \frac{\log^n y}{y} \right]_+ \right) d(y, x),$$

with the denominator function  $d(x, y) = (1 + (1 - x)y)^{-1}$ . Ordering in powers of  $\varepsilon$  leads to

$$S_1 = \int_0^1 dx dy \left[ \frac{-1}{2\varepsilon} \delta(x) + \left( \frac{1}{[x]_+} + \log y \delta(x) \right) + \mathcal{O}(\varepsilon) \right] d(x, y) \quad (C.10)$$

and

$$S_2 = \int_0^1 dx dy \left[ \frac{1}{2\varepsilon^2} \delta(x) \delta(y) - \frac{1}{\varepsilon} \left( \frac{\delta(x)}{[y]_+} + \frac{1}{2} \frac{\delta(y)}{[x]_+} \right) \right. \quad (C.11)$$

$$\left. + \left( \frac{1}{[x]_+} \frac{1}{[y]_+} + 2 \left[ \frac{\log y}{y} \right]_+ \delta(x) + \frac{1}{2} \left[ \frac{\log x}{x} \right]_+ \delta(y) \right) + \mathcal{O}(\varepsilon) \right] d(y, x).$$

The divergences are now manifest as terms with poles at  $\varepsilon = 0$ . These terms have to cancel order by order with terms from other contributions. If for example eq. C.1 is a real radiation diagram, the divergent terms would cancel with contributions from the virtual correction diagrams. This cancellation can be verified numerically, by comparing the coefficients of the divergent terms order by order in  $\varepsilon$ . After this verification the divergent terms can be dropped and the finite terms integrated numerically using standard MC integration techniques.





# Appendix D

## The $H \rightarrow WW$ Decay in FEHiP

With the program FEHiP, as available in [84], Higgs production in the *Gluon-Fusion* channel up to NNLO can be computed (cf. chapter 2). The only implemented decay mode is the di-photon decay. In the following we explain in some detail how we have added to the program the full decay of the Higgs boson into leptons via a pair of W bosons.

The inclusion of this decay mode can be divided into several steps. First we compute the full decay matrix-element for the process  $H \rightarrow WW \rightarrow \ell\nu\ell\nu$ , which has to be integrated over the final-state particle phase-space. In the inclusive case this would simply correspond to the multiplication of the Higgs production cross-section with the branching ratio for the full decay. Since we want to impose selection cuts on the final-state particle observables we have to parametrize the final-state phase space appropriately. Then we are able to write a selection routine, that returns, as a function of the Higgs momentum and potential additional gluon momenta, either zero (if the 'event' does not pass the selection cuts) or the weight of the full decay (otherwise).

Finally we discuss how the numerical integration is highly sensitive to the selection cuts and how we have to modify the numerical integration strategy in order to overcome this obstacle.

### D.1 Concept

FEHiP uses the sector-decomposition techniques to compute the Higgs production cross-section. In this technique the finding of singular phase-space regions is fully automated and the cancellation of  $1/\varepsilon$  poles that describe divergences in dimensional regularization is performed numerically. The result of the procedure is a finite set of sectors  $S_i$ ,  $i \in 1, \dots, N$ , that have to be numerically integrated in a hyper-cube of dimension  $d$ . The dimension

varies with the final-state particle multiplicity. The total cross-section is then the integral over the sum of all these sectors <sup>1</sup>, i.e.

$$\sigma = \int_0^1 \left( \prod_{k=1}^d d\lambda_k \right) \sum_i S_i(\{\lambda_k\}), \quad (\text{D.1})$$

where the sectors are dependent on the integration variables  $\lambda_k$ . The particle momenta can be obtained through a sector-dependent mapping of the  $\lambda$ 's to the Higgs and gluon kinematics. In general each sector consists of several mappings of integration variables to kinematics, i.e. one point in integration phase-space generally corresponds to multiple physical final-state phase-space points. For simplicity we neglect this fact at this stage. Using this we can write the cross-section including the Higgs decay as

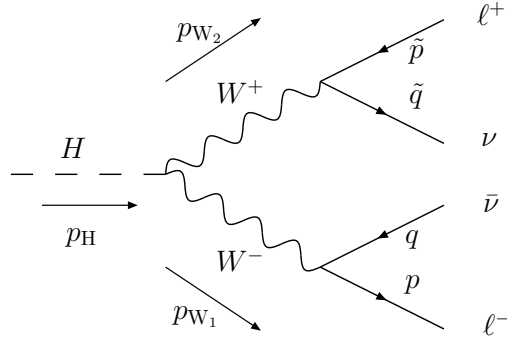
$$\sigma = \int_0^1 \left( \prod_{k=1}^d d\lambda_k \right) \sum_i S_i(\{\lambda_k\}) \Sigma(\{p_i\}), \quad (\text{D.2})$$

where  $\Sigma$  describes the full decay of the Higgs into leptons as well as some selection function, and  $\{p_i\}$  is the collection of the Higgs and gluon momenta. We want to emphasize that the function  $\Sigma$  is not factorizable from the sum over all the sectors. As mentioned before, the mapping of the integration variables to the kinematics  $\{p_i\}$  is sector dependent, furthermore each sector typically consists of several mappings (i.e. even the factorization of  $\Sigma$  within this sum is not generally true, we only use it here to keep the notation simple).

We now compute the decay function  $\Sigma$ . The integral of interest is

$$\Sigma = \frac{\pi}{m_H \Gamma_H (2\pi)^9} \int [dp][dq][d\tilde{p}][d\tilde{q}] |M|^2 \delta^4(p_H - p - q - \tilde{p} - \tilde{q}), \quad (\text{D.3})$$

where  $p_H$  is the Higgs momentum and  $p, q, \tilde{p}, \tilde{q}$  are the final state lepton momenta and  $[dp] = dp^4 \delta(p^2)$  is the Lorentz-invariant measure of the four-dimensional integration. To apply a selection we multiply the integrand with a selection function  $\mathcal{O}$  that then depends on the full event kinematics  $\{p_f\}$  (cf. section 2.3). The prefactor of this function comes from the Higgs propagator, as well as from some constant extracted for the computation of the decay width.


 Figure D.1: Feynman-diagram for the Higgs decaying in  $H \rightarrow WW \rightarrow l\nu l\nu$ .

## D.2 Matrix Element

We show the tree level Feynman diagram for the Higgs decay into leptons via a pair of W bosons in Fig. D.1. Using the Feynman-rules from chapter 1 the matrix element is

$$\begin{aligned}
 i\mathcal{M} = & \bar{u}^s(p) \left( \frac{ig}{2\sqrt{2}} \right) \gamma_\mu (1 - \gamma^5) v^{s'}(q) \left( \frac{-i}{p_{W_1}^2 - m_W^2 + im_W \Gamma_W} \right) \times \\
 & \left( g^{\mu\nu} - \frac{p_{W_1}^\mu p_{W_1}^\nu}{m_W^2 - im_W \Gamma_W} \right) 2i \frac{m_W^2}{v} g_{\nu\sigma} \left( \frac{-i}{p_{W_2}^2 - m_W^2 + im_W \Gamma_W} \right) \times \\
 & \left( g^{\sigma\rho} - \frac{p_{W_2}^\sigma p_{W_2}^\rho}{m_W^2 - im_W \Gamma_W} \right) \bar{u}(\tilde{q})^r \left( \frac{ig}{2\sqrt{2}} \right) \gamma_\rho (1 - \gamma^5) v^{r'}(\tilde{p}),
 \end{aligned} \tag{D.4}$$

where we have used a simple Breit-Wigner propagator for the W boson (see e.g. [85]),  $s^{(\prime)}, r^{(\prime)}$  are the lepton-spin indices and  $m_W$  and  $\Gamma_W$  denote the W mass and width. We square this and sum over all final state spin states. We then use again the tool FORM to perform the trace over the gamma-matrices and to contract all the Lorentz-indices. The final square of the amplitude is then

$$\begin{aligned}
 |\mathcal{M}|^2 = & \frac{4m_W^4 g_w^4}{v^2} \cdot \\
 & \left( \frac{4(p \cdot \tilde{q})(q \cdot \tilde{p})}{\left( m_{W_1}^4 + (\Gamma_W^2 - 2m_{W_1}^2)m_W^2 + m_W^4 \right) \left( m_{W_2}^4 + (\Gamma_W^2 - 2m_{W_2}^2)m_W^2 + m_W^4 \right)} \right).
 \end{aligned} \tag{D.5}$$

We want to point out the difference between  $m_W$ , which is the physical W on-shell mass, and  $m_{W_1}/m_{W_2}$ , which are the square roots of the squares of the W four-momenta  $p_{W_1}$  and  $p_{W_2}$ .

---

<sup>1</sup> If a sector has dimension less than  $d$ , then this sector is simply extended to  $d$  by multiplications with one.

### D.3 H→WW Phase-Space

The phase-space is actually nothing but the 1→4, massive to massless phase-space. We want to parametrize this phase-space by variables  $\lambda \in [0, 1]$ . In order to take explicitly into account the Breit-Wigner shape of the W propagator it is useful to split the decay into two step, namely first to treat the Higgs decay into W bosons, and then the decay of the W bosons into leptons. For this we parametrize the phase-space in four-momenta-transfers, similar to the Higgs production phase-space parametrization. In principle any other parametrization would be possible, i.e. a parametrization taking into account the specific selection cuts on the final state particles  $(p_T, \eta)$ . We tested such a parametrization as well and found no significant improvement for the numerical integration behavior.

By inserting the integration over the mass of both W bosons we rewrite eq. D.3 as

$$\begin{aligned} \Sigma = \frac{4\pi}{m_H \Gamma_H (2\pi)^9} \int dm_{W_1} dm_{W_2} m_{W_1} m_{W_2} d^4 p_{W_1} d^4 p_{W_2} d^4 p d^4 q d^4 \tilde{p} d^4 \tilde{q} |M|^2 \\ \delta^4(p_H - p_{W_1} - p_{W_2}) \delta^4(p_{W_1} - p - q) \delta^4(p_{W_2} - \tilde{p} - \tilde{q}) \\ \delta(p_{W_1}^2 - m_{W_1}^2) \delta(p_{W_2}^2 - m_{W_2}^2) \delta(p^2) \delta(q^2) \delta(\tilde{p}^2) \delta(\tilde{q}^2). \end{aligned} \quad (\text{D.6})$$

The splitting of the phase-space is then manifest and we can parametrize first the H→WW phase space, which is

$$\begin{aligned} \Omega = \int d^4 p_{W_1} d^4 p_{W_2} \delta^4(p_H - p_{W_1} - p_{W_2}) \delta(p_{W_1}^2 - m_{W_1}^2) \delta(p_{W_2}^2 - m_{W_2}^2) = \\ = \int d^4 p_{W_1} \delta(p_{W_1}^2 - m_{W_1}^2) \delta((p_H - p_{W_1})^2 - m_{W_2}^2) \end{aligned} \quad (\text{D.7})$$

$$\text{with } p_{W_2} = p_H - p_{W_1}. \quad (\text{D.8})$$

After inserting integration over two Lorentz invariant scalars  $s_{1w}$  and  $s_{2w}$  one gets

$$\begin{aligned} \Omega = \int ds_{1w} ds_{2w} \int d^4 p_{W_1} \delta(p_{W_1}^2 - m_{W_1}^2) \delta(m_H^2 - 2p_H p_{W_1} + p_{W_1}^2 - m_{W_2}^2) \\ \delta\left(s_{1w} - \frac{(g_1 - p_{W_1})^2}{(g_1 + g_2)^2}\right) \delta\left(s_{2w} - \frac{(g_2 - p_{W_1})^2}{(g_1 + g_2)^2}\right), \end{aligned} \quad (\text{D.9})$$

where  $g_1$  and  $g_2$  are the four-momenta of the two interacting partons from the initial protons  $P_i$  with

$$\begin{aligned} g_1 = x_1 P_1 \\ g_2 = x_2 P_2. \end{aligned} \quad (\text{D.10})$$

Going into the rest frame of the CM system of the two partons this leads to

$$\Omega = \int ds_{1w} ds_{2w} \int d^4 p_{W_1} \delta(p_{W_1}^2 - m_{W_1}^2) \delta(m_H^2 - 2p_H p_{W_1} + p_{W_1}^2 - m_{W_2}^2) \delta\left(s_{1w} - \frac{-p_{W_1}^0 + p_{W_1}^z}{\sqrt{s}} - \frac{p_{W_1}^2}{s}\right) \delta\left(s_{2w} - \frac{-p_{W_1}^0 - p_{W_1}^z}{\sqrt{s}} - \frac{p_{W_1}^2}{s}\right), \quad (\text{D.11})$$

with  $s = (g_1 + g_2)^2$  the squared CM energy of the partons.

Now the integration variables are changed to

$$\Omega = \int ds_{1w} ds_{2w} \int dp_{W_1}^0 dp_{W_1}^z dp_{W_1}^\perp d\phi p_{W_1}^\perp \delta(p_{W_1}^2 - m_{W_1}^2) \delta(m_H^2 - 2p_H p_{W_1} + p_{W_1}^2 - m_{W_2}^2) \delta\left(s_{1w} - \frac{-p_{W_1}^0 + p_{W_1}^z}{\sqrt{s}} - \frac{p_{W_1}^2}{s}\right) \delta\left(s_{2w} - \frac{-p_{W_1}^0 - p_{W_1}^z}{\sqrt{s}} - \frac{p_{W_1}^2}{s}\right). \quad (\text{D.12})$$

Integrating over  $dp_{W_1}^0$ ,  $dp_{W_1}^z$  and  $dp_{W_1}^\perp$  using the first and the two last  $\delta$ -distributions one gets

$$\begin{aligned} p_{W_1}^0 &= \frac{\sqrt{s}}{2}(-s_{1w} - s_{2w}) + \frac{m_{W_1}^2}{\sqrt{s}} \\ p_{W_1}^z &= \frac{\sqrt{s}}{2}(+s_{1w} - s_{2w}) \\ p_{W_1}^\perp &= \left[ \left( \sqrt{s} s_{1w} - \frac{m_{W_1}^2}{\sqrt{s}} \right) \left( \sqrt{s} s_{2w} - \frac{m_{W_1}^2}{\sqrt{s}} \right) - m_{W_1}^2 \right]^{1/2} \end{aligned} \quad (\text{D.13})$$

and the integral  $\Omega$  becomes

$$\Omega = \frac{s}{4} \int ds_{1w} ds_{2w} \int d\phi \delta(m_H^2 - 2p_H p_{W_1} + m_{W_1}^2 - m_{W_2}^2). \quad (\text{D.14})$$

Setting  $B_{1w} := (s_{1w} - m_{W_1}^2/s)$  and  $B_{2w} := (s_{2w} - m_{W_1}^2/s)$  eq. D.13 simplifies to

$$\begin{aligned} p_{W_1}^0 &= \frac{\sqrt{s}}{2}(-B_{2w} - B_{1w}) \\ p_{W_1}^z &= \frac{\sqrt{s}}{2}(-B_{2w} + B_{1w}) \\ p_{W_1}^\perp &= [s(B_{1w} B_{2w} - m_{W_1}^2/s)]^{1/2}. \end{aligned} \quad (\text{D.15})$$

Using eq. D.15 to evaluate the last  $\delta$ -distribution, the restriction for the angle  $\phi$  between  $p_H$  and  $p_{W_1}$  becomes

$$\cos(\phi) = \frac{\delta m^2 + 2p_H^0 p_{W_1}^0 - 2p_H^z p_{W_1}^z}{2p_H^\perp p_{W_1}^\perp} \quad (\text{D.16})$$

with  $\delta m^2 := m_{W_2}^2 - m_{W_1}^2 - m_H^2$  and the integral

$$\Omega = \frac{\sqrt{s}}{2} \int dB_{1w} dB_{2w} I(B_{1w}, B_{2w}) \quad (\text{D.17})$$

with

$$I(B_{1w}, B_{2w}) := \left[ 4p_H^{\perp 2} \left( B_{1w} B_{2w} - \frac{m_{W_1}^2}{s} \right) - \left( \frac{\delta m^2}{\sqrt{s}} - B_{1w} (p_H^0 + p_H^z) - B_{2w} (p_H^0 - p_H^z) \right)^2 \right]^{-1/2}. \quad (\text{D.18})$$

The square root condition leads to the following boundaries for the integration variables:

$$\begin{aligned} \alpha_2 - \beta_2 < B_{2w} < \alpha_2 + \beta_2 \\ \alpha_1(B_{2w}) - \beta_1(B_{2w}) < B_{1w} < \alpha_1(B_{2w}) + \beta_1(B_{2w}) \end{aligned} \quad (\text{D.19})$$

with

$$\begin{aligned} \alpha_2 &:= \frac{-C_{2h}(\tilde{m}_{W_1}^2 - \tilde{m}_{W_2}^2 + \tilde{m}_H^2)}{2\tilde{m}_H^2} \\ \beta_2 &:= \frac{1}{2\tilde{m}_H^2} \sqrt{C_{2h}^2 \delta\tilde{m}_{++} + \delta\tilde{m}_{--} \delta\tilde{m}_{-+} + \delta\tilde{m}_{+-}} \end{aligned} \quad (\text{D.20})$$

and

$$\begin{aligned} \delta\tilde{m}_{\pm\pm} &:= \tilde{m}_{W_1} \pm \tilde{m}_{W_2} \pm \tilde{m}_H \\ \tilde{m}_i &:= m_i / \sqrt{s} \quad \text{with } i = H, W_1, W_2, \end{aligned} \quad (\text{D.21})$$

as well as

$$\begin{aligned} \alpha_1(B_{2w}) &:= \frac{-2B_{2w}\tilde{m}_H^2 + C_{2h}(\tilde{m}_{W_2}^2 - \tilde{m}_{W_1}^2 - \tilde{m}_H^2 + B_{2w}C_{1h})}{C_{2h}^2} \\ \beta_1(B_{2w}) &:= \frac{2}{C_{2h}^2} [(C_{2h}(-B_{2w} + C_{2h})\tilde{m}_{W_1}^2 + C_{2h}B_{2w}\tilde{m}_{W_2}^2 + \\ &\quad B_{2w}(B_{2w} - C_{2h})\tilde{m}_H^2)(\tilde{m}_H^2 - C_{1h}C_{2h})]^{1/2}. \end{aligned} \quad (\text{D.22})$$

Here  $C_{1h}$  and  $C_{2h}$  are defined as

$$\begin{aligned} C_{1h} &:= \frac{m_H^2 - (g_1 - p_H)^2}{(g_1 + g_2)^2} \\ C_{2h} &:= \frac{m_H^2 - (g_2 - p_H)^2}{(g_1 + g_2)^2}. \end{aligned} \quad (\text{D.23})$$

Changing integration variables to  $\lambda_1$  and  $\lambda_2$  with  $\lambda_i \in [0, 1]$  one gets

$$\Omega = \frac{1}{2\tilde{m}_H^2} \int_0^1 d\lambda_1 d\lambda_2 \sqrt{\frac{\delta\tilde{m}_{++} + \delta\tilde{m}_{--} \delta\tilde{m}_{-+} + \delta\tilde{m}_{+-}}{(1 - \lambda_1)\lambda_1}}. \quad (\text{D.24})$$

Furthermore one can change the integration variable  $\lambda_1$  according to

$$\begin{aligned}\lambda_1 &= \frac{\cos(\pi\hat{\lambda}_1) + 1}{2} \\ d\lambda_1 &= -\frac{\pi \sin(\pi\hat{\lambda}_1)d\hat{\lambda}_1}{2}\end{aligned}\tag{D.25}$$

and ends up with

$$\Omega = \frac{\pi}{2\tilde{m}_H^2} \int_0^1 d\hat{\lambda}_1 d\lambda_2 \sqrt{\delta\tilde{m}_{++}\delta\tilde{m}_{--}\delta\tilde{m}_{+-}\delta\tilde{m}_{-+}}.\tag{D.26}$$

The Lorentz invariant scalars  $B_{1w}$  and  $B_{2w}$  become then

$$\begin{aligned}B_{2w} &= \frac{1}{2\tilde{m}_H^2} \left( C_{2h}(\tilde{m}_{W_1}^2 - \tilde{m}_{W_2}^2 + \tilde{m}_H^2) + (2\lambda_2 - 1)\sqrt{C_{2h}^2\delta\tilde{m}_{++}\delta\tilde{m}_{--}\delta\tilde{m}_{+-}\delta\tilde{m}_{-+}} \right) \\ B_{1w} &= \frac{C_{1h}}{2} + \frac{C_{1h}(\tilde{m}_{W_1} - \tilde{m}_{W_2})(\tilde{m}_{W_1} + \tilde{m}_{W_2})}{2\tilde{m}_H^2} + \\ &\quad \frac{(2\lambda_2 - 1)(C_{1h}C_{2h} - 2\tilde{m}_H^2)\sqrt{C_{2h}^2\delta\tilde{m}_{++}\delta\tilde{m}_{--}\delta\tilde{m}_{+-}\delta\tilde{m}_{-+}}}{2C_{2h}^2\tilde{m}_H^2} + \\ &\quad 2\cos(\pi\hat{\lambda}_1)\sqrt{\frac{(1-\lambda_2)\lambda_2(C_{1h}C_{2h} - \tilde{m}_H^2)\delta\tilde{m}_{++}\delta\tilde{m}_{--}\delta\tilde{m}_{+-}\delta\tilde{m}_{-+}}{C_{2h}^2\tilde{m}_H^2}}\end{aligned}\tag{D.27}$$

The momenta in the proton-proton rest frame are then

$$\begin{aligned}p_{W_1}^0 &= \frac{1}{2}\sqrt{X}(-x_1B_{2w} - x_2B_{1w}) \\ p_{W_1}^z &= \frac{1}{2}\sqrt{X}(x_2B_{1w} - x_1B_{2w}) \\ p_{W_1}^\perp &= \sqrt{x_1x_2X}(B_{1w}B_{2w} - \tilde{m}_{W_1}^2)^{1/2},\end{aligned}\tag{D.28}$$

with

$$X = (P_1 + P_2)^2$$

the proton-proton squared CM energy.

## D.4 $W \rightarrow \ell\nu\ell\nu$ Phase-Space

Having parametrized the Higgs decay, we now find a parametrization for the  $W \rightarrow \ell\nu\ell\nu$  phase-space, which is

$$\begin{aligned}\Xi &= \int d^4p d^4q \delta^4(p_{W_1} - p - q)\delta(p^2)\delta(q^2) = \\ &= \int d^4p \delta(p^2)\delta((p_{W_1} - p)^2)\end{aligned}\tag{D.29}$$

with

$$q = p_{W_1} - p. \quad (\text{D.30})$$

Again, we insert Lorentz-scalars such as

$$\begin{aligned} \Xi = \int da_{1l} da_{2l} d^4p \delta(p^2) \delta((p_{W_1} - p)^2) \times \\ \delta\left(a_{1l} - \frac{(g_1 - p)^2}{(g_1 + g_2)^2}\right) \delta\left(a_{2l} - \frac{(g_2 - p)^2}{(g_1 + g_2)^2}\right) \end{aligned} \quad (\text{D.31})$$

with  $g_1$  and  $g_2$  again the momenta of the initial partons.

Using analogue techniques as in the H → WW case with the final-state particle masses set to 0 we find

$$\Xi = \frac{\pi}{2} \int_0^1 d\hat{\lambda}_1 d\lambda_2, \quad (\text{D.32})$$

where the Lorentz invariant scalars  $a_{1l}$  and  $a_{2l}$  are

$$\begin{aligned} a_{2l} &= -B_{2w}(1 - \gamma_2) \\ a_{1l} &= \frac{\tilde{m}_{W_1}^2}{B_{2w}}(1 - 2\gamma_2) - B_{1w}(1 - \gamma_2) + \\ &\quad \frac{2\tilde{m}_{W_1}}{B_{2w}} \cos(\pi \hat{\gamma}_1) \sqrt{(1 - \gamma_2)\gamma_2(B_{1w}B_{2w} - \tilde{m}_{W_1}^2)}. \end{aligned} \quad (\text{D.33})$$

The momenta in the proton-proton rest frame are then

$$\begin{aligned} p^0 &= \frac{1}{2} \sqrt{X} (-x_1 a_{2l} - x_2 a_{1l}) \\ p^z &= \frac{1}{2} \sqrt{X} (x_2 a_{1l} - x_1 a_{2l}) \\ p^\perp &= \sqrt{x_1 x_2 X} (a_{1l} a_{2l})^{1/2}. \end{aligned} \quad (\text{D.34})$$

## D.5 Total Phase-Space

The decay-function  $\Sigma$  reads now

$$\begin{aligned} \Sigma = \frac{\sqrt{s}}{(4\pi)^5 \tilde{m}_H^3 \Gamma_H} \int dm_{W_1} dm_{W_2} m_{W_1} m_{W_2} \times \\ \int_0^1 d\hat{\lambda}_1 d\lambda_2 d\hat{\gamma}_1 d\gamma_2 d\hat{\gamma}_1 d\tilde{\gamma}_2 |M|^2 \sqrt{\delta\tilde{m}_{++} \delta\tilde{m}_{--} \delta\tilde{m}_{+-} \delta\tilde{m}_{-+}} \end{aligned} \quad (\text{D.35})$$

where  $\tilde{\gamma}_i$  refer to the  $p_{W_2} \rightarrow \tilde{p} \tilde{q}$  phase space.

For later manipulation we change the masses under the square root back to the nominal masses

$$\delta m_{\pm\pm} := m_{W_1} \pm m_{W_2} \pm m_H, \quad (\text{D.36})$$



which leads to

$$\Sigma = \frac{1}{(4\pi)^5 m_H^3 \Gamma_H} \int dm_{W_1} dm_{W_2} m_{W_1} m_{W_2} \times \int_0^1 d\hat{\lambda}_1 d\lambda_2 d\hat{\gamma}_1 d\gamma_2 d\hat{\gamma}_1 d\tilde{\gamma}_2 |M|^2 \sqrt{\delta m_{++} \delta m_{--} \delta m_{+-} \delta m_{-+}}. \quad (\text{D.37})$$

Using the square amplitude from eq. D.5 this becomes

$$\Sigma = \frac{m_W^4 g_w^4}{v^2 m_H^3 \Gamma_H^2 6^5 \pi^5} \int dm_{W_1} dm_{W_2} m_{W_1} m_{W_2} \times \int_0^1 d\hat{\lambda}_1 d\lambda_2 d\hat{\gamma}_1 d\gamma_2 d\hat{\gamma}_1 d\tilde{\gamma}_2 \sqrt{\delta m_{++} \delta m_{--} \delta m_{+-} \delta m_{-+}} \times \left( \frac{(p \cdot \tilde{q})(q \cdot \tilde{p})}{\left( (m_{W_1}^2 - m_W^2)^2 + m_W^2 \Gamma_W^2 \right) \left( (m_{W_2}^2 - m_W^2)^2 + m_W^2 \Gamma_W^2 \right)} \right). \quad (\text{D.38})$$

The boundaries of the integrations over  $dm_{W_1}$  and  $dm_{W_2}$  are defined by the square root in the integrand,

$$\delta m_{++} \delta m_{--} \delta m_{+-} \delta m_{-+} \geq 0. \quad (\text{D.39})$$

The boundaries are then

$$\begin{aligned} m_{W_1} &\in [0, m_H] \\ m_{W_2} &\in [0, m_H - m_{W_1}]. \end{aligned} \quad (\text{D.40})$$

Changing the mass integration variables according to

$$\begin{aligned} z_1 &:= \tan^{-1} \left( \frac{m_{W_1}^2 - m_W^2}{m_W \Gamma_W} \right) \\ z_2 &:= \tan^{-1} \left( \frac{m_{W_2}^2 - m_W^2}{m_W \Gamma_W} \right) \end{aligned} \quad (\text{D.41})$$

we find

$$\Sigma = \frac{2\pi^3 m_W^2 g_w^4}{v^2 m_H^3 \Gamma_H \Gamma_W^2 2^8 \pi^5} \int_{z_i^{\min}}^{z_i^{\max}} dz_1 dz_2 \int_0^1 d\hat{\lambda}_1 d\lambda_2 d\hat{\gamma}_1 d\gamma_2 d\hat{\gamma}_1 d\tilde{\gamma}_2 \times \sqrt{\delta m_{++} \delta m_{--} \delta m_{+-} \delta m_{-+}} (p \cdot \tilde{q})(q \cdot \tilde{p}), \quad (\text{D.42})$$

with

$$\begin{aligned} z_1^{\min} &:= \tan^{-1} \left( \frac{-m_W^2}{m_W \Gamma_W} \right) \\ z_1^{\max} &:= \tan^{-1} \left( \frac{m_H^2 - m_W^2}{m_W \Gamma_W} \right) \\ z_2^{\min} &:= \tan^{-1} \left( \frac{-m_W^2}{m_W \Gamma_W} \right) \\ z_2^{\max} &:= \tan^{-1} \left( \frac{(m_H - m_{W_1})^2 - m_W^2}{m_W \Gamma_W} \right), \end{aligned} \quad (\text{D.43})$$

where now all the  $\delta m_{ii}$  and  $m_{W_1}$  are functions of  $z_i$ .

Mapping the  $z_i$  interval to  $\alpha_i \in [0, 1]$  and using the definitions of  $g_w$  and  $v$  the final result reads

$$\Sigma = \frac{\sqrt{2}(G_f m_W^2)^3 (z_1^{\max} - z_1^{\min})(z_2^{\max} - z_2^{\min})}{2^3 \pi^5 m_H^3 \Gamma_H \Gamma_W^2} \times \int_0^1 d\alpha_1 d\alpha_2 d\hat{\lambda}_1 d\lambda_2 d\hat{\gamma}_1 d\gamma_2 d\hat{\gamma}_1 d\tilde{\gamma}_2 \sqrt{\delta m_{++} \delta m_{--} \delta m_{+-} \delta m_{-+}} (p \cdot \tilde{q})(q \cdot \tilde{p}), \quad (\text{D.44})$$

with  $G_f$  the Fermi-constant. For convenience we define this as

$$\Sigma = C \times \int_0^1 d\Lambda D(\{p_f\}), \quad (\text{D.45})$$

with

$$C \equiv \frac{\sqrt{2}(G_f m_W^2)^3 (z_1^{\max} - z_1^{\min})(z_2^{\max} - z_2^{\min})}{2^3 \pi^5 m_H^3 \Gamma_H \Gamma_W^2}, \quad (\text{D.46})$$

$$D(\{p_f\}) \equiv \sqrt{\delta m_{++} \delta m_{--} \delta m_{+-} \delta m_{-+}} (p \cdot \tilde{q})(q \cdot \tilde{p}),$$

and  $d\Lambda$  denotes the integration over all the variables in eq. D.44. Here  $D(\{p_f\})$  symbols the implicit dependence of the integrand on the particle kinematics.

We can now write the total cross-section including the decay as

$$\sigma = \int_0^1 \left( \prod_{k=1}^d d\lambda_k \right) \sum_i \left( S_i(\{\lambda_k\}) \times C \int_0^1 d\Lambda D(\{p_f\}) \mathcal{O}(\{p_f\}) \right), \quad (\text{D.47})$$

where we have now explicitly added a selection function  $\mathcal{O}$ . We can interchange the sum over the sectors and the integration over the decay phase-space in order to only have to integrate over one set of variables. This reads then

$$\sigma = \int_0^1 d\Omega \sum_i (S_i(\{\lambda_k\}) \times C D(\{p_f\}) \mathcal{O}(\{p_f\})), \quad (\text{D.48})$$

where the integration hyper-cube dimension is now  $d + 8$ , i.e. the dimension of the sector plus the dimension of the decay phase-space and

$$d\Omega = \left( \prod_{k=1}^d d\lambda_k \right) d\Lambda. \quad (\text{D.49})$$

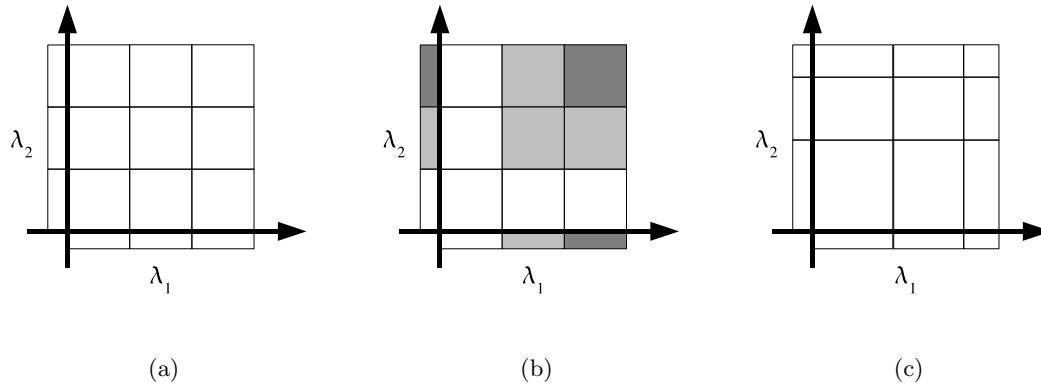


Figure D.2: Schematic example for the VEGAS MC algorithm.

## D.6 Numerical Integration

### D.6.1 VEGAS algorithm

In order to discuss the numerical integration strategy we want to briefly describe the program used in FEHIP, the Vegas program of PVEGAS [78]. The idea of the Vegas algorithm [79] is stratified and importance sampling. We explain this algorithm on a simple two-dimensional example, i.e.

$$\sigma = \int_0^1 d\lambda_1 d\lambda_2 I(\lambda_1, \lambda_2), \quad (\text{D.50})$$

where  $I$  is some function that is finite over the whole two-dimensional integration region. Each integration variable is then divided into a fixed number of bins. As an example we divide each variable in three bins of the same size, see Fig. D.2(a). In the next step we sample the integrand in an appropriate number of phase-space points to estimate the importance of the function  $I$ . We show this in Fig. D.2(b). Dark (light) regions denote phase-space regions where the weight of the integrand is large (small). The information on the importance of the integrand is not stored in each of the sub-regions (these are in general hyper-cubes). For each variable we allocate a one-dimensional histogram storing the projection of the integrand onto this variable. This is shown as the small region below (left) of the variable axis.

In the second step the binning in each integration variable is modified in such a way, that the total weight of the integrand of all the bins is smoothed out (Fig. D.2(c)), i.e. in

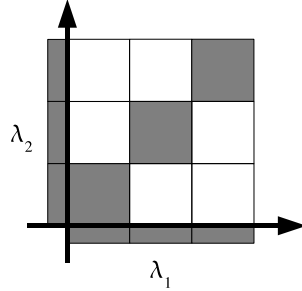


Figure D.3: Example for an integrand with *non-factorizing singularities*.

the important regions the bins get smaller, while in the unimportant regions the bins get wider (the total number of bins stays unchanged).

In the further sampling of the integrand we first choose one of the sub-regions randomly, and then a phase-space point within this sub-region. This procedure is performed iteratively, such that we end up sampling the phase-space in more detail in the important region. The procedure is called the adaptation of the grid, meaning that the binning in each of the variables gets adapted to the shape of the integrand.

This procedure is very successful as long as the important regions can be factorized in the single integration variables. In Fig. D.3 we show an example for an integrand with so-called *non-factorizing singularities*. The projection of the importance on the variable axis is flat and the adaptation cannot take place successfully. Integrands like this usually cannot be integrated accurately with the VEGAS algorithm.

### D.6.2 Integrating the Higgs Process

In principle eq. D.48 is ready for numerical integration using the above described technique. In fact it has been shown that for the inclusive case (i.e.  $\mathcal{O} = 1$ ), the adaptation of the grid is sufficient to obtain an accurate result after a reasonable number of iterations. However, When we include a selection function, this adaptation can be spoiled by introducing *non-factorizable singularities* as discussed above. We want to explain how this singularities can arise, again using simple two-dimensional example.

First notice that the integrand in eq. D.48 is a sum over sectors. There is no general rule that these sectors behave in a similar way. We show an example for the addition of two sectors in Fig. D.4(a).

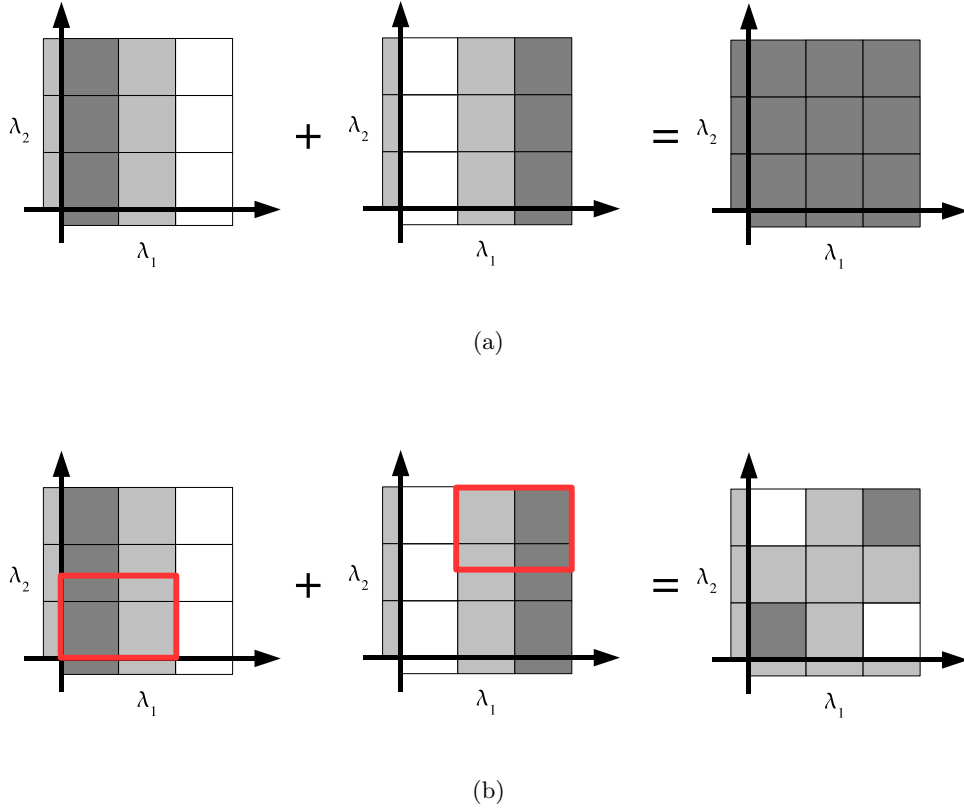


Figure D.4: Example for an integrand as the sum of two sectors with (a) no selection and (b) a selection applied.

Each of the sectors, as well as the sum of both, is well-behaved and we expect adaptation to work fine. In fact, for the sum of both no adaptation is needed since the importance of the total integrand is flat. We now want to apply a selection function. As discussed before, since for every sector we expect a different mapping of the integration variables to the kinematic variables, we cannot expect that the function selects the same integration region. This is shown in Fig. D.4(b). We use the same integrands as before and the red squares denote the integration regions selected by the kinematic cuts. The total integrand now is not flat any more as in the inclusive case, but we introduced *non-factorizing singularities* and the grid adaptation might break down.

This behavior is exactly what we observe in the case of the  $H \rightarrow WW$  process with the selection cuts from section 4.1 applied. The integration strategy that is successful for the inclusive cross-section (as well as for the di-photon decay) does not result in an accurate prediction for the cross-section after the selection cuts. To overcome this problem we

proposed several possible solutions. One of them is the usage of a different integration algorithm that uses binary splitting of the integration region instead of binning in each integration variable (FOAM algorithm [86]). While this approach showed a big improvement concerning the grid-adaptation, it increased the number of needed sampling points dramatically, such that no results could be obtained within a reasonable computing time.

The most successful solution to the problem of the non-factorizing singularities occurring due to the application of the selection cuts is the interchange of the sum and the integration in eq. D.48, reading

$$\sigma = \sum_i \int_0^1 d\Omega (S_i(\{\lambda_k\}) \times CD(\{p_f\})\mathcal{O}(\{p_f\})), \quad (\text{D.51})$$

where each sector is integrated separately and the results of each sector are added at the end. Although the number of sampling points is increased (generally by a factor equal to the number of sectors), the computing time is still much smaller than in the case of the binary splitting (where the number of sampling points generally behaves like a power law). The grid-adaptation for each of the sectors separately is then also guaranteed. This can also be seen in our example. While the sum of the restricted sectors in Fig. D.4(b) behaves badly, the individual sectors do not show any non-factorizable singularities.

An additional benefit of integrating the sectors independently is, that each sector can be integrated on another computational unit, making parallelization and the use of computer clusters straight forward.

# Bibliography

- [1] M. E. Peskin and D. V. Schroeder, *An Introduction to Quantum Field Theory*, Perseus Books (1995)
- [2] M. Kaku, *Quantum Field Theory, A Modern Introduction*, Oxford University Press (1993)
- [3] The Particle Data Group, <http://pdg.lbl.gov>; W.-M. Yao et al., *J. Phys. G* **33** 1 (2006)
- [4] L. M. Brown, M. Dresden, L. Hoddeson and M. Riordan, *The Rise of the Standard Model*, Cambridge University Press (1995)
- [5] M. Goldhaber et al., *Phys. Rev.* **109**, 1015 (1958)
- [6] B. R. Webber, *QCD Phenomenology at High Energy*, CERN Academic Training, February 2008, <http://hr-training.web.cern.ch/hr-training/acad/>
- [7] R. P. Feynman, *Proceedings of the 3rd Topical Conference on High Energy Collision of Hadrons*, Stony Brook, N.Y. (1969)
- [8] G. Altarelli and G. Parisi, *Nucl. Phys. B* **126**, 298 (1977)
- [9] G. Dissertori, I. Knowles and M. Schmelling, *Quantum Chromodynamics, High Energy Experiments and Theory*, International Series of Monographs on Physics Nr. 115, Oxford University Press
- [10] G. Corcella et al., *arXiv:hep-ph/0210213*
- [11] T. Sjostrand, L. Lonnblad and S. Mrenna, *arXiv:hep-ph/0108264*
- [12] J. M. Butterworth, J. R. Forshaw and M. H. Seymour, *Z. Phys. C* **72**, 637 (1996)
- [13] The ALEPH, DELPHI, L3 and OPAL Collaborations and the LEP Working Group for Higgs Searches, *Phys. Lett. B* **565**, 61 (2003)
- [14] M. Bourquin et al., *Preprint 86.02, ECFA* (1981)

- [15] ALEPH, <http://aleph.web.cern.ch/aleph/>;  
DELPHI, <http://delphiwww.cern.ch/>;  
L3, <http://l3.web.cern.ch/l3/>;  
OPAL, <http://opal.web.cern.ch/Opal/>
  
- [16] The LEP Collaborations and the ALEPH, DELPHI, L3 and OPAL Collaborations and the LEP Electroweak Working Group, *arXiv:0712.0929 [hep-ex]*
  
- [17] Particle Data Group, *Eur. Phys. J.* **15**, 1 (2000)
  
- [18] S. Martin, *arXiv:hep-ph/9709356*; L. Pape and D. Treille, *Rept. Prog. Phys.* **69**, 2843-3067 (2006)
  
- [19] L. Randall and R. Sundrum, *Phys. Rev. Lett.* **83**, 3370 (1999); N. Arkani-Hamed, S. Dimopoulos and G. R. Dvali, *Phys. Lett. B* **429**, 263 (1998)
  
- [20] E. Farhi and L. Susskind, *Phys. Rept.* **74**, 277 (1981)
  
- [21] The Large Hadron Collider, <http://lhc.cern.ch/lhc>
  
- [22] M. Spira, VV2H (<http://people.web.psi.ch/spira/vv2h/>)
  
- [23] M. Spira, HQQ (<http://people.web.psi.ch/spira/hqq/>)
  
- [24] A. D. Martin, R. G. Roberts, W. J. Stirling and R. S. Thorne, *Phys. Lett. B* **531**, 216 (2002)
  
- [25] A. Djouadi, J. Kalinowski and M. Spira, *Comput. Phys. Commun.* **108**, 56 (1998)
  
- [26] CMS Collaboration, *Physics Technical Design Report, Vol.2*, *J. Phys. G* **34**, 995 (2007)
  
- [27] M. Dittmar and H. K. Dreiner, *Phys. Rev. D* **55**, 167 (1997)
  
- [28] A. D. Martin, R. G. Roberts, W. J. Stirling and R. S. Thorne, *Phys. Lett. B* **604**, 61 (2004)
  
- [29] R. V. Harlander and W. B. Kilgore, *Phys. Rev. Lett.* **88**, 201801 (2002); C. Anastasiou and K. Melnikov, *Nucl. Phys. B* **646**, 220 (2002); V. Ravindran, J. Smith and W. L. van Neerven, *Nucl. Phys. B* **665**, 325 (2003); O. Brien et al; *Phys. Lett. B* **579**, 149 (2004); R. V. Harlander and W. B. Kilgore, *Phys. Rev. D* **68**, 03001 (2003); R. Hamberg et al, *Nucl. Phys. B* **359**, 343 (1991); C. Anastasiou, L. J. Dixon, K. Melnikov and F. Petriello, *Phys. Rev. Lett.* **91**, 182002 (2003), *Phys. Rev. D* **69**, 094008 (2004)



- [30] R. K. Ellis et al, *Nucl. Phys. B* **178**, 421 (1981); W. T. Giele and E. W. N. Glover, *Phys. Rev. D* **46**, 1980 (1992); K. Fabricius et al, *Phys. Lett. B* **97**, 431 (1980); F. Gutbrod, G. Kramer and G. Schierholz, *Z. Phys. C* **21**, 235 (1984); Z. Kunszt and D. E. Soper, *Phys. Rev. D* **46**, 192 (1992); S. Frixione, Z. Kunszt and A. Signer, *Nucl. Phys. B* **467**, 399 (1996); S. Catani and M. H. Seymour, *Nucl. Phys. B* **485**, 291 (1997)
- [31] S. Catani and M. Grazzini, *Phys. Rev. Lett.* **98**, 222002 (2007)
- [32] C. Anastasiou, K. Melnikov and F. Petriello, *Phys. Rev. D* **69**, 076010 (2004);
- [33] C. Anastasiou, K. Melnikov and F. Petriello, *Phys. Rev. Lett.* **93**, 262002 (2004)
- [34] C. Anastasiou, K. Melnikov and F. Petriello, *Nucl. Phys. B* **724**, 197-246 (2005)
- [35] J. R. Ellis, M. K. Gaillard and D. V. Nanopoulos, *Nucl. Phys. B* **106**, 292 (1976); M. A. Shifman, A. I. Vainshtein, M. B. Voloshin and V. I. Zakharov, *Sov. J. Nucl. Phys.* **30**, 711 (1979)
- [36] M. Spira, A. Djouadi, D. Graudenz and P. M. Zerwas, *Nucl. Phys. B* **453**, 17 (1995)
- [37] S. Moch and A. Vogt, *Phys. Lett. B* **631**, 48 (2005)
- [38] G. Bozzi, S. Catani, D. de Florian and M. Grazzini, *Nucl. Phys. B* **791**, 1 (2008); G. Bozzi, S. Catani, D. de Florian and M. Grazzini, *Nucl. Phys. B* **737**, 73 (2006); G. Bozzi, S. Catani, D. de Florian and M. Grazzini, *Phys. Lett. B* **564**, 65 (2003); S. Catani, D. de Florian and M. Grazzini, *JHEP* **0201**, 015 (2002)
- [39] G. Bozzi, S. Catani, D. de Florian and M. Grazzini,  
<http://arturo.fi.infn.it/grazzini/codes.html>
- [40] S. Frixione and B. R. Webber, *arXiv:hep-ph/0612272*
- [41] S. Frixione and B. R. Webber, *JHEP* **0206**, 029 (2002); S. Frixione, P. Nason and B. R. Webber, *JHEP* **0308**, 007 (2003)
- [42] G. Davatz, G. Dissertori, M. Dittmar, M. Grazzini and F. Pauss, *JHEP* **0405**, 009 (2004); G. Davatz, F. Stöckli, C. Anastasiou, G. Dissertori, M. Dittmar, K. Melnikov and F. Petriello, *JHEP* **0607**, 037 (2006)
- [43] Z. Bern, L. J. Dixon and C. Schmidt, *Phys. Rev. D* **66**, 074018 (2002)
- [44] F. Stöckli, A. G. Holzner and G. Dissertori, *JHEP* **0510**, 079 (2005)
- [45] T. Binoth, J. P. Guillet, E. Pilon, and M. Werlen, *Eur. Phys. J. C* **16**, 311-330 (2000)
- [46] C. Anastasiou, G. Dissertori and F. Stöckli, *JHEP* **0709**, 018 (2007)

- [47] C. Anastasiou, G. Dissertori, F. Stöckli and B. R. Webber, *JHEP* **0803**, 017 (2008)
- [48] G. Davatz, A.-S. Giolo, M. Zanetti, *CMS Note* 2006/048
- [49] T. Binoth, M. Ciccolini, N. Kauer and M. Kraemer, *arXiv:hep-ph/0503094*,  
*arXiv:hep-ph/0604120*, *arXiv:hep-ph/0611170*
- [50] S. Catani, Y. L. Dokshitzer, M. H. Seymour and B. R. Webber, *Nucl. Phys. B* **406**,  
187 (1993); S. D. Ellis and D. E. Soper, *Phys. Rev. D* **48**, 1360 (1993)
- [51] S. Catani, D. de Florian and M. Grazzini, *JHEP* **0201**, 015 (2002)
- [52] G. P. Salam and G. Soyez, *JHEP* **0705**, 086 (2007)
- [53] M. Cacciari and G. P. Salam, *Phys. Lett. B* **641**, 57 (2006)
- [54] M. Dasgupta, L. Magnea and G. P. Salam, *arXiv:0712.3014 [hep-ph]*
- [55] The UA1 Collaboration, *Phys. Lett. B* **122**, 103 (1983); *Phys. Lett. B* **122**, 103 (1983);  
*Phys. Lett. B* **126**, 398 (1983); *Phys. Lett. B* **134**, 469 (1984); *Phys. Lett. B* **147**, 241  
(1984);  
The UA2 Collaboration, *Phys. Lett. B* **122**, 476 (1983); *Phys. Lett. B* **129**, 130 (1983);  
*Z. Phys. C* **24**, 1 (1984).
- [56] The CDF Collaboration, *Phys. Rev. Lett.* **74**, 2626 (1995);  
The D0 Collaboration, *Phys. Rev. Lett.* **74**, 2632 (1995)
- [57] A Large Ion Collider Experiment, <http://aliceinfo.cern.ch>
- [58] The Large Hadron Collider beauty experiment, <http://lhcb.web.cern.ch/lhcb>
- [59] The ATLAS Experiment, <http://atlas.ch>
- [60] The Compact Muon Solenoid Experiment, <http://cms.cern.ch>
- [61] The CMS Collaboration, *The Compact Muon Solenoid Letter of Intent*, CERN/LHCC  
92-3, October 1992;  
The CMS Collaboration, *The Compact Muon Solenoid Technical Proposal*,  
CERN/LHCC 94-38, December 1994.
- [62] CMS, *The Tracker Project, Technical Design Report*, CERN/LHCC 98-6;  
CMS, *The Hadron Calorimeter Project, Technical Design Report*, CERN/LHCC 97-31;  
CMS, *The Electromagnetic Calorimeter Project, Technical Design Report*,  
CERN/LHCC 97-33;  
CMS, *The Muon Project, Technical Design Report*, CERN/LHCC 97-32;  
CMS, *The Trigger and Data Acquisition Project I&II, Technical Design Report*,  
CERN/LHCC 2002-26/27

- [63] The Compact Muon Solenoid Experiment,  
<http://cmsdoc.cern.ch/cms/Publications/detpaper/finaldraft.pdf>, accepted for publication by *JINST*.
- [64] G. Dissertori, *Eur. Phys. J. C* **34**, 85 (2004)
- [65] D. Froidevaux and P. Sphicas, *Ann. Rev. Nucl. Part. Sci.* **56**, 375 (2006)
- [66] <http://cmsdoc.cern.ch/cms/cpt/Software/html/General/>
- [67] CMS Collaboration, *Physics Technical Design Report, Vol.1, CERN/LHCC 2006-001*
- [68] E. Meschi et al., *CMS Note 2001/034*
- [69] R. Frühwirth and T. Speer, *Nucl. Instrum. and Methods A* **534**, 217 (2004)
- [70] G. Davatz, M. Dittmar and F. Pauss, *Phys. Rev. D* **76**, 032001 (2007)
- [71] G. Davatz, M. Dittmar, A.-S. Giolo, *J. Phys. G* **33**, N85 (2007)
- [72] T. Junk, *CERN Preprint, CERN-EP/99-041*
- [73] S. R. Slabospitsky, L. Sonnenschein, *Comput. Phys. Commun.* **148**, 87 (2002)
- [74] M. Dittmar, A.-S. Giolo-Nicollerat, *CMS Internal Note, CMS IN 2004/0.36*
- [75] K. Melnikov and F. Petriello, *Phys. Rev. D* **74**, 114017 (2006); K. Melnikov and F. Petriello, *Phys. Rev. Lett.* **96**, 231803 (2006);
- [76] J. Pumplin, D. R. Stump, J. Huston, H. L. Lai, P. Nadolsky and W. K. Tung, *JHEP* **0207**, 012 (2002)
- [77] <http://www.nikhef.nl/form/>
- [78] R. Kreckel, *arXiv:physics/9710028; arXiv:physics/9812011*
- [79] G. P. Lepage, *CLNS -80/447, Cornell University* (1980)
- [80] <http://projects.hepforge.org/lhapdf/>
- [81] N. N. Bogoliubov and O. S. Parasiuk, *Acta Math.* **97** 227 (1957); K. Hepp, *Commun. Math. Phys.* **2**, 301 (1966); W. Zimmermann, *Commun. Math. Phys.* **15**, 208 (1969)
- [82] C. Anastasiou, K. Melnikov and F. Petriello, *Phys. Rev. Lett.* **93**, 032002 (2004); C. Anastasiou, K. Melnikov and F. Petriello, *Phys. Rev. Lett.* **93**, 262002 (2004); C. Anastasiou, K. Melnikov and F. Petriello, *JHEP* **09**, 014 (2007); G. Heinrich, *Eur. Phys. J. C* **48** 25 (2006);

[83] G. Heinrich, *arXiv:0803.4177 [hep-ph]*

[84] FEHiP, *<http://www.phys.hawaii.edu/~kirill/FEHiP.htm>*

[85] G. Lopez Castro, J. L. M. Lucio and J. Pestiau, *Mod. Phys. Lett.* **A6** 3679 (1991)

[86] S. Jadach, *Comput. Phys. Commun.* **152**, 55 (2003)

# List of Abbreviations

<b>BR</b>	Branching Ratio
<b>CL</b>	Confidence Level
<b>CMS</b>	Compact Muon Solenoid
<b>DIS</b>	Deep Inelastic Scattering
<b>ECAL</b>	Electro-Magnetic Calorimeter
<b>GSF</b>	Gaussian Sum Filter
<b>GWS</b>	Glashow-Salam-Weinberg
<b>HCAL</b>	Hadronic Calorimeter
<b>HO</b>	Higher Order
<b>JES</b>	Jet Energy Scale
<b>KF</b>	Kalman Filter
<b>LHC</b>	Large Hadron Collider
<b>LL</b>	Leading Logarithms
<b>LO</b>	Leading Order
<b>MC</b>	Monte Carlo
<b>NLL</b>	Next-To-Leading Logarithms
<b>NLO</b>	Next-To-Leading Order
<b>NNLL</b>	Next-To-Next-To-Leading Logarithms
<b>NNLO</b>	Next-To-Next-To-Leading Order
<b>PDF</b>	Parton Distribution Function
<b>QCD</b>	Quantum Chromodynamics
<b>QED</b>	Quantum Electrodynamics
<b>QFT</b>	Quantum Field Theory
<b>RGE</b>	Renormalization Group Equation
<b>SM</b>	Standard Model
<b>UE</b>	Underlying Event



# Acknowledgment

I would like to thank Prof. Günther Dissertori, as well as the entire HEP group of the Institute for Particle Physics of ETH Zurich for having given me the possibility to work in this exciting subject of Particle Physics and to write this thesis. Working under the inspiring supervision of Günther Dissertori and collaborating with him as well as with the group of Prof. Felicitas Pauss has been very interesting and fruitful. Having had the possibility of working in a scientifically challenging environment such as the community of the CMS experiment at CERN cannot be taken for granted. Thank you all for letting me participate so intensively.

Further I owe extraordinary thank to Babis Anastasiou, not only for the intense collaboration, but also for many helpful suggestions, by far not only, but especially concerning particle physics phenomenology. Further thank goes to Bryan Webber, Giovanna Davatz, Michael Dittmar, as well as to Frank Petriello and Kirill Melnikov for collaborating with me for several publications.

Many people helped me to finish my PhD studies successfully. I would like to thank all the people sharing time with me at CERN. These are especially the former and present co-workers in the HEP group of the IPP at CERN: André, Alison, Jan, Radek, Giovanna and Ann-Sylvie, who helped me especially in the beginning of my stay at CERN and Joanna, Thomas, Wieland, Matthias, Carmelo, Kostas, Frederic, Pedja and Michael for many partially still ongoing discussions.

Special thank goes to Filip Moortgat, who not only shared office with me for the past two year, but also helped me in many situation, whether related to physics or not.

Last but not least I owe gratitude to my family and to my friends, who have shown great understanding and support for my work. I have to apologize for many missed dinner and movie invitations, as well as for even more missed card, handball and snooker games and numerous guy's-nights-out. I could not have done it without you.





# Curriculum Vitae

**Name** Fabian Stöckli  
**Date of Birth** 11<sup>th</sup> September 1979  
**Nationality** Swiss

---

## Education

2005-2008 **CERN, Switzerland**  
*PhD in Particle Physics, Group of Prof. G. Dissertori, ETH Zurich*

1999-2004 **ETH Zurich, Switzerland**  
*Diploma in Theoretical Physics*

1997-1999 **Kantonschule Wohlen, Switzerland**  
*3rd and 4th year, Matura Typus E*

1996-1997 **Gymnasium Jakobstad, Finland**  
*High School studies*

1995-1996 **Kantonschule Wohlen, Switzerland**  
*1st year, Matura Typus E*

1986-1995 **Primary and Secondary School Wohlen, Switzerland**  
*Elementary and secondary school*

---

## Scientific Publications

2008 **QCD radiation effects on the  $H \rightarrow WW \rightarrow \ell\nu\ell\nu$  signal at the LHC**  
C. Anastasiou, G. Dissertori, F. Stöckli and B. R. Webber  
*JHEP 0803:017,2008*

2007 **NNLO QCD predictions for the  $H \rightarrow WW \rightarrow \ell\nu\ell\nu$  signal at the LHC**  
C. Anastasiou, G. Dissertori and F. Stöckli  
*JHEP 0709:018,2007*

2006 **Combining Monte Carlo generators with next-to-next-to-leading order calculations: Event reweighting for Higgs boson production at the LHC**  
G. Davatz, F. Stöckli, C. Anastasiou, G. Dissertori, M. Dittmar, K. Melnikov and F. Petriello  
*JHEP 0607:037,2006*

2005 **Study of perturbative QCD predictions at next-to-leading order and beyond for  $pp \rightarrow H \rightarrow \gamma\gamma + X$**   
F. Stöckli, A. G. Holzner and G. Dissertori  
*JHEP 0510:079,2005*

2005 **The ALPS project: Open source software for strongly correlated systems**  
F. Alet et al.  
*J.Phys.Soc.Jap.Suppl.74:30,2005*

